Selbstorganisationsprozesse organischer supramolekularer Verbindungen im Bulk und in Kompositmaterialien durch Strukturaufklärungen mit NMR-kristallographischen Methoden

Dissertation

zur Erlangung des akademischen Grades eines

Doktors der Naturwissenschaften (Dr. rer. nat.)

im Fach Chemie

an der Fakultät Biologie, Chemie und Geowissenschaften

der Universität Bayreuth

vorgelegt von

Marko Schmidt

geboren in Berlin

Bayreuth, 2013

Die vorliegende Arbeit wurde in der Zeit von Juni 2009 bis Dezember 2013 in Bayreuth am Lehrstuhl für Anorganische Chemie I/III unter Betreuung von Herrn Prof. Dr. Jürgen Senker angefertigt.

Vollständiger Abdruck der von der Fakultät für Biologie, Chemie und Geowissenschaften der Universität Bayreuth genehmigten Dissertation zur Erlangung des akademischen Grades eines Doktors der Naturwissenschaften (Dr. rer. nat.).

Dissertation eingereicht am: 12.12.2013

Zulassung durch die Promotionskommission: 18.12.2013

Wissenschaftliches Kolloquium: 17.02.2014

Amtierender Dekan: Prof. Dr. Rhett Kempe

Prüfungsausschuss:

Prof. Dr. Jürgen Senker (Erstgutachter)

Prof. Dr. Stephan Förster (Zweitgutachter)

Prof. Dr. Hans-Werner Schmidt (Vorsitz)

Prof. Dr. Karlheinz Seifert

„Are you happy now with all the choices you’ve made?

Are there times in life when you know you should’ve stayed?

Did you compromise and then realize the price was too much to pay?

Winners and losers, which one will you be today?”

(Michael James "Mike" Ness, Musiker)

Meiner Familie.

Inhaltsverzeichnis

1 Summary

The present thesis deals with structure-relation properties of selected organic compounds building macroscopically supramolecular objects of different dimensionality. In this context, the understanding of the self-organisation of the nanoobjects was of fundamental relevance. For this purpose, structure elucidations using NMR-crystallography were used. On the macroscopic scale, 1D objects typically occur as fibre-like structures, while for 2D objects plate-like morphologies are often observed. On a smaller scale the interpretation of the underlying growth mechanisms and thus the influence of non-covalent interactions, dipole moments or even macrodipoles are still demanding due to the lack of detailed structural information. To generate structure models from powder diffraction data the adopted real space methods were examined in dependency of the size and flexibility of the compounds and rated as being very efficient. Moreover, the novel procedure of a forcefield-assisted Rietveld refinement was successfully tested leading to an effective improvement of the conventional method of a “*rigid-body*”-refinement.

As a first 1D supramolecular compound, the bulk crystal structure of an efficient symmetric 1,3,5-benzenetrisamide (BTA) based nucleating agent for *i*-PP (isotactic polypropylene) with additional outstanding clarifying properties was solved. Here, multiple structure models adapted from X-ray powder diffraction data were built, but - based on the quality criterion of the X-ray analysis plus conventional 1D solid-state NMR spectroscopy - they could not be distinguished. Only the usage of quantitative double quantum (DQ) experiments on a particular synthesised ^{13}C labelled species led to the correct symmetry information. On the basis of the structural motif both non-covalent interactions as well as macrodipoles were identified as structure directing elements.

The structure of the former mentioned additive material was then solved within *i*-PP leading to an end of a long-time discussion. For this purpose the ^{13}C enriched compound was incorporated into an *i*-PP matrix using concentrations being moderate for nucleation. The ^{13}C labelled species was identified by ^{13}C CP MAS spectroscopy, while 2D ^{13}C DQ experiments showed a spatial connectivity of the additive molecules. The ^{13}C DQ build-up curve of the enriched nuclei within the

composite material matched excellently with the build-up curve obtained for the bulk material. Performing numerical analysis to evaluate different structural scenarios after all gave proof of a columnar arrangement of the additive within the polymer matrix. However, a linkage between the additive clusters and the polymer was not observed.

To possibly visualize a linkage of the polymer onto the additive clusters *via* NMR spectroscopy, a new ^{19}F labeled BTA was synthesized. The focus was at first again laid on the bulk crystal structure determination. The structure model derived by *ab initio* methods from powder diffraction data could successfully be built within a monoclinic metric. This model was verified using qualitative and quantitative solid-state NMR spectroscopy as well as quantum chemical simulations. It was shown that a hexagonal rod packing with its fast one-dimensional growth being is typical for this substance class was not established, but rather a two-dimensional H-bond mediated zigzag-like structure. The influence of the ^{19}F residue seemed to be crucial for this rarely existing frustrated structure type within the class of BTAs.

As a continuative study, three structurally related cyclohexane-based compounds were synthesized and characterized with respect to their morphological and structural features. SEM measurements revealed the formation of 2D nanosheets with lateral dimensions of several hundred micrometers and with substantial aspect ratios. The macroscopic plate morphology was yet explained on a nanoscale by elucidation of the crystal structures using NMR-crystallography. It was shown that the interplay of the spatial arrangement of the molecules within the unit cell and an extensive hydrogen bond network was responsible for the two-dimensionality. Dipole moments or even macrodipoles which are structure directing for the initially mentioned BTA system did not show any influence on the formation of the structure.

This work is written in the style of a cumulative dissertation. The results are described in detail within the attached publications.

2 Zusammenfassung

Die vorgelegte Arbeit befasst sich mit Struktur-Eigenschafts-Beziehungen ausgewählter organischer Verbindungen, die makroskopisch supramolekulare Objekte unterschiedlicher Dimensionalität ausbilden. Dahingehend ist das Verständnis der Selbstorganisation der Nanoobjekte von fundamentaler Bedeutung. Als Werkzeug hierfür dienten Strukturaufklärungen mit Hilfe der NMR-Kristallographie. Makroskopisch betrachtet existieren 1D-Objekte typischerweise als faserartige Strukturen, während für 2D-Objekte oft plättchenartige Morphologien beobachtet werden. Auf kleineren Größenskalen ist die Deutung der zu Grunde liegenden Wachstumsmechanismen und somit der Einfluss von nichtkovalenten Wechselwirkungen, Dipolmomenten oder gar Makrodipolen aufgrund mangelnder Strukturinformationen nach wie vor anspruchsvoll. Die zur Erzeugung der Strukturmodelle aus Pulverdaten eingesetzten Realraummethoden wurden in Abhängigkeit von Größe und Flexibilität der Verbindungen geprüft und als sehr effizient eingestuft. Zusätzlich wurde die neue Prozedur einer kraftfeldunterstützten Rietveldverfeinerung erfolgreich getestet, welche die klassische Methode der „*rigid-body*“-Verfeinerung wirksam verbessern konnte.

Als eine erste 1D supramolekulare Verbindung wurde die Bulkkristallstruktur eines auf Basis von symmetrischen 1,3,5-Benzoltrisamiden (BTA) sehr effizienten Nukleierungsmittel für *i*-PP (isotaktisches Polypropylen) mit zusätzlich hervorragenden Kläreigenschaften gelöst. Dabei wurden mehrere Strukturmodelle basierend auf Röntgenpulverdaten erstellt, welche aber anhand der röntgenographischen Gütekriterien sowie klassischer 1D Festkörper-NMR-Spektroskopie nicht unterschieden werden konnten. Erst die Anwendung von quantitativen Doppelquantenexperimenten (DQ) an einer speziell synthetisierten ^{13}C isotopenmarkierten Spezies führte zur korrekten Symmetrie. Anhand des Strukturmotivs wurden sowohl nichtkovalente Wechselwirkungen als auch Makrodipole als strukturdirigierende Elemente identifiziert.

Die Struktur des zuvor genannten Additivs wurde dann in *i*-PP aufgeklärt und damit eine langjährige Diskussion beendet. Dafür wurde die ^{13}C angereicherte Spezies in für die Nukleierung angemessene Konzentration in eine *i*-PP Matrix inkorporiert. Die ^{13}C markierte Verbindung wurde durch ^{13}C CP MAS NMR

Spektroskopie identifiziert, während 2D ^{13}C DQ-Experimente eine räumliche Nähe der Additivmoleküle zueinander aufzeigten. Eine ^{13}C DQ-Aufbaukurve der isotopenmarkierten Kerne im Kompositmaterial zeigte dabei eine exzellente Übereinstimmung mit der Aufbaukurve des reinen Bulkmaterials. Eine numerische Auswertung verschiedener struktureller Szenarien lieferte schließlich den Beweis der kolumnaren Anordnung des Additivs im Polymer. Eine Anbindung zwischen den Additivclustern und dem Polymer wurde aber nicht beobachtet.

Um eine Anbindung des Polymers an die Additivcluster mittels NMR-Spektroskopie möglichst sichtbar zu machen, wurde ein neues ^{19}F markiertes BTA synthetisiert. Auch hier lag der Fokus zunächst auf der Bestimmung der Kristallstruktur des Bulkmaterials. Durch *ab initio* Methoden aus Röntgenpulverdaten konnte ein Strukturmodell in einer monoklinen Metrik gewonnen werden. Dieses wurde sowohl qualitativ als auch quantitativ durch FK-NMR-Spektroskopie und quantenchemischen Simulationen verifiziert. Es zeigte sich, dass keine für diese Substanzklasse typische hexagonale Stabpackung mit einem schnellen eindimensionalen Wachstum ausgebildet wurde, sondern vielmehr eine H-Brücken vermittelte zweidimensionale Zick-Zack-Struktur. Der Einfluss des ^{19}F-Substituenten schien dabei ausschlaggebend zu sein für den bisher selten existenten frustrierten Strukturtyp innerhalb der Klasse der BTAs.

Als weiterführende Studie wurden drei strukturverwandte cyclohexanbasierte Verbindungen synthetisiert und ihre morphologischen und strukturellen Aspekte untersucht. Dabei zeigte sich aus REM-Aufnahmen, dass alle Derivate zweidimensionale Nanostrukturen mit großen Aspektverhältnissen ausbilden. Die makroskopische Plättchenmorphologie konnte dann durch Bestimmung der Kristallstrukturen mit Hilfe der NMR-Kristallographie auch auf der Nanoskala erklärt werden. Es wurde gezeigt, dass das Zusammenspiel aus der räumlichen Anordnung der Moleküle in der Elementarzelle sowie einem intensiven Wasserstoffbrückennetzwerk für die Zweidimensionalität verantwortlich war. Dipolmomente oder gar Makrodipole, welche für das anfangs erwähnte BTA-System bedeutend waren, zeigten keinen Einfluss auf die Strukturbildung.

Bei der vorliegenden Arbeit handelt es sich um eine kumulative Dissertation. Die detaillierten Ergebnisse werden thematisch getrennt in den angehängten Publikationen beschrieben.

3 Einführung

3.1 Ziel der Doktorarbeit

Hauptziel der vorgelegten Arbeit war es, mit Hilfe von NMR-kristallographischen Methoden, also einer Kombination aus Synthese, Pulverdiffraktometrie, FK-NMR-Spektroskopie und quantenchemischen Rechnungen, Struktur-Eigenschafts-Beziehungen ausgewählter supramolekularer organischer Verbindungen in Bulkphase herauszuarbeiten, wobei die ausgebildeten supramolekularen Objekte unterschiedliche Dimensionalitäten besitzen. Von den materialchemischen Aspekten her war daher übergeordnet zu klären, wie die Strukturmerkmale auf mikroskopischer Größenskala die jeweilige Form bzw. das Wachstum der Objekte auf makroskopischer Ebene beeinflusst. Die NMR-Kristallographie steht hierbei deshalb im Mittelpunkt, weil der „einfache“ Zugang zu detaillierten Strukturinformationen durch z.B. Einkristallstrukturanalysen verwehrt blieb.

Zur Erzeugung der notwendigen Strukturmodelle *ab initio* aus Pulverdaten wurde dabei auf das relativ neu zur Verfügung stehende Verfahren der Realraummethoden zurückgegriffen. Methodisch betrachtet war einerseits die Frage zu klären, welche Sensitivität diese Methode auf die Größe, Funktionalität sowie Flexibilität der einzelnen molekularen Verbindungen mit ihren funktionellen Gruppierungen besaß. Andererseits galt es zu eruieren, inwieweit eine neuartige kraftfeldgestützte Rietveldverfeinerung der Strukturmodelle auf vorher erwähnte Faktoren reagiert. Diese neue Methode stellt eine Erweiterung der üblicherweise verwendeten „*rigid-body*“-Verfeinerung dar. Die Anwendung eines Kraftfeldes beinhaltet dabei eine erhöhte Flexibilität der strukturellen Verfeinerung, weil lediglich der Bruch bestehender kovalenter Bindungen durch eine Energiebeschränkung verboten ist.

Im Bereich der (formal) eindimensionalen Verbindungen wurde der Fokus auf die Klasse der symmetrischen 1,3,5-Benzoltrisamide gelegt. Es galt zunächst die Bulkkristallstruktur eines kommerziell eingesetzten Nukleierungsmittel für isotaktisches Polypropylen aufzuklären und die strukturellen Aspekte mit den zu Grunde liegenden Wechselwirkungen herauszuarbeiten. Die so gewonnenen strukturellen Daten sollten anschließend mit denen aus einem Additiv/Polymer-

Kompositmaterial verglichen werden. Es wurde im Vorfeld vermutet, dass sich allgemein die Strukturen der BTAs in Bulk und Komposit gleichen. Diese Hypothese sollte FK-NMR-spektroskopisch untersucht und bestätigt oder wiederlegt werden. Ein darauf aufbauendes Ziel war es, sich der Anbindung der kristallinen Bereiche des Polymers an die BTA-Spezies in der Matrix zu widmen, was mit einem vertieften Verständnis des Nukleierungsmechanismus teilkristalliner Polymere einhergeht. Die hierfür notwendigen neuen, fluorhaltigen BTA-Moleküle sollten zunächst synthetisiert und hinsichtlich ihrer strukturellen Eigenschaften im Bulk nachhaltig analytisch untersucht werden, also eine analoge Vorgehensweise wie bei dem eingangs erwähnten BTA-System.

Bei den Benzoltrisamiden handelt es sich mehr oder minder um Moleküle mit kurzen aliphatischen Seitenketten (*t*-Butyl) sowie starren Einheiten (z.B. der Benzolkern als Zentraleinheit oder angeknüpfte Amidgruppierungen). Um die Möglichkeiten bzw. mögliche Grenzen der anfangs erwähnten Realraummethoden und der kraftfeldunterstützten Rietveldverfeinerung auszutesten, sollten diese Verfahren dann bei flexibleren, makroskopisch zweidimensionalen organischen Verbindungen angewendet werden. Das Ziel war, drei symmetrisch 1,4-substituierte Cyclohexanderivate mit verschiedenen Wasserstoffbrückensynthons in der Seitenkette zu synthetisieren und sie hinsichtlich ihrer Morphologie zu untersuchen. Diese Einheiten zeichnen sich dabei durch ihre Anzahl an Donor- und Akzeptorgruppen aus, somit also mit unterschiedlichen Fähigkeiten der intermolekularen H-Brücken-Verknüpfung. Durch die Aufklärung der Kristallstrukturen sollten dabei die makroskopischen Befunde auf molekularer Ebene erklärt werden und die strukturdirigierenden Wechselwirkungen auf der Nanoskala identifiziert werden.

3.2 Supramolekulare Chemie

Als *Friedrich Wöhler* im Jahre 1828 Harnstoff synthetisierte,[1] wurde damit das Feld der molekularen Chemie geboren. Basierend auf der fortwährenden Entwicklung immer neuer und anspruchsvoller Methoden wurde bis heute eine Vielzahl von immer komplexer werdenden molekularen Strukturen erzeugt. Diese Methoden lassen sich - vereinfacht betrachtet - durch den Bruch bestehender sowie die Knüpfung neuer kovalenter Bindungen in präziser und kontrollierter Art und Weise charakterisieren.[2]

Werden darüber hinaus einzelne chemische Baueinheiten über nicht-kovalente, intermolekulare Kräfte zusammengehalten, z.B. über Elektrostatik, Wasserstoffbrückenbindungen, π-π-Wechselwirkungen, van-der-Waals-Wechselwirkungen etc.,[2] gelangt man auf direktem Wege zu dem fachübergreifenden Gebiet der supramolekularen Chemie.[2-5] Die resultierenden supramolekularen Strukturen können dabei Objekte auf praktisch jeder Größenskala ausbilden. Im Vergleich zu den kovalenten Bindungen, welche nach deren Knüpfung unter Normalbedingungen stabil sind und erst unter hohem Energieaufwand gebrochen werden können,[6] ist die Ausbildung nichtkovalenter Bindungen - im einfachsten Fall Wasserstoffbrücken - ein reversibler Vorgang. Die Stärke der Wechselwirkungen hängt dabei stark von der chemischen Umgebung, wie z.B. Lösemittel oder Temperatur, ab.[6] Eine Variation jener Parameter hat dabei einen dramatischen Einfluss auf die mikro- und makroskopischen Eigeschaften[7-9] der resultierenden supramolekularen Aggregate (z.B. mechanische Stabilität), erlaubt aber zusätzlich auch, die gewünschten physikalischen Charakteristika gezielt zu kontrollieren.[10-12]

Das beste Vorbild hinsichtlich der Ausbildung supramolekularer Strukturen repräsentiert wohl die Natur: durch Selbstorganisationsprozesse schafft sie es, *in vivo* komplexe Strukturen wie Proteine,[13] Zellmembranen,[14] Kollagenfasern[15,16] oder Mikrotubuli[17] auszubilden. Im Interesse der supramolekularen Chemie als interdisziplinäres Feld - welches neben den chemischen auch die physikalischen und biologischen Aspekte der komplexen Spezies beleuchten - liegt es nun, die Effekte der Natur zu verstehen, zu imitieren und nachhaltig zu beeinflussen.[11] Dieses Konzept zeigt miteinander eine starke Verflechtung und erstreckt sich von der organischen Chemie mit dem molekularsynthetischen Ansatz, der metallorganischen Komplexchemie bis hin zur physikalischen Chemie mit den experimentellen und theoretischen Studien der intermolekularen Wechselwirkungen. Dazu umfasst die Biochemie die zugehörigen biologischen Prozesse, während die Materialwissenschaft sich mit den mechanischen Eigenschaften der polymolekularen Festkörper beschäftigt.[11] Durch neue Morphologien und geeignete Synthons kann mit Hilfe der supramolekularen Chemie eine Vielzahl neuer

Materialien gewonnen werden, deren Eigenschaften sich auf makroskopischer Ebene einstellen lassen.[4,5] Konsequenterweise wurden im Jahre 1987 *Donald J. Cram*, *Jean-Marie Lehn* und *Charles J. Pedersen* „für ihre Entwicklung und Verwendung von Molekülen mit strukturspezifischer Wechselwirkung von hoher Selektivität“ mit dem Nobelpreis ausgezeichnet.[18]

3.3 Benzoltrisamide als supramolekulare Synthons

Um die in **Kapitel 3.2** erwähnten intermolekularen Wechselwirkungen nachhaltig zu klassifizieren und ihre Beschaffenheit zu charakterisieren, eignen sich besonders niedermolekulare organische Verbindungen. Diese zeichnen sich zum einen durch ihre relativ leichte synthetische Zugänglichkeit, zum anderen durch ihre gute Kristallinität aus, was eine detaillierte Strukturbestimmung vereinfacht. Eine der vielen organischen Substanzklassen, die in der supramolekularen Chemie auch nach vielen Jahren der Erforschung durch ihre Vielfältigkeit und großes Anwendungspotential noch immer großes Interesse hervorruft, sind die aromatischen 1,3,5-Benzoltrisamide (BTAs).

Ausgestattet mit drei Amideinheiten pro Molekül, sind die Monomere formal in der Lage - unter geeigneten Bedingungen - ein durch Wasserstoffbrücken vermitteltes, eindimensionales Wachstum in „supramolekulare Polymere“ zu erzielen. Sie besitzen einen Benzolkern und sind in 1-, 3- und 5-Position mit jeweils einer Amidfunktionalität substituiert.

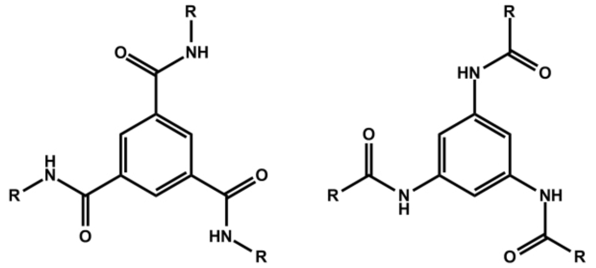

Schema 1: Allgemeine chemische Strukturen von trimesinsäure- (links) und triaminobenzolbasierten (rechts) BTAs

Abhängig von der Verknüpfungsart der Amideinheiten am aromatischen Kern unterscheidet man dabei zwischen trimesinsäure- (C-verknüpft) triaminobenzolbasierten (N-verknüpft) Verbindungen (Schema 1).

Der Rest R kann jegliche Art von funktioneller Gruppe darstellen (polar oder unpolar, neutral, geladen, etc.), dass Molekül kann also - je nach synthetischem Ansatz - sowohl symmetrisch als auch unsymmetrisch substituiert werden. In den vergangen Jahren wurden eine Vielzahl von Molekülen beider Verknüpfungsarten synthetisiert und detailliert charakterisiert. Die Derivate enthielten dabei verschiedene Seitenketten, wie z.B. Alkyl-,[19,20] Aryl-,[21-23] Pyridyl-,[24] Bipyridyl-,[25,26] Porphyrinyl-,[27] Triphenylen-,[28] und Aminosäuregruppen,[29-34] Dipeptid-[35] und Oligopeptideinheiten[36] sowie Benzolkronenether.[37]

Durch die große Anzahl an Substanzen konnte ein umfassendes Screening hinsichtlich diversester Anwendungen realisiert werden. Es wurden dabei neben Organo- und Hydrogelen[21,37-39] auch flüssigkristalline Phasen sowie nanostrukturierte Materialien[40] identifiziert. Außerdem konnten Komplexreagenzien für Metallzentren[32] und Kontrastreagenzien für die Anwendung in der Magnetresonanztomographie[41] gefunden werden. Des Weiteren hat diese Materialklasse eine große Bedeutung für den Einsatz in diversesten Polymersystemen gewonnen. Im Bereich der Nukleierungsagenzien für semikristalline Polymere konnten hervorragende Ergebnisse für z.B. Polyethylen-*co*-Propylen,[42] Polybutylenterephthalat,[43] Polylactide,[44-46] Polyvinylidenfluorid[47] sowie isotaktischem Polypropylen[48-50] erzielt werden (**Vgl. Kapitel 3.3.4**).

Zusätzlich konnte an telechelen Polymeren gezeigt werden, dass durch die Anknüpfung von BTAs als Endgruppen ein thermoplastisch-elastisches Verhalten erzielt wurde,[51] was eine typische Eigenschaft von Gummimaterialien darstellt. Es konnte ebenfalls gezeigt werden, dass chiral funktionalisierte BTA-Moleküle, die als Seitengruppen in Methacrylat-Copolymerate eingesetzt wurden, unter geeigneten Bedingungen eine Selbstorganisation auf Basis nichtkovalenter Wechselwirkungen eingehen.[52,53] Diese Aggregation führt gleichzeitig zu einer spontanen Faltung des Polymers, woraus polymerbasierte Nanopartikel resultieren, die im Prinzip nur aus einer einzelnen Polymerkette bestehen (Abbildung 1).[52,53] Bei Inkorporation von einer katalytisch aktiven Rutheniumspezies war es sogar möglich, die Nanopartikel als Nanoreaktoren für die Hydrierung von Cyclohexanon zum entsprechenden Alkohol in wässrigem Medium zu nutzen.[53]

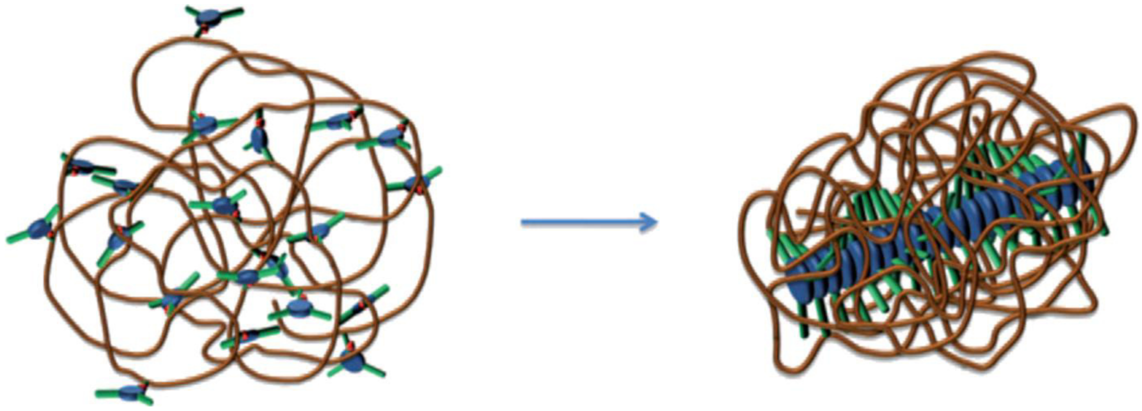

Abbildung 1: Schematische Darstellung der Faltung eines BTA-substituierten „random-coil“ Polymers in einen geordneten polymeren Nanopartikel; Copyright © 2011 WILEY-VCH Verlag GmbH & Co. KGaA, Weinheim

Generell ist neben der Verlinkungsart der Amidgruppierung an den aromatischen Ring auch die Natur der Seitenketten essentiell für die potenziellen Eigenschaften und Anwendungsgebiete. Im Allgemeinen induzieren langkettige aliphatische Endgruppen ein Verhalten als thermotrope Flüssigkristalle,[19,20] während verzweigte Seitenketten in BTAs mehr als Organogelatoren fungieren.[38] Hingegen liegen BTA-Derivate mit sterisch anspruchsvollen, kurzkettigen Aliphatengruppen als hochschmelzende, organische Festkörper vor, die bevorzugt faserartig kristallisieren.[48,54] Solche Derivate finden vorrangig Einsatzmöglichkeiten als Nukleierungs- und Klarmittel für *i*-PP.[48,54]

3.3.1 Synthetische Ansätze

Die in **Kapitel 3.3** aufgeführten Eigenschaften hängen maßgeblich von der Struktur des BTA-Moleküls selbst ab. Die Wahl der Zentraleinheit (z.B. Benzol- oder Cyclohexankern), eine symmetrische oder unsymmetrische Substituierung, die Anknüpfung der Amidgruppierungen oder die Substituentenwahl in der Seitenkette - all dies Faktoren besitzen einzeln oder kombiniert einen Einfluss. Je nach gewünschtem molekular-strukturellen Aspekt mit Hinblick auf die zu erzielende Anwendung werden dabei unterschiedliche synthetische Routen verfolgt, welche im Folgenden näher beleuchtet werden sollen.

Die ersten synthetischen Ansätze zum Erhalt von 1,3,5-Benzoltrisamiden gehen zurück bis ins Jahr 1915, als Curtuis erstmals ein trimesinsäurebasiertes Derivat mit einem Benzolrest synthetisierte („Trimesinsäureanilid“).[55] Dabei ging er nicht von der freien Trimesinsäure aus, sondern setzte den entsprechenden Triethylester mit Hydrazinhydrat zum Trihydrazid um.[55] Die folgende Umsetzung mit Natriumnitrit lieferte das unter Druck und Erhitzen explosionsfähige Triazid, welches wiederrum mit frisch destilliertem Anilin zum gewünschten Produkt umgesetzt wurde (Schema 2).[55] Neben der erschwerten Handhabung durch die explosive Zwischenstufe ist auch eine Umsetzung anderer Moleküle basierend auf dieser Route in größerem Maßstab nicht möglich.

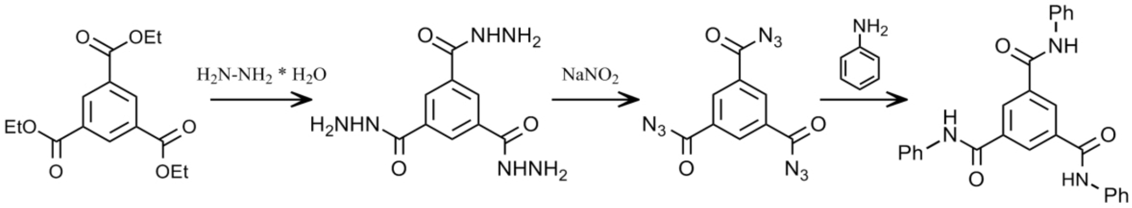

Schema 2: Synthetische Route zu Trimesinsäureanilid ausgehend von Trimesinsäureethylester

Ein großer Durchbruch wurde im Jahre 1959 erzielt, als *Ried* und *Königstein* in einer Zweistufensynthese das *o*-Nitrophenylderivat ausgehend von der freien Trimesinsäure synthetisierten.[56] Durch Umsetzung der Säure mit Thionylchlorid erhielt man zunächst das Säurechlorid, welches in einem zweiten Schritt mit dem freien Amin zur Reaktion gebracht wurde. Der große Vorteil dieses Ansatzes war die Zeiteinsparung aufgrund des reaktiven Chloridintermediats.[56] Generell ist diese Methode in der heutigen Zeit Stand der Technik in Bezug auf die Synthese von symmetrischen trimesinsäurebasierten BTAs. Unsymmetrische Derivate können nach dem von Bayer 1975 patentierten Verfahren hergestellt werden.[57] Ein geschmeidigerer Weg wurde erst viel später von *Roosma et al.* vorgestellt.[51] In einer mehrstufigen Synthese wird, ausgehend von dem Methylester der Trimesinsäure, zunächst durch Versatz mit Natronlauge die 5-Methoxycarbonyl-Isophthalsäure hergestellt, gefolgt von der Umsetzung mit Oxalylchlorid als säureaktivierenden Reagens zum entsprechenden Säuredichlorid.[51] Abschließend findet die erste Aminierung zum Säureamid statt. Der verbleibende Ester wird dann basisch gespalten und die entstandene freie Säure wie bereits oben beschrieben in das Chlorid und schließlich zum Amid umgesetzt.[51] Der generelle Reaktionsweg ist in Schema 3 abgebildet.

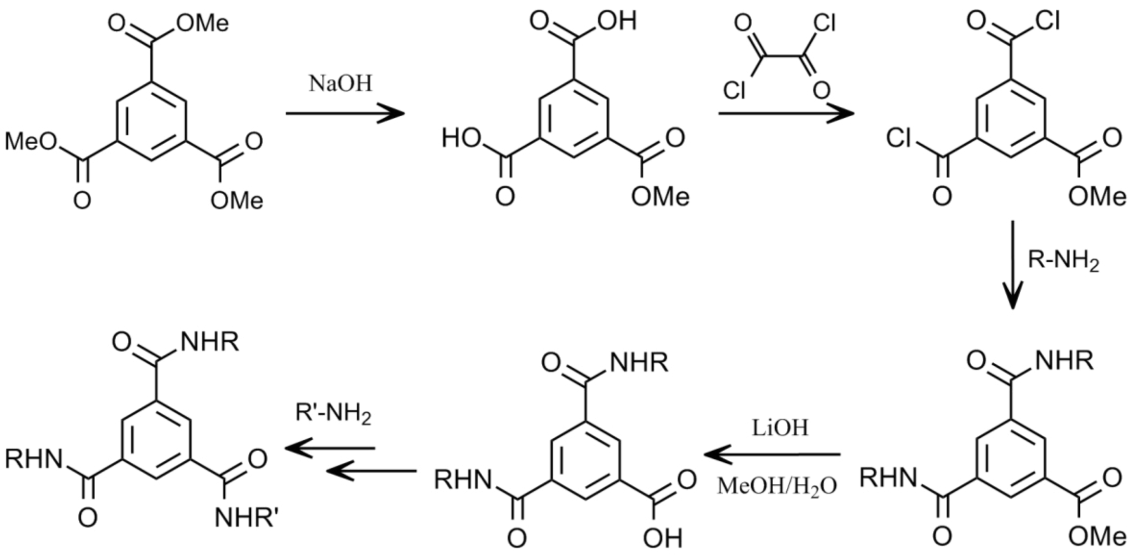

Schema 3: Synthetische Route zu unsymmetrisch substituierten trimesinsäurebasierten 1,3,5-Benzoltrisamiden

Um N-verknüpfte BTAs basierend auf 1,3,5-Triaminobenzol herzustellen, wurden zunächst Methoden mit Hilfe der katalytischen Hydrierung von 1,3,5-Trinitrobenzol verwendet, sei es z.B. mit RANEY®-Nickel[58] oder von Palladium auf Aktivkohle.[59] Das Problem hierbei bestand - neben der Abtrennung der katalytischen Spezies - die Handhabung der dreifach substituierten aromatischen Aminoverbindung, die zu einer recht schnellen Zersetzung neigte.[58,59] Eine alternative Route wurde dann von *Arai et al.* entwickelt, welche die vorher erwähnten Probleme umging, indem als Edukt das Trioxim des Phloroglucinols eingesetzt wurde.[60] Durch konsekutives Acylieren mit anschließenden Reduktionsschritten konnte das entsprechende Triacetamid in hohen Ausbeuten erzielt werden (Schema 4, oben).[60] Dieser Reaktionsverlauf ist prinzipiell auch bei dem Einsatz von anderen Säurechloriden möglich. Neben dieser Methode zum Erhalt von symmetrischen Derivaten, wurde vor ca. 10 Jahren ein Weg vorgestellt, um sehr einfach sowohl symmetrisch auch asymmetrisch substituierte BTAs zu synthetisieren.[61] Als Edukt dient hierbei 3,5-Dinitroanilin, das zunächst mit einem Säurechlorid mit einem Rest R umgesetzt wird. Die anschließende Hydrierung mit Hilfe eines Pd-C-Systems liefert die freien Aminogruppen, welche in einem letzten Schritt zwei weitere Säurechlorideinheiten nukleophil angreifen können.[61] Je nach Wahl der Seitenkette kommt man dabei zu symmetrischen oder asymmetrischen BTAs (Schema 4, unten).

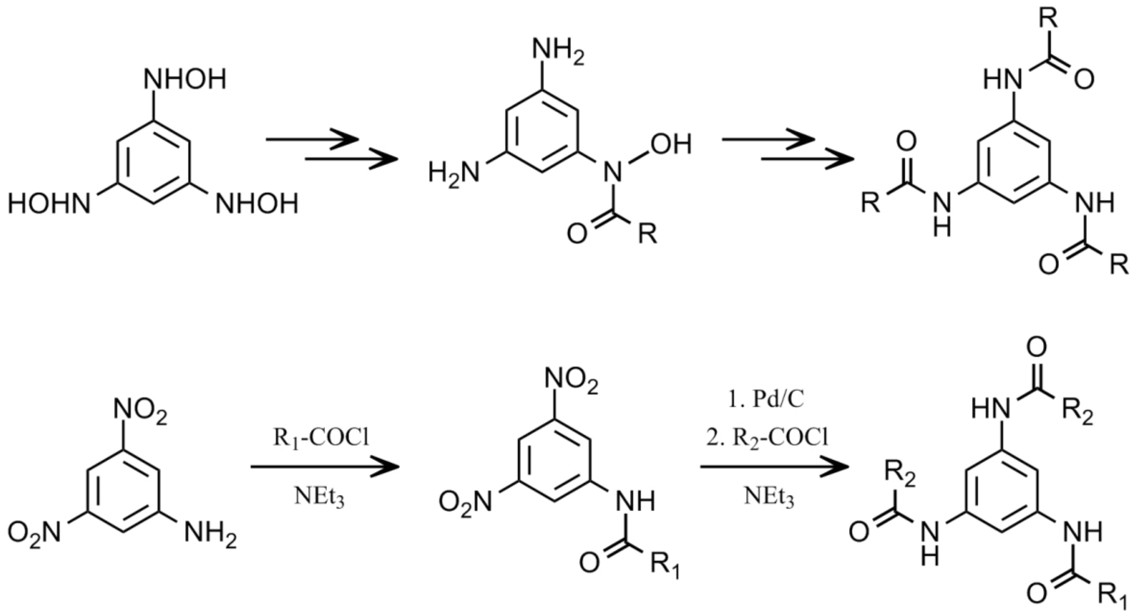

Schema 4: Synthetische Route zu symmetrisch und unsymmetrisch substituierten N-verknüpften 1,3,5-Benzoltrisamiden

3.3.2 Packungsmuster von BTAs im kristallinen Festkörper

Die in **Kapitel 3.3.1** angeführten Syntheserouten liefern die verschiedensten molekularen Strukturen der Benzoltrisamide. Diese Motivdiversität lässt sich auch in den Kristallstrukturen wiederfinden. Da im Rahmen dieser Arbeit die Kristallstrukturen zweier BTAs aufgeklärt wurden (**Kapitel 4.1** und **4.3)**, soll im Folgenden kurz auf eine kleine Auswahl von bereits vorhandenen Strukturen und ihrer Packungsmuster eingegangen werden.

Die Anzahl der existierenden Kristallstrukturen von BTAs hat in den letzten Jahren zwar zugenommen, ist aber dennoch überschaubar. Der Großteil der Strukturen wurde dabei durch Einkristallröntgenbeugung gelöst, zusätzlich wurden teilweise auch komplementäre Charakterisierungsmethoden wie z.B. FK-NMR- oder Infrarotspektroskopie eingesetzt. Letzteres stellt dabei eine empfindliche Methode für die Untersuchung der Organisation von möglichen intermolekularen Wasserstoffbrückenbindungen dar, vor allem dann, wenn reale Strukturinformationen fehlen. Interessanterweise überwiegen bei den bekannten Strukturen im hohen Maße die trimesinsäurebasierten BTAs, was wahrscheinlich an der einfacheren synthetischen Zugänglichkeit und/oder an deren Fähigkeit der besseren Einkristallbildung liegt. Generell spielt dabei die Art der Substituenten in der Seitenkette hinsichtlich der Kristallstruktur und dem Packungsmuster eine große Rolle. Eine Vorhersage der Struktur nach einer minimalen Änderung, z.B. durch einen Austausch eines oder mehrerer Substituenten, ist pauschal aber nicht möglich. Intuitiv würde man für derartige Verbindungen die Existenz einer molekularen C_3-Symmetrie, die Ausbildung intermolekularer Wasserstoffbrückenbindungen aufgrund der Amidfunktionalitäten in den Seitenketten sowie π-π-Wechselwirkungen der aromatischen Benzolkerne erwarten, also z.B. sandwichartige Stapelmuster. Im Folgenden soll gezeigt werden, wie diese nichtkovalenten, supramolekularen Charakteristika gänzlich, teilweise oder gar nicht innerhalb ausgewählter BTA-Systeme realisiert werden.

Zwei der ersten C-verknüpften BTA-Strukturen wurden 1997 gelöst. Eine davon enthielt als Rest eine Methylgruppe,[62] während die zweite mit der etwas sperrigeren Pyridyleinheit substituiert war.[24] Die Anknüpfung des Pyridylsubstituenten an der Amidgruppierung geschah dabei in *meta*-Position bezüglich des Stickstoffatoms im Ring (ausgehend vom Edukt *meta*-Aminopyridin).[24]

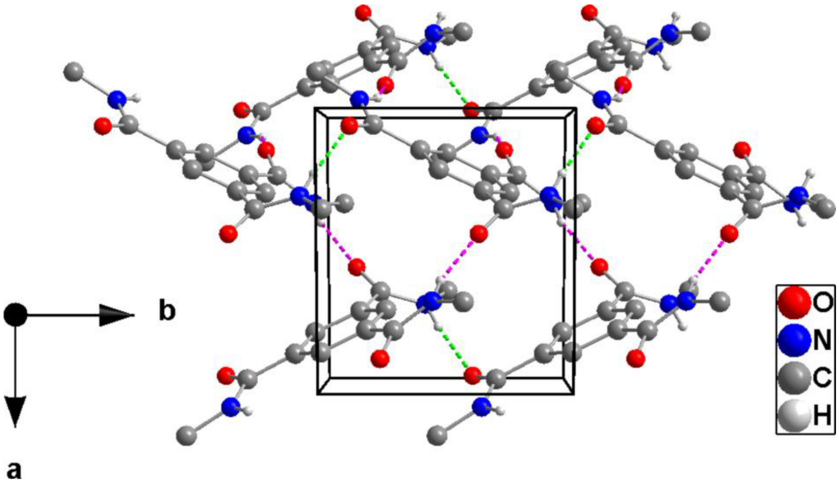

Abbildung 2: Ausschnitt aus Kristallstruktur des methylsubstituierten BTA mit einer Wasserstoffbrücke entlang der Stapelrichtung (kristallographische b-Achse, grün gestrichelt) sowie zwei lateralen Wasserstoffbrückenbindungen (rosa gestrichelt)

Schon an diesen zwei Beispielen wird die Diversität der Strukturen von BTAs deutlich. Das von *Hanabusa et al.* beschriebene Methylderivat kristallisiert monoklin primitiv in $P2_1$ (Abbildung 2).[62]

Es existieren keine π-π-Wechselwirkungen zwischen den Aromaten, dafür aber intermolekulare Wasserstoffbrückenbindungen. Interessanterweise gibt es nur eine H-Brücke innerhalb des Stapelmusters (d(NH---O = 1,95 Å)) (Abbildung 2, grüne Linien),[62] während zwei H-Brücken verantwortlich sind für die lateralen Wechselwirkungen zwischen den Amideinheiten der Moleküle verschiedener Stapel (d(NH---O = 1,91 und 1.98 Å)) (Abbildung 2, rosafarbene Linien).[62] Das Molekül zeigt lediglich eine C_1-Symmetrie, wobei zwei der Carbonylgruppen in den Seitenarmen im Prinzip in die gleiche Richtung zeigen.[62]

Ganz im Gegenteil dazu zeigt die von *Palmans et al.* untersuchte Pyridylspezies ein vollkommen anderes strukturelles Verhalten.[24] Allein die Tatsache, dass diese Verbindung in der zentrosymmetrischen trigonalen Raumgruppe $P\overline{3}$ kristallisiert und vollständige C_3-Symmetrie besitzt,[24] ist bemerkenswert. Hierbei ist der Inhalt der asymmetrischen Einheit auf 1/3 des Moleküls reduziert, was zu insgesamt 2 Molekülen in der Einheitszelle führt.[24]

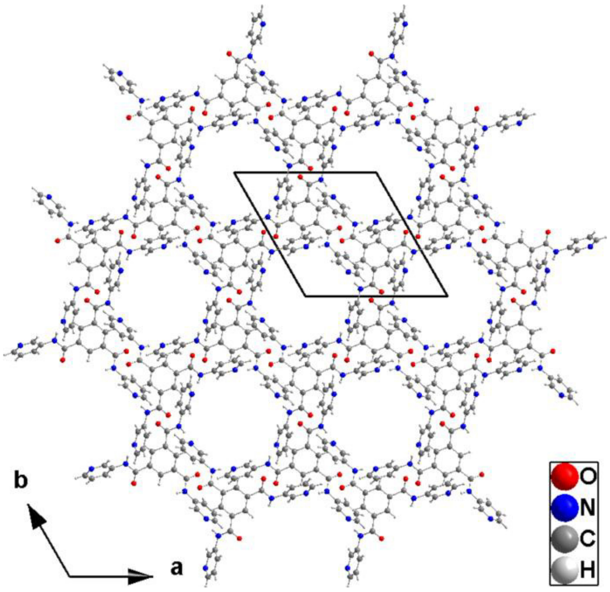

Abbildung 3: Ausschnitt aus Kristallstruktur des pyridylsubstituierten BTA mit Porensystem entlang der kristallographischen c-Achse

Es existiert auch hier kein π-Stacking der aromatischen Ringe und/oder der Pyridyleinheiten und, erstaunlicherweise, werden auch keine intermolekularen

NH---CO Wasserstoffbrücken ausgebildet. Vielmehr werden H-Brücken zwischen den NH-Gruppen und dem Stickstoffatom des Pyridylrestes eines benachbarten Moleküls (d(NH---N = 2,01 Å)) geknüpft.[24] Dieses Packungsmuster führt zu einer honigwabenartigen und damit porösen Struktur (Abbildung 3) mit einem mittleren Porendurchmesser von circa 8,2 Å. In diesen Poren sind zusätzlich noch Methanolmoleküle vom Umkristallisieren eingelagert.[24]

Die erste tatsächliche supramolekulare, kolumnare Struktur wurde von *Lightfoot et al.* präsentiert, wobei als Substituent eine 2-Methoxyehtylgruppe eingeführt wurde.[63] Trotz C_1-Symmetrie existieren dreifache Wasserstoffbrücken zwischen den Amideinheiten der einzelnen Moleküle innerhalb eines Stapels (d(NH---O = 2,09 - 2,19 Å)), zusätzlich kommen nun auch π-π-Wechselwirkungen der Aromaten mit einem Abstand von ca. 3,6 Å zum Tragen (Abbildung 4).[63] Darüber hinaus treffen in der Struktur erstmalig zwei konkurrierende Wechselwirkungen aufeinander. Auch wenn die aromatischen Einheiten mit den angeknüpften Carbonylgruppen ein komplanares System zwecks durchgängiger Konjugation bevorzugen,[64] sind die Amidfunktionen so aus der Ebene gedreht, das alle Sauerstoffatome in Bezug auf den aromatischen Kern in eine Richtung zeigen.[63] Grund hierfür ist wahrscheinlich die Ausbildung der anfangs erwähnten intermolekularen H-Brücken als zusätzlicher Energiebeitrag.

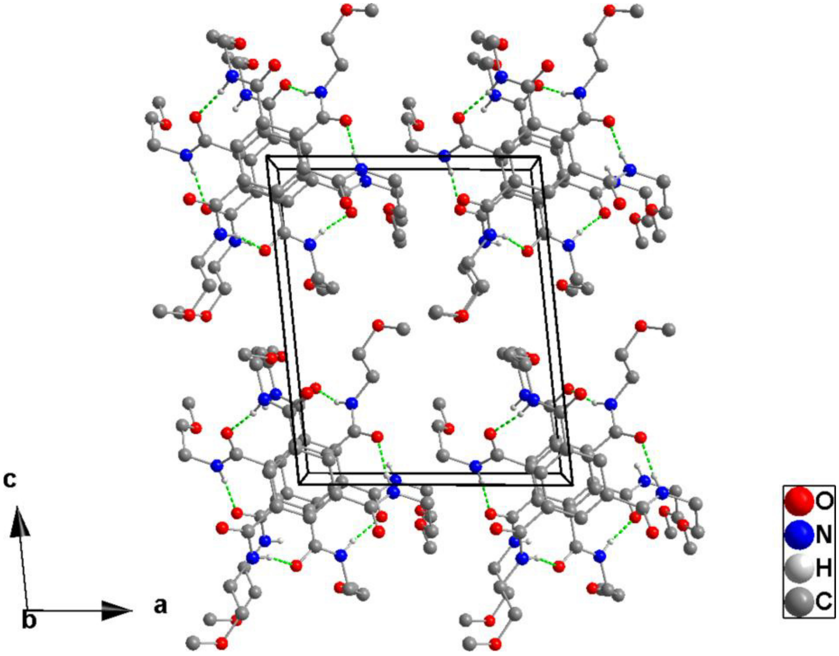

Abbildung 4: Ausschnitt aus der von *Lightfoot et al.*[63] gelösten Kristallstruktur mit Blick auf die Stapelrichtung der Moleküle entlang der b-Achse inkl. den π-π-Wechselwirkungen und den intermolekularen Wasserstoffbrückenbindungen (grün gestrichelt)

Neben diesen hydratfreien Spezies gibt es auch eine Struktur, welche mit eingelagertem Kristallwasser als Trihydrat existiert.[33] So wurde u.a. gezeigt, dass das in $R\bar{3}$ kristallisierende, essigsäurefunktionalisierte Derivat Dimere mit Benzol-Benzol-Abständen von ca. 3,7 Å ausbildet.[33] Die Wasserstoffbrücken werden auch hier nicht zwischen den Amideinheiten in Stapelrichtung geknüpft, sondern zwischen den NH-Gruppen und dem Sauerstoffatom der Carbonylgruppe der freien Säure im benachbarten Molekül (Abbildung 5).[33]

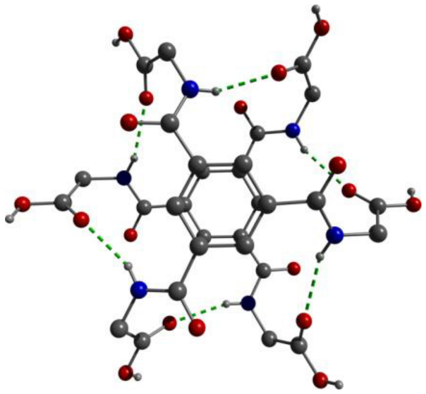

Abbildung 5: Sicht auf ein Dimer des essigsäuresubstituierten BTA mit Wasserstoffbrückenbindungen zwischen den Amidprotonen und dem Sauerstoffatom der Carbonylgruppen der Essigsäureeinheit benachbarter Moleküle (grün gestrichelt)

Die Wassermoleküle spielen dabei die Rolle eines Mediators, welcher durch H-Brücken die einzelnen Dimere verbindet. Dabei dienen die drei Carbonylgruppen der Amideinheiten als Akzeptorgruppen, während die OH-Funktionen der freien Säuren in den Seitenketten die Donorspezies darstellen.[33] Durch dieses Verknüpfungsmuster entsteht somit praktisch ein ausgedehntes Schichtsystem aus Dimereinheiten (Abbildung 6).[33]

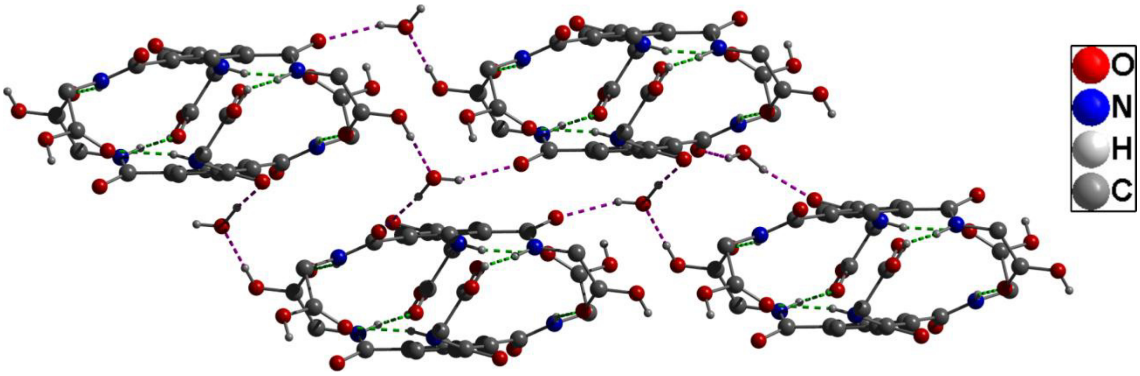

Abbildung 6: Ausschnitt des zweidimensionalen Dimer-Schichtsystems der essigsäuresubstituierten BTA-Moleküle, welche durch H-Brücken zusammengehalten werden (grün gestrichelt); die einzelnen Dimere sind zusätzlich *via* Wasserstoffbrücken über eingelagerte H_2O-Moleküle verknüpft (rosa gestrichelt)

Die Anzahl der bisher bekannten N-verknüpften Kristallstrukturen ist auf zwei beschränkt. Zum einen existiert ein Derivat mit einem zyklisch-aliphatischen Substituent (abgeleitet von 3-Cyclopentylpropionylchlorid)[65] sowie eine Katecholverbindung (2,3-Dimethoxybenzol).[66] Ersteres weist dabei interessanterweise eine zweidimensionale Schichtstruktur in der Raumgruppe $P2_1/n$ auf,[65] welche intermolekular über NH---CO Wasserstoffbrückenbindungen verknüpft ist.[65] Allerdings existieren hier weder eine molekulare Symmetrie (C_1) noch etwaige aromatische π-π-Wechselwirkungen (Abbildung 7).[65]

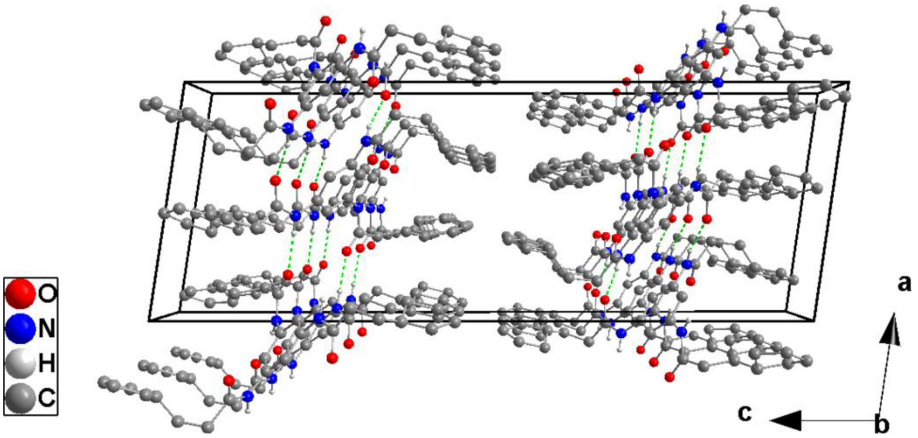

Abbildung 7: Schichtartiges Wachstum der von *Hou et al.*[65] beschriebenen Kristallstruktur mit H-Brücken-Strängen parallel zur kristallographischen a-Achse (grün gestrichelt)

Das Vorhandensein von Akzeptorgruppen für H-Brücken in der Seitenkette, wie z.B. Methoxygruppen in oben erwähnter Katecholverbindung, hindert gänzlich die Ausbildung von intermolekularen Wasserstoffbrückenbindungen[66] zu Gunsten von intramolekularen NH---O-Kontakten mit entsprechenden Abständen von ca. 1,9 Å (Abbildung 8).[66] Dafür sind hier die Amideinheiten praktisch komplanar zum aromatischen Kern ausgerichtet.[66]

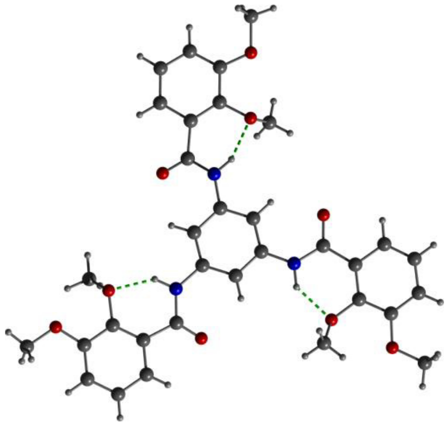

Abbildung 8: Molekulare Struktur des katecholsubstituierten BTA-Derivats mit intramolekularen Kontakten zwischen NH-Proton und benachbarter H_3CO-Gruppe (grün gestrichelt)

3.3.3 Selbstorganisation löslicher Additive in der Polymerschmelze

In **Kapitel 3.3.2** wurde gezeigt, dass BTAs in Abhängigkeit vom molekularen Aufbau unterschiedliche Packungsmuster in ihren Kristallstrukturen aufweisen. Dabei hat die Wahl der Substituenten in der Seitenkette einen maßgeblichen Einfluss auf die gewünschte Eigenschaft.[19,20,38,48,49,54] Wie schon in **Kapitel 3.3** angedeutet, besitzen ausgewählte Derivate aus der Familie der 1,3,5-Benzoltrisamide - neben vielen anderen organischen[67-69] und anorganischen Verbindungen,[70,71] Pigmenten,[71-73] Polymeren[74] oder Sorbitolderivaten[75-79] - hervorragende Nukleierungseigenschaften für semikristalline Polymere.[48,54] Die BTAs gehören dabei - ähnlich wie Sorbitolderivate[78] - zur Klasse der löslichen Additive, also Verbindungen, die in der Polymerschmelze am Beginn des Nukleierungsprozesses molekular gelöst vorkommen. Um nun als effizientes Nukleierungsagens fungieren zu können, muss die als Additiv eingesetzte Verbindung einem thermoreversiblen Kreislauf standhalten können. Während dieses Zyklus müssen die Additivmoleküle dabei verschiedene Selbstorganisationsprozesse durchlaufen. Ein allgemeines Schema des Nukleierungsprozesses für ein lösliches Nukleierungsagens ist in Abbildung 9 schematisch dargestellt.

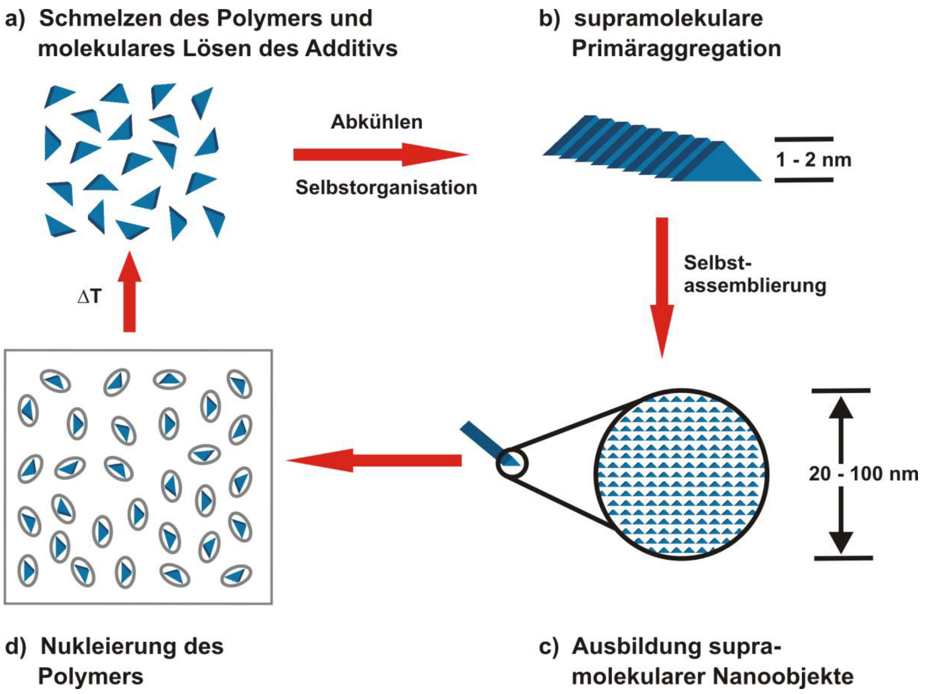

Abbildung 9: Schematische Darstellung des thermoreversiblen Selbstorganisationsprozesses von löslichen Nukleierungsagenzien in der Polymerschmelze

Zunächst liegt das Additiv molekular gelöst in der Polymerschmelze vor (Abbildung 9a), welches sich beim Abkühlen durch intermolekulare Wechselwirkungen zu kleinen, supramolekularen Primäraggregaten organisiert (Abbildung 9b). Diese Aggregate können weiter wachsen zu größeren Nanoobjekten, die nun in der Lage sind, die Polymernukleierung zu initiieren (Abbildung 9c). Bei weiterem Abkühlen schließlich nukleiert das Polymer heterogen auf der Additivoberfläche (Abbildung 9d). Dieser Mechanismus kann nach Aufschmelzen des Polymer-Additiv-Gemisches reversibel durchgeführt werden.

3.3.4 Nukleierung und Klarifizierung von i-PP mit Benzoltrisamiden

Die in **Kapitel 3.3.3** aufgeführten Verbindungsklassen dienen in der heutigen Zeit standardmäßig als Nukleierungsmittel für semikristalline Polymere, so z.B. Polyolefine,[67,70,80,81] -ester,[82,83] -amide[84,85] oder fluorhaltige Polymere.[86,87] Die 1,3,5-Benzoltrisamide haben sich in den letzten Jahren dabei besonders für isotaktisches Polypropylen als geeignet offenbart.[48,49,54] Die daraus resultierenden Vorteile sind deshalb von Bedeutung, da *i*-PP - oder Polypropylen (PP) im Allgemeinen - in der heutigen Zeit mit einer Produktionskapazität von ca. 60 Mio. Tonnen pro Jahr einen der meistproduzierten Kunststoffe überhaupt darstellt.[88]

Isotaktizität entspricht dabei neben der A- und Syndiotaktizität einer der drei möglichen Konfigurationsarten von Polypropylen - herrührend von der räumlichen Anordnung der Methylgruppen an den pro-chiralen Kohlenstoffatomen in der Polymerkette. Bei statistisch verteilter Anordnung der Methylgruppen wird von ataktischem PP gesprochen; bei einer alternierenden *RSRS…*-Konfiguration handelt es sich um syndiotaktisches PP und bei gleicher *R*- oder *S*-Konfiguration der CH_3-Gruppen spricht man von *i*-PP. Letzteres wurde erstmals Mitte der 1950er Jahre etwa parallel von *Rehn* in Deutschland (nicht patentiert) und *Natta* in Italien mit Hilfe von Organo-Metall-Katalysatoren hergestellt.[89] *Natta* konnte dabei auch gleichzeitig die Isotaktizität nachweisen.[89] Die verwendeten Katalysatoren gingen dann letztendlich als „Ziegler-Natta-Katalysatoren“ in die Annalen der Chemie ein. 1963 erhielten beide den Nobelpreis für Chemie für die Arbeiten auf diesem Gebiet.[90]

Der Einsatz anfangs erwähnter Additive hat im Wesentlichen folgende Funktionen: zum einen wird im starken Maße die Kristallisation des Polymers aus der Schmelze durch den massiven Anstieg der heterogenen Nukleierung beeinflusst.[91] Dadurch wird das notwendige Unterkühlen der Schmelze, was benötigt wird um die Kristallisation zu initiieren,[76,91] verringert, was schlussendlich eine höhere Kristallisationstemperatur mit sich bringt. Das führt gleichermaßen zu einer Erhöhung der Kristallisationsgeschwindigkeit,[91-93] wobei die Konzentration des Additivs zusätzlich eine Rolle spielen kann. Zum anderen können unter geeigneten Umständen auch die optischen[74,91,94] und mechanischen[70] Eigenschaften verbessert werden, was durch die Reduzierung der Sphärulitgröße[92] der amorphen und kristallinen Anteile des Polymers erreicht wird (Abbildung 10).[50,70,95]

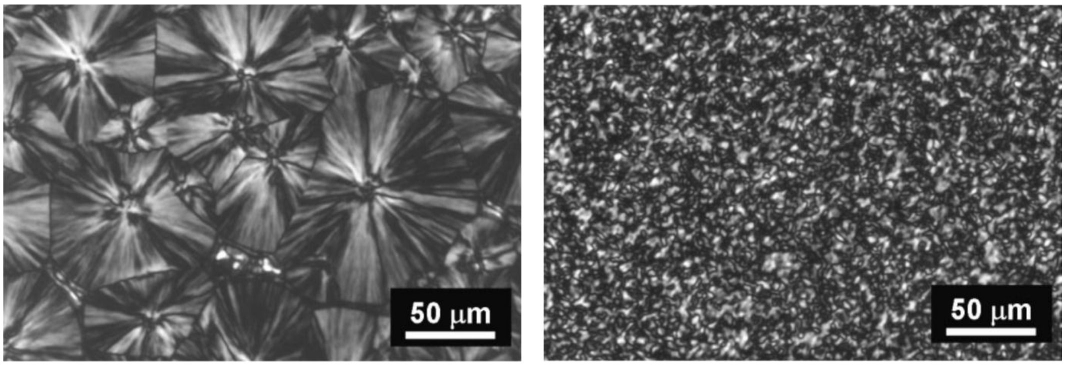

Abbildung 10: Mikroskopieaufnahmen von kristallisiertem *i*-PP nach Abkühlen auf RT mit 10 K/min; links: pures *i*-PP; rechts: nukleiertes *i*-PP mit 0,13 wt% eines BTA-Derivats; Copyright © 2010 WILEY-VCH Verlag GmbH & Co. KGaA, Weinheim

Isotaktisches Polypropylen stellt aufgrund des breiten Anwendungsspektrums in vielen Bereichen des gesellschaftlichen Lebens sowie dem wirtschaftlichen Interesse das möglicherweise am intensivsten untersuchte Polymer hinsichtlich Nukleierung und Klarifizierung dar. Seit den 1970er Jahren wurden Tausende an Verbindungen entwickelt,[67] die gänzlich diesen Zweck erfüllen sollen. Ein effektives Nukleierungs-/Klarmittel auf Basis von 1,3,5-Benzoltrisamiden soll dabei folgende allgemeine Kriterien erfüllen:[93,96]

i Das eingesetzte Additiv sollte einen polaren und einen unpolaren Teil besitzen, die zusammen ein supramolekulares Aggregieren bzw. Kristallisieren erlauben.

ii Die Verbindung sollte in der Polymerschmelze löslich sein.

iii Kurz oberhalb der Kristallisationstemperatur des Polymers sollte das Additiv unlöslich sein.

iv Der Schmelzpunkt des Additivs sollte daher höher sein als der Schmelzbereich der kristallinen Bereiche des Polymers.

v Es sollte eine angemessene epitaktische Übereinstimmung vorliegen um die Polymerkristallisation zu induzieren.

An dieser Stelle sei nur erwähnt, dass isotaktisches Polypropylen mehrere polymorphe Phasen (α-, β-, γ-Phase) sowie eine Mesophase besitzt.[97-104] Die monokline α-Form stellt dabei die thermodynamisch stabile Variante dar, während beide anderen Modifikationen metastabile Phasen darstellen. Im Bereich der BTAs sowie deren symmetrische und unsymmetrische strukturverwandte Verbindungen existieren Beispiele, welche die α-Modifikation, die β-Form oder gar Mischphasen beider Polymorphe nukleieren können.[48,105]

3.4 Organische supramolekulare 2D-Strukturen

Werden bei niedermolekularen organischen Strukturen große Aspektverhältnisse erreicht, sprich laterale Ausdehnungen bis in den Mikrometermaßstab, aber maximale topologische Dicken von wenigen 100 Nanometern, spricht man von zweidimensionalen Nanoarchitekturen. Während die lateralen Ausdehnungen mittels REM-Experimenten gut zugänglich sind, können die Schichtdicken unter geeigneten Bedingungen sehr gut durch Rasterkraftmikroskopie bestimmt werden. Eines der wohl bekanntesten Beispiele für solche eine Struktur stellt Graphen mit seinen außergewöhnlichen Eigenschaften dar,[106-108] dessen Entdeckung als Konsequenz eine nachhaltige Forschung nach adäquaten Alternativen mit analogen Eigenschaftspotenzial im Bereich der supramolekularen 2D-Strukturen mit sich führte. Hierbei spielen besonders anorganische Materialien, wie z.B. Metalloxide,[109-115] -disulfide[106,116,117] oder Bornitride,[106,117-120] eine große Rolle.

Organische „2D-Nanosheets“ können auf verschiedenste Weise hergestellt werden, sei es durch Exfolierung von geschichteten Kristallen, CVD-Techniken, klassischen organischen Syntheserouten, die Verwendung von Templaten an verschiedenen Grenzflächen (flüssig-gasförmig, flüssig-flüssig, flüssig-fest) sowie durch Selbstorganisation.[121-124] Für letzteres gilt, - analog zu den in **Kapitel 3.2** vorgestellten BTAs - dass intermolekulare, nicht-kovalente Wechselwirkungen die Hauptrolle für die Ausbildung der 2D Strukturen spielt (Abbildung 11). Mittlerweile existieren solche Strukturen basierend auf den verschiedensten supramolekularen Synthons, so zum Beispiel Bisacylharnstoffe,[125-128] zyklische Dipeptide,[129-132] Peptoide,[133] Naphthalendiimide,[134] Perylene,[135] Phenantrilydine,[136] Biphenyl-SAMs[137] sowie Pyrrol-SAMs (SAM = self-assembled monolayers).[138]

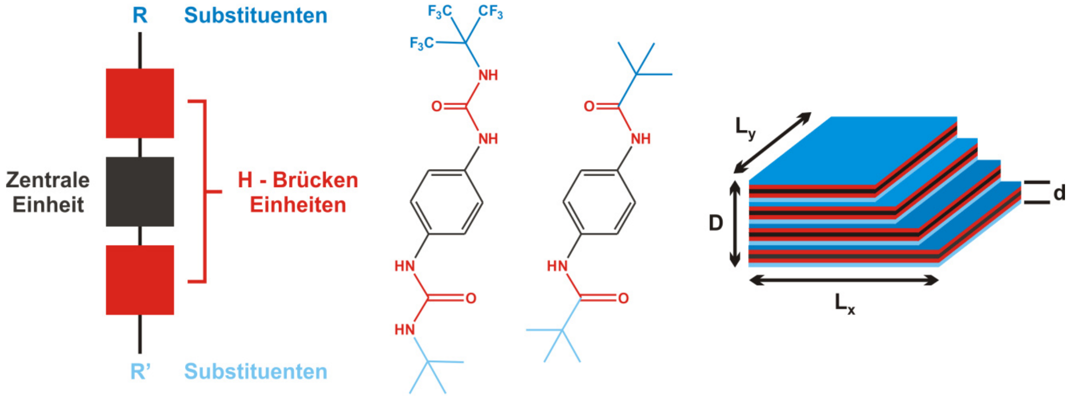

Abbildung 11: Schematische Darstellung der Ausbildung benzolbasierter symmetrischer und unsymmetrischer zweidimensionaler Nanoarchitekturen mit Harnstoff- und Amidfunktion als H-Brücken bildende Einheit

3.5 NMR-Kristallographie

Um Strukturen kristalliner Verbindungen zu lösen, wird routinemäßig die Einkristallstrukturanalyse (EKSA) eingesetzt. Es gibt aber eine Vielzahl von (mikrokristallinen) Substanzen, von denen keine Einkristalle erhalten werden können. Dies hat zur Folge, dass auch vermehrt Strukturen aus Röntgenpulverdaten eindeutig gelöst werden (müssen).[139,140] Neben *ab initio* Strukturlösungen oder Strukturmodellen im Allgemeinen, liefert die Röntgenpulverdiffraktometrie wichtige kristallographische Informationen, so z.B. die Metrik der Elementarzelle als auch Symmetrieinformationen (Raumgruppe).[139,140] Um komplementäre Informationen über die molekulare Zusammensetzung sowie über die Kristallstruktur zu erhalten, kann die FK-NMR-Spektroskopie zu Hilfe genommen werden. Auch hier können Informationen hinsichtlich der Symmetrie und der asymmetrischen Einheit gewonnen werden,[141-145] aber auch lokale Informationen wie z.B. Konfigurationen von molekularen Einheiten, Abstände oder gar Torsionen können extrahiert werden.[146-150] Für die beiden letztgenannten Aspekte ist es oftmals notwendig, die Substanzen gezielt isotopenmarkiert herzustellen (^{2}H, ^{13}C, ^{15}N, ^{29}Si), da die natürliche Häufigkeit der Kerne und/oder das schlechte gyromagnetische Moment es nahezu unmöglich machen, die vorher erwähnten Informationen in überschaubarer Zeit zu erhalten. Einen nicht zu vernachlässigenden Aspekt spielt auch der Einsatz von quantenmechanischen Rechnungen und Simulationen, welche mit den Experimenten einhergehen.[147,151-153] Exemplarisch sei hier die Entfaltung von 1D-FK-NMR Spektren zu nennen, das Anfitten von DQ-Aufbaukurven, die Geometrieoptimierung von Molekülen für die Strukturlösung als auch Berechnungen der chemischen Verschiebungen eines Kerns anhand eines Strukturmodells. All diese vier Teilbereiche beschreiben als Kombination betrachtet den Terminus „NMR-Kristallographie“ (Schema 5). Es sei an dieser Stelle erwähnt, dass nicht zwangsläufig immer alle vier Teilbereiche gleichzeitig zum Einsatz kommen müssen.

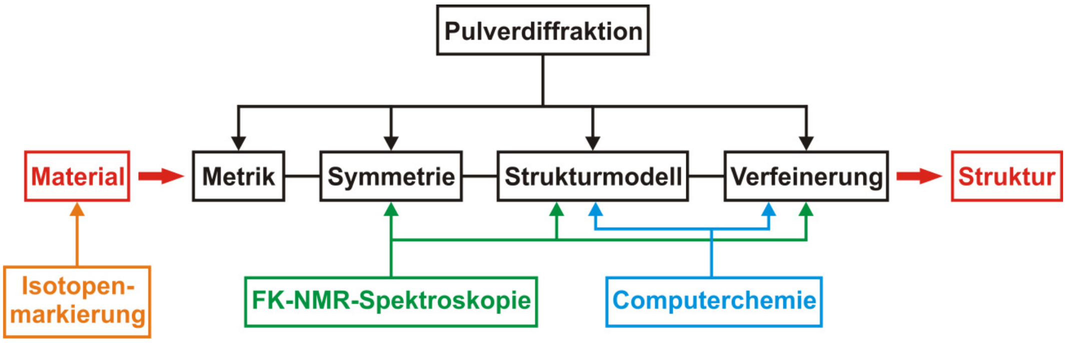

Schema 5: Der NMR-kristallographische Ansatz: vom Material bis zur Kristallstruktur

3.5.1 Kristallstrukturbestimmung mit Realraum-Methoden

Wie in **Kapitel 3.5** schon angedeutet, spielt für eine Vielzahl von mikrokristallinen organischen Substanzen die Pulverdiffraktion im Bereich der NMR-Kristallographie eine tragende Rolle und liefert wichtige kristallographische Informationen in allen Stadien der Strukturfindung (Vergleich Schema 5).[139,140]

Leider versagen bei dem Erstellen der Strukturmodelle oftmals die direkten Methoden[154-156] und das Verfahren nach Patterson,[156-158] also jene Methoden, die sich besonders bei der Einkristalldiffraktion bewährt haben.

Ersteres scheitert aufgrund der Tatsache, dass in Pulverdiffraktogrammen die Reflexe sehr stark überlappen, was die Anzahl unabhängiger Informationen drastisch reduziert.[159] Dies hat zur Folge, dass eine exakte Bestimmung ihrer Phasenbeziehung zueinander aufgrund unzureichender Extraktion der absoluten Intensitäten sehr erschwert wird, was letztendlich die Bestimmung der Atompositionen in der Zelle unmöglich macht, da in der Phaseninformation die Atompositionen als explizite Parameter auftauchen.[156,160] Die Pattersonmethode hingegen funktioniert - einfach ausgedrückt - nur sehr gut bei der Existenz von schweren Atomen innerhalb der Struktur bzw. des Moleküls.[156] Da die in dieser Arbeit untersuchten Substanzen als stärkste Streuzentren nur Kohlenstoff-, Stickstoff-, Sauerstoff- sowie Fluoratome besitzen (die Wasserstoffatome sind hier zu vernachlässigen), ist der Ansatz an dieser Stelle nicht geeignet.[156]

Eine gute Alternative zu den oben erwähnten Methoden stellt der Realraumansatz dar, welche nicht im reziproken Raum wie bei den klassischen Methoden, sondern im realen Raum stattfindet. Im Prinzip beinhaltet eine derartige Strukturlösung fünf elementare Aspekte, angefangen von der Indizierung des Pulverdiffraktogramms (mit den Standard-Algorithmen nach Werner, Visser und Louër)[161-163] und dessen Anpassung nach Pawley oder LeBail,[164-166] das Entwickeln eines Startmodells, die Strukturlösung mit Realraum-Methoden bis hin zur Rietveldverfeinerung.[167-172]

Für das Entwickeln eines Strukturmodells als Startpunkt[169,171-174] sind prinzipiell zwei Dinge wesentlich: zum einen muss man die Raumgruppe kennen, was durch vorhandene systematische Auslöschungen der Reflexe erleichtert wird.[139,140] Grundsätzlich gilt dabei, stets die höchstmögliche Symmetrie des Kristallsystems zu suchen.[139,140] Der zweite Aspekt befasst sich mit dem Inhalt der asymmetrischen Einheit, also dem Atom/Molekül oder dem Molekülfragment. Hier können bereits quantenmechanische Rechnungen und/oder FK-NMR-Experimente hilfreich sein, eine Vorentscheidung zu treffen. Ein anderer sehr schöner Weg führt über das Zellvolumen in Kombination mit dem - grob abgeschätztem - Molekülvolumen. Hier können sowohl Raumgruppen eliminiert werden bzw. die Anzahl der Untereinheiten in der asymmetrischen Einheit bestimmt werden. Faktisch ist das Startmodell eine Zelle mit exakter Raumgruppe, in welche entsprechend viele Untereinheiten - zunächst willkürlich - platziert sind. Während des Strukturlösungsalgorithmus müssen anschließend die korrekten Positionen der Einheiten - unter Berücksichtigung weiter Freiheitsgrade wie z.B. Torsionswinkel - bestimmt werden. Diese spezielle Methode wird auch als „*Grid-Search* im Kristallraum“ bezeichnet.[160]

Während der eigentlichen Strukturlösung werden die erwähnten Positionen und Freiheitsgrade zufällig variiert, für die daraus resultierenden Teststrukturen das Pulverdiffraktogramm mit den nach Pawley gewonnen Profilparametern berechnet und mit dem experimentellem Diffraktogramm verglichen. Neben den an die Natur angelehnten genetischen Algorithmen sind dabei die Monte-Carlo-basierten (MC) Algorithmen am weitesten verbreitet.[159,169,173,175] Bei letzterem wird zufällig die möglichst komplette Energiehyperfläche nach dem globalen Minimum, sprich der Struktur mit der niedrigsten potentiellen Energie, abgesucht. Allerdings ist dabei ein wesentlicher Faktor, die Temperatur, nicht implementiert, was das Auffinden des globalen Minimums erschwert, da im Prinzip alle möglichen Bewegungen und Freiheitsgrade möglich sind.

Die notwendige Erweiterung spiegelt sich in der Einführung des „*simulated annealing*“ (SA)[176-178] und „*parallel tempering*“ (PT)[179] wieder, wo der gesamte konformative Raum temperaturabhängig gescreent wird. Da in drei der vier vorgestellten Arbeiten (**Kapitel 6**) hinsichtlich der Strukturaufklärung beide Algorithmen angewendet wurden und in der verwendeten Software (*PowderSolve*[167] von MaterialStudio[180] implementiert sind, soll an dieser Stelle eine kurze Abgrenzung beider Szenarien stattfinden.

3.5.2 Der „Simulated Annealing“ Algorithmus

Der SA-Algorithmus benutzt eine einzige Referenzstruktur und erniedrigt sukzessive die Simulationstemperatur, d.h. die Wahrscheinlichkeit, dass Teststrukturen mit einem vergleichsweise ungünstigen R_{comb}-Wert (zur Definition von R_{comb} siehe **Kapitel 3.5.4**) dennoch als eine mögliche Struktur akzeptiert werden. Die Starttemperatur ist zu Beginn ausreichend hoch, so dass die gesamte Energiehyperfläche nach potenziellen Strukturen abgerastert werden kann. Mit weiterem Verlauf wird die Temperatur derart erniedrigt, dass am Ende lediglich lokale Bereiche um ein tiefliegendes Energieminimum (im besten Fall das globale Minimum) untersucht werden. Der generelle Verlauf für einen Monte-Carlo-basierten SA-Durchlauf ist in Schema 6 gezeigt. Man sieht sehr schön, dass zu Beginn des Durchlaufs, sprich bei wenigen Monte-Carlo-Schritten, aufgrund der hohen Temperatur eine große Bandbreite an möglichen Teststrukturen mit breiter Energieverteilung ($\asymp R_{comb}$) existiert (schwarze Punkte). Mit zunehmender Anzahl der MC-Schritte und abnehmender Temperatur laufen alle Teststrukturen in Richtung eines Energieminimums, was im besten Fall der Struktur mit der niedrigsten potentiellen Energie und damit dem niedrigsten R_{comb}-Wert im globalen Minimum entspricht.

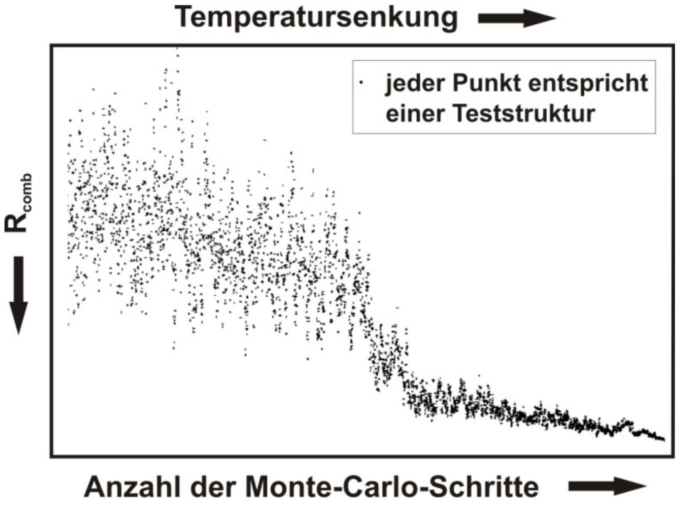

Schema 6: Verlauf eines Monte-Carlo basierten „*simulated annealing*“ Durchlaufs

Die einzelnen Schritte des SA zum Auffinden der Struktur im globalen Minimum vom Startmodell aus sind[167,176,180]:

1) Ausbildung einer neuen Teststruktur ausgehend von der Referenzstruktur (entspricht hier dem Startmodell) durch eine zufällige Änderung einer der Freiheitsgrade um -0,5 bis 0,5 mal die maximale Schrittweite

2) Erstellen eines simulierten Pulverdiffraktogramms der Teststruktur und Berechnung von R_{comb}

3) Berechnung von ΔR_{comb}, also dem Unterschied zwischen den R_{comb}-Werten der Test- und Referenzstruktur:

$$\Delta R_{comb} = R_{comb}^{Test} - R_{comb}^{Referenz} \qquad (1)$$

Die Teststruktur wird als neue Referenzstruktur akzeptiert, wenn:

a) $\Delta R_{comb} < 0$ $(R_{comb}^{Test} < R_{comb}^{Referenz})$ sowie

b) $\Delta R_{comb} > 0$ $(R_{comb}^{Test} > R_{comb}^{Referenz})$, jedoch nur mit der Wahrscheinlichkeit $e^{-\Delta R_{comb}/T}$, d.h. es wird eine Zufallszahl ξ zwischen 0 und 1 ausgewählt, und wenn $\xi < e^{-\Delta R_{comb}/T}$, wird die Teststruktur ebenfalls akzeptiert

4) Bei Akzeptanz der Teststruktur wird sie neue Referenzstruktur

5) Anpassung der Schrittweite und Temperatur; nach einer gewissen Anzahl an Schritten werden maximale Schrittweite und Temperatur in Abhängigkeit der Standardabweichung von R_{comb} der letzten Schritte erniedrigt

6) Wiederholung der Schritte 1) - 5) so oft wie benutzerdefiniert vorgegeben

3.5.3 Der „Parallel Tempering“ Algorithmus

Im Gegensatz zum „*simulated annealing*“ verwendet der PT-Algorithmus mehrere verschiedene Referenzstrukturen parallel, wobei sich jede einzelne bei einer individuellen, aber konstanten Temperatur entwickeln kann.[179,180] Dieses Szenario, sprich die Existenz *einer* Referenzstruktur bei *einer* konstanten Temperatur, wird in dem Zusammenhang auch als „System“ bezeichnet. Die entsprechenden Temperaturen werden automatisiert so ausgewählt, dass das System mit höchster Temperatur (HT) eine globale Suche auf der Energiehyperfläche ermöglicht, während bei niedrigster Temperatur (LT) die lokale Suche nah bei einem tiefen Minimum gewährleistet ist.[179,180] Die einzelnen Strukturen können dabei durch sogenannte „*swap moves*“ zwischen den einzelnen Systemen ausgetauscht werden (Schema 7).[179,180] Dies beinhaltet zum einen den Effekt, dass geeignete Strukturen aus dem HT-System in das LT-System überführt werden um eine lokalere Suche zu ermöglichen. Zum anderen wird durch die „*swap moves*“ aber auch gewährleistet, dass Strukturen in LT-Systemen nicht in einem lokalen Minimum eingefroren werden können.[179,180]

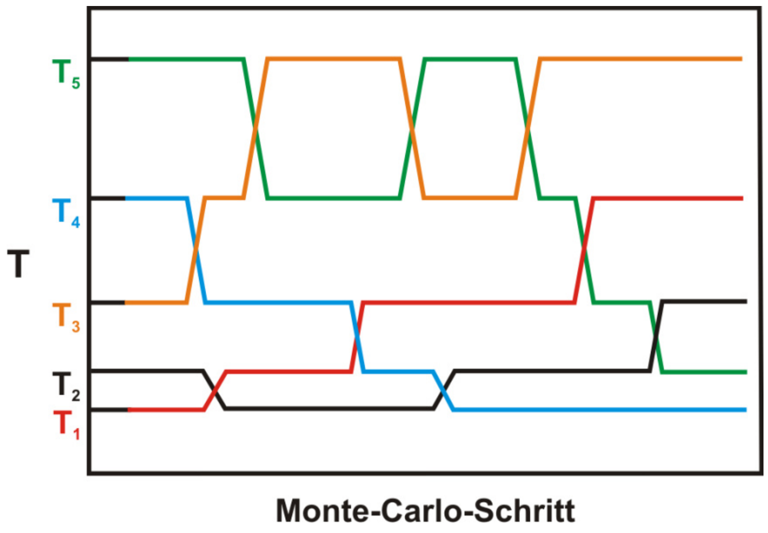

Schema 7: „*swap moves*“ zwischen den einzelnen Temperatursystemen T_1 - T_5

Zunächst wird ein System (bezüglich der Temperatur) ausgewählt. Während eines „*parallel tempering*“-Durchlaufs gibt es nun grundsätzlich zwei mögliche Szenarien. Entweder es wird im selben Temperatursystem durch Variation einer der Freiheitsgrade eine neue Teststruktur erzeugt. In diesem Falle sind die nachfolgenden Schritte analog wie die für den „*simulated annealing*“-Prozess; lediglich unter Punkt 5) kommt neben der Anpassung der Schrittweite auch die Adaption der Anzahl der Temperatursysteme und den entsprechenden Temperaturen hinzu, was letztendlich dazu führen soll, dass gewünschte globale Minimum zu erreichen.

Das zweite Szenario beinhaltet den „*swap move*“, wo die Teststruktur des einen Temperatursystems (z.B. T_3, siehe Schema 7) gegen die eines höheren Systems (T_4, siehe Schema 7) ausgetauscht werden kann. Analog zu Punkt 3) des SA-Verfahrens wird der R_{comb}-Wert der jeweiligen Teststrukturen innerhalb der unterschiedlichen Systeme berechnet und bewertet. Bei einem negativen ΔR_{comb}-Wert werden die Strukturen tatsächlich ausgetauscht. Handelt es sich um einen positiven ΔR_{comb}-Wert, liegt die Wahrscheinlichkeit eines Austauschs - in Analogie zum „*simulated annealing*“ - bei $e^{-\Delta R_{comb}/(\frac{1}{T_{aktuell}}-\frac{1}{T_{höher}})}$.

Diese beiden Szenarien werden während des PT-Durchlaufs so lange zufällig durchgeführt, bis die vorab benutzerdefinierte Anzahl an Schritten erreicht ist.

3.5.4 Der kombinierte R-Wert R_{comb}

Wie bereits in den zwei vorangehenden Kapiteln erwähnt, wird zur Auswertung der simulierten Pulverdiffraktogramme ein kombinierter R-Wert verwendet, welche neben dem klassischen gewichteten kristallographischen R-Wert auch die berechnete potentielle Energie berücksichtigt. Für die Strukturlösungen welche in **Kapitel 6** vorgestellt werden, wurde folgende Kombination verwendet:

$$R_{comb} = (1 - f)wRp + fR_{ccp} \qquad (3)$$

wobei *wRp* der gewichtete R-Wert und R_{ccp} (ccp für *close contact penalty*) der Anteil ist, der eine Überlappung der Atome und damit der Moleküle/ Molekülfragmente verhindern soll. Die Gewichtung erfolgt bei beiden Anteilen über den Wichtungsfaktor *f*. Der Berechnung von R_{ccp} liegt die Definition eines kleinstmöglichen Abstandes R_{ij}^0 zwischen jedem Atompaar *ij* basierend auf den van-der-Waals-Radien zugrunde. Wenn in einer Teststruktur der Abstand R_{ij} kleiner ist als R_{ij}^0, wird für das Atompaar eine Straffunktion e_{ccp}^{ij} berechnet, welche von R_{ij}/R_{ij}^0 abhängt, wobei e_{ccp}^{ij} dabei Werte zwischen 0 und 1 annehmen kann. Dieser Ausdruck geht dann über die Summe

$$E_{ccp} = \sum_{ij} e_{ccp}^{ij} \qquad (4)$$

in den R_{ccp}-Wert ein:

$$R_{ccp} = tanh\left(0{,}1 * \frac{E_{ccp} - E_{min}}{E_{tol}}\right) \qquad (5)$$

wobei

$$E_{tol} = N_{Atome} * 0{,}05 \qquad (6)$$

ist (N_{Atome} entspricht der Gesamtanzahl der Atome in der Elementarzelle) und die minimale Energie E_{min} aus der zufälligen Startstruktur abgeschätzt wird. Als grobe Richtlinie gilt, dass ein direkter Atomüberlapp pro 20 Atome den energetischen Gütefaktor R_{ccp} um ca. 10% erhöht.

4 Synopsis

Die vorgelegte Dissertation enthält vier Publikationen bzw. Manuskripte, die sich mit Struktur-Eigenschafts-Beziehungen ausgewählter supramolekularer organischer Verbindungen beschäftigen. Die Moleküle selbst unterscheiden sich in ihrer Größe, Funktionalität und Flexibilität, wobei die ausgebildeten supramolekularen Objekte sich durch ihre unterschiedliche Dimensionalität auszeichnen. Als Werkzeug zum Herausarbeiten dieser Struktur-Eigenschafts-Beziehungen wurde die NMR-Kristallographie eingesetzt. Der inhaltliche Zusammenhang von den Strukturaufklärungen formal eindimensionaler Benzoltrisamide in Bulkphase und in einer Polymermatrix, bis hin zur Bestimmung der Kristallstrukturen dreier makroskopisch zweidimensionaler Verbindungen ist aufgezeigt. Die notwendigen Strukturmodelle wurden *ab initio* aus Pulverdaten mit Hilfe von Realraummethoden erstellt und eine neue, kraftfeldunterstützte Rietveldverfeinerung ausgenutzt.

4.1 Strukturaufklärung eines effizienten Nukleierungs- und Klarmittel für *i*-PP

Eine überaus wichtige Additivklasse, welche für die industrielle Produktion von Kunststoffen eine große Bedeutung hat, sind Nukleierungsmittel. Durch den Zusatz solcher Verbindungen wird - vereinfacht betrachtet - die Verarbeitungstemperatur des Polymers deutlich erhöht, was im Umkehrschluss die Zyklenanzahl heruntersetzt und somit in gleicher Zeit die Produktionskapazität gesteigert werden kann. Allerdings ist nach wie vor noch nicht geklärt, welche komplexen Prozesse auf welcher Größenskala während der Nukleierung tatsächlich stattfinden und welche Rolle das entsprechende Additiv spielt. Es gibt jedoch Überlegungen, dass die im Polymer enthaltenen „Nanocluster“ des Additivmaterials gleiche Strukturmerkmale aufweisen wie im reinen Bulkmaterial.

In der bereits erschienenen Veröffentlichung (**Kapitel 6.1.1**) wurde zunächst die Kristallstruktur eines sehr effizienten BTA-basierten Nukleierungsagens für isotaktisches Polypropylen gelöst. Die Kombination aus synthetischer Arbeit, Pulverdiffraktion, Multikern-FK-NMR-Spektroskopie sowie quantenchemischen

Rechnungen entspricht dabei einem klassischen NMR-kristallographischen Ansatz.

Bei dem effizienten Nukleierungsreagenz handelt es sich um 1,3,5-tris(2,2-dimethylpropionylamino)benzol (Schema 8). Für quantitative FK-NMR-Experimente wurde eine ^{13}C-angereicherte Variante in einer mehrstufigen Synthese hergestellt und charakterisiert. Die Anreicherung fand dabei an allen drei Carbonylkohlenstoffatomen statt.

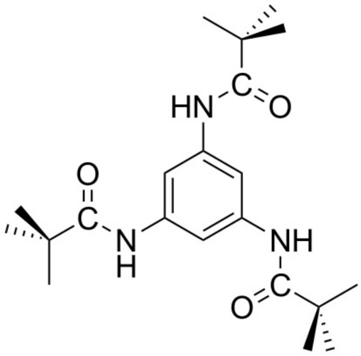

Schema 8: Molekulare Struktur von 1,3,5-tris(2,2-dimethylpropionylamino)benzol

Strukturmodelle konnten mit Hilfe von *ab initio* Realraum-Methoden aus Röntgenpulverdaten erzielt werden. Dabei stellte sich heraus, dass nur anhand der R-Werte als klassische Kostenfunktion dieser Methode verschiedene Strukturmodelle bzw. unterschiedliche Raumgruppen im orthorhombischen Kristallsystem möglich waren. Durch die eindimensionale FK-NMR-Spektroskopie, welche die Existenz von einem Molekül in der asymmetrischen Einheit offenbarte, konnte dabei die Anzahl der potenziellen Raumgruppen drastisch reduziert werden. Die endgültige Unterscheidung der verbliebenen Raumgruppen wurde durch quantitative ^{13}C^{13}C DQ-Experimente an der ^{13}C-angereicherten Spezies erreicht.

Abbildung 12a zeigt die experimentelle und die simulierten DQ-Aufbaukurven der verschiedenen Raumgruppen für die ^{13}C-angereicherte Spezies. Die dazugehörigen *rms*-Abweichungen zw. Experiment und Simulation sind als Histogramm mit den dazugehörigen wRp-Werten der Raumgruppen nach der Rietveldverfeinerung in Abbildung 12b zu sehen. Die Evaluation der Aufbaukurven in einem 9-Spin-System lieferte für die Raumgruppe $P2_12_12_1$ das beste Strukturmodell.

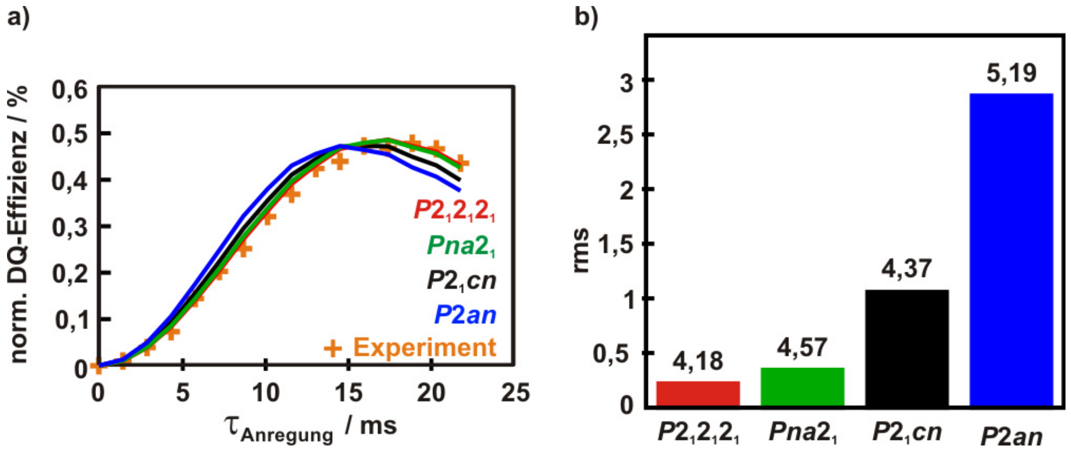

Abbildung 12: (a) Experimentelle (+) und simulierte (durchgezogene Linien) $^{13}C^{13}C$ DQ-Aufbaukurven der angereicherten Spezies; (b) Histogramm der *rms*-Abweichung zwischen experimenteller und simulierten Aufbaukurven für alle vier Raumgruppen mit den entsprechenden wRp-Werten nach den Rietveldverfeinerungen

Die Struktur in der vorher bestimmten Raumgruppe konnte als hexagonale Stabpackung identifiziert werden (Abbildung 13), wobei sich die einzelnen Moleküle über nicht-kovalente Wechselwirkungen (H-Brücken, π-Stacking) innerhalb eines Stabes anlagern.

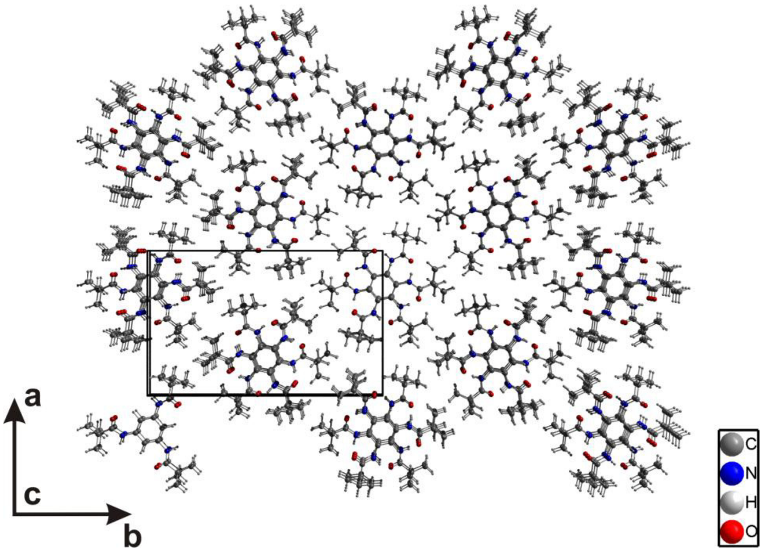

Abbildung 13: Kristallstruktur von 1,3,5-tris(2,2-dimethyl-propionylamino)benzol mit Blick entlang der c-Achse. Die Elementarzelle enthält vier symmetrieäquivalente Moleküle mit Atomen auf allgemeinen Lagen

Basierend auf der molekularen Geometrie führt diese Tatsache unweigerlich zu der Ausbildung von makroskopischen Dipolmomenten innerhalb eines Stabes. Diese Tatsache für sich allein betrachtet würde ein klassisch frustriertes System darstellen. Ein effizienter Ausgleich und somit ein schnelles Wachstum in eine

Richtung wurde aber durch die antiparallele Anordnung der Stäbe erreicht was im Endeffekt zu einem antiferroelektrischen Kristall führte (Abbildung 14).

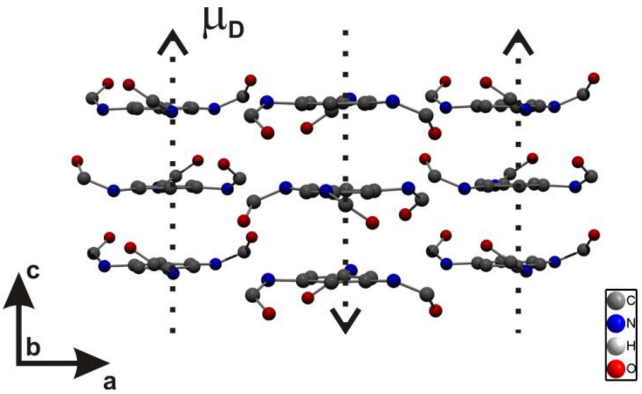

Abbildung 14: Ausschnitt der Kristallstruktur mit Hauptrichtung der Dipolmomente im Stab (gepunktete Pfeile) entlang der c-Achse im Kristall. Alle Protonen und die Seitengruppen wurden zur Verdeutlichung entfernt

Die Struktur konnte mit Hilfe NMR-kristallographischer Methoden erfolgreich gelöst werden. Die gewonnen strukturellen Aspekte sind essentiell, da sie den Weg für ein besseres Verständnis der Nukleierung in einem Polymer-Additiv-Gemisch eröffnen.

4.2 Selbstorganisation eines Additivs in einer *i*-PP Matrix

Basierend auf den Strukturinformationen, die aus der Bulkphase gewonnen wurden (**Kapitel 4.1**), widmete sich die Untersuchung hinsichtlich der Nukleierung nun einem Kompositmaterial bestehend aus dem Additiv inkorporiert in eine Matrix aus isotaktischem Polypropylen. Die vermutete geringe Größe der Additivcluster sowie die niedrige Konzentration (< 1000 ppm) verhinderten allerdings den Einsatz klassischer Methoden wie z.B. Röntgenbeugungsexperimente. Hier wurde die FK-NMR-Spektroskopie als lokale Analytik zur Methode der Wahl. Aus diesem Grund wurde 900 ppm der ^{13}C-angereicherten Spezies ins Polymer eingearbeitet, das Kompositmaterial mechanisch zerkleinert und spektroskopisch untersucht (**Kapitel 6.2.1**).

Zunächst wurde von dem Kompositmaterial ein ^{13}C CP MAS Spektrum aufgenommen. Hier galt es zunächst qualitativ zu verifizieren, ob die ^{13}C-Signale der

Carbonylgruppe des Additivs die gleiche chemische Verschiebung besitzen wie in der Bulkverbindung. Es konnte dabei ein schwaches Signal bei $\delta \approx 177$ ppm identifiziert werden, was einer analogen Signalposition des reinen Materials entspricht (Abbildung 15).

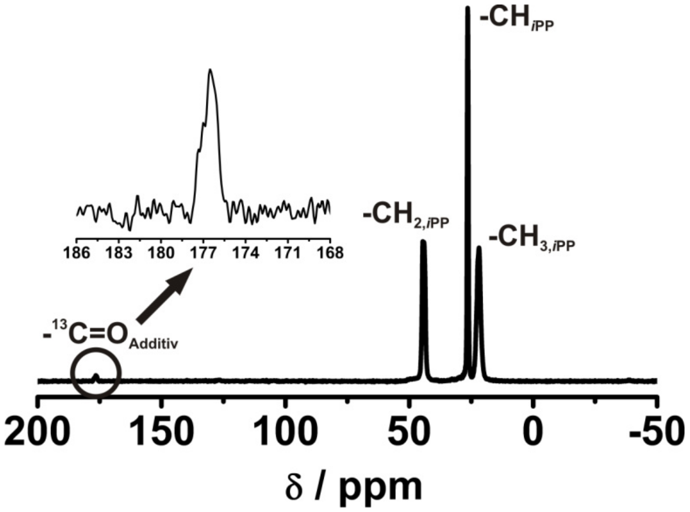

Abbildung 15: Experimentelles ^{1}H-^{13}C CP MAS Spektrum des Additiv/Polymer-Gemisches (^{13}C-angereichertes 1,3,5-tris(2,2-dimethylpropionylamino)benzol in *i*-PP) mit Signalbenennung für *i*-PP ($\delta \approx 22$ - ≈ 45 ppm) und dem Carbonylsignal ($\delta \approx 177$ ppm) der angereicherten ^{13}C=O-Gruppe des Additivs

Um Informationen bezüglich einer möglichen Anbindung des Polymers an das Additiv zu erhalten, wurden zweidimensionale ^{13}C^{13}C Doppelquantenspektren mit verschiedenen Anregungszeiten aufgenommen. Das 2D-Spekturm bei einer Anregungszeit von 15,36 ms (Abbildung 16) zeigt dabei Korrelationen zwischen allen Signalen, die dem Polymer zugeordnet werden können. Des Weiteren kann eine Resonanz bei $\delta \approx 177$ ppm in der Einquantendomäne identifiziert werden, was nach mehrfacher Rückfaltung dem Autokorrelationspeak der Carbonylgruppe des Additivs entsprach. Eine Korrelation zwischen der Additivspezies und dem Polymer wurde hingegen nicht beobachtet.

Das ^{13}C=O Autokorrelationssignal impliziert lediglich eine räumliche Nähe der Additivmoleküle zueinander. Um eine genaueres Bild über strukturelle Aspekte dieser Additivcluster zu erhalten, wurde eine symmetrische DQ-Aufbaukurve aufgenommen, welche in Abbildung 17 zu sehen ist. Als Vergleich wurde zusätzlich die Aufbaukurve der ^{13}C-angereicherten Carbonylgruppen des Bulkmaterials abgebildet.

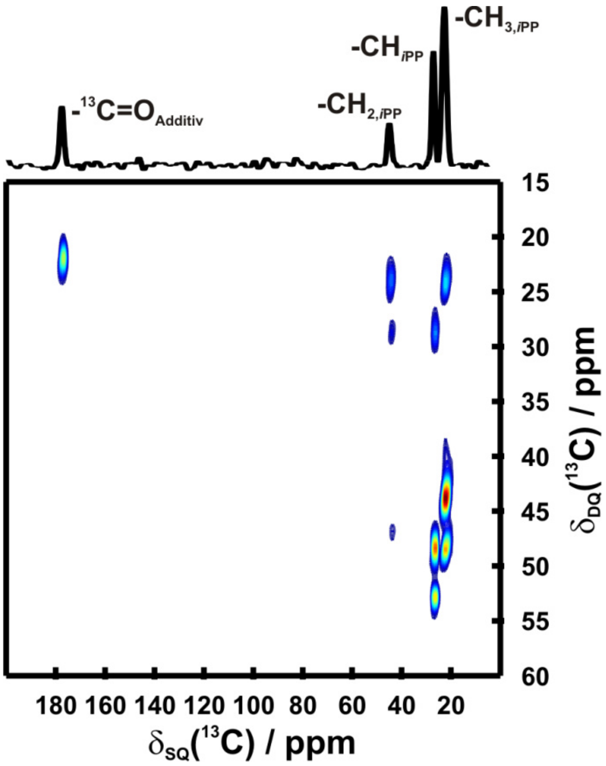

Abbildung 16: Experimentelles 2D DQ-SQ ^{13}C Spektrum der *i*-PP/Additiv-Mischung. Die F2-Projektion inklusive Signalbenennung entspricht der Summe aller Resonanzen in der Einquantendomäne

Trotz der extrem niedrigen Konzentration des Additivs in der Polymermatrix (< 0.1wt %) konnte gezeigt werden, dass im Rahmen des experimentellen Fehlers beide Kurven sehr gut übereinstimmen. Das legte den Schluss nahe, dass die Additivcluster in der *i*-PP Matrix ebenfalls eine Stabstruktur analog zum Bulkmaterial besitzen.

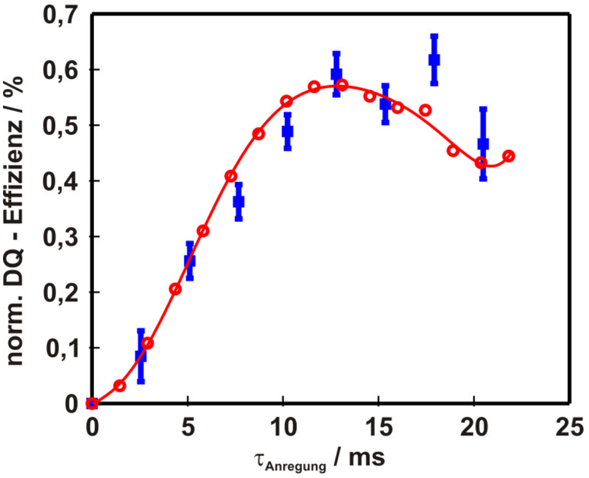

Abbildung 17: Experimentelle symmetrische ^{13}C DQ-Aufbaukurve der angereicherten Carbonylgruppen in purem 1,3,5-tris(2,2-dimethylpropionylamino)benzol (rote Kreise) und im *i*-PP/Additiv-Gemisch (blaue Vierecke mit Fehlerbalken)

Mit der hier angeführten Methode ist man somit in der Lage, die kolumnare Anordnung der Moleküle zu erfassen, allerdings nicht die Anordnung der Stäbe zueinander. Auch ein Vergleich der d_{rss}-Werte - vereinfacht gesagt eine gemittelte dipolare Kopplungskonstante - liefert für verschiedene Szenarien komplementäre Ergebnisse. Während für isolierte Moleküle ein d_{rss}-Wert von 37 Hz berechnet werden konnte, was einen viel schwächeren DQ-Aufbau zur Folge hätte als beobachtet wurde, sind die entsprechenden Kopplungskonstanten eines einzelnen Stranges und der Stabpackung des Kristalls mit ca. 130 Hz praktisch identisch.

Des Weiteren zeigte das experimentelle ^{13}C DQ-Signal der Carbonylgruppen im *i*-PP/Additiv-Gemisch eine signifikante Verbreiterung der Linienform (Abbildung 18). Diese „Maskierung“ der Feinstruktur des Signals, welche für das Bulk-material noch beobachtet wurde, lässt nicht nur eine schwächer ausgeprägte Fernordnung im Vergleich zum reinen Additivmaterial vermuten, sondern auch die Existenz von Kristallitgrößen im unteren Nanometerbereich innerhalb der Polymermatrix.

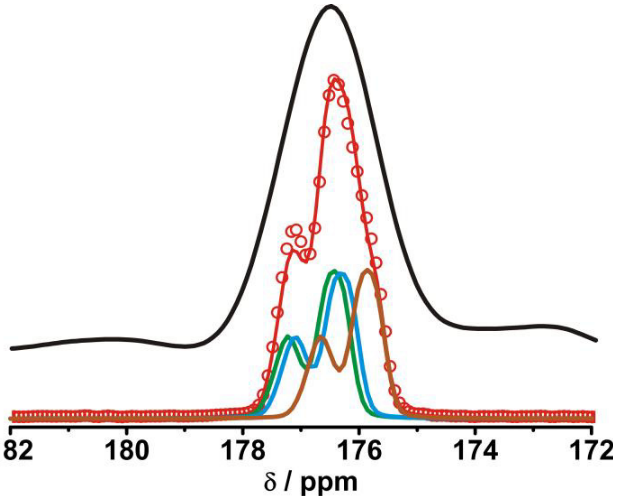

Abbildung 18: Experimentelles (rote Kreise) und simuliertes (rote Linie) ^{13}C DQ gefiltertes Spektrum des Additivs im Bulk mit Entfaltung in drei einzelne Resonanzen (grüne, blaue und braune Linie) mit Feinstrukturen aufgrund der Quadrupolwechselwirkung zweiter Ordnung des benachbarten ^{14}N-Kerns auf den detektierten ^{13}C-Kern (unten); experimentelles ^{13}C DQ gefiltertes Spektrum des Additiv/Polymer-Gemisches als Summe aller aus der Aufbaukurve extrahierten 1D Spektren (oben)

Es ist somit zum ersten Mal experimentell gelungen, trotz geringster Konzentrationen, die Struktur des Additivs in einer Polymermatrix nachzuweisen. Dabei stellte sich heraus, dass das zentrale Strukturmotiv der Cluster im Polymer gleich dem der Bulkkristallstruktur ist.

4.3 Strukturaufklärung eines ^{19}F-haltigen 1,3,5-Benzoltrisamids

Nachdem für das kommerzielle BTA-System sowohl im Bulk als auch im *i*-PP/Additiv-Kompositmaterial eine kolumnare Anordnung nachgewiesen wurde (**Kapitel 4.1** und **4.2**), galt es nun der Anbindung des Polymers an die Additivcluster zu widmen. Basierend auf den Erfahrungen aus den Messungen des ^{13}C-angereicherten Derivates in *i*-PP war eindeutig, dass der Abstand zwischen den Additivclustern und dem Polymer minimal gehalten werden muss. Zu diesem Zweck müssen NMR-aktive Sonden eingeführt werden, die zum einen eine höhere Empfindlichkeit besitzen als ^{13}C, zum anderen wäre auch ein höheres gyromagnetisches Verhältnis von großem Vorteil, da dadurch wesentlich größere Abstände detektiert werden könnten. Um dies synthetisch zu realisieren, wurde ein zu dem in **Kapitel 4.1** beschriebenes chemisch ähnliches Derivat hergestellt. Der einzige Unterschied bestand lediglich darin, dass eine CH_3-Gruppe in jeder *t*-Butyl-Einheit im Seitenarm gegen ein Fluoratom ersetzt wurde (Schema 9).

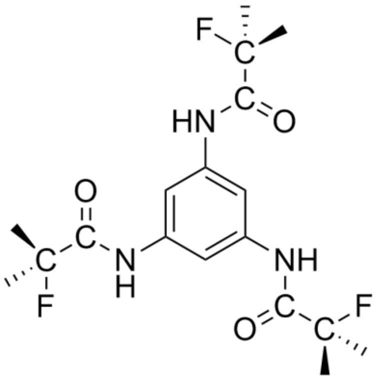

Schema 9: Molekulare Struktur von 1,3,5-tris(2-fluor-2-methylpropionylamino)benzol

Auch hier galt es zunächst, die Kristallstruktur des Bulkmaterials zu bestimmen und das Packungsmotiv der Moleküle in der Elementarzelle herauszuarbeiten. Hier wurde der bereits in **Kapitel 4.1** erfolgreiche Ansatz der NMR-Kristallographie angewendet. Eine Charakterisierung der Verbindung mittels 1D FK-NMR-Spektroskopie an unterschiedlichen Kernen (^{1}H,^{13}C,^{15}N,^{19}F) offenbarte zum einen die Existenz von NH---CO Wasserstoffbrückenbindungen innerhalb der

Kristallstruktur, was durch die chemische Verschiebung der NH-Protonen im ^{1}H-Spektrum verifiziert wurde. Eine unterschiedliche Anzahl an Resonanzen für die aromatischen Protonen legt dabei die Existenz von zwei unabhängigen Molekülen in der asymmetrischen Einheit nahe. Weiterhin konnte aufgrund der überlagerten Signale der aromatischen Protonen eine Koplanarität - wie für das BTA-System in **Kapitel 4.1** beschrieben - ausgeschlossen werden.

Zum anderen konnten im ^{19}F-Spektrum eine Aufspaltung in fünf Signalgruppen zw. $\delta \approx -145$ bis $\delta \approx -135$ ppm identifiziert werden, welche sich aber insgesamt in sechs Signale entfalten ließ (Abbildung 19, schwarze und blaue Linien).

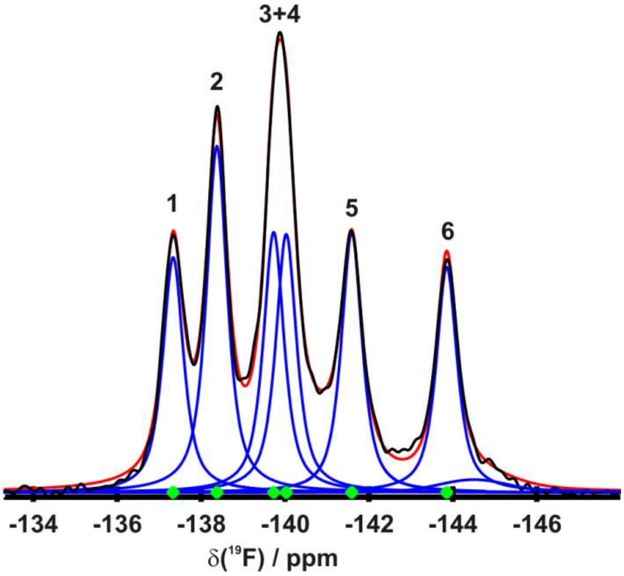

Abbildung 19: 1D ^{19}F FK-NMR-Spektrum der fluorierten Verbindung (schwarze Linie) mit Signalbenennung (Ziffern 1-6), Entfaltung in sechs Einzelresonanzen (blaue Linien) sowie dem daraus resultierenden gefitteten Gesamtspektrum (rote Linie); die grünen Punkte markieren die jeweilige isotrope chemische Verschiebung der Fluoratome 1-6; der kleine Hügel bei $\delta \approx -145$ ppm gehört möglicherweise zu einer zweiten Phase

Daraus ließ sich schlussfolgern, dass sich insgesamt sechs unterschiedliche Fluoratome von zwei unabhängigen Molekülen in der asymmetrischen Einheit innerhalb der Kristallstruktur befinden müssen. Ein absolut vergleichbarer Trend wurde ebenfalls in den ^{13}C- und ^{15}N CP MAS Spektren anhand der Anzahl und Überlappungen der Resonanzen wiedergefunden.

Basierend auf den Erkenntnissen aus den 1D FK-NMR-Spektren, wurde ein Strukturmodell aus Röntgenpulverdaten erstellt. Die Indizierung des Pulverdiffraktogramms lieferte eindeutig eine monokline Metrik, das Profil konnte dann in der niedrigsten Raumgruppe ohne Translationselemente (*P*2) hervorragend angepasst werden. Anhand der Reflexlagen in Kombination mit den Auslöschungsbedingungen sowie Abschätzungen aus dem molekularen Volumen im Vergleich zum Zellvolumen konnte ausschließlich in Raumgruppe $P2_1$ ein geeignetes Strukturmodell mit abschließender Rietveldverfeinerung erstellt werden. Demnach existierten zwei unabhängige Moleküle in der asymmetrischen Einheit, welche lediglich eine intrinsische C_1-Symmetrie aufzeigten. Dadurch bedingt enthält die Elementarzelle also vier Moleküle.

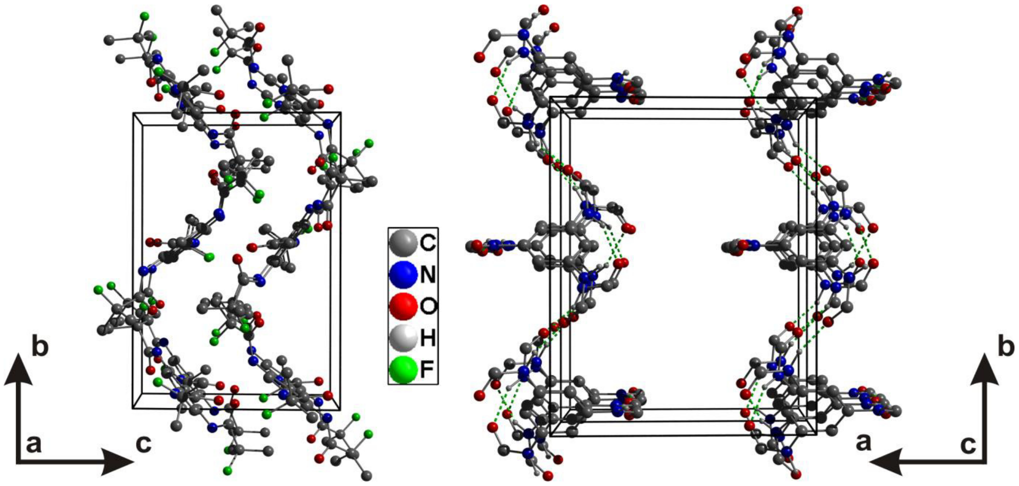

Abbildung 20: Ausschnitt aus der Kristallstruktur von 1,3,5-tris(2-fluor-2-methylpropionylamino)benzol; links: Blickrichtung entlang der a-Achse mit Zick-Zack-Motiv parallel zur monoklinen b-Achse; rechts: perspektivische Sicht entlang der c-Achse einer doppelten Elementarzelle mit intermolekularen H-Brücken (grüne gestrichelte Linien) entlang der kristallographischen b- und c-Achse

Das Packungsmuster der Moleküle ist dabei entgegen anfänglichen Erwartungen sehr verschieden von jenem der ^{13}C-angereicherten BTA-Spezies (**Kapitel 4.1**). Es existieren keine π-π-Wechselwirkungen zwischen den aromatischen Einheiten (analog zu den Ergebnissen aus dem ^{1}H-Spektrum), auch ein intermolekulares, helixartiges H-Brücken-Muster zwischen den einzelnen molekularen Amideinheiten wird nicht beobachtet. Es besteht vielmehr ein komplexes NH---CO Wasserstoffbrückenmuster zwischen den zwei unabhängigen Molekülen, welches sich entlang von zwei Kristallachsen ausdehnt, während in der dritten Richtung lediglich van-der-Waals-Kräfte dominieren. Hinzu kommt, dass die Fluoratome selbst an schwachen, intramolekularen H-Brücken zum Amidproton beteiligt sind. Generell kann dieses Packungsmotiv als ein zweidimensionales Zick-Zack-Muster beschrieben werden (Abbildung 20). Welche Rolle Dipolmomente in der Struktur spielen ist nicht leicht zu beantworten, da im Vergleich zu dem BTA-Derivat aus **Kapitel 4.1** lediglich eine C_1-Symmetrie vorliegt, zusätzlich aber durch die Fluoratome weitere zu berücksichtigende Faktoren hinzukommen. Eine detaillierte Aussage dahingehend wäre nur durch quantenchemische Rechnungen möglich.

Um eine quantitative Bestätigung des vorher angeführten Strukturmodells zu erhalten, wurden $^{19}F^{19}F$ DQ-Experimente durchgeführt. Die zweidimensionale NMR-Spektroskopie offenbarte dabei komplexe Korrelationen zwischen allen Fluorspezies in der Struktur, was eine eindeutige Zuordnung der Signale zu den entsprechenden Fluoratomen innerhalb der Elementarzelle nicht möglich machte. Es wurde dann eine ^{19}F DQ-Aufbaukurve gemessen und daraus für jede einzelne ^{19}F-Resonanz (Zuordnung siehe 1D-Spektrum in Abbildung 19) eine Aufbaukurve extrahiert. Es stellte sich trotz relativ ähnlichen Verlaufs heraus, dass vier der Aufbaukurven ihre Maxima bei niedrigeren Anregungszeiten besaßen als die anderen beiden, was umgekehrt dafür sprach, das zwei Fluoratome in der Struktur einen längeren Abstand zum nächsten Fluoratom besitzen als die übrigen vier. Diese grundsätzliche Zuordnung - und somit auch die Kristallstruktur - wurden dann anhand der sehr guten Übereinstimmungen zwischen den simulierten und gemessenen Aufbaukurven bestätigt (Abbildung 21).

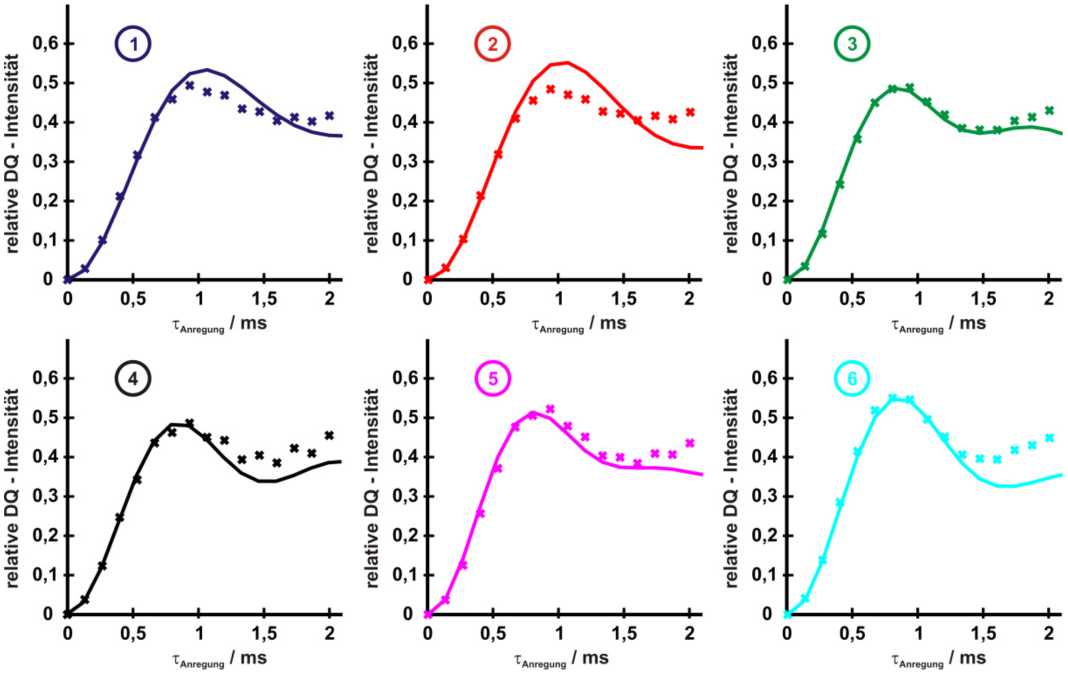

Abbildung 21: Experimentelle (Kreuze) und simulierte (Linien) $^{19}F^{19}F$ DQ-Aufbaukurven der sechs unterschiedlichen Fluoratome basierend auf einem 9-Spin-System mit Zuordnung entsprechend der Benennung aus dem 1D-Spektrum (Abbildung 19)

In diesem Manuskript gelang es, die komplizierte Struktur einer organischen, fluorhaltigen BTA-basierten Verbindung mit Hilfe von NMR-kristallographischen Methoden zu lösen, wobei erstmalig $^{19}F^{19}F$ DQ-Experimente bei einer organischen Verbindung erfolgreichen angewendet wurde. In Zukunft ist auch eine Strukturbestimmung dieses Additivs im Polymer durchführbar, da diese $^{19}F^{19}F$ Doppelquantenexperimente sehr sensitiv auf die molekulare Anordnung reagieren. Somit würden z.B. isolierte, nicht assemblierte Moleküle aufgrund längerer, intramolekularer ^{19}F-^{19}F-Abstände einen viel schwächeren DQ-Aufbau liefern als die hier im Bulkmaterial supramolekularen 2D-Aggregate.

4.4 Zweidimensionale organische Nanosheets

Das Verhalten der Selbstassemblierung supramolekularer Verbindungen kann durch kleinste molekular-strukturelle Veränderungen wesentlich beeinflusst werden. Dies wurde bereits bei den vermeintlich eindimensionalen BTA-basierten Nanostrukturen gezeigt (Vgl. **Kapitel 4.1** und **4.3**) sowie in **Kapitel 3.3.2** aufgeführt. Somit kann allein anhand des Moleküldesigns pauschal keine Aussage über Struktur-Eigenschafts-Beziehungen - weder in Bulkphase noch in einem möglichen Kompositmaterial - getroffen werden. Die in **Kapitel 6.1.4** präsentierte Veröffentlichung beschäftigt sich mit der NMR-kristallographischen Charakterisierung dreier Verbindungen, deren supramolekularen Aggregate formal eine höhere Dimensionalität besitzen als BTAs und sich - neben der Größe und Flexibilität - im Wesentlichen nur durch ihre intrinsischen Wasserstoffbrückenmuster unterscheiden. Der Fokus liegt dabei auf den Kristallstrukturen, dem Bildungsmechanismus der selbstassemblierten Nanostrukturen in der Bulkphase sowie die mögliche Abgrenzung von den eindimensionalen Nanostrukturen. Dabei galt es weiterhin zu eruieren, ob die in **Kapitel 4.1** und **4.3** verwendeten Realraummethoden sowie die kraftfeldunterstütze Rietveldverfeinerung auch bei dieser Substanzklasse erfolgreich Strukturlösungen hervorbringen.

Die drei durch klassische organische Synthese hergestellten Verbindungen sind in Schema 10 zu erkennen. Alle basieren auf einem Cyclohexankern, besitzen eine symmetrische 1,4-Substituierung sowie eine *tert*-Butylgruppe in der

Seitenkette. Als Verbindungsstück zwischen Kern und Rest wurden eine Amid- (**1**), eine Harnstoff- (**2**) sowie eine Acylharnstoffgruppe (**3**) eingebracht, *per se* also Moleküle mit drei unterschiedlichen Wasserstoffbrückenkapazitäten.

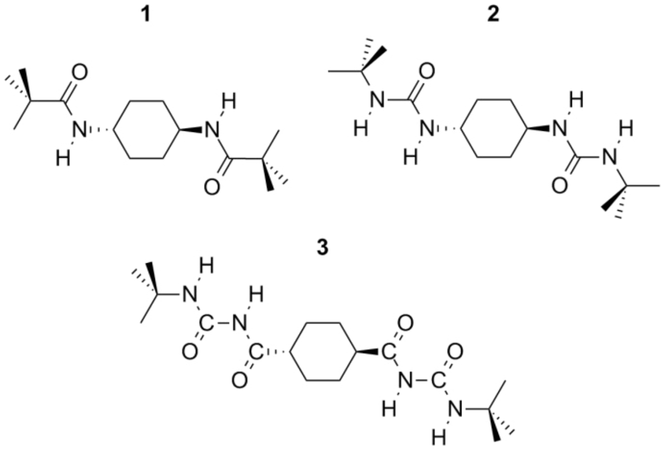

Schema 10: Molekulare Strukturen der synthetisierten cyclohexanbasierten Verbindungen

Um einen Einblick in die Morphologie der niedermolekularen Verbindungen zu erlangen, wurden diese zunächst mit Rasterelektronenmikroskopie untersucht. Dabei stellte sich heraus, dass alle drei Verbindungen in Schichten vorliegen und über große laterale Ausdehnungen im Mikrometerbereich verfügen (Abbildung 22).

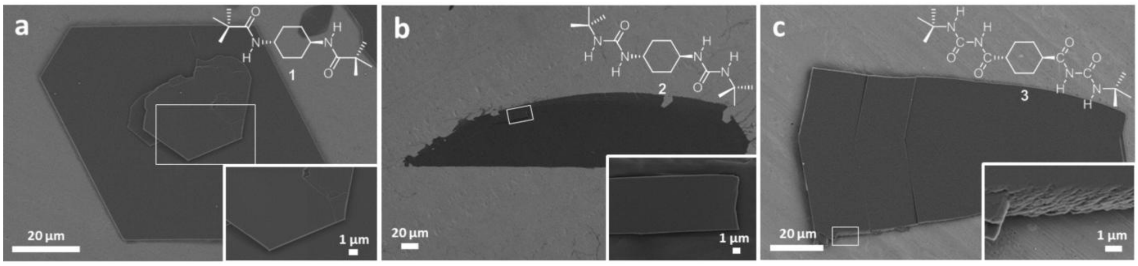

Abbildung 22: REM-Aufnahmen zweidimensionaler Strukturen mit Vergrößerungen von a) Bisamid 1, b) Bisharnstoff 2 und c) Bisacylharnstoff 3

Die topologische Höhe wurde nicht quantifiziert, Abschätzungen legen aber nahe, dass diese um einige Größenordnungen geringer ist, was im Umkehrschluss zu großen Aspektverhältnissen führen sollte. Eine genauere Betrachtung zeigte, dass für **1** und **2** eine sehr homogene Oberfläche mit wohldefinierten Kanten beobachtet wurden, wohingegen bei **3** eine signifikante Feinstruktur erkennbar war, was auf einer Überlagerung von vielen einzelnen dünnen Schichten basiert.

Erste strukturelle Informationen wurden durch 1D FK-NMR-Experimente (^{1}H,^{13}C,^{15}N) gewonnen, wobei eine genaue Zuordnung aller Resonanzen im

Protonenspektrum schließlich über zweidimensionale ^{1}H-^{13}C sowie ^{1}H-^{15}N HETCOR-Messungen erzielt werden konnte. Daraus ergaben sich im Wesentlichen zwei für die nachfolgende Strukturaufklärung elementare Erkenntnisse. Zum einen konnte basierend auf der Anzahl der Resonanzen in den ^{13}C und ^{15}N CP MAS Spektren der Inhalt der asymmetrischen Einheit für alle drei Verbindungen auf ein halbes Molekül bestimmt werden. Dies implizierte gleichzeitig eine intrinsische molekulare C_2- oder C_i-Symmetrie. Des Weiteren wurde anhand der entsprechenden chemischen Verschiebung im Protonenspektrum die Existenz von Wasserstoffbrückenbindungen in der Struktur nachgewiesen.

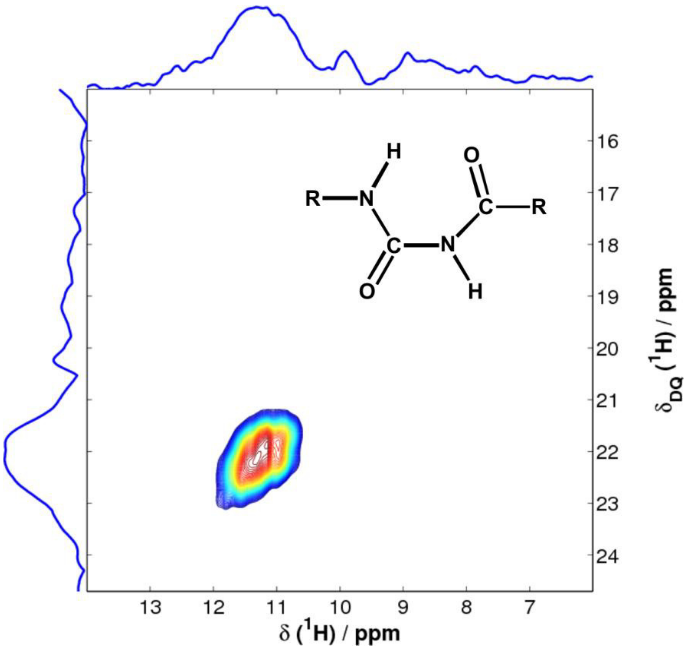

Abbildung 23: ^{1}H-^{1}H DQ-SQ Korrelationsspektrum (Bereich der NH-Protonen) von Verbindung 3 mit Ausschnitt der Acylharnstoffgruppe in vorliegender *trans-cis-trans*-Konfiguration

Zusätzlich konnte durch die Anwendung von ^{1}H^{1}H DQ-SQ Experimenten eindeutig die Konformation der Acylharnstoffgruppe in Verbindung **3** herausgearbeitet werden. Da in der Harnstoffspezies die beiden NH-Protonen mit ca. 2.0 Å - 2.5 Å eine räumliche Nähe aufweisen, ergibt diese bei geringer Anregungszeit bereits ein Korrelationssignal im entsprechenden Doppelquanten-spektrum. Im Falle des Acylharnstoffderivates konnte lediglich ein Autokorrelationssignal einer der beiden NH-Gruppen identifiziert werden. Dies spricht eindeutig für eine größere Entfernung dieser beiden Protonen, was wiederum den Schluss nahe legt, dass die Acylharnstoffgruppe in einer *trans-cis-trans*-

Konfiguration vorliegt und dabei eine intramolekulare Wasserstoffbrückenbindung zu einem Sechsring ausbildet (Abbildung 23).

Die gewonnen Strukturinformationen wurden dann in *ab initio* Strukturlösungen basierend auf Röntgenpulverdaten implementiert. Alle drei Derivate wiesen dabei eine intrinsische Inversionssymmetrie sowie eine Sesselkonformation des Cyclohexanringes auf. Für Verbindung **3** konnte zusätzlich die bereits aus FK-NMR-Daten vermutete *trans*-*cis*-*trans*-Konfiguration der Acylharnstoffgruppe mit intramolekularer Wasserstoffbrückenbindung identifiziert werden.

Es konnte gezeigt werden, dass Verbindung **1** und **2** isostrukturell in der monoklinen Raumgruppe $P2_1/c$ kristallisieren. Die Strukturen zeichnen sich durch ein schnelles Wachstum in zwei Richtungen in Bezug auf die Kristallachsen aus, was auf der Ausbildung von moderaten Wasserstoffbrückenbindungen in Kombination mit einer Verdrehung der Moleküle gegeneinander basiert (Abbildung 24). Es zeigte sich, dass jede Donor- und Akzeptoreinheit innerhalb eines Moleküls mit einem unabhängigen Gegenpart in einem anderen Molekül verbunden ist. Das hat unmittelbar zu Folge, dass jedes Molekül vier Nachbarmoleküle besitzt. Das Wachstum in die dritte Raumrichtung ist aufgrund von van-der-Waals-Kräften als einzige Wechselwirkung verlangsamt. Es konnte außerdem gezeigt werden, dass durch die intrinsische molekulare Punktsymmetrie Dipolmomente beim Wachstum des Kristalls keinen Einfluss besitzen.

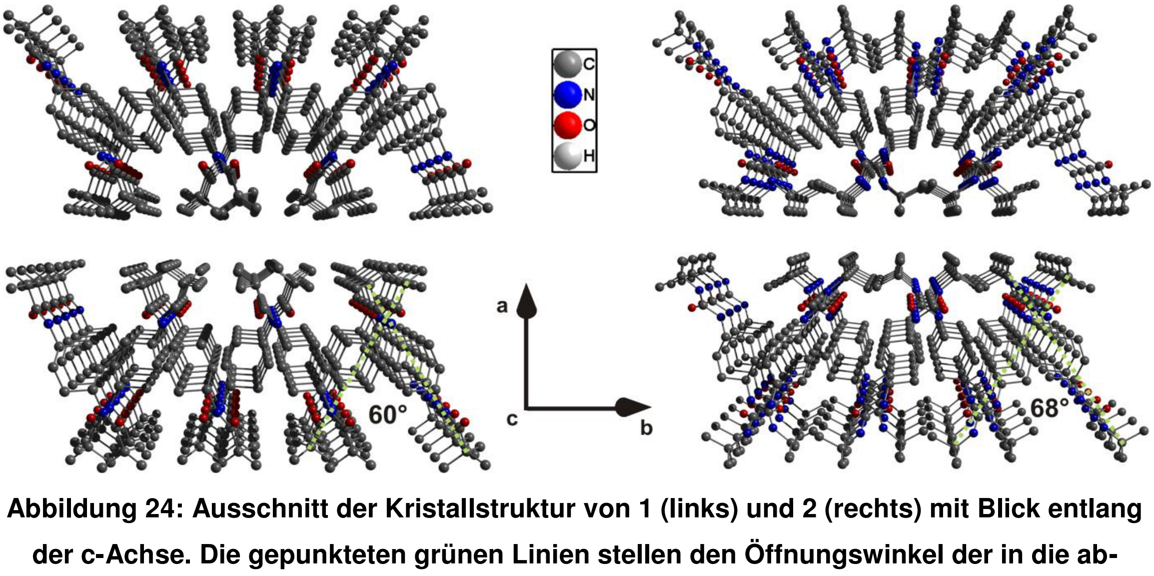

Abbildung 24: Ausschnitt der Kristallstruktur von 1 (links) und 2 (rechts) mit Blick entlang der c-Achse. Die gepunkteten grünen Linien stellen den Öffnungswinkel der in die ab-Ebene des Kristalls projizierten molekularen Hauptachsen dar

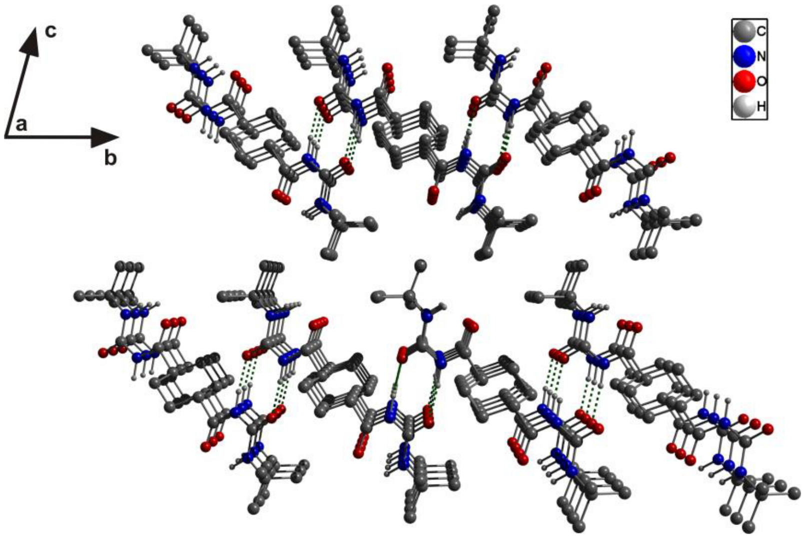

Abbildung 25: Ausschnitt der Kristallstruktur von 3 mit Blick entlang der a-Achse. Die gestrichelten grünen Linien stellen die intermolekularen Wasserstoffbrückenbindungen dar

Für Verbindung **3** wurde die Kristallstruktur in der triklinen Raumgruppe $P\bar{1}$ gelöst. Die Moleküle sind dabei mittels starken Wasserstoffbrücken über Kopf-Schwanz-Verknüpfungen miteinander verbunden, was somit zu einem sehr schnellen Wachstum in eine Richtung in Bezug auf die Kristallachsen führt (Abbildung 25). Entlang der anderen beiden Achsen können ebenfalls lediglich van-der-Waals-Wechselwirkungen ausgemacht werden. Warum sich dennoch eine zweidimensionale Morphologie einstellt, bleibt offen, jedoch spielen auch hier Dipolmomente für das schnelle Wachstum keine Rolle.

In dieser Publikation konnten die Kristallstrukturen von drei morphologisch zweidimensionalen niedermolekularen organischen Verbindungen mit NMR-kristallographischen Methoden gelöst werden. Dabei konnte erklärt werden, dass durch ein komplexes Wasserstoffbrückennetzwerk in Kombination mit der geometrischen Anordnung der Moleküle innerhalb der Elementarzelle auf mikroskopischer Ebene die Zweidimensionalität im Makroskopischen erzielt wurde. Die eingesetzten Realraummethoden sowie die kraftfeldunterstützte Rietveldverfeinerung lieferten trotz höherer Flexibilität und anderen Wasserstoffbrückensynthons innerhalb der Moleküle auch hier exzellente Ergebnisse.

5 Quellen

1 F. Wöhler. Über die künstliche Bildung des Harnstoffs. *Poggendorfs Ann. Physik* **1828**, *12*, 253.

2 J.-M. Lehn. Supramolekulare Chemie - Moleküle, Übermoleküle und molekulare Funktionseinheiten. *Angewandte Chemie* **1988**, *100*, 91.

3 J.-M. Lehn. Perspectives in Supramolecular Chemistry - From Molecular Recognition towards Molecular Information Processing and Self-Organization. *Angew. Chem. Int. Ed. Engl.* **1990**, *29*, 1304.

4 J.-M. Lehn. Supramolecular chemistry: from molecular information towards self-organization and complex matter. *Rep. Prog. Phys.* **2004**, *67*, 249.

5 J.-M. Lehn. From supramolecular chemistry towards constitutional dynamic chemistry and adaptive chemistry. *Chem. Soc. Rev.* **2007**, *36*, 151.

6 C. Schmuck, W. Wienand. Self-Complementary Quadruple Hydrogen-Bonding Motifs as a Functional Principle: From Dimeric Supramolecules to Supramolecular Polymers. *Angew. Chem. Int. Ed.* **2001**, *40*, 4363.

7 G. Whitesides, J. Mathias, C. Seto. Molecular self-assembly and nanochemistry: a chemical strategy for the synthesis of nanostructures. *Science* **1991**, *254*, 1312.

8 N. B. Bowden, M. Weck, I. S. Choi, G. M. Whitesides. Molecule-Mimetic Chemistry and Mesoscale Self-Assembly. *Acc. Chem. Res.* **2001**, *34*, 231.

9 C. V. K. Sharma. Designing Advanced Materials As Simple As Assembling Lego® Blocks! *J. Chem. Educ.* **2001**, *78*, 617.

10 F. Vögtle, *Supramolecular Chemistry: An Introduction*, Wiley, Chichester, **1993**.

11 J. Lehn, *Supramolecular Chemistry; Concepts and Perspectives*, Wiley, Chichester, **1995**.

12 J. Steed, J. Atwood, *Supramolecular Chemistry*, John Wiley & Sons, **2009**.

13 S. Neidle, *Oxford Handbook of Nucleic Acid Structure*, Oxford University Press, USA, **1999**.

14 C. Wang, Z. Wang, X. Zhang. Amphiphilic Building Blocks for Self-Assembly: From Amphiphiles to Supra-amphiphiles. *Acc. Chem. Res.* **2012**, *45*, 608.

15 A. Rich, F. Crick. The molecular structure of collagen. *J. Mol. Biol.* **1961**, *3*, 483.

16 K. Okuyama, K. Okuyama, S. Arnott, M. Takayanagi, M. Kakudo. Crystal and molecular structure of a collagen-like polypeptide (Pro-Pro-Gly)10. *J. Mol. Biol.* **1981**, *152*, 427.

17 D. B. Murphy, K. T. Wallis. Erythrocyte Microtubule Assembly in Vitro. *J. Biol. Chem.* **1986**, *261*, 2319.

18 http://www.nobelprize.org/nobel_prizes/chemistry/laureates/1987.

19 Y. Matsunaga, N. Miyajima, Y. Nakayasu, S. Sakai, M. Yonenaga. Design of Novel Mesomorphic Compounds - N,N',N"-trialkyl-1,3,5-benzenetricarboxamides. *Bull. Chem. Soc. Jpn.* **1988**, *61*, 207.

20 P. J. M. Stals, J. C. Everts, R. de Bruijn, I. A. W. Filot, M. M. J. Smulders, R. Martin-Rapun, E. A. Pidko, T. F. A. de Greef, A. R. A. Palmans, E. W. Meijer. Dynamic Supramolecular Polymers Based on Benzene-1,3,5-tricarboxamides: The Influence of Amide Connectivity on Aggregate Stability and Amplification of Chirality. *Chem. Eur. J.* **2010**, *16*, 810.

21 A. Bernet, R. Q. Albuquerque, M. Behr, S. T. Hoffmann, H.-W. Schmidt. Formation of a supramolecular chromophore: a spectroscopic and theoretical study. *Soft Matter* **2012**, *8*, 66.

22 J. Y. Chang, J. H. Baik, C. B. Lee, M. J. Han, S.-K. Hong. Liquid Crystals Obtained from Disclike Mesogenic Diacetylenes and Their Polymerization. *J. Am. Chem. Soc.* **1997**, *119*, 3197.

23 J. J. van Gorp, J. A. J. M. Vekemans, E. W. Meijer. C_3-Symmetrical Supramolecular Architectures: Fibers and Organic Gels from Discotic Trisamides and Trisureas. *J. Am. Chem. Soc.* **2002**, *124*, 14759.

24 A. R. A. Palmans, J. A. J. M. Vekemans, E. W. Meijer, A. R. A. Palmans, H. Kooijman, A. L. Spek. Hydrogen-bonded porous solid derived from trimesic amide. *Chem. Commun.* **1997**, 2247.

25 L. Brunsveld, A. P. H. J. Schenning, M. A. C. Broeren, H. M. Janssen, J. A. J. M. Vekemans, E. W. Meijer. Chiral amplification in columns of self-assembled N,N',N"-tris((S)-3,7-dimethyloctyl)benzene-1,3,5-tricarboxamide in dilute solution. *Chem. Lett.* **2000**, 292.

26 A. R. A. Palmans, J. A. J. M. Vekemans, H. Fischer, R. A. Hikmet, E. W. Meijer. Extended-Core Discotic Liquid Crystals Based on the Intramolecular H-Bonding in N-Acylated 2,2'-Bipyridine-3,3'-diamine Moieties. *Chem. Eur. J.* **1997**, *3*, 300.

27 R. van Hameren, P. Schön, A. M. van Buul, J. Hoogboom, S. V. Lazarenko, J. W. Gerritsen, H. Engelkamp, P. C. M. Christianen, H. A. Heus, J. C. Maan, T. Rasing, S. Speller, A. E. Rowan, J. A. A. W. Elemans, R. J. M. Nolte. Macroscopic Hierarchical Surface Patterning of Porphyrin Trimers via Self-Assembly and Dewetting. *Science* **2006**, *314*, 1433.

28 I. Paraschiv, M. Giesbers, B. van Lagen, F. C. Grozema, R. D. Abellon, L. D. A. Siebbeles, A. T. M. Marcelis, H. Zuilhof, E. J. R. Sudhölter. H-Bond-Stabilized Triphenylene-Based Columnar Discotic Liquid Crystals. *Chem. Mater.* **2006**, *18*, 968.

29 P. Besenius, G. Portale, P. H. H. Bomans, H. M. Janssen, A. R. A. Palmans, E. W. Meijer. Controlling the growth and shape of chiral supramolecular polymers in water. *Proc. Natl. Acad. Sci. U. S. A.* **2010**, *107*, 17888.

30 P. P. Bose, M. G. B. Drew, A. K. Das, A. Banerjee. Formation of triple helical nanofibers using self-assembling chiral benzene-1,3,5-tricarboxamides and reversal of the nanostructure's handedness using mirror image building blocks. *Chem. Commun.* **2006**, 3196.

31 M. de Loos, J. H. van Esch, R. M. Kellogg, B. L. Feringa. C_3-Symmetric, amino acid based organogelators and thickeners: a systematic study of structure-property relations. *Tetrahedron* **2007**, *63*, 7285.

32 M. Gelinsky, R. Vogler, H. Vahrenkamp. Tripodal Pseudopeptides with Three Histidine or Cysteine Donors: Synthesis and Zinc Complexation. *Inorg. Chem.* **2002**, *41*, 2560.

33 B. Gong, C. Zheng, Y. Yan. Structure of N,N',N"-tris(carboxymethyl)-1,3,5-benzenetricarboxamide trihydrate. *J. Chem. Crystallogr.* **1999**, *29*, 649.

34 M. A. J. Veld, D. Haveman, A. R. A. Palmans, E. W. Meijer. Sterically demanding benzene-1,3,5-tricarboxamides: tuning the mechanisms of supramolecular polymerization and chiral amplification. *Soft Matter* **2011**, *7*, 524.

35 K. P. van den Hout, R. Martín-Rapún, J. A. J. M. Vekemans, E. W. Meijer. Tuning the Stacking Properties of C_3-Symmetrical Molecules by Modifying a Dipeptide Motif. *Chem. Eur. J.* **2007**, *13*, 8111.

36 K. Matsuura, K. Murasato, N. Kimizuka. Artificial Peptide-Nanospheres Self-Assembled from Three-Way Junctions of ß-Sheet-Forming Peptides. *J. Am. Chem. Soc.* **2005**, *127*, 10148.

37 S. Lee, J.-S. Lee, C. H. Lee, Y.-S. Jung, J.-M. Kim. Nonpolymeric Thermosensitive Benzenetricarboxamides. *Langmuir* **2011**, *27*, 1560.

38 T. Shikata, D. Ogata, K. Hanabusa. Viscoelastic Behavior of Supramolecular Polymeric Systems Consisting of N,N',N"-Tris(3,7-dimethyloctyl)benzene-1,3,5-tricarboxamide and n-Alkanes. *J. Phys. Chem. B* **2004**, *108*, 508.

39 N. Shi, H. Dong, G. Yin, Z. Xu, S. Li. A Smart Supramolecular Hydrogel Exhibiting pH-Modulated Viscoelastic Properties. *Adv. Funct. Mater.* **2007**, *17*, 1837.

40 C. F. C. Fitié, I. Tomatsu, D. Byelov, W. H. de Jeu, R. P. Sijbesma. Nanostructured Materials through Orthogonal Self-Assembly in a Columnar Liquid Crystal. *Chem. Mater.* **2008**, *20*, 2394.

41 P. Besenius, J. L. M. Heynens, R. Straathof, M. M. L. Nieuwenhuizen, P. H. H. Bomans, E. Terreno, S. Aime, G. J. Strijkers, K. Nicolay, E. W. Meijer. Paramagnetic self-assembled nanoparticles as supramolecular MRI contrast agents. *Contrast Media Mol. Imaging* **2012**, *7*, 356.

42 J. Wang, Q. Dou, X. Chen, D. Li. Crystal structure and morphologies of polypropylene homopolymer and propylene-ethylene random copolymer: Effect of the substituted 1,3,5-benzenetrisamides. *J. Polym. Sci. B Polym. Phys.* **2008**, *46*, 1067.

43 F. Richter, H.-W. Schmidt. Supramolecular Nucleating Agents for Poly(butylene terephthalate) Based on 1,3,5-Benzenetrisamides. *Macromol. Mater. Eng.* **2013**, *298*, 190.

44 H. Nakajima, M. Takahashi, Y. Kimura. Induced Crystallization of PLLA in the Presence of 1,3,5-Benzenetricarboxylamide Derivatives as Nucleators: Preparation of Haze-Free Crystalline PLLA Materials. *Macromol. Mater. Eng.* **2010**, *295*, 460.

45 H. Bai, W. Zhang, H. Deng, Q. Zhang, Q. Fu. Control of Crystal Morphology in Poly(L-lactide) by Adding Nucleating Agent. *Macromolecules* **2011**, *44*, 1233.

46 P. Song, Z. Wei, J. Liang, G. Chen, W. Zhang. Crystallization behavior and nucleation analysis of poly(L-lactic acid) with a multiamide nucleating agent. *Polym. Eng. Sci.* **2012**, *52*, 1058.

47 F. Abraham, H.-W. Schmidt. 1,3,5-Benzenetrisamide based nucleating agents for poly(vinylidene fluoride). *Polymer* **2010**, *51*, 913.

48 M. Blomenhofer, S. Ganzleben, D. Hanft, H.-W. Schmidt, M. Kristiansen, P. Smith, K. Stoll, D. Maeder, K. Hoffmann. "Designer" Nucleating Agents for Polypropylene. *Macromolecules* **2005**, *38*, 3688.

49 P. M. Kristiansen, A. Gress, P. Smith, D. Hanft, H.-W. Schmidt. Phase behavior, nucleation and optical properties of the binary system isotactic polypropylene/N,N',N"-tris-isopentyl-1,3,5-benzene-tricarboxamide. *Polymer* **2006**, *47*, 249.

50 F. Abraham, S. Ganzleben, D. Hanft, P. Smith, H.-W. Schmidt. Synthesis and Structure-Efficiency Relations of 1,3,5-Benzenetrisamides as Nucleating Agents and Clarifiers for Isotactic Poly(propylene). *Macromol. Chem. Phys.* **2010**, *211*, 171.

51 J. Roosma, T. Mes, P. Leclère, A. R. A. Palmans, E. W. Meijer. Supramolecular Materials from Benzene-1,3,5-tricarboxamide-Based Nanorods. *J. Am. Chem. Soc.* **2008**, *130*, 1120.

52 T. Mes, R. van der Weegen, A. R. A. Palmans, E. W. Meijer. Single-Chain Polymeric Nanoparticles by Stepwise Folding. *Angew. Chem. Int. Ed.* **2011**, *50*, 5085.

53 T. Terashima, T. Mes, T. F. A. De Greef, M. A. J. Gillissen, P. Besenius, A. R. A. Palmans, E. W. Meijer. Single-Chain Folding of Polymers for Catalytic Systems in Water. *J. Am. Chem. Soc.* **2011**, *133*, 4742.

54 M. Kristiansen, P. Smith, H. Chanzy, C. Baerlocher, V. Gramlich, L. McCusker, T. Weber, P. Pattison, M. Blomenhofer, H.-W. Schmidt. Structural Aspects of 1,3,5-Benzenetrisamides-A New Family of Nucleating Agents. *Cryst. Growth Des.* **2009**, *9*, 2556.

55 T. Curtius. Hydrazide und Azide organischer Säuren. XXX. Abhandlung. Bildung von Hydrazihydraziden und Hydraziaziden dreibasischer Säuren. *J. Prakt. Chem.* **1915**, *91*, 39.

56 W. Ried, F.-J. Königstein. Über das 1,3,5-Triformyl-benzol (Benzol-trialdehyd-(1,3,5)). *Chem. Ber.* **1959**, *92*, 2532.

57 Bayer, 2417763, *DE*, **1975**.

58 J. E. Gill, R. MacGillivray, J. Munro. The preparation of symmetrical aromatic triamines and triisocyanates. *J. Chem. Soc.* **1949**, 1753.

59 H. Stetter, D. Theise, G. J. Steffens. Über Verbindungen mit Urotropin-Struktur, XLV Cyclisierungsreaktionen ausgehend von 1.3.5-Triamino-cyclohexan. *Chem. Ber.* **1970**, *103*, 200.

60 I. Arai, Y. Sei, I. Muramatsu. Preparation of 1,3,5-triaminobenzene by reduction of phloroglucinol trioxime. *J. Org. Chem.* **1981**, *46*, 4597.

61 J. J. van Gorp, J. A. J. M. Vekemans, E. W. Meijer. Supramolecular architectures of C_3*-symmetrical and asymmetrical discotics*. *Mol. Cryst. Liq. Cryst.* **2003**, 397, 491.

62 K. Hanabusa, C. Koto, M. Kimura, H. Shirai, A. Kakehi. Remarkable Viscoelasticity of Organic Solvents Containing Trialkyl-1,3,5-benzenetricarboxamides and Their Intermolecular Hydrogen Bonding. *Chem. Lett.* **1997**, *26*, 429.

63 M. P. Lightfoot, F. S. Mair, R. G. Pritchard, J. E. Warren. New supramolecular packing motifs: pi-stacked rods encased in triply-helical hydrogen bonded amide strands. *Chem. Commun.* **1999**, 1945.

64 B. Koenig, O. Moeller, P. Bubenitschek, P. G. Jones. Binding of Heptanedioic Acid to a Threefold Pyridine Arylamide Receptor. Enhancement of the Stability of Supramolecular Solution Structures by Multiple Binding Sites. *J. Org. Chem.* **1995**, *60*, 4291.

65 X. Hou, M. Schober, Q. Chu. A Chiral Nanosheet Connected by Amide Hydrogen Bonds. *Cryst. Growth Des.* **2012**, *12*, 5159.

66 D. L. Caulder, C. Brückner, R. E. Powers, S. König, T. N. Parac, J. A. Leary, K. N. Raymond. Design, Formation and Properties of Tetrahedral M_4L_4 and M_4L_6 Supramolecular Clusters. *J. Am. Chem. Soc.* **2001**, *123*, 8923.

67 F. Binsbergen. Heterogeneous nucleation in the crystallization of polyolefins: Part 1. Chemical and physical nature of nucleating agents. *Polymer* **1970**, *11*, 253.

68 C. Marco, M. A. Gómez, G. Ellis, J. M. Arribas. Highly efficient nucleating additive for isotactic polypropylene studied by differential scanning calorimetry. *J. Appl. Polym. Sci.* **2002**, *84*, 1669.

69 G.-p. Zhang, Z. Xin, J.-y. Yu, Q.-d. Gui, S.-y. Wang. Nucleating Efficiency of Organic Phosphates in Polypropylene. *J. Macromol. Sci., Part B: Phys.* **2003**, *42*, 467.

70 H. N. Beck, H. D. Ledbetter. DTA study of heterogeneous nucleation of crystallization in polypropylene. *J. Appl. Polym. Sci.* **1965**, *9*, 2131.

71 M. Fujiyama. Structure and Properties of Inflation Films of beta-Phase Nucleating Agent-Added Polypropylene. *Int. Polym. Process.* **1996**, *2*, 159.

72 J. Broda. Nucleating activity of the quinacridone and phthalocyanine pigments in polypropylene crystallization. *J. Appl. Polym. Sci.* **2003**, *90*, 3957.

73 J. Garbarczyk, T. Sterzynski, D. Paukszta. *Polym. Comm.* **1989**, *30*, 153.

74 D.-H. Lee, K.-B. Yoon. Effect of polycyclopentene on crystallization of isotactic polypropylene. *J. Appl. Polym. Sci.* **1994**, *54*, 1507.

75 T. L. Smith, D. Masilamani, L. K. Bui, R. Brambilla, Y. P. Khanna, K. A. Garbriel. Acetals as nucleating agents for polypropylene. *J. Appl. Polym. Sci.* **1994**, *52*, 591.

76 Y. C. Kim, C. Y. Kim, S. C. Kim. Crystallization characteristics of isotactic polypropylene with and without nucleating agents. *Polym. Eng. Sci.* **1991**, *31*, 1009.

77 C. Marco, G. Ellis, M. A. Gómez, J. M. Arribas. Comparative study of the nucleation activity of third-generation sorbitol-based nucleating agents for isotactic polypropylene. *J. Appl. Polym. Sci.* **2002**, *84*, 2440.

78 C. Marco, G. Ellis, M. A. Gómez, J. M. Arribas. Analysis of the isothermal crystallization of isotactic polypropylene nucleated with sorbitol derivatives. *J. Appl. Polym. Sci.* **2003**, *88*, 2261.

79 M. Kristiansen, M. Werner, T. Tervoort, P. Smith, M. Blomenhofer, H.-W. Schmidt. The Binary System Isotactic Polypropylene/Bis(3,4-dimethylbenzylidene)sorbitol: Phase Behavior, Nucleation, and Optical Properties. *Macromolecules* **2003**, *36*, 5150.

80 F. Binsbergen, B. de Lange. Heterogeneous nucleation in the crystallization of polyolefins: Part 2. Kinetics of crystallization of nucleated polypropylene. *Polymer* **1970**, *11*, 309.

81 F. Rybnikár. Orientation in composite of polypropylene and talc. *J. Appl. Polym. Sci.* **1989**, *38*, 1479.

82 A. Dobreva, M. Alonso, M. Gonzalez, J. A. De Saja. Activity of substrates in the catalyzed nucleation of poly(ethylene terephthalate) melts. *J. Appl. Polym. Sci.* **1997**, *63*, 349.

83 M. Xanthos, B. C. Baltzis, P. P. Hsu. Effects of carbonate salts on crystallization kinetics and properties of recycled poly(ethylene terephthalate). *J. Appl. Polym. Sci.* **1997**, *64*, 1423.

84 J. T. Muellerleile, J. J. Freeman, J. C. Middleton. Effect of calcium fluoride concentration on nylon 6,6 crystallization behavior and morphology. *J. Appl. Polym. Sci.* **1998**, *69*, 1675.

85 B. Li, L. Zhang, W. Shi. Heterogeneous Nucleation Effects of Neodymium Oxide on Polyamide-1010. *J. Polym. Eng.* **2011**, *17*, 171.

86 S. Schneider, X. Drujon, B. Lotz, J. Wittmann. Self-nucleation and enhanced nucleation of polyvinylidene fluoride (alpha-phase). *Polymer* **2001**, *42*, 8787.

87 T. Miyazaki, Y. Takeda, M. Akasaka, M. Sakai, A. Hoshiko. Preparation of Isothermally Crystallized gamma-Form Poly(vinylidene fluoride) Films by Adding a KBr Powder as a Nucleating Agent. *Macromolecules* **2008**, *41*, 2749.

88 http://www.ceresana.com/de/marktstudien/kunststoffe/polypropylen.

89 G. Natta, P. Pino, P. Corradini, F. Danusso, E. Mantica, G. Mazzanti, G. Moraglio. Crystalline high polymers of α-olefines. *J. Am. Chem. Soc.* **1955**, *77*, 1708.

90 http://www.nobelprize.org/nobel_prizes/chemistry/laureates/1963/.

91 K. Hoffmann, G. Huber, D. Mäder. Nucleating and clarifying agents for polyolefins. *Macromol. Symp.* **2001**, *176*, 83.

92 Y. P. Khanna. Rheological mechanism and overview of nucleated crystallization kinetics. *Macromolecules* **1993**, *26*, 3639.

93 Y. P. Khanna. A barometer of crystallization rates of polymeric materials. *Polym. Eng. Sci.* **1990**, *30*, 1615.

94 S. Fairgrieve, *Nucleating agents*, *16*, RAPRA Review Reports, Reports187, **2005**.

95 D. I. Bower, *An Introduction to Polymer Physics*, **2002**.

96 I. J. Jansen, *Plastics Additives Handbook*, Hanser: München, Wien, New York, Barcelona, **1993**.

97 J. F. J. Padden, H. D. Keith. Spherulitic Crystallization in Polypropylene. *J. Appl. Phys.* **1959**, *30*, 1479.

98 H. D. Keith, J. F. J. Padden, N. M. Walter, H. W. Wyckoff. Evidence for a Second Crystal Form of Polypropylene. *J. Appl. Phys.* **1959**, *30*, 1485.

99 G. Natta, P. Corradini. Structure and properties of isotactic polypropylene. *Nuovo Cimento* **1960**, *15*, 40.

100 A. T. Jones, J. M. Aizlewood, D. R. Beckett. Crystalline forms of isotactic polypropylene. *Makromol. Chem.* **1964**, *75*, 134.

101 D. Norton, A. Keller. The spherulitic and lamellar morphology of melt-crystallized isotactic polypropylene. *Polymer* **1985**, *26*, 704.

102 S. V. Meille, S. Bruckner, W. Porzio. γ-Isotactic polypropylene. A structure with nonparallel chain axes. *Macromolecules* **1990**, *23*, 4114.

103 J. Varga. Supermolecular structure of isotactic polypropylene. *J. Mater. Sci.* **1992**, *27*, 2557.

104 S. V. Meille, D. R. Ferro, S. Brueckner, A. J. Lovinger, F. J. Padden. Structure of β-Isotactic Polypropylene: A Long-Standing Structural Puzzle. *Macromolecules* **1994**, *27*, 2615.

105 M. Kristiansen, *Nucleation and Clarification of Semi-Crystalline Polymers*, ETH Zürich, **2004**.

106 K. S. Novoselov, D. Jiang, F. Schedin, T. J. Booth, V. V. Khotkevich, S. V. Morozov, A. K. Geim. Two-dimensional atomic crystals. *Proc. Natl. Acad. Sci. U. S. A.* **2005**, *102*, 10451.

107 J. C. Meyer, A. K. Geim, M. I. Katsnelson, K. S. Novoselov, T. J. Booth, S. Roth. The structure of suspended graphene sheets. *Nature* **2007**, *446*, 60.

108 A. K. Geim, K. S. Novoselov. The rise of graphene. *Nat. Mater.* **2007**, *6*, 183.

109 T. Sasaki, M. Watanabe, H. Hashizume, H. Yamada, H. Nakazawa. Macromolecule-like Aspects for a Colloidal Suspension of an Exfoliated Titanate. Pairwise Association of Nanosheets and Dynamic Reassembling Process Initiated from It. *J. Am. Chem. Soc.* **1996**, *118*, 8329.

110 T. Sasaki, M. Watanabe. Osmotic Swelling to Exfoliation. Exceptionally High Degrees of Hydration of a Layered Titanate. *J. Am. Chem. Soc.* **1998**, *120*, 4682.

111 M. M. J. Treacy, S. B. Rice, A. J. Jacobson, J. T. Lewandowski. Electron microscopy study of delamination in dispersions of the perovskite-related layered phases $K[Ca_2Na_{n-3}Nb_nO_{3n+1}]$: evidence for single-layer formation. *Chem. Mater.* **1990**, *2*, 279.

112 M. Fang, C. H. Kim, G. B. Saupe, H.-N. Kim, C. C. Waraksa, T. Miwa, A. Fujishima, T. E. Mallouk. Layer-by-Layer Growth and Condensation Reactions of Niobate and Titanoniobate Thin Films. *Chem. Mater.* **1999**, *11*, 1526.

113 R. E. Schaak, T. E. Mallouk. Self-assembly of Tiled Perovskite Monolayer and Multilayer Thin Films. *Chem. Mater.* **2000**, *12*, 2513.

114 R. E. Schaak, T. E. Mallouk. Perovskites by Design: A Toolbox of Solid-State Reactions. *Chem. Mater.* **2002**, *14*, 1455.

115 J.-Y. Kim, I. Chung, J.-H. Choy, G.-S. Park. Macromolecular Nanoplatelet of Aurivillius-type Layered Perovskite Oxide, $Bi_4Ti_3O_{12}$. *Chem. Mater.* **2001**, *13*, 2759.

116 H. S. S. R. Matte, A. Gomathi, A. K. Manna, D. J. Late, R. Datta, S. K. Pati, C. N. R. Rao. MoS_2 and WS_2 Analogues of Graphene. *Angew. Chem. Int. Ed.* **2010**, *49*, 4059.

117 J. N. Coleman, M. Lotya, A. O'Neill, S. D. Bergin, P. J. King, U. Khan, K. Young, A. Gaucher, S. De, R. J. Smith, I. V. Shvets, S. K. Arora, G. Stanton, H.-Y. Kim, K. Lee, G. T. Kim, G. S. Duesberg, T. Hallam, J. J. Boland, J. J. Wang, J. F. Donegan, J. C. Grunlan, G. Moriarty, A. Shmeliov, R. J. Nicholls, J. M. Perkins, E. M. Grieveson, K. Theuwissen, D. W. McComb, P. D. Nellist, V. Nicolosi. Two-Dimensional Nanosheets Produced by Liquid Exfoliation of Layered Materials. *Science* **2011**, *331*, 568.

118 A. Nag, K. Raidongia, K. P. S. S. Hembram, R. Datta, U. V. Waghmare, C. N. R. Rao. Graphene Analogues of BN: Novel Synthesis and Properties. *ACS Nano* **2010**, *4*, 1539.

119 D. Pacile, J. C. Meyer, C. O. Girit, A. Zettl. The two-dimensional phase of boron nitride: Few-atomic-layer sheets and suspended membranes. *Appl. Phys. Lett.* **2008**, *92*, 133107.

120 C. Zhi, Y. Bando, C. Tang, H. Kuwahara, D. Golberg. Large-Scale Fabrication of Boron Nitride Nanosheets and Their Utilization in Polymeric Composites with Improved Thermal and Mechanical Properties. *Adv. Mater.* **2009**, *21*, 2889.

121 J. Sakamoto, J. van Heijst, O. Lukin, A. D. Schlüter. Two-Dimensional Polymers: Just a Dream of Synthetic Chemists? *Angew. Chem. Int. Ed.* **2009**, *48*, 1030.

122 M. Osada, T. Sasaki. Two-Dimensional Dielectric Nanosheets: Novel Nanoelectronics From Nanocrystal Building Blocks. *Adv. Mater.* **2012**, *24*, 210.

123 R. Mas-Ballesté, C. Gomez-Navarro, J. Gomez-Herrero, F. Zamora. 2D materials: to graphene and beyond. *Nanoscale* **2011**, *3*, 20.

124 C. N. R. Rao, A. K. Sood, K. S. Subrahmanyam, A. Govindaraj. Graphene: The New Two-Dimensional Nanomaterial. *Angew. Chem. Int. Ed.* **2009**, *48*, 7752.

125 R. Davis, R. Berger, R. Zentel. Two-Dimensional Aggregation of Organogelators Induced by Biaxial Hydrogen-Bonding Gives Supramolecular Nanosheets. *Adv. Mater.* **2007**, *19*, 3878.

126 R. Meziane, M. Brehmer, U. Maschke, R. Zentel. Gelling and the collective dynamics in ferroelectric liquid crystals. *Soft Matter* **2008**, *4*, 1237.

127 J.-U. Kim, K.-H. Kim, N. Haberkorn, P. J. Roth, J.-C. Lee, P. Theato, R. Zentel. Two-dimensional self-assembly of disulfide functionalized bis-acylurea: a nanosheet template for gold nanoparticle arrays. *Chem. Commun.* **2010**, *46*, 5343.

128 J.-U. Kim, R. Zentel. Organic nanosheets with charged surface: two dimensional self-assembly of a non-symmetric bis-acylurea with pyridyl end group. *Soft Matter* **2011**, *7*, 2019.

129 Y. B. Li, Y. Bando, D. Golberg. MoS_2 nanoflowers and their field-emission properties. *Appl. Phys. Lett.* **2003**, *82*, 1962.

130 A. Lomander, W. Hwang, S. Zhang. Hierarchical Self-Assembly of a Coiled-Coil Peptide into Fractal Structure. *Nano Lett.* **2005**, *5*, 1255.

131 W. Wang, Y. Chau. Self-assembled peptide nanorods as building blocks of fractal patterns. *Soft Matter* **2009**, *5*, 4893.

132 T. Govindaraju, M. Pandeeswar, K. Jayaramulu, G. Jaipuria, H. S. Atreya. Spontaneous self-assembly of designed cyclic dipeptide (Phg-Phg) into two-dimensional nano- and mesosheets. *Supramol. Chem.* **2011**, *23*, 487.

133 K. T. Nam, S. A. Shelby, P. H. Choi, A. B. Marciel, R. Chen, L. Tan, T. K. Chu, R. A. Mesch, B.-C. Lee, M. D. Connolly, C. Kisielowski, R. N. Zuckermann. Free-floating ultrathin two-dimensional crystals from sequence-specific peptoid polymers. *Nat. Mater.* **2010**, *9*, 454.

134 M. B. Avinash, T. Govindaraju. Engineering Molecular Organization of Naphthalenediimides: Large Nanosheets with Metallic Conductivity and Attoliter Containers. *Adv. Funct. Mater.* **2011**, *21*, 3875.

135 Y. Lei, Q. Liao, H. Fu, J. Yao. Phase- and Shape-Controlled Synthesis of Single Crystalline Perylene Nanosheets and Its Optical Properties. *J. Phys. Chem. C* **2009**, *113*, 10038.

136 D. Wu, R. Liu, W. Pisula, X. Feng, K. Müllen. Two-Dimensional Nanostructures from Positively Charged Polycyclic Aromatic Hydrocarbons. *Angew. Chem. Int. Ed.* **2011**, *50*, 2791.

137 W. Eck, A. Küller, M. Grunze, B. Völkel, A. Gölzhäuser. Freestanding Nanosheets from Crosslinked Biphenyl Self-Assembled Monolayers. *Adv. Mater.* **2005**, *17*, 2583.

138 W. Zhang, J. Cui, C.-a. Tao, Y. Wu, Z. Li, L. Ma, Y. Wen, G. Li. A Strategy for Producing Pure Single-Layer Graphene Sheets Based on a Confined Self-Assembly Approach. *Angew. Chem. Int. Ed.* **2009**, *48*, 5864.

139 R. E. Dinnebier, *Kristallstrukturbestimmung molekularer Substanzen aus Röntgenbeugungsaufnahmen an Pulvern*, Berichte aus den Arbeitskreisen der DGK, Nr. 7, Deutsche Gesellschaft für Kristallographie, **2000**.

140 R. E. Dinnebier, *Structure Determination and Refinement from Powder Diffraction Data*, Berichte aus Arbeitskreisen der DGK, Nr. 9, Deutsche Gesellschaft für Kristallographie, **2000**.

141 J. Senker, L. Seyfarth, J. Voll. Determination of rotational symmetry elements in NMR crystallography. *Solid State Sci.* **2004**, *6*, 1039.

142 F. W. Karau, L. Seyfarth, O. Oeckler, J. Senker, K. Landskron, W. Schnick. The Stuffed Framework Structure of SrP_2N_4: Challenges to Synthesis and Crystal Structure Determination. *Chem. Eur. J.* **2007**, *13*, 6841.

143 F. Taulelle. NMR crystallography: crystallochemical formula and space group selection. *Solid State Sci.* **2004**, *6*, 1053.

144 J. Senker, J. Sehnert, S. Correll. Microscopic description of the polyamorphic phases of triphenyl phosphite by means of multidimensional solid-state NMR Spectroscopy. *J. Am. Chem. Soc.* **2005**, *127*, 337.

145 J. Sehnert, J. Senker. A concerted approach for the determination of molecular conformation in ordered and disordered materials. *Chem. Eur. J.* **2007**, *13*, 6339.

146 L. Seyfarth, J. Seyfarth, B. V. Lotsch, W. Schnick, J. Senker. Tackling the stacking disorder of melon-structure elucidation in a semicrystalline material. *Phys. Chem. Chem. Phys.* **2010**, *12*, 2227.

147 L. Seyfarth, J. Sehnert, N. El-Gamel, W. Milius, E. Kroke, J. Breu, J. Senker. Structure elucidation of cyameluric acid by combining solid-state NMR spectroscopy, molecular modeling and direct-space methods. *J. Mol. Struct.* **2008**, *889*, 217.

148 L. Seyfarth, J. Senker. An NMR crystallographic approach for the determination of the hydrogen substructure of nitrogen bonded protons. *Phys. Chem. Chem. Phys.* **2009**, *11*, 3522.

149 E. Wirnhier, M. Döblinger, D. Gunzelmann, J. Senker, B. V. Lotsch, W. Schnick. Poly(triazine imide) with Intercalation of Lithium and Chloride Ions $[(C_3N_3)_2(NH_xLi_{1-x})_3 \cdot LiCl]$: A Crystalline 2D Carbon Nitride Network. *Chem. Eur. J.* **2011**, *17*, 3213.

150 D. Hirsemann, T. K.-J. Köster, J. Wack, L. van Wüllen, J. Breu, J. Senker. Covalent Grafting to μ-Hydroxy-Capped Surfaces? A Kaolinite Case Study. *Chem. Mater.* **2011**, *23*, 3152.

151 J. Sehnert, K. Bärwinkel, J. Senker. Theoretical calculations of hypersurfaces of the ^{13}C chemical shift anisotropy in the C=O···H-N hydrogen bond and the benefit for the ab initio structure determination. *J. Mol. Struct.: THEOCHEM* **2007**, *824*, 58.

152 J. Sehnert, K. Baerwinkel, J. Senker. Ab Initio Calculation of Solid-State NMR Spectra for Different Triazine and Heptazine Based Structure Proposals of g-C_3N_4. *J. Phys. Chem. B* **2007**, *111*, 10671.

153 J. Schmidt, A. Hoffmann, H. W. Spiess, D. Sebastiani. Bulk Chemical Shifts in Hydrogen-Bonded Systems from First-Principles Calculations and Solid-State-NMR. *J. Phys. Chem. B* **2006**, *110*, 23204.

154 H. Hauptman, J. Karle. Solution of the phase problem for space group $P\bar{1}$. *Acta Cryst.* **1954**, *7*, 369.

155 J. Karle, H. Hauptman. The phases and magnitudes of the structure factors. *Acta Cryst.* **1950**, *3*, 181.

156 G. H. Stout, L. H. Jensen, *X-ray Structure Determination - A Practical Guide*, Macmillan Publishing Co., Inc., **1968**.

157 C. Giacovazzo, *Fundamentals of Crystallography*, Oxford University Press, **2002**.

158 A. L. Patterson. A Fourier Series Method for the Determination of the Components of Interatomic Distances in Crystals. *Phys. Rev.* **1934**, *46*, 372.

159 K. D. M. Harris, R. L. Johnston, B. M. Kariuki. The Genetic Algorithm: Foundations and Applications in Structure Solution from Powder Diffraction Data. *Acta Cryst. Sect. A* **1998**, *54*, 632.

160 R. E. Dinnebier, *Kristallstrukturbestimmung molekularer Substanzen aus Röntgenbeugungsaufnahmen an Pulvern*, **1992**, Berichte aus Arbeitskreisen der DGK Nr. 7.

161 P.-E. Werner, L. Eriksson, M. Westdahl. TREOR, a semi-exhaustive trial-and-error powder indexing program for all symmetries. *J. Appl. Crystallogr.* **1985**, *18*, 367.

162 J. W. Visser. A fully automatic program for finding the unit cell from powder data. *J. Appl. Crystallogr.* **1969**, *2*, 89.

163 A. Boultif, D. Louer. Indexing of powder diffraction patterns for low-symmetry lattices by the successive dichotomy method. *J. Appl. Crystallogr.* **1991**, *24*, 987.

164 G. S. Pawley. Unit-cell refinement from powder diffraction scans. *J. Appl. Crystallogr.* **1981**, *14*, 357.

165 A. L. Bail, H. Duroy, J. Fourquet. Ab-initio structure determination of $LiSbWO_6$ by X-ray powder diffraction. *Mat. Res. Bull.* **1988**, *23*, 447.

166 A. Altomare, M. C. Burla, G. Cascarano, C. Giacovazzo, A. Guagliardi, A. G. G. Moliterni, G. Polidori. EXTRA: a program for extracting structure-factor amplitudes from powder diffraction data. *J. Appl. Crystallogr.* **1995**, *28*, 842.

167 G. E. Engel, S. Wilke, O. König, K. D. M. Harris, F. J. J. Leusen. PowderSolve - a complete package for crystal structure solution from powder diffraction patterns. *J. Appl. Crystallogr.* **1999**, *32*, 1169.

168 H. Putz, J. C. Schön, M. Jansen. Combined method for ab initio structure solution from powder diffraction data. *J. Appl. Crystallogr.* **1999**, *32*, 864.

169 K. D. M. Harris, M. Tremayne, B. M. Kariuki. Contemporary advances in the use of powder X-ray diffraction for structure determination. *Angew. Chem. Int. Ed.* **2001**, *40*, 1626.

170 W. I. F. David, K. Shankland, *Structure Determination from Powder Diffraction Data*, L. McCusker, C. Baerlocher, IUCr Monographs on Crystallography, Oxford University Press, **2002**.

171 K. D. M. Harris. New opportunities for structure determination of molecular materials directly from powder diffraction data. *Cryst. Growth Des.* **2003**, *3*, 887.

172 K. D. M. Harris, E. Y. Cheung. How to determine structures when single crystals cannot be grown: opportunities for structure determination of molecular materials using powder diffraction data. *Chem. Soc. Rev.* **2004**, *33*, 526.

173 R. Cerny. Crystal structure of non-molecular compounds from powder diffraction. *Croat. Chem. Acta* **2006**, *79*, 319.

174 M. Tremayne. The impact of powder diffraction on the structural characterization of organic crystalline materials. *Phil. Trans. R. Soc. Lond. A* **2004**, *362*, 2691.

175 K. D. M. Harris, M. Tremayne, P. Lightfoot, P. G. Bruce. Crystal Structure Determination from Powder Diffraction Data by Monte Carlo Methods. *J. Am. Chem. Soc.* **1994**, *116*, 3543.

176 N. Metropolis, A. W. Rosenbluth, M. N. Rosenbluth, A. H. Teller, E. Teller. Equation of State Calculations by Fast Computing Machines. *J. Chem. Phys.* **1953**, *21*, 1087.

177 M. W. Deem, J. M. Newsam. Determination of 4-connected framework crystal structures by simulated annealing. *Nature* **1989**, *342*, 260.

178 M. W. Deem, J. M. Newsam. Framework crystal structure solution by simulated annealing: test application to known zeolite structures. *J. Am. Chem. Soc.* **1992**, *114*, 7189.

179 M. Falcioni, M. W. Deem. A biased Monte Carlo scheme for zeolite structure solution. *J. Chem. Phys.* **1999**, *110*, 1754.

180 *Accelrys software inc. MS Modeling v5.0.0.0 Copyright 2009*.

6 Ergebnisse

6.1 Strukturaufklärung eines effizienten Nukleierungs- und Klarmittels für i-PP

Marko Schmidt,[a] Johannes J. Wittmann,[a] Roman Kress,[b] Denis Schneider,[c] Stefan Steuernagel,[c] Hans-Werner Schmidt*[b] and Jürgen Senker*[a]

Crystal Structure of a Highly Efficient Clarifying Agent for Isotactic Polypropylene

Erschienen in: *Cryst. Growth & Des.* 2012, **12(5)**, 2543. Reprinted with permission, Copyright (2013) American Chemical Society.

[a] Lehrstuhl für Anorganische Chemie III, Universität Bayreuth, 95447 Bayreuth, Deutschland
[b] Lehrstuhl für Makromolekulare Chemie I, Universität Bayreuth, 95447 Bayreuth, Deutschland
[c] Bruker Biospin GmbH, Silberstreifen 4, 76287 Rheinstetten, Deutschland
*juergen.senker@uni-bayreuth.de
*hans-werner.schmidt@uni-bayreuth.de

Darstellung des Eigenanteils:

Bei dieser Publikation handelt es sich um ein lehrstuhlübergreifendes Gemeinschaftsprojekt zur Synthese und Charakterisierung der ^{13}C angereicherten BTA-Spezies. Ich koordinierte zusammen mit Prof. Dr. *Jürgen Senker* das Projekt, führte grundlegende Experimente zur Charakterisierung durch und löste die Kristallstruktur. Die Synthese und Vorcharakterisierung der ^{13}C-markierten Verbindung wurde von *Roman Kress* unter Aufsicht von Prof. Dr. *Hans-Werner Schmidt* durchgeführt, während die DQ-Aufbaukurven von *Johannes Wittmann* simuliert wurden. Die Hochfeld-NMR-Messungen bei Bruker wurden von Dr. *Stefan Steuernagel* genehmigt und von Dr. *Denis Schneider* betreut. Verfasst wurde die Publikation hauptsächlich von Prof. Dr. *Jürgen Senker*, Prof. Dr. *Hans-Werner Schmidt* und mir. Mein Eigenanteil beläuft sich auf ca. 75 %.

6.1.1 Crystal Structure of a Highly Efficient Clarifying Agent for Isotactic Polypropylene

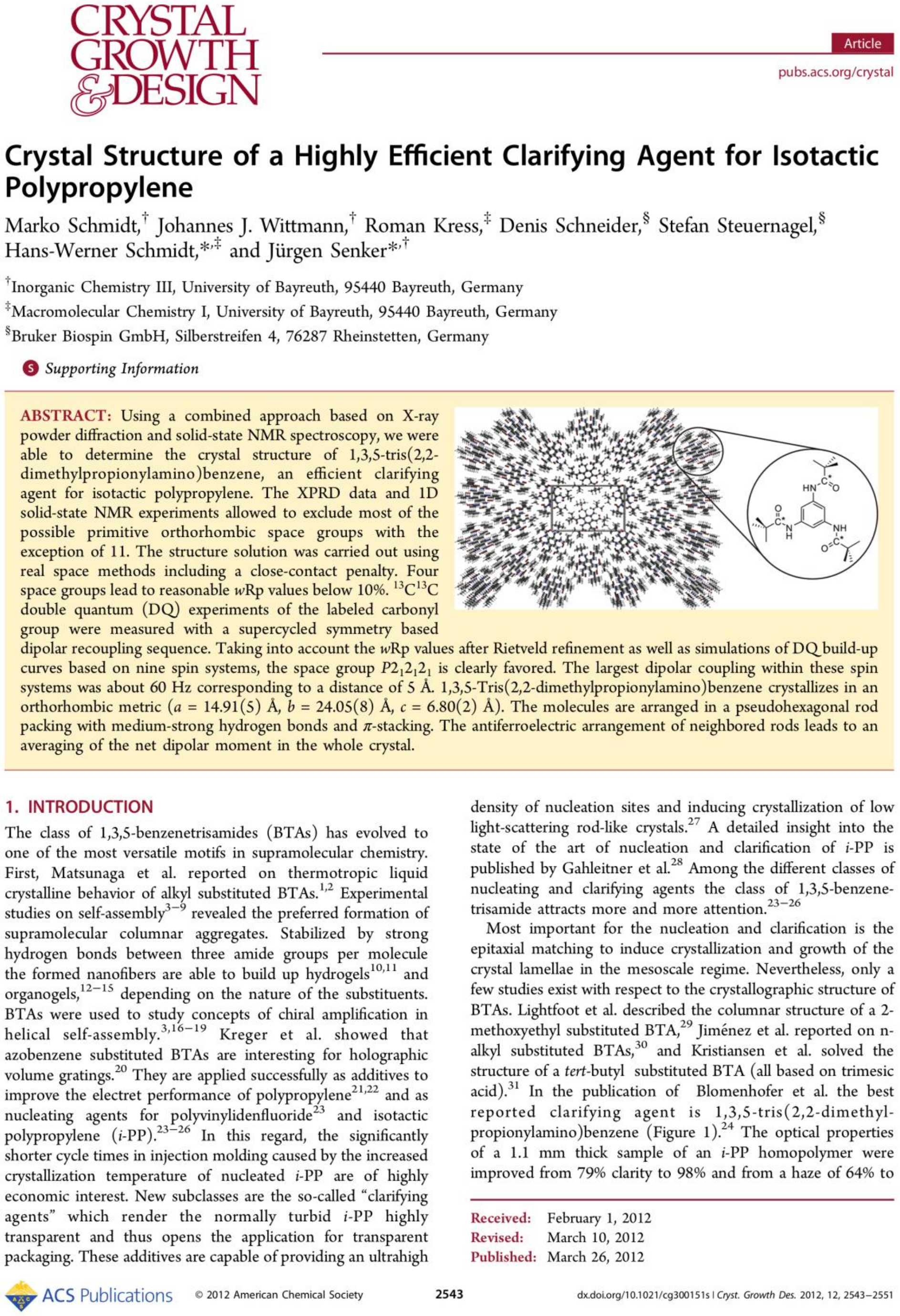

CRYSTAL GROWTH & DESIGN
Article
pubs.acs.org/crystal

Crystal Structure of a Highly Efficient Clarifying Agent for Isotactic Polypropylene

Marko Schmidt,† Johannes J. Wittmann,† Roman Kress,‡ Denis Schneider,§ Stefan Steuernagel,§ Hans-Werner Schmidt,*,‡ and Jürgen Senker*,†

†Inorganic Chemistry III, University of Bayreuth, 95440 Bayreuth, Germany
‡Macromolecular Chemistry I, University of Bayreuth, 95440 Bayreuth, Germany
§Bruker Biospin GmbH, Silberstreifen 4, 76287 Rheinstetten, Germany

Supporting Information

ABSTRACT: Using a combined approach based on X-ray powder diffraction and solid-state NMR spectroscopy, we were able to determine the crystal structure of 1,3,5-tris(2,2-dimethylpropionylamino)benzene, an efficient clarifying agent for isotactic polypropylene. The XPRD data and 1D solid-state NMR experiments allowed to exclude most of the possible primitive orthorhombic space groups with the exception of 11. The structure solution was carried out using real space methods including a close-contact penalty. Four space groups lead to reasonable *w*Rp values below 10%. $^{13}C^{13}C$ double quantum (DQ) experiments of the labeled carbonyl group were measured with a supercycled symmetry based dipolar recoupling sequence. Taking into account the *w*Rp values after Rietveld refinement as well as simulations of DQ build-up curves based on nine spin systems, the space group $P2_12_12_1$ is clearly favored. The largest dipolar coupling within these spin systems was about 60 Hz corresponding to a distance of 5 Å. 1,3,5-Tris(2,2-dimethylpropionylamino)benzene crystallizes in an orthorhombic metric ($a = 14.91(5)$ Å, $b = 24.05(8)$ Å, $c = 6.80(2)$ Å). The molecules are arranged in a pseudohexagonal rod packing with medium-strong hydrogen bonds and π-stacking. The antiferroelectric arrangement of neighbored rods leads to an averaging of the net dipolar moment in the whole crystal.

1. INTRODUCTION

The class of 1,3,5-benzenetrisamides (BTAs) has evolved to one of the most versatile motifs in supramolecular chemistry. First, Matsunaga et al. reported on thermotropic liquid crystalline behavior of alkyl substituted BTAs.[1,2] Experimental studies on self-assembly[3−9] revealed the preferred formation of supramolecular columnar aggregates. Stabilized by strong hydrogen bonds between three amide groups per molecule the formed nanofibers are able to build up hydrogels[10,11] and organogels,[12−15] depending on the nature of the substituents. BTAs were used to study concepts of chiral amplification in helical self-assembly.[3,16−19] Kreger et al. showed that azobenzene substituted BTAs are interesting for holographic volume gratings.[20] They are applied successfully as additives to improve the electret performance of polypropylene[21,22] and as nucleating agents for polyvinylidenfluoride[23] and isotactic polypropylene (*i*-PP).[23−26] In this regard, the significantly shorter cycle times in injection molding caused by the increased crystallization temperature of nucleated *i*-PP are of highly economic interest. New subclasses are the so-called "clarifying agents" which render the normally turbid *i*-PP highly transparent and thus opens the application for transparent packaging. These additives are capable of providing an ultrahigh density of nucleation sites and inducing crystallization of low light-scattering rod-like crystals.[27] A detailed insight into the state of the art of nucleation and clarification of *i*-PP is published by Gahleitner et al.[28] Among the different classes of nucleating and clarifying agents the class of 1,3,5-benzene-trisamide attracts more and more attention.[23−26]

Most important for the nucleation and clarification is the epitaxial matching to induce crystallization and growth of the crystal lamellae in the mesoscale regime. Nevertheless, only a few studies exist with respect to the crystallographic structure of BTAs. Lightfoot et al. described the columnar structure of a 2-methoxyethyl substituted BTA,[29] Jiménez et al. reported on n-alkyl substituted BTAs,[30] and Kristiansen et al. solved the structure of a *tert*-butyl substituted BTA (all based on trimesic acid).[31] In the publication of Blomenhofer et al. the best reported clarifying agent is 1,3,5-tris(2,2-dimethyl-propionylamino)benzene (Figure 1).[24] The optical properties of a 1.1 mm thick sample of an *i*-PP homopolymer were improved from 79% clarity to 98% and from a haze of 64% to

Received: February 1, 2012
Revised: March 10, 2012
Published: March 26, 2012

ACS Publications dx.doi.org/10.1021/cg300151s | *Cryst. Growth Des.* 2012, 12, 2543−2551

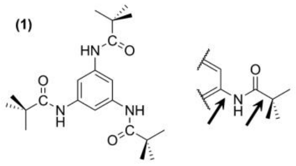

Figure 1. Left: Chemical structure of 1,3,5-tris(2,2-dimethylpropionylamino)benzene **1** (if ^{13}C labeled at all three carbonyl groups, the compound will then be shorten as **1***). Right: Section of compound **1** highlighting the main motional degrees of freedom; the black arrows assign the structure directing torsion angles $C_{Ar}C_{Ar}N_HC_O$ (left) and $C_{Me}C_qC_OO$ (right).

10%. In the present work we focus on elucidating the structure of 1,3,5-tris(2,2-dimethylpropionylamino)benzene **1** by means of NMR crystallographic strategies.

The main problem with solving the crystal structure of 1,3,5-tris(2,2-dimethylpropionylamino)benzene is its microcrystallinity. As a consequence, all attempts to prepare suitable single crystals failed which is often the case also for many other substance classes like pharmaceuticals, dyes and pigments, biochemical macromolecules, or inorganic network compounds.[32−34] Coping with powder data only complicates *ab initio* structure solutions.[35−38] NMR crystallographic strategies help to overcome this problem by complementing powder diffraction data with solid-state NMR experiments at various steps of the crystal structure determination.[39] Many of these experiments are based on the three main interactions in solid-state NMR, namely the chemical shift, the dipolar interaction, and the quadrupolar splitting.[40,41] The chemical shift and the quadrupolar splitting help to determine the correct space group, the asymmetric unit, the local symmetry of molecular units in the crystal structure, and dynamical disorder of individual building units.[39,42−51] Furthermore, using adequate pulse sequences, the dipolar coupling allows to extract distances[52−59] between homo- and heteronuclear nuclei or even torsion angles. Thus, it is possible to validate or falsify structure models, and the structure determination of ambivalent diffraction data becomes less difficult. However, it is hardly possible to get sufficient structural information based on nuclei with a low natural abundance. Therefore, isotope enrichment, for example ^{13}C or ^{15}N, is often inevitable. During the past years, these complementary methods have shown that NMR crystallography is a powerful tool to solve substructures and even complete crystal structures of molecular compounds and inorganic network compounds, respectively.[60−69]

2. EXPERIMENTAL SECTION

2.1. Synthesis and Characterization of 1*. All solvents were purified and dried using standard procedures. ^1H NMR spectra were recorded on a Bruker AC250 spectrometer at room temperature and referenced on TMS. Mass spectra were recorded on a VARIAN MAT 7 instrument with direct probe inlet and electron impact ionization. The labeled $Ba^{13}CO_3$ was purchased from Deutero GmbH and used without further purification. 3,5-Dinitroaniline was obtained from Aldrich and used as received.

The ^{13}C enriched 2,2-dimethylpropanoyl chloride (labeled at the carbonyl group) was synthesized from $Ba^{13}CO_3$.[70] A 15 mL portion of concentrated sulfuric acid was dropped slowly to 5 g of enriched barium carbonate (0.025 mol). The generated $^{13}CO_2$ was caught in a second flask that was cooled with a mixture of acetone, dry ice, and liquid nitrogen to a temperature of roughly −120 °C. To 0.99 g of $^{13}CO_2$ (0.0225 mol) was added 30 mL of dried and cold Et_2O dropwise, followed by 0.04 mol of *t*-butyl magnesium chloride (2.0 M in Et_2O; used in excess due to the age of the solution). The mixture was stirred for several hours at −80 °C (acetone/dry ice) and defrosted overnight. Et_2O was evaporated under reduced pressure, and a white solid precipitated. This solid (3.62 g, 0.0225 mol) was solved in 35 mL of dichloromethane (DCM) and 3.9 mL of oxalyl chloride (0.04 mol, equimolar to *t*-butyl magnesium chloride) to gain ^{13}C enriched 2,2-dimethylpropanoyl chloride and $MgCl_2$. The solids were solved in 80 mL of *N*-methyl-2-pyrrolidone (NMP), and potassium stearate was added dropwise (to react excess oxalyl chloride) until no further gas evolution was observed. The ^{13}C labeled product was used without further purification. All resonances in the ^1H NMR could be unequivocally assigned to the solvents used during the synthesis and the ^{13}C labeled acid chloride. Yield: 1.6 g (13 mmol, 51.8%). ^1H NMR (250 MHz, $CDCl_3$): $\delta = 1.14$ ppm (s, 9H, $-CH_3$).

1,3,5-Triaminobenzene was freshly synthesized by hydrogenation of the nitro compound: 3,5-dinitroaniline (8.0 g, 44 mmol) was stirred in a mixture of THF (400 mL), MeOH (50 mL), and palladium (0.6 g, 10% on activated carbon) in an autoclave at 35 °C for 12 h using a H_2 pressure of 3.5 bar. The palladium catalyst was filtered off under argon with Alox N, the solvents were evaporated under reduced pressure, and the product was subsequently dried under high vacuum. Yield: 5.3 g (43.1 mmol, 98%). ^1H NMR (250 MHz, [d^6]DMSO): $\delta = 4.30$ ppm (s, 6H, −NH); 5.13 ppm (s, 3H, Ar−H).

Compound **1*** was synthesized by dropping ^{13}C enriched acid chloride (0.46 g, 3.8 mmol) to a mixture of 1,3,5-triaminobenzene (0.15 g, 1.2 mmol), NMP (30 mL), pyridine (5 mL), and LiCl (0.05 g) at 0 °C under argon atmosphere. The reaction was stirred overnight at 60° C, and the reaction mixture was precipitated into an excess of ice water. The precipitate was filtered off, dried, and recrystallized from methanol. Yield: 0.174 g (0.46 mmol, 38%). ^1H NMR (250 MHz, [d^6]DMSO): $\delta = 1.21$ ppm (d, $^3J(^1H,^{13}C) = 3.5$ Hz, 27H, $-CH_3$); 7.62 ppm (s, 3H, Ar−H); 9.2 ppm (d, $^2J(^1H,^{13}C) = 3$ Hz, 3H, −NH). MS (70 eV), *m/z* (%): 378 (M+, 67); 321 (8); 293 (63); 236 (7); 208 (16); 123 (6); 57 (100).

2.2. Powder X-ray Diffraction. The powder pattern was recorded in transmission using a STOE StadiP with a germanium (111) monochromator (Cu $K\alpha_1$ radiation, 1.5406 Å). The sample was filled in a capillary tube with a diameter of 0.7 mm and measured in the 2θ range 5−40° at room temperature. The data were fully handled using the module Reflex Plus of the program package Accelerys MS Modeling[71] (version 5.0). The structure solution step was performed by real-space methods using the simulated annealing algorithm including a close-contact penalty. As starting model four molecules were placed into the unit cell which were geometry optimized before using DFT methods (see section 2.5). During the structure solution these molecules were allowed to rotate and translate freely as rigid bodies with two torsion angles in each side chain as additional degrees of freedom. The first Rietveld refinement step was performed including energy considerations using the COMPASS forcefield where each atom was allowed to relax freely. The additional energy weighting was set to 50%, and for the energy window the default value of 40 kcal/mol was used.

2.3. Solid-State NMR. ^1H and ^{13}C shifts are reported with respect to TMS, ^{15}N shifts were referenced on liquid NH_3. Compared to nitromethane all values are shifted by 380.5 ppm. ^1H spectra of compound **1** were recorded on a Bruker Avance III spectrometer operating at a proton frequency of 500 MHz. The sample was filled in a 1.3 mm ZrO_2 MAS rotor. The MAS frequency and the 90° pulse length were set to 65 kHz and 2.5 μs, respectively. The ^{15}N and ^{13}C spectra of the nonlabeled compound were recorded on a Bruker Avance II 300 spectrometer using triple resonance probes (7 mm and 4 mm) at a MAS frequency of 5 kHz and 12.5 kHz, respectively. Cross-polarization (CP) from proton to nitrogen and carbon was used to enhance the signal-to-noise ratio. The 90° pulse on the proton channel was set to 4.8 μs (3.0 μs), and the contact time was adjusted to 2 and 5 ms, respectively. ^{13}C 1D spectra and double quantum build-up curves of compound **1*** were recorded on a Bruker Avance III 700 in a 3.2 mm ZrO_2 rotor. For 1D spectra, cross-polarization

Scheme 1. Synthetic Route to ^{13}C Labeled 1,3,5-Tris(2,2-dimethylpropionylamino)benzene 1*[a]

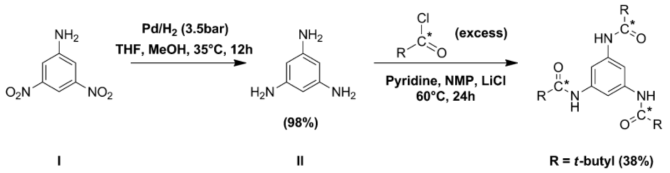

[a]Precursors are numbered with **I** and **II**. The asterisk marks the ^{13}C labeled carbonyl groups.

experiments at a MAS frequency of 12.5 kHz were performed. The ^{1}H 90° pulse length was adjusted to 3.0 μs by applying a contact pulse of 5 ms. The recycle delay was set to 5 s (not fully relaxed for the −NH and aromatic protons). For the double quantum build-up curves, the symmetry-based pulse sequence SR26$_4^{11}$ was used.[72] The performance of this sequence was checked by recording and evaluating DQ build-up curves for ^{13}C labeled glycine (γ-polymorph). Here, the intermolecular ^{13}C−^{13}C distances could be reproduced with high accuracy possessing rms values below 0.2 (compare to section 2.4).

The MAS frequency was set to 5.5 kHz corresponding to a nutation frequency of roughly 36 kHz. The R-block was implemented as a 90°−270° composite pulse. The filtering corresponding coherence pathway 0 ±2 0 −1 was performed with the conventional 16-fold phase cycle.[52] Additionally, a standardization experiment was collected with the coherence pathway 0 0 0 −1. The number of repetitions for each 1D experiment was set to 32. Cross-polarization from proton to ^{13}C with a ^{1}H 90° pulse length of 3.0 μs and a contact time of 5 ms was used. The read-out 90° pulse on ^{13}C was set to 3.0 μs. During excitation and reconversion CW decoupling with a nutation frequency of roughly 105 kHz was performed. For all experiments, a broadband SPINAL64 proton decoupling with a nutation frequency of about 85 kHz was used during data collection.

2.4. Solid-State NMR Simulations. Simulations for ^{13}C^{13}C build-up curves with the SR26 experiments were performed with the simulation package SIMPSON.[73] Magnitude and relative orientation of the carbon−carbon dipole tensors were extracted from the structure solutions after Rietveld refinement. The parameters for the ^{13}C chemical shift tensors were estimated from a static 1D spectrum and included in the spin system. We first performed the simulations within a seven spin system and completed in a nine spin system to reduce finite size effects. The Euler angles for the CSA were found to have only a minor contribution to the shape of the build-up curves. Due to strong proton decoupling in the experiments, the influence of further proton interactions could be neglected. The simulations were carried out using a crystal file of 144 orientations and seven γ angles.

For each simulated build-up curve of the four space groups the root-mean-square deviation (rms) was calculated with MATLAB[74] according to

$$\mathrm{rms} = \frac{\sum_i (\mathrm{sim}_i - \exp_i)^2}{\sum_i \exp_i^2} \qquad (1)$$

where sim$_i$ are the simulated and exp$_i$ the experimental data points. The choice of the correct space group was then made based on the minimal rms values.

2.5. Computational Methods. The geometry optimization of the molecule before the *ab initio* structure solution was performed by DFT methods with the module DMol3 from MS Modeling.[71] Within the DNP (double numerical plus polarization) basis set the GGA minimization was performed using the PW91 functional. The SCF (self-consistent field) density convergence was set to 1.0e^{-6} eV per atom.

3. RESULTS AND DISCUSSION

3.1. Synthesis and Characterization of ^{13}C Labeled 1,3,5-Tris(2,2-dimethylpropionylamino)benzene. The synthesis we here present is well established,[26] and the starting material, 3,5-dinitroaniline (**I**), is commercially available. The first step is the reduction of **I** in order to gain 1,3,5-triaminobenzene (**II**) in almost quantitative yields of 98%. The formation of **II** was characterized by ^{1}H solution-state NMR spectroscopy. The spectrum displayed two singlets at δ = 4.30 and 5.13 ppm. The signal at δ = 4.30 ppm can be assigned to the amino groups while the signal at δ = 5.13 ppm belongs to the aromatic protons. The upfield shift of the aromatic resonance is caused by a strong decreasing of the shielding of the protons due to the electronegativity of the three nitrogen atoms of the NH$_2$-groups. The expected intensity ratio of 2:1 clearly shows the complete formation as well as the purity of the product. For the formation of the target molecule (**1***) ^{13}C labeled 2,2-dimethylpropanoyl chloride was synthesized from commercialized Ba^{13}CO$_3$ as described by Parnes et al.[70] with a yield of 51.8%. The product was characterized by ^{1}H solution-state NMR where only one signal corresponding to the methyl group of the enriched acid chloride was observed reflecting the complete conversion to the labeled product. In a third step, the conversion of **II** with an excess of ^{13}C labeled 2,2-dimethylpropanoyl chloride gives the product with a yield of 38% after recrystallization from MeOH (Scheme 1). The ^{13}C labeled product **1*** was characterized by ^{1}H solution-state NMR, solid-state NMR, mass spectrometry, and powder X-ray diffraction.

The formation of compound **1*** leads to three signal groups in the ^{1}H solution-state NMR spectrum. The resonances at δ = 1.209 ppm and δ = 9.205 ppm show an additional doublet splitting while the signal at δ = 7.625 ppm occurs only as singlet which can be assigned as the aromatic resonance. The signal at δ = 1.209 ppm belongs to the CH$_3$-group, and the signal at δ = 9.205 ppm can be assigned to the NH-group. Both proton resonances show a splitting due to the coupling to the neighbored ^{13}C labeled carbonyl group over three bonds and two bonds, respectively. The corresponding coupling constants amount to 3.5 Hz for the methyl protons (^3J-coupling) and 3.0 Hz (^2J-coupling) for the amide protons. All three signal groups show an integral ratio of 1:1:8.99 which fits very well to the theoretical exception of a ratio of 1:1:9 resulting in a high purity of the product.

3.2. Symmetry Considerations from 1D Solid-State NMR Spectra. The ^{1}H, ^{15}N, and the ^{13}C solid-state NMR spectra of compound **1** are shown in Figure 2a−c. The proton spectrum displays three different signal groups at roughly δ = 2.0, 6.5, and 9.5 ppm clearly corresponding to the methyl protons, the aromatic protons, and the protons of the amide

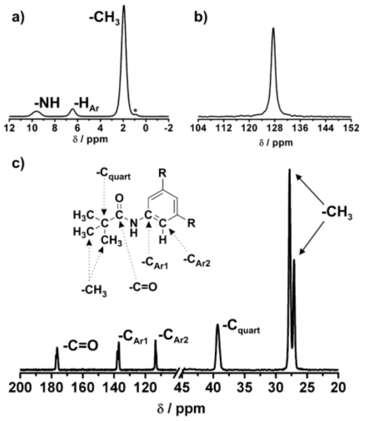

Figure 2. 1D MAS spectra of 1,3,5-tris(2,2-dimethylpropionylamino)-benzene: (a) ^{1}H spectrum (ν_{rot} = 65 kHz, B_0 = 11.7 T), with signal assignment for **1** given in Figure 1, the asterisk marks an impurity; (b) ^{15}N CP-MAS spectrum (ν_{rot} = 5 kHz); (c) ^{13}C CP-MAS spectrum (ν_{rot} = 12.5 kHz, with signal assignment on top).

groups. In comparison to the isotropic chemical shift in solution-state, the resonance of the amide protons is shifted downfield of about 0.3 ppm. The aromatic protons, on the other hand, show an upfield shift of roughly 1 ppm (Figure 2a). Both aspects indicate the existence of packing effects like hydrogen bonds and $\pi-\pi$ interactions due to aromatic ring currents.[9] Furthermore, the single sharp ^{1}H resonance of the NH-group suggests a quite narrow distribution of the hydrogen bond lengths. For similar systems, i.e., symmetric 1,3,5-benzenetrisamides ("N-centered"- based on 1,3,5-triaminobenzene and "C-centered" - based on trimesic acid), such effects have recently been reported and verified with solid-state NMR[9] and quantum chemical calculations[9] as well as temperature depending infrared spectroscopy.[75]

The upfield shift of the aromatic protons of 1.2 ppm is in the same range as the ^{1}H chemical shift presented in ref 9 for the aromatic protons which points to a parallel arrangement of benzene rings within a columnar packing. The $\pi-\pi$ stacking within these columns with intermolecular distances of roughly 3.5 Å leads to an additional shielding of the protons due to strong ring currents of neighboring molecules. In our ^{1}H spectrum, we find one resonance for the aromatic protons. Therefore, compound **1** seems to possess a coplanar arrangement of the benzene rings, ideally with a helical rod stacking which would maintain C_3 symmetry of the molecules including a high symmetry within the crystal structure. However, this is in contrast to the N-centered tricarboxamide recently investigated by Wegner and co-workers.[9] Indeed, they reported about significant upfield shifts for the aromatic proton signals due to the ring current effect like in our case, but in contrast, they observed three distinct signals for the aromatic resonances for N-BTA 3 (N-centered benzene-1,3,5-tricarboxamide with (*S*)-2,6-dimethylheptyl side chains). They explain their observance with a symmetry-breaking within the local packing motif. For their system it is possible that one carbonyl group of a molecule points in the opposite direction. This new stacking order can be described as quasihelical structure accompanying with a partial loss of the coplanarity leading to a splitting of the aromatic protons.

The ^{15}N CP spectrum (Figure 2b) displays one single resonance at δ = 127.5 ppm corresponding to the amide nitrogen atom. The appearance of only one signal, on one hand, indicates the entire conversion from 1,3,5-triaminobenzene to the product due to an absence of the resonance being typical for an amino group. On the other hand, the single resonance suggests that all amide groups depict similar torsion angles with respect to the aromatic core and the *t*-butyl groups. This in turn suggests that only one molecule or one-third is located in the asymmetric unit. Both aspects display useful hints with regard to the structure solution which will be discussed at a later point. Finally, the narrow signal in the ^{15}N CP spectrum is in very good agreement with the results from the proton signal of the amide group with respect to the hydrogen bonding situation.

Complementary results can be obtained from the ^{13}C CP spectrum of **1** (not labeled, Figure 2c) where five signal groups can be obtained. At roughly δ = 27 ppm the resonance for the methyl carbon atoms occurs. Interestingly, two different chemical shifts can be identified in an integral ratio of 2:1 suggesting a staggered conformation of the methyl groups concerning the adjacent OC−NH bond. The resonance at δ = 39 ppm belongs to the quaternary carbon atom of the *t*-butyl group, and the two aromatic carbon atoms are located at δ = 112 ppm and δ = 138 ppm, respectively, whereas the carbon atom of the carbonyl group has a chemical shift of δ = 177 ppm. The existence of only five resonances shows the high purity of 1,3,5-tris(2,2-dimethylpropionylamino)benzene without any residual educts as well as high order within the structure.

Moreover, the narrow line shape of the signals of the quaternary carbon atom and the upfield shifted aromatic carbon atom indicates a high symmetry in the packing of the molecules with uniformly distributed C−C distances between the benzene rings in the packing pattern. In the case of a tilted conformation of the benzene rings, more signals with a broader distribution of chemical shifts are expected. The ^{13}C CP signal of the carbonyl group for the enriched BTA measured at a high external magnetic field (B_0 = 16.4 T), where the ^{14}N interaction (I = 1) is eliminated due to its ω^{-2} dependence, depicts a marginally structured resonance due to the slightly different environment of the carbonyl atoms within one molecule. The signal was deconvoluted into three resonances (δ = 176.6, 177.0, and 177.2 ppm) possessing equal FWHM with an intensity ratio 1.02(2):1:00(2):1.01(2) (Figure 3). The FWHM of roughly 0.5 ppm pictures a typical value for an α-carbon signal of ^{13}C-enriched amino acids. This clearly shows that only one molecule is arranged within the asymmetric unit.

3.3. Crystal Structure of 1,3,5-Tris(2,2-dimethylpropionylamino)benzene. For developing a structure model, compound **1** was investigated by X-ray powder diffraction and solid-state NMR. Indexing of the powder pattern leads unequivocally to an orthorhombic metric which could subsequently be refined using the Pawley algorithm (a = 14.79(3) Å, b = 23.85(5) Å, c = 6.75(1) Å, V = 2381(13) Å^3, wRp = 2.6%). Assuming that carbon, nitrogen, and oxygen atoms possess a volume of roughly 18 Å^3, the molecular volume of compound **1** can be estimated to 490 Å^3. Including the hydrogen atoms would even increase this volume. This size restriction just allows at maximum four molecules within the unit cell. The reflection conditions, however, provide

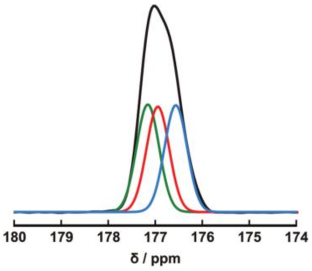

Figure 3. ^{13}C CP-MAS signal of the carbonyl group of ^{13}C enriched 1,3,5-tris(2,2-dimethylpropionylamino)benzene (ν_{rot} = 12.5 kHz; B_0 = 16.4 T) with deconvolution into three distinct ^{13}C resonances with an intensity ratio of 1.02(2):1.00(2):1.01(2). For all three resonances the same restriction for the FWHM was used.

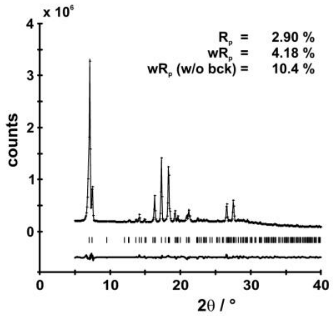

Figure 4. Rietveld profile plot of the X-ray powder diffraction pattern for the solution in space group $P2_12_12_1$ collected at room temperature in a 2θ range 5−40°.

reasonable results for 19 primitive and six body-centered space groups. On the basis of the nonplanarity of the molecule itself and the absence of an intrinsic C_2 symmetry, they cannot be placed on special positions in the unit cell. Therefore, only space groups possessing a multiplicity of 4 on general positions have to be taken into consideration for a further investigation. Nevertheless, 11 primitive space groups remain for a possible structure elucidation.

For all these space groups an *ab initio* structure solution with real-space methods was performed using a combination of a close-contact penalty and *w*Rp as cost functions. The DFT geometry optimized molecule was taken as rigid body with the rotational and translational degrees of freedom during the solution step. Additionally, the six most important and structure directing torsion angles (two in each side chain, see Figure 1, right) were refined during the optimization process. At the end, only four space groups remain possessing a comparable low *w*Rp value well below 10% (see Table 1), whereas all other structure solutions possess *w*Rp values far above 10%. An initial Rietveld refinement of these space groups leads to similar *w*Rp values which are listed in Table 1. Exemplarily, the Rietveld plot for space group $P2_12_12_1$ is depicted in Figure 4.

Table 1. *w*Rp Values of the Four Most Probable Space Groups after the Powder Solution Step and Rietveld Refinement

space group	solution *w*Rp/%	refinement *w*Rp/%
$P2_12_12_1$	5.73	4.18
$Pna2_1$	5.96	4.57
$P2an$	7.49	5.19
$P2_1cn$	7.16	4.37

Selecting the correct structure model just from the observed structures from the powder data is difficult since the *w*Rp values are almost equal. All four structures show a similar behavior concerning their topology where the molecules build a pseudohexagonal rod packing along the *c*-axis. The major difference is the arrangement of the molecules within the packing pattern that can be distinguished in hydrogen-bonding ($P2_12_12_1$ and $Pna2_1$) and non-hydrogen-bonding ($P2an$ and $P2_1cn$) patterns (see Figure 5).

To further distinguish the structure models the intermolecular distances between the ^{13}C labeled carbon atoms of the carbonyl groups were taken into consideration (see Table 2). While the intramolecular distances for all four space groups essentially show the same values, the intermolecular ones can

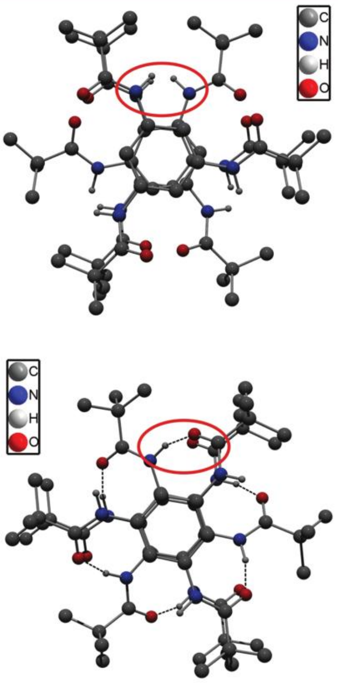

Figure 5. Top view on one rod of the different packing patterns where the NH-protons are emphasized. Top: pattern for the space groups $P2an$ and $P2_1cn$ without hydrogen bonding. Bottom: pattern for the space groups $P2_12_12_1$ and $Pna2_1$ with a hydrogen bonding network. All other protons are omitted for clarity.

Table 2. Intramolecular and Intermolecular $^{13}C-^{13}C$ Distances between Labeled Carbonyl Groups from a Nine Spin System Used as Input for the Simulations

distance/Å	$P2_12_12_1$	$Pna2_1$	$P2_1cn$	$P2an$
intramolecular	6.622−6.628	6.586−6.601	6.634−6.715	6.633−6.654
intermolecular	4.927−5.259	4.983−5.229	4.616−5.740	4.189−6.105

clearly be distinguished. For the space groups possessing a hydrogen bond network the minimum and maximum distances are almost equal (~ 4.9 and ~5.2 Å), and moreover, the length distribution is quite narrow. On the other hand, both space groups without H-bonds show a significantly different behavior. The minimum distances amount to 4.19 and 4.62 Å, respectively, while the maximum distance is drastically extended up to 6.1 Å. Thus, the length distribution is much broader than in the first case.

To support the structure selection we therefore performed quantitative solid-state NMR experiments. For this purpose we carried out $^{13}C^{13}C$ DQ experiments taking advantage of the dipolar coupling between the carbonyl atoms using the $SR26_4^{11}$ pulse sequence (see section 2.3). The constant thereby is proportional to r^{-3} where r represents the $^{13}C-^{13}C$ distance. The normalized experimental build-up curve of the carbonyl resonance is depicted in Figure 6b.

It shows a very slow increase with a quite broad maximum at about $\tau = 17$ ms, and the double quantum efficiency reaches roughly 50%. For simulating the experimental build-up curve we cut out a characteristic element of one rod of each crystal structure after the Rietveld refinements. Hence, the generated spin system had to be sufficiently large to avoid finite size effects and small enough to be handled with reasonable computation time. A nine spin system (Figure 6c) turned out to be the best choice. Here, each triangle represents one molecule within one rod of the structure, while the black circles illustrate the labeled carbonyl groups. The nine spin system used for our simulations is hence spanned by the three carbonyl spins of each molecule.

In Figure 6a, the root-mean-square errors (rms) between experiment and simulation (see section 2.4) are given for the four remaining space groups. It can be distinguished between space groups containing hydrogen bonds and without hydrogen bonds. While the latter possess rms values of 1.1 and 2.9, respectively, the former shows significantly lower values of 0.25 and 0.35. The simulated build-up curves for $P2an$ and $P2_1cn$ therefore badly reproduce the experiment. Due to the shorter intermolecular distances (see Table 2) the slope of the simulated curves is stronger leading to a maximum excitation time of roughly $\tau = 14$ ms. In fact, the simulated curves for $P2_12_12_1$ and $Pna2_1$ match the experimental build-up curve very well on the basis of the longer $^{13}C-^{13}C$ distances and the narrower distribution of the distances between the ^{13}C atoms in the spin system. However, the best fit could be achieved for space group $P2_12_12_1$ (see rms values, Figure 6a). On the basis of the higher *w*Rp and rms values as well as the fact that peculiar gliding planes (like in $Pna2_1$) are uncommon for molecular compounds which prefer crystallizing in rather simple lattices and point groups, the structure model in space group $Pna2_1$ can definitely be excluded.

1,3,5-Tris(2,2-dimethylpropionylamino)benzene therefore crystallizes in the orthorhombic noncentrosymmetric space group $P2_12_12_1$ ($a = 14.91(5)$ Å, $b = 24.05(8)$ Å, $c = 6.80(2)$ Å) containing four molecules in the unit cell, all on general positions. The *w*Rp of 4.18% is a very good value for an *ab initio* structure solution picturing the high order of the sample despite the presence of only light atoms leading to weak scattering.

The molecular structure after the Rietveld refinement can be seen in Figure 7. The $C_{Ar}C_{Ar}N_HC_O$ torsion angles seem to play a major role for the formation of the structure. Two side arms exhibit almost identical values for this torsion angle (31.36° and 31.46°, respectively), while the third one is a little bit higher (34.56°). This fact in addition to the deconvoluted $^{13}C{=}O$ signal of **1*** (Figure 3) slightly breaks the perfect regularity; however, a pseudo-C_3 symmetry remains as assumed from ^1H and ^{15}N solid-state NMR experiments. The HNCO torsion angles picturing the amide bonds are 178.78°, 178.93°, and 179.66°. This is in very good agreement with the expected value of 180° due to the behavior as partial double bonds. The oxygen atoms of the three carbonyl groups in one molecule point in the same direction out of the plane of the central aromatic ring system which is a precondition to form hydrogen bond patterns within the structure (Figure 8).

In 2009, Jiménez et al. reported the structure of a "C-centered" BTA (connected with the carbonyl carbon atom to the benzene ring) carrying a propyl moiety in each side arm instead of a *t*-butyl group.[30] The molecules within the crystal packing build up a supramolecular 3D H-bond network within a primitive cubic metric. However, in contrast to **1**, π-stackings are avoided with the linear side arms. Also in 2009, Kristiansen

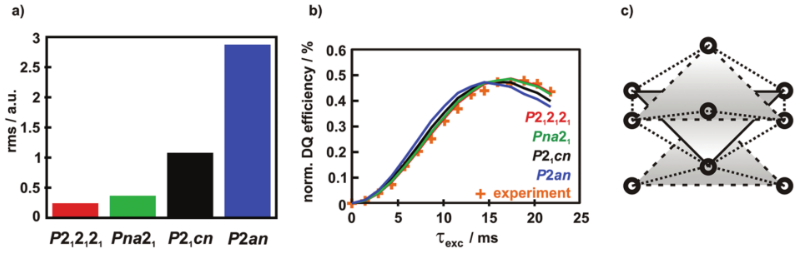

Figure 6. (a) Histogram with root-mean-square deviation between experimental and simulated symmetric build-up curve of all four space groups. (b) Experimental (orange plus) and simulated (solid lines) symmetric $^{13}C^{13}C$ SR26 build-up curves of **1*** after Rietveld refinement. (c) Scheme of a nine spin system for all simulations where each triangle represents one molecule within the packing of the structures. The ^{13}C spins (three in each molecule) are marked as circles; intermolecular distances are highlighted with dotted lines.

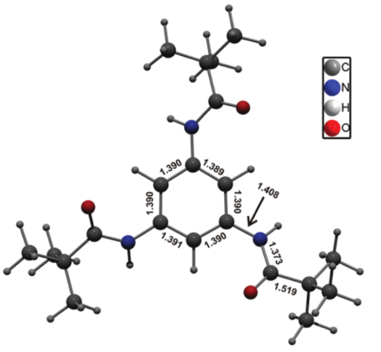

Figure 7. Molecular structure of 1,3,5-tris(2,2-dimethylpropionylamino)benzene with distances in angstroms as derived from the X-ray powder diffraction experiment.

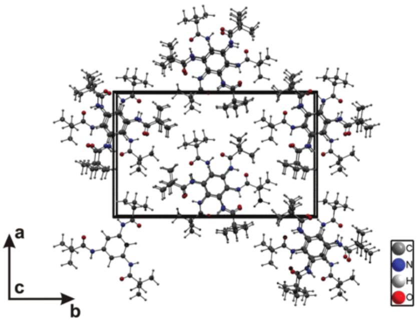

Figure 8. Section of the crystal structure of 1,3,5-tris(2,2-dimethylpropionylamino)benzene with view along the *c*-axis. The unit cell contains four molecules on general positions.

et al. reported about the crystal structure of a similar 1,3,5-benzenetrisamide (compared to compound **1**) on the basis of transmission electron microscopy and electron and X-ray diffraction studies,[31] carrying the same moieties in the side arms (*t*-butyl), but, in contrast, with a "C-centering" of the amide group. Here the molecules are reported to possess a complete C_3 symmetry, and moreover, all three oxygen atoms of the carbonyl groups show in one direction with $C_{Ar}C_{Ar}N_HC_O$ torsion angles of 53.21° each of which is roughly 20° higher than for our benzene based trisamide.

The crystal structure of **1** can be described as hexagonal rod-packing where the molecules build long rods parallel to the *c*-axis (see Figure 8). Due to the 2_1 screw axis and the additional pseudo-C_3 symmetry, the molecules are twisted around 60° within one rod leading to a helical arrangement which has also been reported for similar benzene based supramolecular systems.[31] An extensive hydrogen bond network is built between the amide protons and the oxygen atoms of the neighboring molecules in one rod. The NH···O distances with 2.04−2.14 Å, picturing medium strong H-bonds, are narrowly distributed which is in very good agreement with the results from ^{1}H and ^{15}N solid-state NMR. The corresponding N−O distances account for 2.97−3.06 Å. In addition to the H-bond network the helical structure is characterized by sandwich stacked π-systems within one rod. The aromatic rings and therefore the molecules are stacked in a coplanar arrangement where the aromatic rings are tilted less than 1°. Typical distances of the benzene carbon atoms of two molecules are between 3.37 and 3.42 Å which is similar to the distances in π-stacked discotic liquid crystals.[76]

In comparison, the structure presented in ref 31 crystallizes in a hexagonal unit cell where two molecules are sited on special positions. The structure is also characterized by an extensive hydrogen bonding network within the rod packing as well as a helical arrangement. The N−O distance with 2.65 Å is roughly 0.3 Å shorter than for compound **1** indicating stronger hydrogen bonds. This is also supported by the increased jut of the oxygen atoms from the aromatic ring system in comparison to compound **1**. Due to the 6_3 screw axis the molecules are also twisted around 60°. The sandwich-like $\pi-\pi$ contacts picture the second structure directing interaction whereupon the distances between two benzene rings amount to 3.45 and 3.47 Å, respectively, which is in the same range as that observed for compound **1**. Surprisingly, the synchrotron X-ray pattern of this "C-centered" trisamide reveals an immense diffuse scattering. This pictures a structural disorder where the two rods within the unit cell can be slid against each other. For the "N-centered" trisamide, on the other hand, no diffuse scattering was observed during investigation indicating a high order within the crystal structure.

The molecules of compound **1** and the ones from ref 31 remain nearly C_3 symmetric where all carbonyl groups point in one direction. Due to this out-plane arrangement of the oxygen atoms the molecules itself possess a quite large dipolar moment leading to the formation of macrodipoles for individual rods of the packing. One common mechanism of choice to reduce this moment within the unit cell and with it the potential energy is to form an antiferroelectric arrangement.[77] For compound **1**, indeed, the molecules in neighbored columns show in the opposite direction (Figure 9) canceling out the net dipolar moment. Due to avoid frustration while canceling the dipole moment, compound **1** undergoes an orthorhombic distortion ("pseudohexagonal") in contrast to the BTA reported by Kristiansen et al. where all rods are aligned parallel. Consequently, the net dipolar moment increases drastically leading to a complete ferroelectric arrangement. Interestingly,

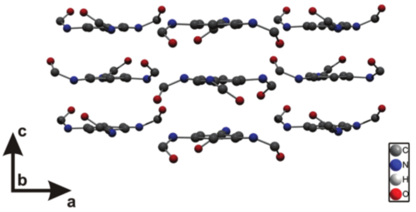

Figure 9. Part of the crystal structure of **1** with view along the *b*-axis. The oxygen atoms of the carbonyl groups point in the opposite direction leading to an averaging of the net dipolar moment. All protons and the carbon atoms of the *t*-butyl groups were omitted for clarity.

the structure of compound **1** in $P2_12_12_1$ could easily be transferred into the one of $Pna2_1$ by twisting the $C_{Ar}C_{Ar}N_HC_O$ torsion angle (see Figure 1) in each side chain of every second rod by roughly 60° leading also to a ferroelectric arrangement analogous to that of ref 31.

4. CONCLUSIONS

We have presented an approach for the determination of the crystal structure of 1,3,5-tris(2,2-dimethylpropionylamino)-benzene, an efficient clarifying agent for isotactic polypropylene. The structure was solved in the orthorhombic space group $P2_12_12_1$ using X-ray powder diffraction in combination with multinuclear solid-state NMR experiments and computer simulations. During structure elucidation, only four space groups led to reasonable structure models. DQ experiments allowed excluding the three remaining space groups. Using the symmetry-based $SR26^{11}_4$ pulse sequence, $^{13}C-^{13}C$ distances of nearly 5 Å could be reproduced with high precision. The simulation of the build-up curves fitted best for the space group $P2_12_12_1$ with a root-mean-square deviation of 0.25. The *c*-axis with a length 6.80(2) Å is in this connection in the similar range with the *c*-axis of the crystalline part of *i*-PP (~6.50 Å) which possesses a helical structure as well.[81] The additive crystallites within the polymer melt therefore might serve as a surface which allows the polymer to grow epitactically. This remarkable fact may cause *i*-PP to appear highly transparent. Therefore, further investigations in the additive/polymer composite systems are mandatory and will be discussed in a forthcoming publication.

The structure itself can be described as a hexagonal rod packing where the pseudo-C_3 symmetric molecules are twisted by 60° due to the 2_1 screw axis. The rods are stabilized via moderate hydrogen bonds with NH···O distances of roughly 2.0 Å and, moreover, via π-interactions due to a sandwich stacking of the aromatic cores with distances of about 3.4 Å. Each molecule possesses an intrinsic dipolar moment due to the fact that all oxygen atoms point in one direction. Therefore, the dipolar moment in one rod strongly increases. This H-bond mediated growth within one rod is in principle possible since the increasing potential energy is counterbalanced by the energy advantage based on the formation of hydrogen bonds. Moreover, the occurrence of such macrodipoles is not completely unknown within the BTA systems. Such phenomena have recently been demonstrated by Kulkarni et al.[80] on the basis of quantum chemical calculations. In addition, experimental proof was given by Sakamoto et al. where benzene-1,3,5-tricarboxamides with long side chains formed one-dimensional macrodipoles in solution of *n*-decane leading to highly viscous liquids.[78] In thin films it was even possible to generate macrodipoles in a three-dimensional ordered system.[79] However, a ferroelectric arrangement could not be achieved *per se* rather than by applying an external electrical field. Obtaining ferroelectricity by crystallization from solution seems to be improbable. Once a macrodipole in one rod is built, the second one must be arranged antiparallel since parallel formation strongly increases the potential energy of the system that cannot be compensated by the 1D H-bond network. In this case only small nanocrystals would be observed. Therefore, an antiferroelectric arrangement with antiparallel aligned rods as observed for compound **1** leading to a net dipolar moment of zero represents the driving force for the fast needlelike crystal growth of this class of materials.

■ ASSOCIATED CONTENT

Ⓢ Supporting Information

Spin system extracted from the structure solution as input file for SIMPSON used for the simulation of the DQ build-up curve as well as a CIF file of **1** including the crystallographic data. This material is available free of charge via the Internet at http://pubs.acs.org.

■ AUTHOR INFORMATION

Corresponding Author

*Fax: (+49) 921-55-3206 (H.-W.-S.); (+49) 921-55-2788 (J.S.). E-mail: hans-werner.schmidt@uni-bayreuth.de (H.-W.S.); juergen.senker@uni-bayreuth.de (J.S.).

Notes

The authors declare no competing financial interest.

■ ACKNOWLEDGMENTS

The authors want to thank the DFG (SFB 840, Project B4) for financial support of this work, Sandra Ganzleben for her careful assistance with the synthesis of the carbon-enriched compound, and Dr. Wolfgang Milius for the fruitful discussions with respect to crystallographic issues.

■ REFERENCES

(1) Matsunaga, Y.; Nakayasu, Y.; Sakai, S.; Yonenaga, M. *Mol. Cryst. Liq. Cryst.* **1986**, *141*, 327.

(2) Matsunaga, Y.; Miyajima, N.; Nakayasu, Y.; Sakai, S.; Yonenaga, M. *Bull. Chem. Soc. Jpn.* **1988**, *61*, 207.

(3) Brunsveld, L.; Schenning, A. P. H. J.; Broeren, M. A. C.; Janssen, H. M.; Vekemans, J. A. J. M.; Meijer, E. W. *Chem. Lett.* **2000**, 292.

(4) Xue, C.; Ilhan, F.; Cheng, S. Z.; Meador, M. A.; Eby, R. *Polym. Prepr.* **2004**, *45*, 820.

(5) Stals, P. J. M.; Smulders, M. M. J.; Martin-Rapun, R.; Palmans, A. R. A.; Meijer, E. W. *Chem. Eur. J.* **2009**, *15*, 2071.

(6) Stals, P. J. M.; Everts, J. C.; de Bruijn, R.; Filot, I. A. W.; Smulders, M. M. J.; Martin-Rapun, R.; Pidko, E. A.; de Greef, T. F. A.; Palmans, A. R. A.; Meijer, E. W. *Chem. Eur. J.* **2010**, *16*, 810.

(7) Kluge, D.; Abraham, F.; Schmidt, S.; Schmidt, H.-W.; Fery, A. *Langmuir* **2010**, *26*, 3020.

(8) Besenius, P.; van den Hout, K. P.; Albers, H. M. H. G.; de Greef, T. F. A.; Olijve, L. L. C.; Hermans, T. M.; de Waal, B. F. M.; Bomans, P. H. H.; Sommerdijk, N. A. J. M.; Portale, G.; Palmans, A. R. A.; van Genderen, M. H. P.; Vekemans, J. A. J. M.; Meijer, E. W. *Chem. Eur. J.* **2011**, *17*, 5193.

(9) Wegner, M.; Dudenko, D.; Sebastiani, D.; Palmans, A. R. A.; de Greef, T. F. A.; Graf, R.; Spiess, H. W. *Chem. Sci.* **2011**, *2*, 2040.

(10) Shi, N.; Dong, H.; Yin, G.; Xu, Z.; Li, S. *Adv. Funct. Mater.* **2007**, *17*, 1837.

(11) Bernet, A.; Albuquerque, R. Q.; Behr, M.; Hoffmann, S. T.; Schmidt, H.-W. *Soft Matter* **2012**, *8*, 66.

(12) Yasuda, Y.; Iishi, E.; Inada, H.; Shirota, Y. *Chem. Lett.* **1996**, *25*, 575.

(13) Hanabusa, K.; Koto, C.; Kimura, M.; Shirai, H.; Kakehi, A. *Chem. Lett.* **1997**, *26*, 429.

(14) van Gorp, J. J.; Vekemans, J. A. J. M.; Meijer, E. W. *J. Am. Chem. Soc.* **2002**, *124*, 14759.

(15) de Loos, M.; van Esch, J. H.; Kellogg, R. M.; Feringa, B. L. *Tetrahedron* **2007**, *63*, 7285.

(16) Ogata, D.; Shikata, T.; Hanabusa, K. *J. Phys. Chem. B* **2004**, *108*, 15503.

(17) Smulders, M. M. J.; Schenning, A. P. H. J.; Meijer, E. W. *J. Am. Chem. Soc.* **2008**, *130*, 606.

(18) Smulders, M. M. J.; Stals, P. J. M.; Mes, T.; Paffen, T. F. E.; Schenning, A. P. H. J.; Palmans, A. R. A.; Meijer, E. W. *J. Am. Chem. Soc.* **2010**, *132*, 620.

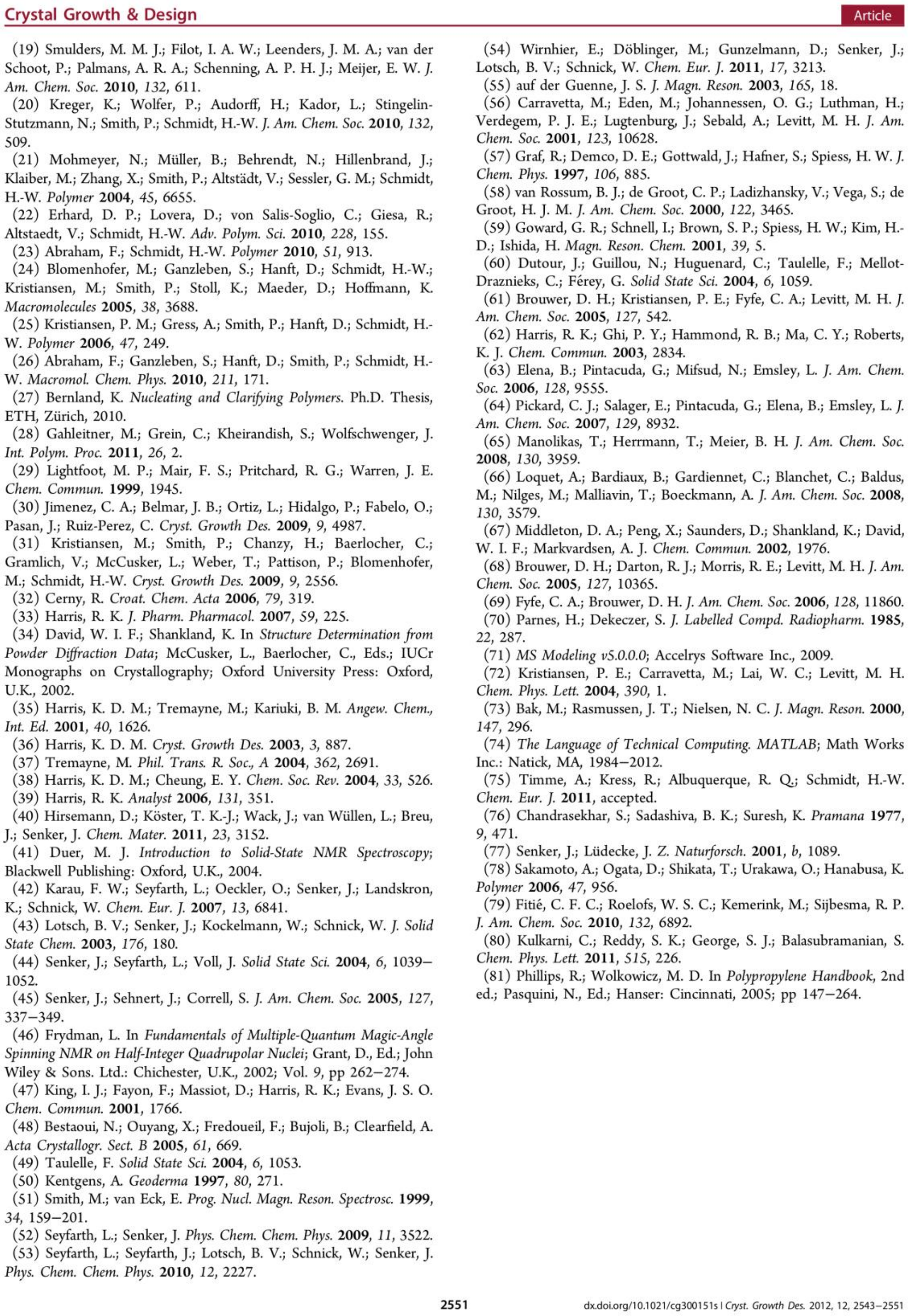

(19) Smulders, M. M. J.; Filot, I. A. W.; Leenders, J. M. A.; van der Schoot, P.; Palmans, A. R. A.; Schenning, A. P. H. J.; Meijer, E. W. *J. Am. Chem. Soc.* **2010**, *132*, 611.

(20) Kreger, K.; Wolfer, P.; Audorff, H.; Kador, L.; Stingelin-Stutzmann, N.; Smith, P.; Schmidt, H.-W. *J. Am. Chem. Soc.* **2010**, *132*, 509.

(21) Mohmeyer, N.; Müller, B.; Behrendt, N.; Hillenbrand, J.; Klaiber, M.; Zhang, X.; Smith, P.; Altstädt, V.; Sessler, G. M.; Schmidt, H.-W. *Polymer* **2004**, *45*, 6655.

(22) Erhard, D. P.; Lovera, D.; von Salis-Soglio, C.; Giesa, R.; Altstaedt, V.; Schmidt, H.-W. *Adv. Polym. Sci.* **2010**, *228*, 155.

(23) Abraham, F.; Schmidt, H.-W. *Polymer* **2010**, *51*, 913.

(24) Blomenhofer, M.; Ganzleben, S.; Hanft, D.; Schmidt, H.-W.; Kristiansen, M.; Smith, P.; Stoll, K.; Maeder, D.; Hoffmann, K. *Macromolecules* **2005**, *38*, 3688.

(25) Kristiansen, P. M.; Gress, A.; Smith, P.; Hanft, D.; Schmidt, H.-W. *Polymer* **2006**, *47*, 249.

(26) Abraham, F.; Ganzleben, S.; Hanft, D.; Smith, P.; Schmidt, H.-W. *Macromol. Chem. Phys.* **2010**, *211*, 171.

(27) Bernland, K. *Nucleating and Clarifying Polymers*. Ph.D. Thesis, ETH, Zürich, 2010.

(28) Gahleitner, M.; Grein, C.; Kheirandish, S.; Wolfschwenger, J. *Int. Polym. Proc.* **2011**, *26*, 2.

(29) Lightfoot, M. P.; Mair, F. S.; Pritchard, R. G.; Warren, J. E. *Chem. Commun.* **1999**, 1945.

(30) Jimenez, C. A.; Belmar, J. B.; Ortiz, L.; Hidalgo, P.; Fabelo, O.; Pasan, J.; Ruiz-Perez, C. *Cryst. Growth Des.* **2009**, *9*, 4987.

(31) Kristiansen, M.; Smith, P.; Chanzy, H.; Baerlocher, C.; Gramlich, V.; McCusker, L.; Weber, T.; Pattison, P.; Blomenhofer, M.; Schmidt, H.-W. *Cryst. Growth Des.* **2009**, *9*, 2556.

(32) Cerny, R. *Croat. Chem. Acta* **2006**, *79*, 319.

(33) Harris, R. K. *J. Pharm. Pharmacol.* **2007**, *59*, 225.

(34) David, W. I. F.; Shankland, K. In *Structure Determination from Powder Diffraction Data*; McCusker, L., Baerlocher, C., Eds.; IUCr Monographs on Crystallography; Oxford University Press: Oxford, U.K., 2002.

(35) Harris, K. D. M.; Tremayne, M.; Kariuki, B. M. *Angew. Chem., Int. Ed.* **2001**, *40*, 1626.

(36) Harris, K. D. M. *Cryst. Growth Des.* **2003**, *3*, 887.

(37) Tremayne, M. *Phil. Trans. R. Soc., A* **2004**, *362*, 2691.

(38) Harris, K. D. M.; Cheung, E. Y. *Chem. Soc. Rev.* **2004**, *33*, 526.

(39) Harris, R. K. *Analyst* **2006**, *131*, 351.

(40) Hirsemann, D.; Köster, T. K.-J.; Wack, J.; van Wüllen, L.; Breu, J.; Senker, J. *Chem. Mater.* **2011**, *23*, 3152.

(41) Duer, M. J. *Introduction to Solid-State NMR Spectroscopy*; Blackwell Publishing: Oxford, U.K., 2004.

(42) Karau, F. W.; Seyfarth, L.; Oeckler, O.; Senker, J.; Landskron, K.; Schnick, W. *Chem. Eur. J.* **2007**, *13*, 6841.

(43) Lotsch, B. V.; Senker, J.; Kockelmann, W.; Schnick, W. *J. Solid State Chem.* **2003**, *176*, 180.

(44) Senker, J.; Seyfarth, L.; Voll, J. *Solid State Sci.* **2004**, *6*, 1039−1052.

(45) Senker, J.; Sehnert, J.; Correll, S. *J. Am. Chem. Soc.* **2005**, *127*, 337−349.

(46) Frydman, L. In *Fundamentals of Multiple-Quantum Magic-Angle Spinning NMR on Half-Integer Quadrupolar Nuclei*; Grant, D., Ed.; John Wiley & Sons. Ltd.: Chichester, U.K., 2002; Vol. *9*, pp 262−274.

(47) King, I. J.; Fayon, F.; Massiot, D.; Harris, R. K.; Evans, J. S. O. *Chem. Commun.* **2001**, 1766.

(48) Bestaoui, N.; Ouyang, X.; Fredoueil, F.; Bujoli, B.; Clearfield, A. *Acta Crystallogr. Sect. B* **2005**, *61*, 669.

(49) Taulelle, F. *Solid State Sci.* **2004**, *6*, 1053.

(50) Kentgens, A. *Geoderma* **1997**, *80*, 271.

(51) Smith, M.; van Eck, E. *Prog. Nucl. Magn. Reson. Spectrosc.* **1999**, *34*, 159−201.

(52) Seyfarth, L.; Senker, J. *Phys. Chem. Chem. Phys.* **2009**, *11*, 3522.

(53) Seyfarth, L.; Seyfarth, J.; Lotsch, B. V.; Schnick, W.; Senker, J. *Phys. Chem. Chem. Phys.* **2010**, *12*, 2227.

(54) Wirnhier, E.; Döblinger, M.; Gunzelmann, D.; Senker, J.; Lotsch, B. V.; Schnick, W. *Chem. Eur. J.* **2011**, *17*, 3213.

(55) auf der Guenne, J. S. *J. Magn. Reson.* **2003**, *165*, 18.

(56) Carravetta, M.; Eden, M.; Johannessen, O. G.; Luthman, H.; Verdegem, P. J. E.; Lugtenburg, J.; Sebald, A.; Levitt, M. H. *J. Am. Chem. Soc.* **2001**, *123*, 10628.

(57) Graf, R.; Demco, D. E.; Gottwald, J.; Hafner, S.; Spiess, H. W. *J. Chem. Phys.* **1997**, *106*, 885.

(58) van Rossum, B. J.; de Groot, C. P.; Ladizhansky, V.; Vega, S.; de Groot, H. J. M. *J. Am. Chem. Soc.* **2000**, *122*, 3465.

(59) Goward, G. R.; Schnell, I.; Brown, S. P.; Spiess, H. W.; Kim, H.-D.; Ishida, H. *Magn. Reson. Chem.* **2001**, *39*, 5.

(60) Dutour, J.; Guillou, N.; Huguenard, C.; Taulelle, F.; Mellot-Draznieks, C.; Férey, G. *Solid State Sci.* **2004**, *6*, 1059.

(61) Brouwer, D. H.; Kristiansen, P. E.; Fyfe, C. A.; Levitt, M. H. *J. Am. Chem. Soc.* **2005**, *127*, 542.

(62) Harris, R. K.; Ghi, P. Y.; Hammond, R. B.; Ma, C. Y.; Roberts, K. J. *Chem. Commun.* **2003**, 2834.

(63) Elena, B.; Pintacuda, G.; Mifsud, N.; Emsley, L. *J. Am. Chem. Soc.* **2006**, *128*, 9555.

(64) Pickard, C. J.; Salager, E.; Pintacuda, G.; Elena, B.; Emsley, L. *J. Am. Chem. Soc.* **2007**, *129*, 8932.

(65) Manolikas, T.; Herrmann, T.; Meier, B. H. *J. Am. Chem. Soc.* **2008**, *130*, 3959.

(66) Loquet, A.; Bardiaux, B.; Gardiennet, C.; Blanchet, C.; Baldus, M.; Nilges, M.; Malliavin, T.; Boeckmann, A. *J. Am. Chem. Soc.* **2008**, *130*, 3579.

(67) Middleton, D. A.; Peng, X.; Saunders, D.; Shankland, K.; David, W. I. F.; Markvardsen, A. J. *Chem. Commun.* **2002**, 1976.

(68) Brouwer, D. H.; Darton, R. J.; Morris, R. E.; Levitt, M. H. *J. Am. Chem. Soc.* **2005**, *127*, 10365.

(69) Fyfe, C. A.; Brouwer, D. H. *J. Am. Chem. Soc.* **2006**, *128*, 11860.

(70) Parnes, H.; Dekeczer, S. *J. Labelled Compd. Radiopharm.* **1985**, *22*, 287.

(71) *MS Modeling v5.0.0.0*; Accelrys Software Inc., 2009.

(72) Kristiansen, P. E.; Carravetta, M.; Lai, W. C.; Levitt, M. H. *Chem. Phys. Lett.* **2004**, *390*, 1.

(73) Bak, M.; Rasmussen, J. T.; Nielsen, N. C. *J. Magn. Reson.* **2000**, *147*, 296.

(74) *The Language of Technical Computing. MATLAB*; Math Works Inc.: Natick, MA, 1984−2012.

(75) Timme, A.; Kress, R.; Albuquerque, R. Q.; Schmidt, H.-W. *Chem. Eur. J.* **2011**, accepted.

(76) Chandrasekhar, S.; Sadashiva, B. K.; Suresh, K. *Pramana* **1977**, *9*, 471.

(77) Senker, J.; Lüdecke, J. *Z. Naturforsch.* **2001**, *b*, 1089.

(78) Sakamoto, A.; Ogata, D.; Shikata, T.; Urakawa, O.; Hanabusa, K. *Polymer* **2006**, *47*, 956.

(79) Fitié, C. F. C.; Roelofs, W. S. C.; Kemerink, M.; Sijbesma, R. P. *J. Am. Chem. Soc.* **2010**, *132*, 6892.

(80) Kulkarni, C.; Reddy, S. K.; George, S. J.; Balasubramanian, S. *Chem. Phys. Lett.* **2011**, *515*, 226.

(81) Phillips, R.; Wolkowicz, M. D. In *Polypropylene Handbook*, 2nd ed.; Pasquini, N., Ed.; Hanser: Cincinnati, 2005; pp 147−264.

6.1.2 Supporting Information

Crystal Structure of a Highly Efficient Clarifying Agent for Isotactic Polypropylene

Marko Schmidt,[a] Johannes J. Wittmann,[a] Roman Kress,[b] Denis Schneider,[c] Stefan Steuernagel,[c] Hans-Werner Schmidt*[b] and Jürgen Senker*[a]

[a] Lehrstuhl für Anorganische Chemie III, Universität Bayreuth, 95447 Bayreuth,
Deutschland

[b] Lehrstuhl für Makromolekulare Chemie I, Universität Bayreuth, 95447 Bayreuth, Deutschland

[c] Bruker Biospin GmbH, Silberstreifen 4, 76287 Rheinstetten, Deutschland

* juergen.senker@uni-bayreuth.de, * hans-werner.schmidt@uni-bayreuth.de

Supporting Information

Content:

1) Inputfile for Simpsonsimulation
2) Crystallographic Information File

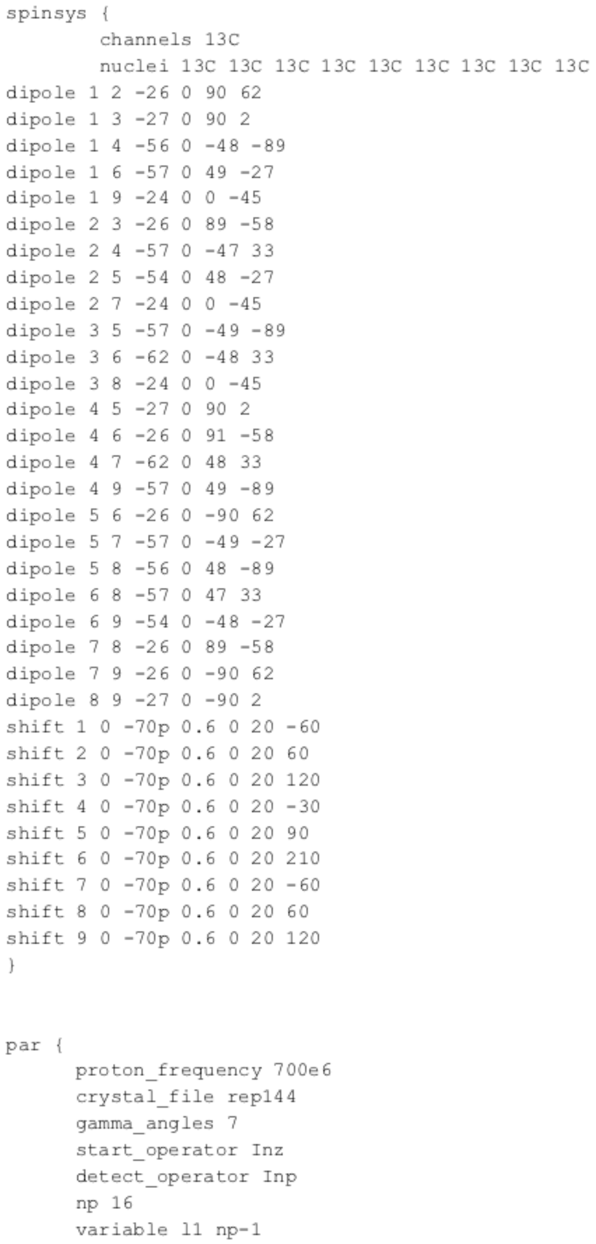

```
spinsys {
        channels 13C
        nuclei 13C 13C 13C 13C 13C 13C 13C 13C 13C
dipole 1 2 -26 0 90 62
dipole 1 3 -27 0 90 2
dipole 1 4 -56 0 -48 -89
dipole 1 6 -57 0 49 -27
dipole 1 9 -24 0 0 -45
dipole 2 3 -26 0 89 -58
dipole 2 4 -57 0 -47 33
dipole 2 5 -54 0 48 -27
dipole 2 7 -24 0 0 -45
dipole 3 5 -57 0 -49 -89
dipole 3 6 -62 0 -48 33
dipole 3 8 -24 0 0 -45
dipole 4 5 -27 0 90 2
dipole 4 6 -26 0 91 -58
dipole 4 7 -62 0 48 33
dipole 4 9 -57 0 49 -89
dipole 5 6 -26 0 -90 62
dipole 5 7 -57 0 -49 -27
dipole 5 8 -56 0 48 -89
dipole 6 8 -57 0 47 33
dipole 6 9 -54 0 -48 -27
dipole 7 8 -26 0 89 -58
dipole 7 9 -26 0 -90 62
dipole 8 9 -27 0 -90 2
shift 1 0 -70p 0.6 0 20 -60
shift 2 0 -70p 0.6 0 20 60
shift 3 0 -70p 0.6 0 20 120
shift 4 0 -70p 0.6 0 20 -30
shift 5 0 -70p 0.6 0 20 90
shift 6 0 -70p 0.6 0 20 210
shift 7 0 -70p 0.6 0 20 -60
shift 8 0 -70p 0.6 0 20 60
shift 9 0 -70p 0.6 0 20 120
}


par {
      proton_frequency 700e6
      crystal_file rep144
      gamma_angles 7
      start_operator Inz
      detect_operator Inp
      np 16
      variable l1 np-1
```

```
# Set Symmetry for SR26 DQ Recoupling
      variable N 26.
      variable n 4.
      variable nu 11.

      verbose 111111
}
proc pulseq {} {
      global par
      maxdt 1.0

# Additional Parameters
      set rf [expr $par(spin_rate)*$par(N)/$par(n)]
      set p90  [expr 0.25e6/$rf]
      set p270 [expr 0.75e6/$rf]

      set ph10 [expr 180.00*$par(nu)/$par(N)]
      set ph11 [expr 180.00*$par(nu)/$par(N)+180.0]
      set ph12 [expr (-1)*180.00/$par(N)*$par(nu)+360.00]
      set ph13 [expr (-1)*180.00/$par(N)*$par(nu)+180.0]

# Propagators for SR26
    reset
    for {set a 0} {$a < [expr $par(N)/2]} {incr a} {

        pulse $p90 $rf $ph10
        pulse $p270 $rf $ph11

        pulse $p90 $rf $ph12
        pulse $p270 $rf $ph13
    }
    for {set b 0} {$b < [expr $par(N)/2]} {incr b} {

        pulse $p90 $rf $ph12
        pulse $p270 $rf $ph13

        pulse $p90 $rf $ph10
        pulse $p270 $rf $ph11
    }
    store 2
    reset

     for {set c 0} {$c < [expr $par(N)/2]} {incr c} {

        pulse $p90 $rf $ph13
        pulse $p270 $rf $ph12

        pulse $p90 $rf $ph11
        pulse $p270 $rf $ph10
    }
```

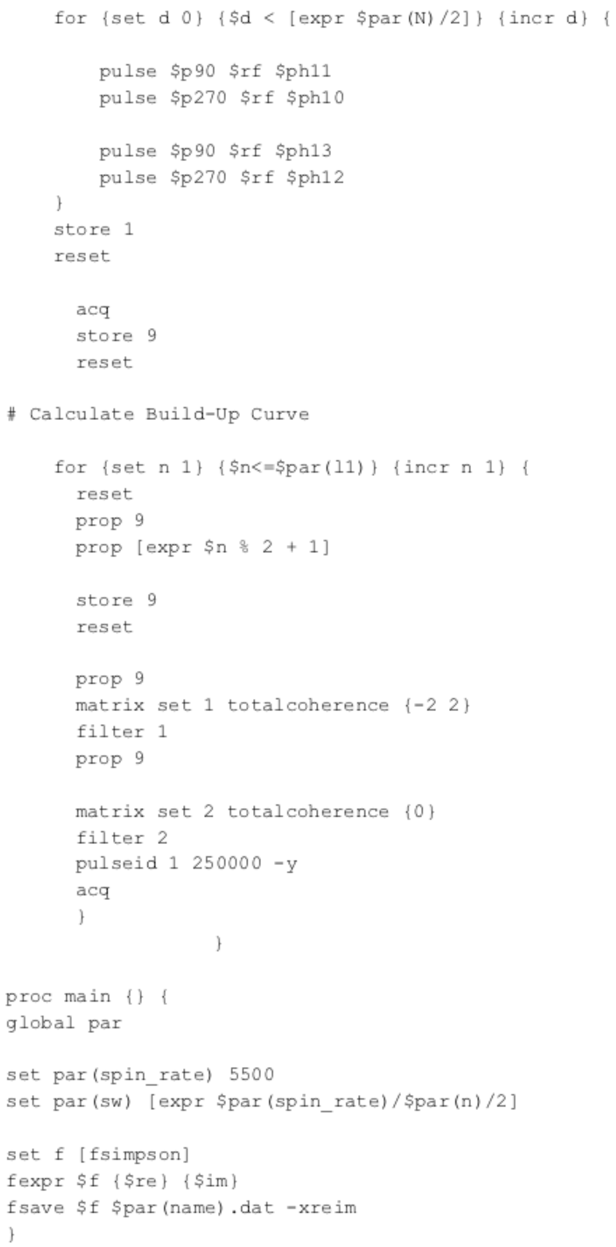

```
    for {set d 0} {$d < [expr $par(N)/2]} {incr d} {

        pulse $p90 $rf $ph11
        pulse $p270 $rf $ph10

        pulse $p90 $rf $ph13
        pulse $p270 $rf $ph12
    }
    store 1
    reset

      acq
      store 9
      reset

# Calculate Build-Up Curve

    for {set n 1} {$n<=$par(11)} {incr n 1} {
      reset
      prop 9
      prop [expr $n % 2 + 1]

      store 9
      reset

      prop 9
      matrix set 1 totalcoherence {-2 2}
      filter 1
      prop 9

      matrix set 2 totalcoherence {0}
      filter 2
      pulseid 1 250000 -y
      acq
      }
                  }

proc main {} {
global par

set par(spin_rate) 5500
set par(sw) [expr $par(spin_rate)/$par(n)/2]

set f [fsimpson]
fexpr $f {$re} {$im}
fsave $f $par(name).dat -xreim
}
```

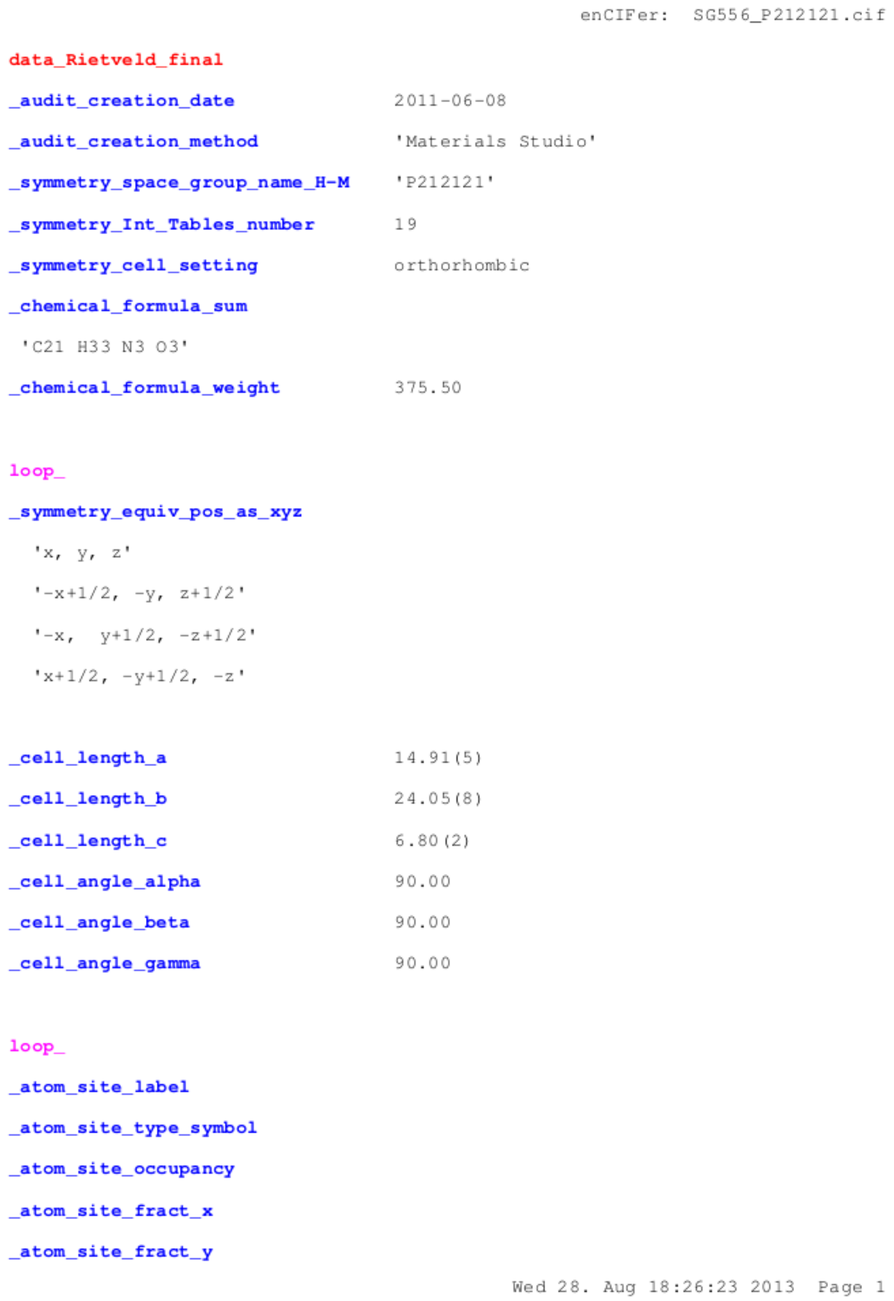

```
                                          enCIFer:  SG556_P212121.cif

data_Rietveld_final

_audit_creation_date                  2011-06-08

_audit_creation_method                'Materials Studio'

_symmetry_space_group_name_H-M        'P212121'

_symmetry_Int_Tables_number           19

_symmetry_cell_setting                orthorhombic

_chemical_formula_sum

 'C21 H33 N3 O3'

_chemical_formula_weight              375.50


loop_

_symmetry_equiv_pos_as_xyz

  'x, y, z'

  '-x+1/2, -y, z+1/2'

  '-x,  y+1/2, -z+1/2'

  'x+1/2, -y+1/2, -z'


_cell_length_a                        14.91(5)

_cell_length_b                        24.05(8)

_cell_length_c                        6.80(2)

_cell_angle_alpha                     90.00

_cell_angle_beta                      90.00

_cell_angle_gamma                     90.00


loop_

_atom_site_label

_atom_site_type_symbol

_atom_site_occupancy

_atom_site_fract_x

_atom_site_fract_y
                                 Wed 28. Aug 18:26:23 2013   Page 1
```

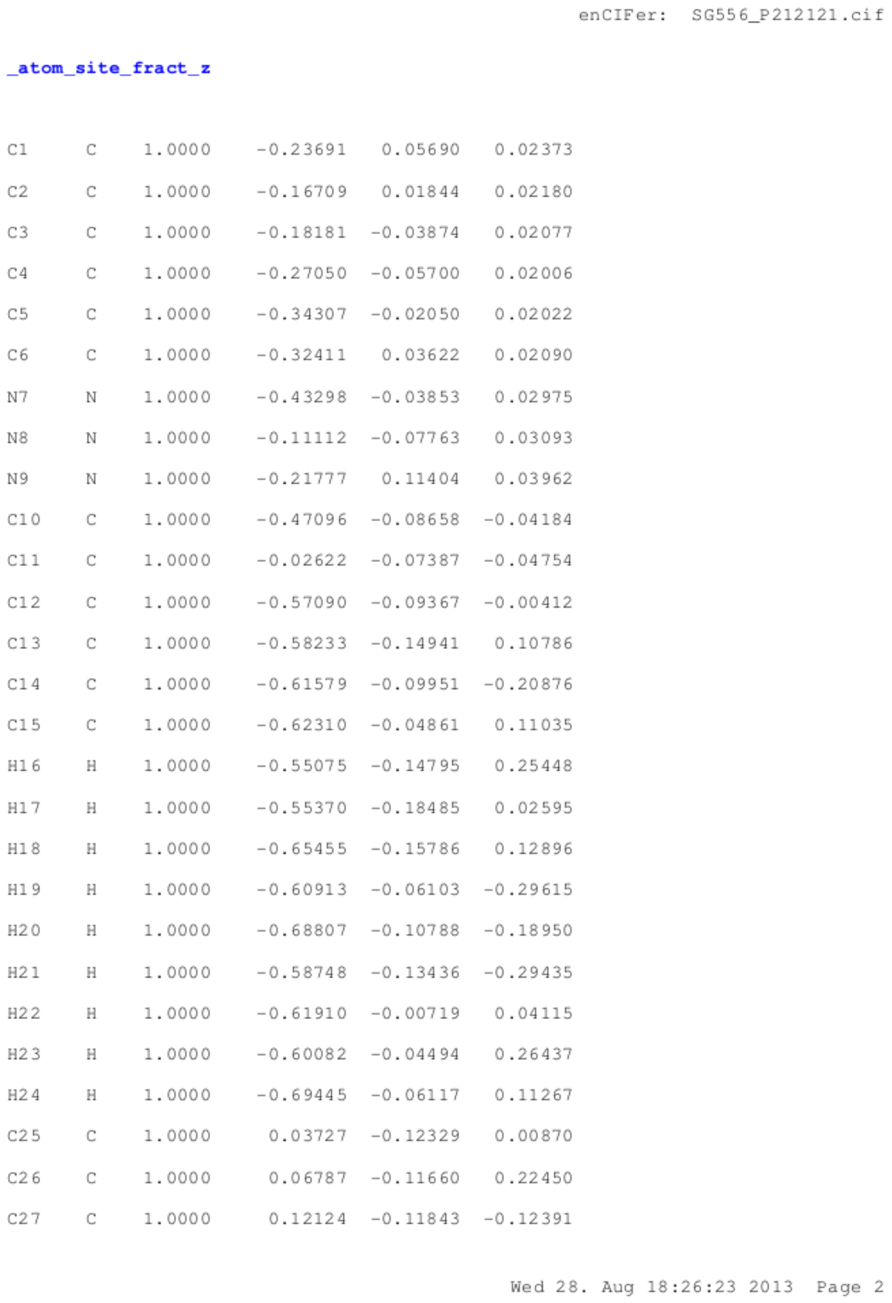

enCIFer: SG556_P212121.cif

```
_atom_site_fract_z

C1     C   1.0000   -0.23691   0.05690   0.02373
C2     C   1.0000   -0.16709   0.01844   0.02180
C3     C   1.0000   -0.18181  -0.03874   0.02077
C4     C   1.0000   -0.27050  -0.05700   0.02006
C5     C   1.0000   -0.34307  -0.02050   0.02022
C6     C   1.0000   -0.32411   0.03622   0.02090
N7     N   1.0000   -0.43298  -0.03853   0.02975
N8     N   1.0000   -0.11112  -0.07763   0.03093
N9     N   1.0000   -0.21777   0.11404   0.03962
C10    C   1.0000   -0.47096  -0.08658  -0.04184
C11    C   1.0000   -0.02622  -0.07387  -0.04754
C12    C   1.0000   -0.57090  -0.09367  -0.00412
C13    C   1.0000   -0.58233  -0.14941   0.10786
C14    C   1.0000   -0.61579  -0.09951  -0.20876
C15    C   1.0000   -0.62310  -0.04861   0.11035
H16    H   1.0000   -0.55075  -0.14795   0.25448
H17    H   1.0000   -0.55370  -0.18485   0.02595
H18    H   1.0000   -0.65455  -0.15786   0.12896
H19    H   1.0000   -0.60913  -0.06103  -0.29615
H20    H   1.0000   -0.68807  -0.10788  -0.18950
H21    H   1.0000   -0.58748  -0.13436  -0.29435
H22    H   1.0000   -0.61910  -0.00719   0.04115
H23    H   1.0000   -0.60082  -0.04494   0.26437
H24    H   1.0000   -0.69445  -0.06117   0.11267
C25    C   1.0000    0.03727  -0.12329   0.00870
C26    C   1.0000    0.06787  -0.11660   0.22450
C27    C   1.0000    0.12124  -0.11843  -0.12391
```

Wed 28. Aug 18:26:23 2013   Page 2

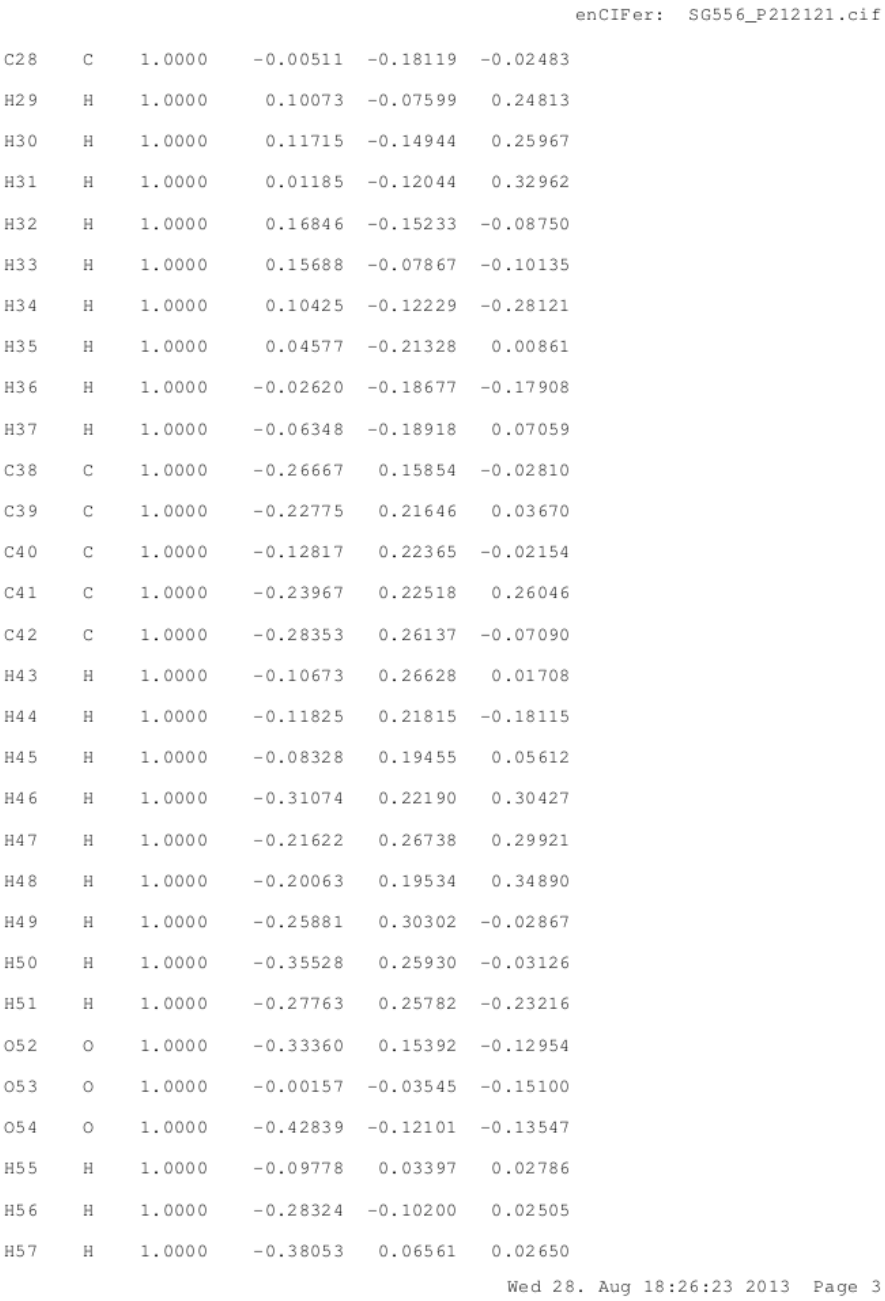

enCIFer: SG556_P212121.cif

C28	C	1.0000	-0.00511	-0.18119	-0.02483
H29	H	1.0000	0.10073	-0.07599	0.24813
H30	H	1.0000	0.11715	-0.14944	0.25967
H31	H	1.0000	0.01185	-0.12044	0.32962
H32	H	1.0000	0.16846	-0.15233	-0.08750
H33	H	1.0000	0.15688	-0.07867	-0.10135
H34	H	1.0000	0.10425	-0.12229	-0.28121
H35	H	1.0000	0.04577	-0.21328	0.00861
H36	H	1.0000	-0.02620	-0.18677	-0.17908
H37	H	1.0000	-0.06348	-0.18918	0.07059
C38	C	1.0000	-0.26667	0.15854	-0.02810
C39	C	1.0000	-0.22775	0.21646	0.03670
C40	C	1.0000	-0.12817	0.22365	-0.02154
C41	C	1.0000	-0.23967	0.22518	0.26046
C42	C	1.0000	-0.28353	0.26137	-0.07090
H43	H	1.0000	-0.10673	0.26628	0.01708
H44	H	1.0000	-0.11825	0.21815	-0.18115
H45	H	1.0000	-0.08328	0.19455	0.05612
H46	H	1.0000	-0.31074	0.22190	0.30427
H47	H	1.0000	-0.21622	0.26738	0.29921
H48	H	1.0000	-0.20063	0.19534	0.34890
H49	H	1.0000	-0.25881	0.30302	-0.02867
H50	H	1.0000	-0.35528	0.25930	-0.03126
H51	H	1.0000	-0.27763	0.25782	-0.23216
O52	O	1.0000	-0.33360	0.15392	-0.12954
O53	O	1.0000	-0.00157	-0.03545	-0.15100
O54	O	1.0000	-0.42839	-0.12101	-0.13547
H55	H	1.0000	-0.09778	0.03397	0.02786
H56	H	1.0000	-0.28324	-0.10200	0.02505
H57	H	1.0000	-0.38053	0.06561	0.02650

Wed 28. Aug 18:26:23 2013 Page 3

```
                                            enCIFer:  SG556_P212121.cif

H58    H    1.0000    -0.47324  -0.01287   0.10802
H59    H    1.0000    -0.12428  -0.11127   0.11552
H60    H    1.0000    -0.16271   0.12291   0.12073





                                 Wed 28. Aug 18:26:23 2013  Page 4
```

6.2 *Selbstorganisation eines effizienten Nukleierungsagens in einer i-PP Matrix*

Marko Schmidt,[a] Johannes J. Wittmann,[a] Roman Kress,[b] Hans-Werner Schmidt[b] and Jürgen Senker*[a]

Probing self-assembled 1,3,5-benzenetrisamides in isotactic polypropylene by ^{13}C DQ solid-state NMR spectroscopy

Erschienen in: *Chem. Commun.* 2013, **49**, 267. Reproduced by permission of The Royal Society of Chemistry.

[a] Lehrstuhl für Anorganische Chemie III, Universität Bayreuth, 95447 Bayreuth,
Deutschland
[b] Lehrstuhl für Makromolekulare Chemie I, Universität Bayreuth, 95447 Bayreuth, Deutschland
* juergen.senker@uni-bayreuth.de

Darstellung des Eigenanteils:

Die für diese Publikation notwendigen FK-NMR-Messungen wurden hauptsächlich von mir mit durchgeführt, während die sowie Computersimulationen von *Johannes Wittmann* erstellt wurden. Das benötigte Kompositmaterial bestehend aus dem ^{13}C-isotopenmarkierten Additiv in einer *i*-PP Matrix wurde von *Roman Kress* präpariert. Die Publikation wurde von Prof. Dr. *Jürgen Senker*, Prof. Dr. *Hans-Werner Schmidt* und mir verfasst. Mein Eigenanteil beläuft sich auf ca. 80 %.

6.2.1 Probing self-assembled 1,3,5-benzenetrisamides in isotactic polypropylene by ^{13}C DQ solid-state NMR spectroscopy

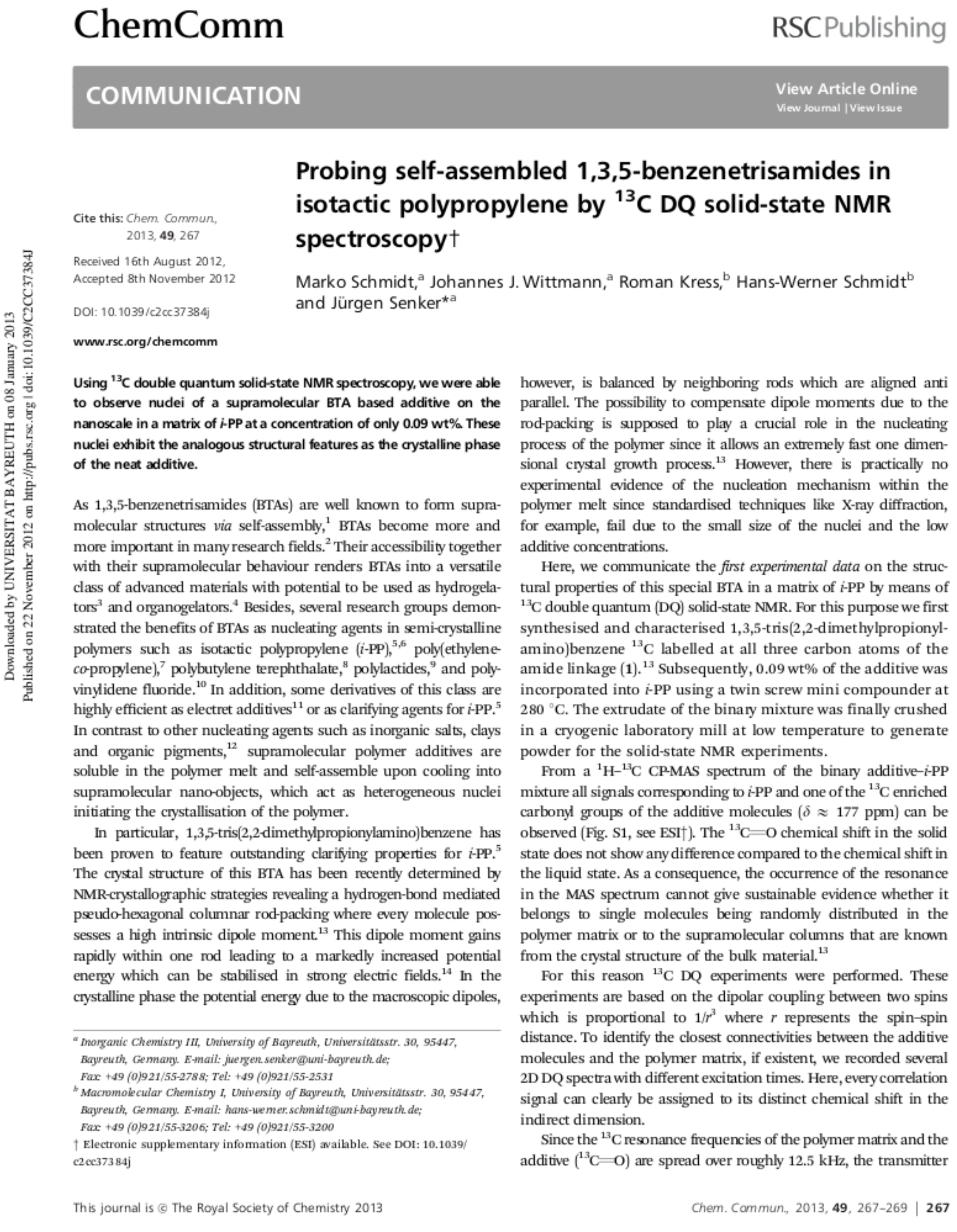

ChemComm
RSC Publishing

COMMUNICATION

View Article Online
View Journal | View Issue

Cite this: *Chem. Commun.*, 2013, **49**, 267

Received 16th August 2012,
Accepted 8th November 2012

DOI: 10.1039/c2cc37384j

www.rsc.org/chemcomm

Probing self-assembled 1,3,5-benzenetrisamides in isotactic polypropylene by ^{13}C DQ solid-state NMR spectroscopy†

Marko Schmidt,[a] Johannes J. Wittmann,[a] Roman Kress,[b] Hans-Werner Schmidt[b] and Jürgen Senker*[a]

Using ^{13}C double quantum solid-state NMR spectroscopy, we were able to observe nuclei of a supramolecular BTA based additive on the nanoscale in a matrix of *i*-PP at a concentration of only 0.09 wt%. These nuclei exhibit the analogous structural features as the crystalline phase of the neat additive.

As 1,3,5-benzenetrisamides (BTAs) are well known to form supramolecular structures *via* self-assembly,[1] BTAs become more and more important in many research fields.[2] Their accessibility together with their supramolecular behaviour renders BTAs into a versatile class of advanced materials with potential to be used as hydrogelators[3] and organogelators.[4] Besides, several research groups demonstrated the benefits of BTAs as nucleating agents in semi-crystalline polymers such as isotactic polypropylene (*i*-PP),[5,6] poly(ethylene-*co*-propylene),[7] polybutylene terephthalate,[8] polylactides,[9] and polyvinylidene fluoride.[10] In addition, some derivatives of this class are highly efficient as electret additives[11] or as clarifying agents for *i*-PP.[5] In contrast to other nucleating agents such as inorganic salts, clays and organic pigments,[12] supramolecular polymer additives are soluble in the polymer melt and self-assemble upon cooling into supramolecular nano-objects, which act as heterogeneous nuclei initiating the crystallisation of the polymer.

In particular, 1,3,5-tris(2,2-dimethylpropionylamino)benzene has been proven to feature outstanding clarifying properties for *i*-PP.[5] The crystal structure of this BTA has been recently determined by NMR-crystallographic strategies revealing a hydrogen-bond mediated pseudo-hexagonal columnar rod-packing where every molecule possesses a high intrinsic dipole moment.[13] This dipole moment gains rapidly within one rod leading to a markedly increased potential energy which can be stabilised in strong electric fields.[14] In the crystalline phase the potential energy due to the macroscopic dipoles, however, is balanced by neighboring rods which are aligned anti parallel. The possibility to compensate dipole moments due to the rod-packing is supposed to play a crucial role in the nucleating process of the polymer since it allows an extremely fast one dimensional crystal growth process.[13] However, there is practically no experimental evidence of the nucleation mechanism within the polymer melt since standardised techniques like X-ray diffraction, for example, fail due to the small size of the nuclei and the low additive concentrations.

Here, we communicate the *first experimental data* on the structural properties of this special BTA in a matrix of *i*-PP by means of ^{13}C double quantum (DQ) solid-state NMR. For this purpose we first synthesised and characterised 1,3,5-tris(2,2-dimethylpropionylamino)benzene ^{13}C labelled at all three carbon atoms of the amide linkage (**1**).[13] Subsequently, 0.09 wt% of the additive was incorporated into *i*-PP using a twin screw mini compounder at 280 °C. The extrudate of the binary mixture was finally crushed in a cryogenic laboratory mill at low temperature to generate powder for the solid-state NMR experiments.

From a ^{1}H–^{13}C CP-MAS spectrum of the binary additive–*i*-PP mixture all signals corresponding to *i*-PP and one of the ^{13}C enriched carbonyl groups of the additive molecules ($\delta \approx 177$ ppm) can be observed (Fig. S1, see ESI†). The ^{13}C=O chemical shift in the solid state does not show any difference compared to the chemical shift in the liquid state. As a consequence, the occurrence of the resonance in the MAS spectrum cannot give sustainable evidence whether it belongs to single molecules being randomly distributed in the polymer matrix or to the supramolecular columns that are known from the crystal structure of the bulk material.[13]

For this reason ^{13}C DQ experiments were performed. These experiments are based on the dipolar coupling between two spins which is proportional to $1/r^3$ where r represents the spin–spin distance. To identify the closest connectivities between the additive molecules and the polymer matrix, if existent, we recorded several 2D DQ spectra with different excitation times. Here, every correlation signal can clearly be assigned to its distinct chemical shift in the indirect dimension.

Since the ^{13}C resonance frequencies of the polymer matrix and the additive (^{13}C=O) are spread over roughly 12.5 kHz, the transmitter

---

[a] *Inorganic Chemistry III, University of Bayreuth, Universitätsstr. 30, 95447, Bayreuth, Germany. E-mail: juergen.senker@uni-bayreuth.de; Fax: +49 (0)921/55-2788; Tel: +49 (0)921/55-2531*

[b] *Macromolecular Chemistry I, University of Bayreuth, Universitätsstr. 30, 95447, Bayreuth, Germany. E-mail: hans-werner.schmidt@uni-bayreuth.de; Fax: +49 (0)921/55-3206; Tel: +49 (0)921/55-3200*

† Electronic supplementary information (ESI) available. See DOI: 10.1039/c2cc37384j

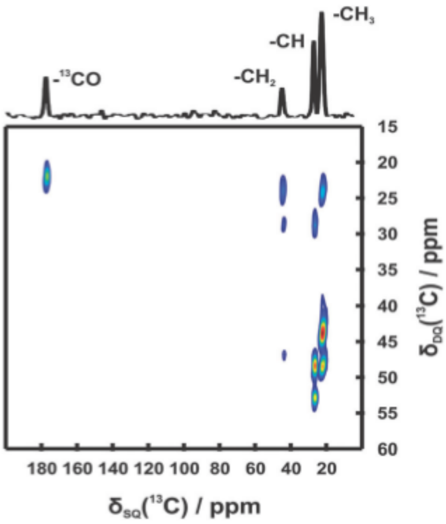

Fig. 1 Experimental 2D DQ-SQ ^{13}C spectrum of the additive–*i*-PP mixture using the $SR26_4^{11}$ sequence at B_0 = 7.04 T, ν_{rot} = 6.25 kHz and τ_{exc} = 15.36 ms. The F2 projection is the sum of all signals in the SQ domain – signal assignment included. Additional information is given in the ESI.†

frequency offset was placed in the middle of these resonances. This leads to an off-resonant excitation of about 6 kHz which does have only a minor influence on the spectrum due to the robustness of the pulse sequence against offset effects.[15] A rotation frequency of 6.25 kHz was used with the non-γ-encoded $SR26_4^{11}$ sequence[16] (see ESI†) since previous results showed that faster spinning does not lead to an efficient DQ build-up, especially for large distances of ≈ 5 Å which we expect from the structure model of the neat additive. In addition, to obtain pure absorptive 2D spectra without any rotational sidebands in the DQ-domain, t_1 must be an integer multiple of the rotor period and, moreover, possess equal values in the direct and indirect dimension (in our case two times τ_{rot}). As a consequence the spectral width in the indirect domain is just 41.5 ppm (19.5–61 ppm) causing a refolding of the DQ signals in the indirect dimension which were theoretically placed outside the Nyquist frequencies (Nyquist theorem[17]).

Fig. 1 displays the DQ-SQ ^{13}C spectrum of the *i*-PP–additive material at B_0 = 7.04 T, ν_{rot} = 6.25 kHz and τ_{exc} = 15.36 ms. The spectrum exhibits DQ correlations between all resonances corresponding to the *i*-PP and the auto-correlation signal of the ^{13}C=O group of the additive. The auto-correlation peak of the CH-group served as internal shift calibration.

The chemical shift of the CH$_3$-group in the direct domain of $\delta_{SQ} \approx 22.5$ ppm leads at the same time to a signal at $\delta_{DQ} \approx 45$ ppm in the indirect dimension. This can also be observed for the CH-group where the peak in the DQ domain at $\delta_{DQ} \approx 53$ ppm corresponds to the signal at $\delta_{SQ} \approx 26.5$ ppm in the SQ domain. The signal at $\delta_{DQ} \approx 49$ ppm can be identified as the one-bond correlation between the methyl and the methine group. The auto-correlation signal of the CH$_2$-group with a chemical shift $\delta_{SQ} \approx 44$ ppm ($\delta_{DQ,exp} \approx 88$ ppm) occurs at $\delta_{DQ,obs} \approx 46.5$ ppm after being refolded once into the spectrum. However, the intensity of this signal at τ_{exc} = 15.36 ms is very weak, in comparison, for instance, with the auto-correlation peak of the CH-group. We additionally observe refolded correlation peaks between the CH$_2$-group of the polymer and the CH- and CH$_3$-group at $\delta_{DQ} \approx 25$ ppm and $\delta_{DQ} \approx 29$ ppm. At $\delta_{SQ} \approx 177$ ppm, a signal corresponding to the carbonyl group of the additive occurs. After an eightfold refolding of the signal into the spectrum, the peak at $\delta_{DQ} \approx 22$ ppm can clearly be identified as the auto-correlation signal of the ^{13}C=O group ($\delta_{DQ,exp} \approx 354$ ppm), while other correlations that include the carbonyl groups, *i.e.* interaction with the polymer matrix, are not observed. This fact can also be seen in 2D DQ-SQ spectra with lower and even higher excitation times, respectively (see Fig. S2 in the ESI†). In Table S2 (see ESI†) the expected and observed chemical shifts after refolding of all correlation signals in the indirect domain are summarized.

The existence of the ^{13}C=O auto-correlation indicates a spatial connectivity of the additive carbonyl groups but, still, is no unequivocal evidence. To get a more detailed picture of the structural features of the additive clusters in the polymer matrix, we recorded a symmetric DQ build-up curve. The absence of correlations between the additive and the polymer matrix allows treating the signal of the carbonyl group independently. Thus, the intensities being extracted from the build-up curve of the *i*-PP–BTA material can be directly compared to one of the neat ^{13}C labelled additive **1**.

Fig. 2 displays the experimental symmetric ^{13}C DQ build-up curves of the labelled carbonyl groups of the bulk material (red circles) and the additive within the polymer (blue squares with error bars according to equation S3 in the ESI†). Both build-up curves are normalised according to equation S1 (see ESI†).

Within the experimental error, the progression of both curves matches perfectly. In this respect, the slight shift of the maximum of the DQ build-up curve for the *i*-PP–additive mixture is negligible. As a consequence, the ^{13}C^{13}C DQ data provide solid evidence that the structural motifs for the additive

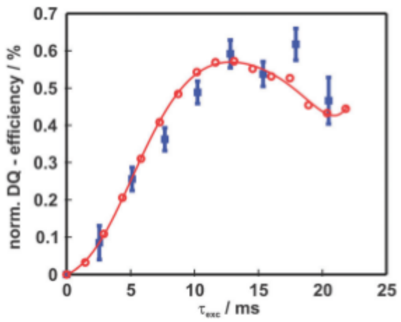

Fig. 2 Experimental symmetric ^{13}C DQ build-up curves of the labelled carbonyl groups within neat 1,3,5-tris(2,2-dimethylpropionylamino)benzene (red circles, ν_{rot} = 5.5 kHz) and the *i*-PP–additive binary mixture (blue squares with error bars, ν_{rot} = 6.25 kHz). Both measurements were performed using the $SR26_4^{11}$ pulse sequence (B_0 = 7.04 T) with a maximum excitation time τ_{exc} of 21.76 (bulk) and 20.48 ms (mixture), respectively. Further information is given in the ESI.†

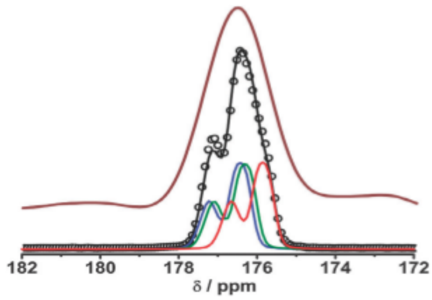

Fig. 3 Bottom: experimental (black circles) and simulated (black line) ^{13}C DQ filtered spectra of the neat BTA with deconvolution into three distinct resonances (blue, green and red lines). Their fine structure is caused by a second order ^{14}N quadrupolar interaction on a dipolar coupled ^{13}C^{14}N spin pair (compare ESI†). Top: experimental ^{13}C DQ filtered spectrum of the binary mixture (as sum over all 1D spectra extracted from the build-up curve).

clusters in the polymer matrix and in the bulk material are similar. As demonstrated in ref. 13 the applied DQ filtered ^{13}C NMR experiment is able to probe the columnar arrangement of the molecules but not the alignment of neighbouring rods. This could also be successfully demonstrated by evaluating the root-sum-square dipolar coupling d_{rss} for different scenarios (see ESI†).[18] For diluted molecules, d_{rss} accounts to roughly 37 Hz and thus a slower DQ build-up would be observed, while a single molecular strand and the rod packing in the crystal lead to nearly identical values of 127 Hz and 128 Hz.

The DQ-SQ spectra (Fig. 1 and Fig. S2, ESI†) display intensive peaks for all correlations with the exception of the signal between the BTA carbonyl group and the polymer units. Although a quantitative analysis is demanding due to the influence of the DQ intensity on the nuclear distances,[19] the geometry of the aggregates, the low additive concentration and possible motional processes its absence hints at the formation of larger clusters consisting of several rods. Nevertheless, the significant broadening of the DQ signal of the carbonyl groups in the BTA–*i*-PP mixture where the fine structure is masked – compared to the neat BTA (Fig. 3) – suggests a less well defined long-range order and crystallite sizes in the lower nanometre regime within the polymer matrix.

Our experiments demonstrate that the additive molecules form columns within the polymer matrix which are similar to the ones observed for the neat material. The compensation of the macrodipole arising in one rod requires a pseudo-hexagonal rod packing accounting also for the fast 1D growth behaviour. Thus, even at low concentrations the BTAs can form long and thin needle-like objects which provide enough surface area to initiate heteronuclear nucleation of the polymer. Interestingly, the spacing of the additive molecules within one rod leads to a surface modulation with similar characteristic distances (6.8 Å)[13] as compared to neat *i*-PP (6.5 Å) indicating that the growth mechanism of the *i*-PP is indeed epitactic in nature.

In conclusion, we have presented a powerful approach to visualise nuclei on a nanoscale of an efficient BTA-based nucleating and clarifying agent for *i*-PP at a concentration below 0.1 wt% within the polymer matrix. We successfully used ^{13}C DQ solid-state NMR to clearly demonstrate the structural analogy of the supramolecular aggregates of the additive within the binary *i*-PP–additive material compared to the neat bulk material.

With this approach it will be possible to study nucleation processes from solutions and melts in an early stage for a wide range of molecular compounds including pharmaceuticals in the future. This is important especially for systems with polymorphism where probably small structural changes of the nuclei may lead to a different polymorph.

We gratefully acknowledge financial support that was granted by the Deutsche Forschungsgemeinschaft DFG (SFB 840).

Notes and references

1 (*a*) M. P. Lightfoot, F. S. Mair, R. G. Pritchard and J. E. Warren, *Chem. Commun.*, 1999, 1945; (*b*) L. Brunsveld, A. P. H. J. Schenning, M. A. C. Broeren, H. M. Janssen, J. A. J. M. Vekemans and E. W. Meijer, *Chem. Lett.*, 2000, 292; (*c*) M. Kristiansen, P. Smith, H. Chanzy, C. Baerlocher, V. Gramlich, L. McCusker, T. Weber, P. Pattison, M. Blomenhofer and H.-W. Schmidt, *Cryst. Growth Des.*, 2009, **9**, 2556; (*d*) D. Kluge, F. Abraham, S. Schmidt, H.-W. Schmidt and A. Fery, *Langmuir*, 2010, **26**, 3020; (*e*) M. Wegner, D. Dudenko, D. Sebastiani, A. R. A. Palmans, T. F. A. de Greef, R. Graf and H. W. Spiess, *Chem. Sci.*, 2011, **2**, 2040; (*f*) D. Kluge, J. C. Singer, J. W. Neubauer, F. Abraham, H.-W. Schmidt and A. Fery, *Small*, 2012, **8**, 2563.

2 S. Cantekin, T. F. A. de Greef and A. R. A. Palmans, *Chem. Soc. Rev.*, 2012, **41**, 6125.

3 (*a*) N. Shi, H. Dong, G. Yin, Z. Xu and S. Li, *Adv. Funct. Mater.*, 2007, **17**, 1837; (*b*) A. Bernet, R. Q. Albuquerque, M. Behr, S. T. Hoffmann and H.-W. Schmidt, *Soft Matter*, 2012, **8**, 66.

4 (*a*) Y. Yasuda, E. Iishi, H. Inada and Y. Shirota, *Chem. Lett.*, 1996, **25**, 575; (*b*) K. Hanabusa, C. Koto, M. Kimura, H. Shirai and A. Kakehi, *Chem. Lett.*, 1997, **26**, 429; (*c*) J. J. van Gorp, J. A. J. M. Vekemans and E. W. Meijer, *J. Am. Chem. Soc.*, 2002, **124**, 14759.

5 M. Blomenhofer, S. Ganzleben, D. Hanft, H.-W. Schmidt, M. Kristiansen, P. Smith, K. Stoll, D. Maeder and K. Hoffmann, *Macromolecules*, 2005, **38**, 3688.

6 (*a*) P. M. Kristiansen, A. Gress, P. Smith, D. Hanft and H.-W. Schmidt, *Polymer*, 2006, **47**, 249; (*b*) F. Abraham, S. Ganzleben, D. Hanft, P. Smith and H.-W. Schmidt, *Macromol. Chem. Phys.*, 2010, **211**, 171.

7 J. Wang, Q. Dou, X. Chen and D. Li, *J. Polym. Sci., Part B: Polym. Phys.*, 2008, **46**, 1067.

8 F. Richter and H.-W. Schmidt, *Macromol. Mater. Eng.*, 2012, DOI: 10.1002/mame.201200034.

9 (*a*) H. Nakajima, M. Takahashi and Y. Kimura, *Macromol. Mater. Eng.*, 2010, **295**, 460; (*b*) H. Bai, W. Zhang, H. Deng, Q. Zhang and Q. Fu, *Macromolecules*, 2011, **44**, 1233; (*c*) P. Song, Z. Wei, J. Liang, G. Chen and W. Zhang, *Polym. Eng. Sci.*, 2012, **52**, 1058.

10 F. Abraham and H.-W. Schmidt, *Polymer*, 2010, **51**, 913.

11 (*a*) N. Mohmeyer, N. Behrendt, X. Zhang, P. Smith, V. Altstädt, G. M. Sessler and H.-W. Schmidt, *Polymer*, 2007, **48**, 1612; (*b*) J. Hillenbrand, T. Motz, G. M. Sessler, X. Zhang, N. Behrendt, C. von Salis-Soglio, D. P. Erhard, V. Altstädt and H.-W. Schmidt, *J. Phys. D: Appl. Phys.*, 2009, **42**, 65410; (*c*) D. P. Erhard, D. Lovera, C. von Salis-Soglio, R. Giesa, V. Altstaedt and H.-W. Schmidt, *Adv. Polym. Sci.*, 2010, **228**, 155.

12 (*a*) F. Binsbergen, *Polymer*, 1970, **11**, 253; (*b*) F. Binsbergen and B. de Lange, *Polymer*, 1970, **11**, 309; (*c*) F. Binsbergen, *J. Polym. Sci., Polym. Lett. Ed.*, 1973, **11**, 117.

13 M. Schmidt, J. J. Wittmann, R. Kress, D. Schneider, S. Steuernagel, H.-W. Schmidt and J. Senker, *Cryst. Growth Des.*, 2012, **12**, 2543.

14 C. F. C. Fitié, W. S. C. Roelofs, M. Kemerink and R. P. Sijbesma, *J. Am. Chem. Soc.*, 2010, **132**, 6892.

15 P. E. Kristiansen, M. Carravetta, J. D. van Beek, W. C. Lai and M. H. Levitt, *J. Chem. Phys.*, 2006, **124**, 234510.

16 P. E. Kristiansen, M. Carravetta, W. C. Lai and M. H. Levitt, *Chem. Phys. Lett.*, 2004, **390**, 1.

17 J. Keeler, *Understanding NMR Spectroscopy*, Wiley, Chichester, 2nd edn, 2010.

18 V. E. Zorin, S. P. Brown and P. Hodgkinson, *Mol. Phys.*, 2006, **104**, 293.

19 J. P. Bradley, C. Tripon, C. Filip and S. Brown, *Phys. Chem. Chem. Phys.*, 2009, **11**, 6941.

6.2.2 Supporting Information

Electronic Supplementary Material (ESI) for Chemical Communications
This journal is © The Royal Society of Chemistry 2013

Electronic Supplementary Information

to

Probing self-assembled 1,3,5-benzenetrisamides in isotactic polypropylene by ^{13}C DQ solid-state NMR spectroscopy†

Marko Schmidt,[a] Johannes J. Wittmann,[a] Roman Kress,[b] Hans-Werner Schmidt[b]
and Jürgen Senker*[a]

[a] Inorganic Chemistry III, University of Bayreuth, Universitätsstr. 30, 95447 Bayreuth, Germany.

Tel: +49(0)921552532; E-mail: juergen.senker@uni-bayreuth.de

[b] Macromolecular Chemistry I, University of Bayreuth, Universitätsstr. 30, 95447 Bayreuth, Germany.

Tel: +49(0)921553200; E-mail: hans-werner.schmidt@uni-bayreuth.de

Electronic Supplementary Material (ESI) for Chemical Communications
This journal is © The Royal Society of Chemistry 2013

Experimental Section

Materials and Preparation

The *i*-PP homopolymer grade Profax PH 350 was purchased from LyondellBasell. The polymer contained about 0.05 wt% of the antioxidant Irganox 1010, 0.10 wt% Irgafos 168 and 0.1 wt% Ca-stearate. The polymer pellets were pulverized in a freezer mill (Retsch ZM100, Schieritz & Hauenstein AG, Switzerland) before usage. The ^{13}C labelled 1,3,5-tris(2,2-dimethylpropionylamino)benzene was synthesised and characterised as described in Ref 1.

The *i*-PP/additive material was prepared by compounding a dry-blended powdery mixture of *i*-PP and the additive using a laboratory, co-rotating mini-twin-screw mixer (Technical University Eindhoven, The Netherlands) at 280 °C under nitrogen blanket for 5 minutes. The concentration of the additive was directly adjusted to 0.09 wt%. The extruded strand was mechanically cut and pulverized in a freezer mill (Spex CertiPrep 6750, Metuchen, NJ 08840, USA) using two cycles of 3 minutes each.

Solid-State NMR

The ^{13}C chemical shifts are reported with respect to TMS. The ^{1}H-^{13}C CP MAS spectrum, the ^{13}C double quantum build-up curve, and the ^{13}C 2D DQ-SQ spectrum of the *i*-PP/additive material were recorded at $B_0 = 7.04$ T using a standard ZrO_2 rotor on a Bruker Avance II 300 spectrometer with a 4 mm triple resonance probe. For the 1D CP MAS (ν_{rot} = 12.5 kHz) spectrum a contact time of 6 ms was used. The 90° pulse on the proton channel and the recycle delay were set to 3.0 µs and 2 s, respectively. The number of scans accounted for 4096 leading to a total experiment time of 6 h.

For the double quantum experiments, the symmetry-based pulse sequence $SR26^{11}_{4}$ was used. Before exciting DQ coherences, a ramped shaped cross polarization from proton to ^{13}C with a ^{1}H 90° pulse length of 3.0 µs and a contact time of 6 ms was used for an increased signal-to-noise ratio. The recycle delay was set to 2 seconds which matched the full T_1 relaxation time for the aliphatic protons of the polymer as well as of the methyl groups of the additive. The 90° read-out pulse on the ^{13}C channel accounted to 3.0 µs. The MAS frequency was set to 6.25 kHz and the R-block was implemented as a 90°-270° composite pulse corresponding to a nutation frequency of roughly 40.5 kHz ($\tau_{90°}$ = 6.15 µs). The transmitter frequency offset was placed between the resonances of the polymer and the additive leading to an off-resonant excitation of roughly 6 kHz.

For the build-up curve, the establishing of the coherence pathway 0 ±2 0 -1 was performed with the conventional 16-fold phase cycle.[2] An additional standardisation experiment was performed with the zero-quantum coherence pathway 0 0 0 -1. From both data sets the normalised DQ intensity is calculated according to equation S1. The number of repetitions for each of the nine 1D experiments was set to 4096. The step size for incrementing τ_{exc} was set to 52 corresponding to 2.56 ms accounting for a maximum excitation time of 20.48 ms. During excitation and reconversion CW decoupling with a nutation frequency of roughly 120 kHz was performed.

For the 2D DQ-SQ ^{13}C spectra excitation times of 6.4, 15.36 and 20.48 ms (shown in Figure 1 and S2) were established. The quadrature along the indirect dimension was obtained using the STATES procedure.[3] For τ_{exc} = 15.36 ms the 50 t_1 increments were set rotor synchronised with two times τ_{rot} (t_1 = 320 µs) while for τ_{exc} = 6.4 and 20.48 ms, respectively, only one time τ_{rot} (t_1 = 160 µs) was applied. During t_1 a heteronuclear CW decoupling with reduced power irradiating a nutation frequency of roughly 85 kHz was applied. Each t_1 increment was repeated 3072 times resulting in a total experimental time of 4d. During excitation and reconversion a heteronuclear broadband decoupling was necessary to gain signals with acceptable intensities beyond the noise level. To avoid Hartmann-Hahn conditions a strong decoupling during the DQ blocks following $\nu_{nutation}(^{1}H) = 3 \cdot \nu_{nutation}(^{13}C)$ was used.[4] The strong irradiation on the proton channel with roughly $\nu_{nutation}(^{1}H)$ = 120 kHz is thereby the power-limiting factor of the probe.

For all experiments, a broadband SPINAL64 proton decoupling with a nutation frequency of about 85 kHz was used during data collection.

Experimental ^1H-^{13}C CP MAS spectrum

The signals of the polymer are quite broad reflecting the partly crystalline and amorphous nature of *i*-PP with different chemical environments. The S/N ratios in the range of the signals account for 675.4 (*i*-PP) to 10.6 (^{13}C=O) reflecting the weak intensity of the additive signal despite of the ^{13}C enrichment.

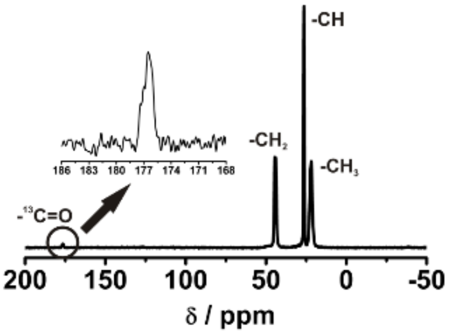

Figure S1 Experimental ^1H-^{13}C CP-MAS spectrum (B_0 = 7.04 T, ν_{rot} = 12.5 kHz) of the binary mixture (1,3,5-tris(2,2-dimethylpropionylamino)benzene in isotactic polypropylene, $c_{additive}$ = 0.09 wt%) with a signal assignment for *i*-PP (δ ≈ 22 - ≈ 45 ppm) and the carbonyl signal (δ ≈ 177 ppm) of the enriched ^{13}C=O group of the additive.

Comparison of the DQ-filtered ^{13}C signal of neat BTA and i-PP/BTA mixture

Both the SQ ^{13}C CPMAS (not shown) and the DQ filtered ^{13}C MAS (Figure 3, black circles) spectra of the neat BTA were measured at a external magnetic field of B_0 = 7.04 T and a spinning speed of ν_{rot} = 6.25 kHz. They exhibit a distinct fine structure which arises from the second-order quadrupolar interaction of neighboured ^{14}N nuclei (I = 1) mediated by the $^{13}C^{14}N$ dipole interaction. The experimental DQ filtered ^{13}C MAS spectrum was deconvoluted using the freeware program WSOLIDS1.[5] For getting reasonable starting values a comparable OC=NH system was taken from literature.[6] Here the quadrupolar coupling constant (C_Q = -3.2 MHz), the asymmetry parameter (η = 0.22), the angle between the V_{xx} component of the ^{14}N electric field gradient (EFG) and the projection of the internuclear ^{13}C-^{14}N vector into the equatorial plane (α = 43 °) and the angle between the V_{zz} component of the ^{14}N EFG and the internuclear ^{13}C-^{14}N vector (β = 90 °) were extracted. From the data presented in Ref. 1 the isotropic chemical shift and the direct dipolar coupling constant ($d^{13}{}_{C-}{}^{14}{}_{N}$ = 840 Hz) was used. For the indirect scalar dipolar coupling between ^{13}C and ^{14}N ("*J*-coupling") 11 Hz were chosen which is typical for peptide bonds. The values of β, $d^{13}{}_{C-}{}^{14}{}_{N}$ and $J^{13}{}_{C-}{}^{14}{}_{N}$ were not varied, all other values were refined during the simulation. All relevant parameter for the simulation are given in Table S1.

In accordance to the crystallographic data[1] the simulated spectrum (Figure 3, black line) can be described as a superposition of three sub-spectra (Figure 3, coloured lines). Each of the resonances is split due to the influence of the ^{14}N quadrupolar interaction on a dipolar coupled ^{13}C-^{14}N spin pair. For a more detailed description of the theoretical background the reader is referred to Ref. 6.

Table S1 Summary of the parameters used for the simulation of the three sub-spectra; the superscripted numbers in brackets (1-3) represent the three different carbonyl groups.

	$^{*}C{=}O^{(1)}$	**$^{*}C{=}O^{(2)}$**	**$^{*}C{=}O^{(3)}$**
δ_{CS} / ppm	**176.65(1)**	**176.53(1)**	**176.08(1)**
$d^{13}{}_{C-}{}^{14}{}_{N}$ / Hz	**840**	**840**	**840**
$J^{13}{}_{C-}{}^{14}{}_{N}$ / Hz	**11**	**11**	**11**
C_Q / MHz	**-3.18(2)**	**-3.18(2)**	**-3.18(2)**
η	**0.40(2)**	**0.40(2)**	**0.40(2)**
α / °	**51(1)**	**51(1)**	**52(1)**
β / °	**90**	**90**	**90**

To increase the signal-to-noise ratio of the DQ-filtered signal of the *i*-PP/BTA mixture all 1D spectra extracted from the DQ build-up curve (Figure 3, brown line) were summed up.

Evaluation of 2D ^{13}C DQ spectra

For the *i*-PP/additive material a series of 2D ^{13}C DQ spectra with different excitation times were measured and processed using standard procedures within the software package TopSpin™ and further handled using Matlab scripts.[7] Exemplarily, Figure S2 reveals the spectra for τ_{exc} = 6.4 and 20.48 ms representing excitation times below and above the one shown in the main article. The sweep width in the F1 domain - in comparison to the spectrum with τ_{exc} = 15.36 ms - is doubled (83 ppm) due to the halved t_1 increment. This leads to a reduction of the refolding problematic as discussed in the main article. In addition, since the t_1

increment is halved but the numbers of transients in the F1 domain are equal, the spectral resolution is reduced by a factor of two. Still all relevant DQ coherences are resolved. For τ_{exc} = 6.4 ms all signals according to the polymer as well as the autocorrelation signal oft the carbonyl group are observed (in analogy to the spectrum in Figure 1). At higher excitation times the signals including the CH_2-group are missing due to T_2 effects. However, a correlation signal between the carbonyl group of the additive and the polymer matrix could not be observed for any excitation time.

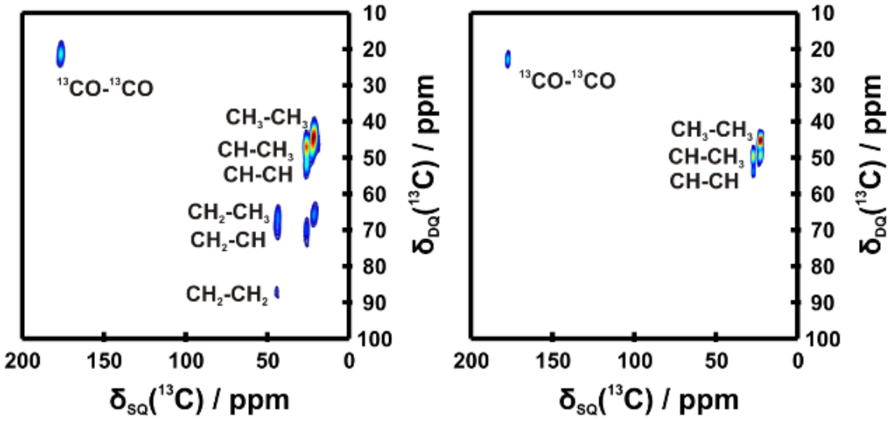

Figure S2 Two dimensional ^{13}C DQ-SQ spectra at excitation times of 6.4 ms (left) and 20.48 ms (right) with assignment of the correlation signals in the spectrum. In comparison to the spectrum with τ_{exc} = 15.36 ms (see Figure 1 in the main article) the spectral width in the indirect domain is doubled to 83 ppm since t_1 was set only one time τ_{rot}. Therefore, only the ^{13}CO-^{13}CO autocorrelation signal was refolded into the spectrum.

For the spectrum with τ_{exc} = 15.36 ms (see Figure 1) four signal groups were refolded into the spectrum. In Table S2 the expected and the observed chemical shifts in the indirect dimension are summarised.

Table S2 Summary of expected and observed signals including assignment in the 2D DQ-SQ ^{13}C spectrum at τ_{exc} = 15.36 ms (see Figure 1); the subscripted figures in brackets represent how many times the correlation signal is refolded into the spectrum.

Correlation	**$\delta_{DQ,exp}$ /**	**$\delta_{DQ,obs}$ / ppm**
CH_3 - CH_3	**45**	**45**
CH_3 - CH	**49**	**49**
CH - CH	**53**	**53**
CH_3 - CH_2	**66.5**	**$25_{(-1)}$**
CH_2 - CH	**70.5**	**$29_{(-1)}$**
CH_2 - CH_2	**88**	**$46.5_{(-1)}$**
^{13}CO - ^{13}CO	**354**	**$22_{(-8)}$**

Data Evaluation of the DQ build-up curve of the *i*-PP/additive system

The DQ build-up curve of the carbonyl group within the composite material was extracted using a self-written Matlab script.[7] For both the double-quantum filtered (DQF) and the reference experiment filtering the zero-quantum intensities (ZQF) of the neat BTA the *C=O signal and the first two sidebands were taken into account for extracting the intensities. For the *i*-PP/BTA mixture only the main signal could be resolved. The ZQF experiment is necessary to normalise the build-up curve and to eliminate relaxation effects. For more information the reader is referred to Ref. 8. The normalised double quantum efficiency is therefore given by

$$DQ_{\mathrm{norm}} = \frac{I_{DQF}}{I_{DQF} + I_{ZQF}} \qquad \text{(S1)}$$

where I_{DQF} and I_{ZQF} are the absolute intensities extracted from the DQF and ZQF experiments, respectively, and the error Δy can be defined through

$$\Delta y = \sqrt{\left(\frac{\partial DQ_{norm}}{\partial I_{DQF}}\right)^2 \cdot \left(\sigma I_{DQF}\right)^2 + \left(\frac{\partial DQ_{norm}}{\partial I_{ZQF}}\right)^2 \cdot \left(\sigma I_{ZQF}\right)^2} \qquad \text{(S2)}$$

where the partial derivative of S1 leads to

$$\Delta y = \sqrt{\left(\frac{I_{ZQF}}{(I_{DQF} + I_{ZQF})^2}\right)^2 \cdot \left(\sigma I_{DQF}\right)^2 + \left(-\frac{I_{DQF}}{(I_{DQF} + I_{ZQF})^2}\right)^2 \cdot \left(\sigma I_{ZQF}\right)^2} \qquad \text{(S3)}$$

For every 1D spectrum of both the DQF and the ZQF experiments the signal-to-noise (S/N) ratio was directly calculated using the TopSpin™ software. The error of the absolute intensity for the experiment with the highest absolute DQ intensity (τ_{exc} = 12.8 ms) was set to 10 %. Based on the different S/N ratios the errors of the intensities - σI_{DQF} and σI_{ZQF} - were calculated separately. In Table S3 the errors Δy for every excitation time are summarised.

Table S3 Summary of the experimental errors Δy for all data points for the experimental DQ build-up curve of the *i*-PP/additive material according to equation S3 and the corresponding signal-to-noise ratios for each 1D experiment.

τ_{exc} / ms	S/N$_{(DQF)}$ / %	S/N$_{(ZQF)}$ / %	$\Delta y \cdot 10^{-2}$
0	---	---	---
2.56	1.84	22.4	4.57
5.12	5.16	18.8	3.12
7.68	6.50	18.5	3.08
10.24	7.63	14.1	3.02
12.80	8.13	7.0	3.70
15.36	8.24	9.0	3.31
17.92	5.56	7.6	4.26
20.48	3.30	14.9	6.27

Validating the existence of supramolecular aggregates in the binary mixture

The DQ build-up of the neat BTA and the BTA/*i*-PP mixture is very similar. Within the experimental error both curves match perfectly. We take this as a strong indication that in both samples the BTA molecules are arranged in similar structural motifs. The characteristic feature of the crystal structure of the neat BTA is the pseudo-hexagonal rod packing of BTA molecules. As demonstrated in ref. 1 by applying a DQ filtered ^{13}C NMR experiment for the BTA molecules which are fully ^{13}C enriched at the carbonyl position we are able to probe the columnar arrangement of the molecules but not the alignment of neighbouring rods. To stress this point we used the concept of the root-sum-squared dipolar coupling (d_{rss}) as introduced by Zorin et al.[9] We calculated d_{rss} for three different models: i) isolated molecules in the case when no self-organization would occur, ii) one infinite molecular strand and iii) the crystal structure taken from ref. 1. For one molecule, the d_{rss} accounts to roughly 36.7 Hz corresponding to a mean distance of about 5.9 Å. For the two models mentioned in ii) and iii), however, both coupling constants converge at values of 127.3 Hz and 128.4 Hz, respectively, corresponding to mean distances of 3.91 and 3.90 Å.

Consequently, in the case of single molecules, the progression of the build-up for the binary mixture would be much slower compared to the one of the neat BTA. The other two scenarios lead to nearly identical build-up curves which cannot be distinguished experimentally. In both

Electronic Supplementary Material (ESI) for Chemical Communications
This journal is © The Royal Society of Chemistry 2013

compounds - the neat BTA and the BTA/*i*-PP mixture - therefore, columnar arranged supramolecular aggregates exist. The d_{rss} values, however, demonstrate that no information about the size of these aggregates can be derived based on the DQ build-up curves.

References

1 M. Schmidt, J. J. Wittmann, R. Kress, D. Schneider, S. Steuernagel, H.-W. Schmidt and J. Senker, *Cryst. Growth Des.*, 2012, **12**, 2543.

2 L. Seyfarth and J. Senker, *Phys. Chem. Chem. Phys.*, 2009, **11**, 3522.

3 M. H. Levitt, *Spin Dynamics: Basics of Nuclear Magnetic Resonance*, Wiley, Chichester, 2nd edn., 2008.

4 I. Marin-Montesinos, D. Brouwer, G. Antonioli, W. Lai, A. Brinkmann and M. Levitt, *J. Magn. Reson.*, 2005, **177**, 307.

5 K. Eichele, *WSolids1 ver. 1.20.17*, Universität Tübingen, 2012.

6 K. Eichele, M. D. Lumdsen and R. E. Wasylishen, *J. Phys. Chem.*, 1993, **97**, 8909.

7 *The language of technical computing. MATLAB; Math Works Inc., 24 Prime Park Way, Natick, MA 01760-1500*, Copyright 1984 - 2012.

8 K. Saalwächter, P. Ziegler, O. Spyckerelle, B. Haidar, A. Vidal, J.-U. Sommer, *J. Chem. Phys.*, 2003, **119**, 3468.

9 V. E. Zorin, S. P. Brown and P. Hodgkinson, *Mol. Phys.*, 2006, **104**, 293.

6.3 Strukturaufklärung eines ^{19}F-substituierten 1,3,5-Benzoltrisamids

Christoph S. Zehe,&[a] Marko Schmidt,&[a] Renée Siegel,[a] Sandra Ganzleben,[b] Hans-Werner Schmidt[b] and Jürgen Senker*[a]

Crystal Structure Determination of a Symmetrically Substituted Fluorine Containing BTA with NMR-crystallographic Strategies

to be submitted

[a] Lehrstuhl für Anorganische Chemie III, Universität Bayreuth, 95447 Bayreuth, Deutschland

[b] Lehrstuhl für Makromolekulare Chemie I, Universität Bayreuth, 95447 Bayreuth, Deutschland

* juergen.senker@uni-bayreuth.de

& Gleicher Beitrag zu je 50 %

Darstellung des Eigenanteils:

Das Konzept für dieses Manuskript wurde von Prof. Dr. *Jürgen Senker* und mir erarbeitet, zusätzlich löste ich die Kristallstruktur aus Pulverdaten. Die ^{19}F-substituierte Verbindung wurde von *Sandra Ganzleben* synthetisiert. Sämtliche FK-NMR-Experimente wurden von *Christoph S. Zehe* unter Beratung von Dr. *Renée Siegel* durchgeführt, weiterhin war er für die Simulationen der DQ-Aufbaukurven verantwortlich. Verfasst wurde das Manuskript von Prof. Dr. *Jürgen Senker*, *Christoph S. Zehe* und mir. Zu dieser Publikation haben *Christoph S. Zehe* und ich mit einem Anteil von je 50 % beigetragen.

6.3.1 Crystal Structure Determination of a Symmetrically Substituted Fluorine Containing BTA Using NMR-crystallographic Strategies

Crystal Structure Determination of a Symmetrically Substituted Fluorine Containing BTA Using NMR-crystallographic Strategies†

Christoph Zehe,[a] Marko Schmidt,[a] Renée Siegel,[a] Venita Daebel,[c] Sandra Ganzleben,[b] Hans-Werner Schmidt,[b] and Jürgen Senker*[a]

[a] Inorganic Chemistry III and Bayreuth Center for Colloids and Interfaces
University of Bayreuth, 95447, Bayreuth, Germany
Fax: (+49) 921-55-2788
E-mail: juergen.senker@uni-bayreuth.de

[b] Macromolecular Chemistry I, Bayreuth Institute of Macromolecular Research and Bayreuth Center for Colloids and Interfaces
University of Bayreuth, 95447, Bayreuth, Germany
Fax: (+49) 921-55-3206
E-mail: hans-werner.schmidt@uni-bayreuth.de

[c] Dr. V. Daebel
Bruker Biospin GmbH
Silberstreifen 4, 76287 Rheinstetten, Germany
E-mail: venita.daebel@bruker-biospin.de

Abstract

Combining synthesis, powder X-ray diffraction, 1D and 2D multinuclear solid-state NMR spectroscopy as well as computational calculations, we were able to determine the crystal structure of 1,3,5-tris(2-fluoro-2-methylpropionylamino)benzene **1**, a fluorine containing symmetric substituted 1,3,5-benzenetrisamide. Based on a quantitative evaluation of the resonances within the 1D solid-state NMR spectra (^{1}H, ^{13}C, ^{15}N, ^{19}F), the content of the asymmetric unit was determined to contain two independent molecules. Moreover, the ^{1}H spectrum confirmed the existence of hydrogen bonds, but the number of resonances for the aromatic protons also revealed a tilt of the aromatic rings against each other within the structure. The structure solution from powder data was carried out applying real space methods with an included close-contact penalty. The following Rietveld refinement led to a very good wRp-value of 5.3%. ^{19}F^{19}F double quantum (DQ) build-up curves were measured using a symmetry based dipolar recoupling sequence. The simulations of the build-up curves for each single ^{19}F resonance within a nine spin system fitted the experimental ones very well. Compound **1** crystallizes in the monoclinic space group $P2_1$ (a = 11.886(4) Å, b = 15.394(5) Å, c = 10.553(4) Å, β = 95.011(2) °). Both independent molecules only possess an intrinsic C_1

symmetry with weak intramolecular NH---F contacts. Additionally, these molecules are connected non-covalently by NH---OC hydrogen bonds along two crystallographic axes. Since along the third axis only van-der-Waals interactions are dominant, the growth can be described as two-dimensional where the layers grow fast parallel to the bc-plane, while in general the molecules reveal a zig-zag like packing.

Introduction

The field of supramolecular chemistry with its increasing number of complex one- and two-dimensional structures has become more and more attractive in many scientific fields. The targeted synthesis and design of molecules where non-covalent interactions - like hydrogen bonding, aromatic π-π stacking, CH-π interactions, electrostatic or hydrophobic interactions, or electrostatic interactions between the constituting parts[1] - play a major role, show well-ordered superstructures that possess tuneable properties. However, to synthetically access these supramolecular building units, it is highly important to keep in mind that even slight changes in the molecular structure might strongly affect the self-assembly properties.

During the last few years the class of benzene-1,3,5-tricarboxamides (BTAs) has evolved to an attractive supramolecular motif usually forming one-dimensional nanostructures via self-assembly[2-7] and getting more and more important in many fields of research.[8] Their supramolecular behaviour together with their comparatively facile accessibility renders BTAs into a versatile class of advanced materials with potential to be used as organogelators,[9-11] hydrogelators,[12,13] liquid crystals,[14] MRI contrast reagents,[15] and metal complexation reagents.[16] Furthermore, some derivatives of this substance class are known to be very efficient as electret additives[17-19] or as clarifying agents for i-PP.[20] In addition, the benefit of BTAs as nucleating agents in semi-crystalline polymers, e.g. isotactic polypropylene (i-PP),[20-22] polybutylene terephthalate,[23] poly-(ethylene-co-propylene),[24] polyvinylidene fluoride[22] or polylactides,[25-27] was recently demonstrated.

One of the most difficult aspects concerning the nucleation of polymers is the development of a fundamental understanding of the complex self-assembly processes of the additive molecules in the polymer melt. This is experimentally still challenging due to both the small size of the nuclei in the polymer and the low concentration of the additive and routinely applied analytical methods, for example X-ray diffraction, are inappropriate so that alternative methods of characterization are required. Here, solid-state NMR represents an auspicious technique gathering structural information within the polymer since it addresses local environments. For an efficient BTA-based nucleating and clarifying agent for i-PP (^{13}C enriched at all three carbonyl groups), for example, it could recently be demonstrated by means of ^{13}C double quantum solid-state NMR that the structural features of the nuclei in the polymer matrix and in the neat additive material are similar.[28,29] Due to a lack of detectable connections between the additive clusters and the i-PP, however, a statement concerning the linkage of the polymer could not be done within this special polymer/additive system.

To increase the possibility to detect such contacts, a new kind of BTA-based molecular building unit was chosen. Here, a fluorine atom as NMR-active marker was introduced in the outer sphere of the molecule by adjusting the moieties in each side chain. In case of a similar one-dimensional growth mechanism as observed for the BTA investigated in ref. 28, the resulting distances between polymer and additive would be decreased and the chance of detecting any correlations is significantly higher. In this article, we focus on the ab initio structure solution as well as the crystal packing of compound **1** (see Scheme 1). Since only microcrystalline powder samples are accessible which prevent us from performing single crystal X-ray diffraction experiments, we use NMR-crystallographic strategies to gain important structural information. The approach of complementing powder diffraction data with solid-state NMR experiments at different steps of the structure elucidation[30-33] is thereby an efficient way to prove or disprove structure models.

(1)

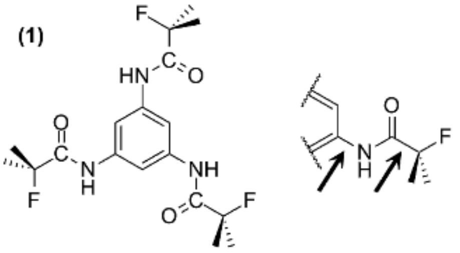

Scheme 1. Molecular structure of 1,3,5-tris(2-fluoro-2-methylpropionylamino)benzene **1** (left) with section of compound **1** highlighting the main motional degrees of freedom (right); the black arrows assign the structure directing torsion angles $C_{Ar}C_{Ar}N_HC_O$ and $N_HC_OC_QF$.

Experimental Details

Synthesis and Characterization of 1: All solvents were purified and dried using standard procedures. ^{1}H- and ^{19}F solution-state NMR spectra were recorded on a Bruker Avance 300 spectrometer at room temperature and referenced on TMS and $CFCl_3$, respectively. Mass spectra were recorded on a VARIAN MAT 8500 instrument using direct probe inlet and electron impact ionization. 2-fluoroisobutyric acid (97%) was purchased from ABCR and used without further purification. 1,3,5-triaminobenzene was freshly synthesized from 3,5-dinitroaniline (obtained from Aldrich, used as received) as described elsewhere.[28]

2-fluoroisobutyric acid chloride was synthesized from 2-fluoroisobutyric acid and oxalyl chloride. 2g (18.8 mmol) of 2-fluoroisobutyric acid was solved in 30 mL CH_2Cl_2 (DCM). The mixture was cooled down to 0 °C, 4.78 g (37.7 mmol) oxalyl chloride and three drops of DMF was added slowly under argon atmosphere and refluxed over night. After cooling to room temperature, an excess of potassium stearate was added drop wise (to react excess oxalyl chloride) till no further gas evolution was observed. The 2-fluoroisobutyric acid chloride was then distilled under normal pressure. All resonances in the ^{1}H NMR could be unequivocally assigned to the solvents and the product. For the ^{19}F NMR additionally hexafluorobenzene was added as internal standard (δ = -162.12 ppm). Yield: 1.9 g (15.3 mmol, 81.4 %); ^{1}H-NMR (300 MHz, $CDCl_3$): δ = 1.65 ppm (d, $^3J(^1H,^{19}F)$ = 20.7 Hz, 6H, -CH_3); ^{19}F-NMR (300 MHz, $CDCl_3$): δ = -76.4 ppm (s, 1F, -R_2C_qF).

Compound **1** was synthesized by dropping 2-fluoroisobutyric acid chloride (1.07 g, 8.59 mmol in DCM) to a mixture of 1,3,5-triaminobenzene (0.32 g, 2.6 mmol), pyridine (15 mL) and LiCl (0.05 g) in 50 mL THF at 0 °C under argon atmosphere. The reaction was stirred over two days at 70 °C, cooled down to RT and the solvents were evaporated under vacuum. The residual reaction mixture was precipitated into an excess of water, the precipitate was filtered off, dried under reduced pressure and recrystallised from methanol. To remove further impurities, the solid was refluxed in 50 mL n-hexane for three hours, filtered off hot and dried again. Yield: 0.096 g (0.77 mmol, 9 %). ^{1}H-NMR (300 MHz, $CDCl_3$): δ = 1.62 ppm (d, $^3J(^1H,^{19}F)$ = 22.4 Hz, 6H, -CH_3); 7.77 ppm (s, 3H, Ar-H); 8.15 ppm (d, $^4J(^1H,^{19}F)$ = 8.7 Hz, 3H, -NH); ^{19}F-NMR (300 MHz, $CDCl_3$): δ = -145.58 ppm (m, $^3J(^{19}F,^1H)$ = 22.4 Hz, $^4J(^{19}F,^1H)$ = 8.7 Hz, 1F, -R_2C_qF); MS (70eV), m/z (%): 387 (M+, 100); 344 (22); 326 (47); 299 (17); 69 (8); 61 (31).

Solid-State NMR experiments: ^{1}H and ^{13}C chemical shifts are referenced on TMS, ^{19}F chemical shifts are referenced on NaF and ^{15}N chemical shifts are reported with respect to nitromethane, where all values are shifted by -380.5 ppm compared to liquid NH_3. All ^{13}C and ^{15}N experiments were performed in a 4 mm triple resonance probe at a Bruker Avance II spectrometer with at a field strength of $B_0 = 7.1$ T, where the spin rate for MAS was set to $\nu_{rot} = 12500 \pm 1$ Hz. All ^{1}H and ^{19}F experiments were performed in a 1.3 mm double resonance probe at a Bruker Avance III spectrometer with at a field strength of $B_0 = 14.1$ T, where the spin rate for MAS was set to $\nu_{rot} = 60000 \pm 3$ Hz for ^{19}F and to $\nu_{rot} = 65000 \pm 3$ Hz for ^{1}H, respectively.

The ^{13}C and ^{15}N CP spectra were recorded using a ramp on the ^{1}H/^{19}F channel and a contact time of 3 ms with nutation frequencies of 70/30 kHz for ^{13}C/^{15}N. Proton broadband decoupling was realized with a SPINAL64 sequence during acquisition where the nutation frequency and pulse length were set to 65 kHz and 7 µs, respectively. For ^{19}F decoupling a XiX sequence[34] with a pulse length of 7 µs and a nutation frequency of 70 kHz was used. The ^{1}H direct excitation experiments were performed using a nutation frequency of $\nu_{nut} = 179$ kHz for the 90° pulse.

For the ^{19}F^{19}F double quantum experiments, a symmetric double quantum recoupling protocol was used. Excitation and reconversion was achieved through the $SR14_4^5$ with 90°-270° composite pulses as R-elements and an according nutation frequency of $\nu_{nut} = 210$ kHz. For the ^{19}F direct excitation experiments the nutation frequency of the 90° pulse was set to $\nu_{nut} = 150$ kHz.

Solid-State NMR simulations: Simulations of the ^{19}F^{19}F DQ build-up curves were performed with the simulation software SIMPSON.[35] Relative orientations and principal values of the ^{19}F^{19}F dipole tensors were calculated based on the PXRD structure solution. The asymmetry and anisotropy parameters for the chemical shift anisotropy where estimated from a slow-MAS 1D experiment. The corresponding Euler angles where set to zero for all spins since they seem to show only negligible influences on the build-up curves. For powder averaging the crystal file zcw232 containing 232 orientations was used in combination with 40 γ-angles. Due to the high spinning speed proton influences were assumed to only dampen the normalized build-up curves. Therefore, they were neglected for simulations and the resulting build-up curves were fitted to the normalized experimental data by applying a constant scaling factor for all curves. The optimum scaling factor was found by minimizing the quadratic sum of deviations between experimental and simulated data for all curves simultaneously with the software package MATLAB.[36]

Ab initio structure determination using PXRD: PXRD measurements on compound **1** were carried out in Debye-Scherrer geometry on a STOE StadiP diffractometer being equipped with CuKα_1 radiation (λ = 1.5406 Å) and a curved germanium monochromator (oriented according to the 111 plane). The sample was filled in a capillary tube with a diameter of 0.7 mm and measured in the 2Θ range of 2° - 50° with a step size of 0.015° each. The powder pattern was fully handled using REFLEX PLUS from the commercial program package Accelrys MS Modeling (version 5.0).[37] After indexing, Pawley refinement and space group assignment, the structure solution step was performed by means of real space methods using the simulated annealing algorithm.[38,39] For the structure solution the molecule was first geometry optimised using DFT methods (see section Computational Methods). As starting model two independent molecules were set into the asymmetric unit as one motion group each. Besides the possible rotational and translational degrees of freedom, the most structure directing torsion angles in each molecule were set free during the structure solution (see Scheme 1, right side). Additionally, the March-Dollase equation for a preferred orientation was applied during the solution with focus on the shape of the crystallites (R_0) as well as the orientation of the normal of the crystal faces (a*, b*, c*).[40]

Concerning the Rietveld refinement, at first four cycles including a relaxation of atomic parameters, a global isotropic temperature factor for all atoms and a preferred orientation correction according to the March-Dollase equation[40] were carried out. By taking into account additional energy considerations using the COMPASS forcefield[41] the molecular structure was allowed to maintain without limiting rotational and translational degrees of freedom. However, the final number of refined structural parameters (see Table 1) is not strictly representative due to the applied energy constraint during the refinement. This force field assisted refinement is based on a combined figure of merit (R_{comb}) with

$$R_{comb} = (1 - w_{comb}) * wRp + w_{comb} * R_{Energy} \qquad (1)$$

where w_{comb} represents a energy weighting factor that was set to 0.5. The energetic contribution, R_{Energy}, to the combined figure of merit is defined as follows:

$$R_{Energy} = \tanh(0.1 * \frac{E - E_{min}}{E_{tol}}) \qquad (2)$$

where E represents the total energy, E_{min} the energy in the global minimum and E_{tol} the energy window above E_{min} in which possible structure solutions are tolerated. Here, the default value of 40 kcal/mol was used prohibiting the breaking of covalent bonds during the refinement step reducing the real number of refined structural parameters markedly.

Afterwards, the peak profile including FWHM (pseudo-voigt) with its profile parameters NA and NB were optimized. The pseudo-Voigt peak shape function as a linear combination of a Lorentzian (L) and a Gaussian (G) includes a Θ-dependent mixing parameter η whose Θ-dependence is thus given by

$$\eta(\Theta) = (NA + NB) * 2\Theta \qquad (3)$$

where NA and NB are adjustable parameters. Besides, the lattice parameters, the zero-point shift, sample off-centering, asymmetry correction (Finger-Cox-Jephcoat)[42] and the experimental background using 20 orthogonal polynomials were refined. For both refinement steps, 15 evaluations per cycle per degree of freedom were performed. Relevant crystallographic data are summarized in Table 1. Atomic parameters, the temperature factor and the occupancy of compound **1** are included in the crystallographic information file being available in the electronic supporting information.

Table 1. Relevant crystallographic data for **1** from PRXD

	1
Formula	$C_{18}H_{24}F_3N_3O_3$
M / g * mol^{-1}	387.38
Crystal system	Monoclinic
Space group	$P2_1$
a / Å	11.886(4)
b / Å	15.394(5)
c / Å	10.553(4)
α / °	90
β / °	95.011(2)
γ / °	90
V / Å^3	1923(2)
Z'	2
Z	4
ρ / g * cm^{-3}	1.337
T / K	293
U	0.24(1)
V	-0.033(3)

W	0.0024(2)
zero-point shift	0.0061(9)
R_0(‡)	0.845(3)
a*	0.184(14)
b*	0.911(3)
c*	0.366(6)
Rp	0.0387
wRp	0.0532

(‡) Preferred orientation coefficient of the sample according to the March-Dollase function representing a dimensionless value reflecting the shape of the crystallites; R0 < 1 for platelets, R0 > 1 for needles.

Computational Methods: Before the ab initio structure solution of compound **1**, the molecule was geometry optimised by DFT methods using the module DMol3 from the program package Accelrys MS Modeling (version 5.0).[37] Here, the double zeta plus polarisation basis set with the GGA functional PW91 was applied.[43] The self-consistent field (SCF) energy convergence was set to 1.0e-6 eV per atom.

Results and Discussion

Symmetry considerations using solid-state NMR: Ab initio structure solutions employing solely PXRD data are often hampered by a severe loss of information. On the one hand symmetry equivalent reflexes always coincide and on the other hand higher order reflexes overlap heavily.[44] While topological information might still be obtained with reasonable accuracy, local structural details are strongly affected.[31,44] Here, solid-state NMR is able to participate in nearly all steps of the structure solution process starting from space group selection, over model building up to the final Rietveld refinement.[28,44-47] Symmetry information including the content of the asymmetric unit might be obtained by deriving Wyckoff spectra[45,48] from high-resolution experiments and by determining rotational symmetry elements[44,49,50] based on orientation correlations of CSA tensors of neighbouring nuclei. Analysing hetero- and homonuclear connectivities, distances, distance sums and even torsion angles measured by 1D and 2D dipolar recoupling experiments support the construction and allow a verification of structure models.[28,29,31-33,46,47] In certain circumstances even complete structure solutions are possible using DQ dipolar recoupling experiments.[51,52]

Here, we deduce the content of the asymmetric unit from high-resolution 1D MAS of ^{19}F, ^{13}C and ^{15}N and preselect appropriate space groups for an ab initio PXRD structure solution. The derived structure model will be probed with symmetry based DQ recoupling experiments and simulations.

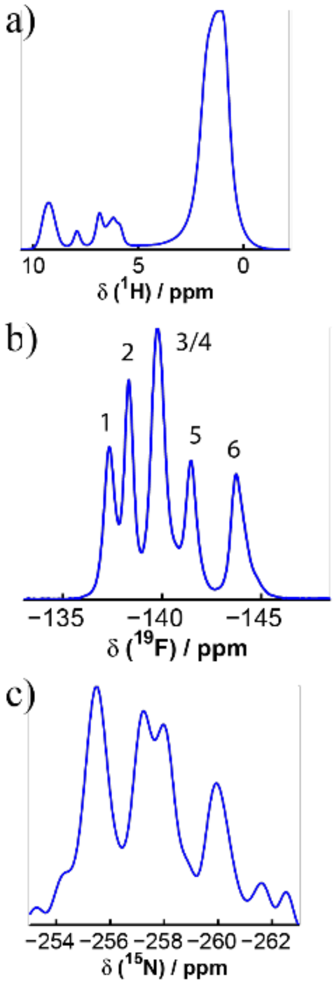

Figure 1. Solid-state NMR spectra of compound **1**. Direct excitation measurements of a) ^{1}H and b) ^{19}F; c) ^{1}H-^{15}N CP MAS.

Figure 1 depicts 1D high resolution MAS experiments of ^{1}H, ^{19}F, and ^{15}N. The ^{1}H spectrum (Figure 1a) shows one signal around $\delta = 9$ ppm being characteristic for NH protons participating in hydrogen bonds. The signal group between $\delta = 9\ 5$ and $\delta = 8.5$ ppm is split in at least four distinct resonances and the chemical shift is characteristic for aromatic CH groups. The remaining aliphatic protons give rise to the broad signal group below δ = 4 ppm. The ^{19}F spectrum (Figure 1b) shows five separated signals. While the signals 1, 2, 5 and 6 have approximately the same intensity, the central peak 3/4 appears to be more intense. High resolution 2D DQ-SQ correlation experiments (see ESI Figure S1) show that this signal consists of two coinciding peaks. Moreover, signal 6 at δ = -144 ppm shows a slight asymmetry on the right flank. As will be shown in a forthcoming paper, this can unequivocally be assigned to a second polymorph with chemical shifts below δ = -144 ppm. Since the signal arising from that is apparently small, it will be ignored in the following part. Therefore, six distinct ^{19}F signals are present. Finally, in the ^{1}H-^{15}N CP spectrum (Figure 1c) one signal group around δ = -258 ppm is observed with at least four distinct signals which belongs to the amide units.

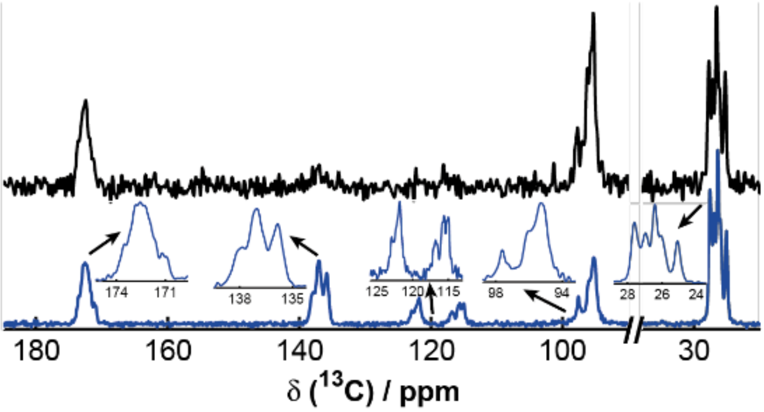

Figure 2. ^{1}H-^{13}C CP MAS spectrum (bottom, blue) with close-ups and ^{19}F-^{13}C CP MAS spectrum (top, black) of compound **1**.

In order to assign the carbon atoms, ^{1}H-^{13}C and ^{19}F-^{13}C CP experiments are used (Figure 2). Due to the high abundance of protons, all carbon signals appear in the first experiment, whereas in the latter only carbon atoms in spatial proximity to the ^{19}F labels appear. First, the signal at δ = 172 ppm is characteristic for carbonyl groups and the signals around δ = 25 ppm for methyl groups. Since the group around δ = 96 ppm has the highest intensity in the ^{19}F-^{13}C CP, it must belong to the quaternary carbon which is directly bound to the ^{19}F atoms. Therefore, the three remaining signals being almost invisible in the ^{19}F-^{13}C CP spectrum belong to the aromatic carbon atoms since they have the highest distance to the fluorine labels. The group at δ = 137 ppm has a typical shift for quaternary aromatic carbon atoms and hence the two signal groups at δ = 122 ppm and δ = 115 ppm belong to the aromatic CH units. Again, all signal groups show a splitting with up to five visibly distinguishable signals.

Since the ^{19}F spectrum (Figure 1b) shows six distinct signals, which is twice the number as expected from the molecular structure, we conclude that the asymmetric unit contains six independent ^{19}F atoms and, therefore, two molecules. This is in good agreement with the CH signals of the ^{1}H spectrum (Figure 1a) and all ^{15}N and ^{13}C signals (Figures 1c and 2), since also a splitting is observed. This reduces the number of possible space groups, which will be discussed at a later point. Moreover, as mentioned above, the ^{1}H shift of the NH group is indicative for moderate hydrogen bonds.[28,53] This is a well-known structural motif for BTAs[4,28] and should therefore be reproduced from the PXRD structure solution, which is another boundary for possible structure models. The number of resonances for the aromatic protons in the ^{1}H spectrum is also strong evidence for the orientation of the benzene rings within the structure. Even in the case of two molecules within the asymmetric unit, an imaginable coplanarity of the aromatic cores would lead to maximum two different signals in the proton spectrum since the local environment were hardly distinguishable. This fact also would accompany with an intrinsic molecular (pseudo) C_3-symmetry. Since we observed at least 5 distinct signals for the aromatic protons we clearly can exclude a coplanar arrangement of the molecules. This is in very good agreement with the splitting of the signals within the 1D ^{13}C spectrum (Figure 1c) and former solid-state NMR investigations on comparable BTAs by Wegner and co-workers,[6] respectively.

Crystal structure solution of 1,3,5-tris(2-fluoro-2-methylpropionylamino)benzene from PXRD: With these preliminaries, a structure model of compound **1** was developed by PXRD. Indexing of the powder pattern leads unequivocally to a monoclinic metric and could subsequently be refined in P2 using the Pawley algorithm.[54] Assuming that all non-hydrogen atoms within this compound (C,F,N,O) possesses a volume of approximately 18 Å^3, the molecular volume can be estimated to roughly 490 Å^3. This size restriction allows maximum four molecules within the unit cell only. Taking into account the reflection conditions for all 13 possible monoclinic space groups, however, just five primitive ones remained (P2, $P2_1$, Pm, P2/m, $P2_1/m$). Here, for all space groups containing a glide plane (Pc, P2/c, $P2_1/c$) the corresponding reflection conditions h0l : l = 2n and 00l : l = 2n, respectively, are not fulfilled. Analogous results were obtained for all C-centered space groups. Since the molecule itself does not possess a mirror plane or an intrinsic C_2 symmetry, a location on special positions within the unit cell is excluded. Additionally, as we know from 1D solid-state NMR experiments (see Figures 1 and 2), there must be two independent molecules within the asymmetric unit. Therefore, the space groups P2/m and $P2_1$/m are inappropriate since this would lead to overall 8 molecules at general positions in the unit cell. A more detailed view at the experimental powder pattern reveals that only even reflections of the 0k0 series are existent and all odd ones are absent. In fact, this can only be fulfilled within the space group $P2_1$ since in P2 or Pm, respectively, all 0k0-reflections are possible.

Within the space group $P2_1$ an ab initio structure solution with real space methods was performed whereupon a combination of a close-contact penalty and wRp as cost functions was used. The DFT geometry optimized molecule was set twice in the unit cell and treated independently as rigid body with the rotational and translational degrees of freedom during the solution step. Additionally, the most important and structure directing torsion angles (two in each side chain, see Scheme 1, right side) were varied during the solution step.

The wRp value after the solution accounted for 14.66 %, a full Rietveld refinement finally led to a wRp value of only 5.3 % (see lattice parameters in Table 1). The Rietveld profile is depicted in Figure 3.

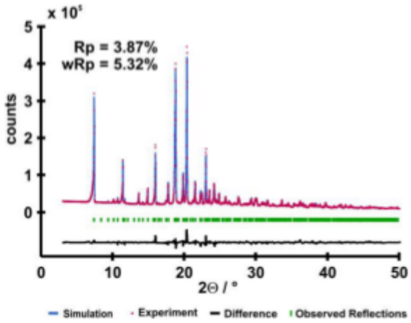

Figure 3. Rietveld profile plot of the powder X-ray diffraction pattern in space group $P2_1$ collected at room temperature in a 2Θ range of 2° - 50°.

1,3,5-tris(2-fluoro-2-methylpropionylamino)benzene thus crystallizes in the monoclinic non-centrosymmetric space group $P2_1$ (a = 11.886(4) Å, b = 15.394(5) Å, c = 10.553(4) Å, β = 95.011(2) °) containing four molecules in the unit cell, arising from two independent molecules in the asymmetric unit. Despite of the presence of only light atoms (C,H,F,N,O) leading to weak scattering, the final wRp of 5.3 % represents an excellent value for an ab initio structure solution picturing, however, the good crystallinity of the sample. The molecular structures of the two independent molecules (**1a** and **1b**) after the Rietveld refinement are depicted in Figure 4.

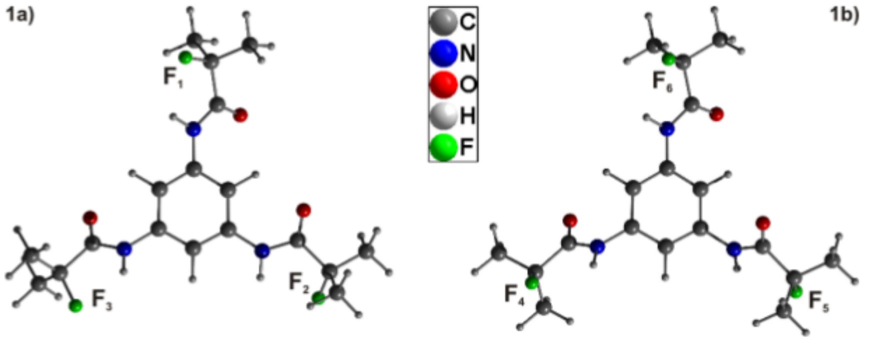

Figure 4. Molecular structures of the two independent molecules of 1,3,5-tris(2-fluoro-2-methylpropionylamino)benzene as derived from the PXRD experiment with labeling of the fluorine atoms.

The $C_{Ar}C_{Ar}N_HC_O$ torsion angles (see Scheme 1, right) as possibly crucial motif for the formation of the crystal structure show a broad distribution. The corresponding values are 40.11°, 26.31° and 47.44° for the first molecule, and 36.42°, 56.55° and 57.09° for the second one, respectively. Surprisingly, for both molecules only two out of three oxygen atoms of the carbonyl groups point in one direction compared to the planar aromatic core. These significant aspects clearly show the reduction of an intuitively expected C_3 or pseudo-C_3 symmetry to just C_1 symmetry. These results are also verified by ^{13}C solid-state NMR where the aromatic CH carbon signals are split into two groups at $\delta = 117$ ppm and $\delta = 123$ ppm. The HNCO torsion angles representing the amide bonds are in good agreement with an expected value of roughly 180° since it behaves as partial double bond. For **1a** the values account for 173.15°, 174.5° and 177.09°, **1b** possess torsion angles of 176.48°, 177.04° and 176.71°.

Another structure directing factor is presented by the $N_HC_OC_qF$ torsion angle. For the first molecule values of roughly 6.9°, 17.6° and 25° are observed while in case of the second one the range shows a closer distribution with values between 26.2° and 31.8°. A similar trend is obtained by comparing the molecular fluorine environments where the NH---F contacts play the important role. For **1a**, the intramolecular NH---F distances are shorter in contrast to **1b** while the corresponding NH---F angles are bigger. These values as well as other important molecular distances and angles are listed in Table 2.

Table 2. Molecular distances in angstrom and angles in degree derived from the powder X-ray diffraction experiment.

	Molecule 1	**Molecule 2**
d(C = O)	1.214	1.211 - 1.213
d(C_{Ar} - N)	1.390 - 1.396	1.397 - 1.398
d(C_O - N)	1.368 - 1.369	1.368 - 1.373
d(C_{Ar} - C_{Ar})	1.381 - 1.387	1.382 - 1.386
d(C_q - C_{Me})	1.525 - 1.529	1.526 - 1.533
d(C - F)	1.390	1.388 - 1.391
d(C - H)	1.094 - 1.100	1.096 - 1.100
d(N - H)	1.011 - 1.012	1.011
d(NH---F)	2.121 - 2.171	2.239 - 2.268
∡(NH---F)	107.0 - 109.2	103.9 - 105.9
∡(HNCO)	173.2 - 177.1	176.5 - 177.0
∡($C_{Ar}C_{Ar}N_HC_O$)	26.3 - 47.44	36.4 - 57.1
∡($N_HC_OC_qF$)	6.86 - 25.04	26.15 - 31.81
∡(OC_OC_qF)	156.0 - 175.1	150.7 - 158.4

From that point of view these proton-fluorine contacts may be described as weak intramolecular hydrogen bonds. Here, this neighbored NH-function seems acting as kind of trap for the fluorine atom strongly constricting the motion of the whole side group. These six different fluorine environments are thereby in perfect agreement with the results obtained by 1D ^{19}F solid-state NMR.

Recently, a crystal structure of very similar 1,3,5-benzentrisamide was elucidated in our group by means of NMR-crystallographic strategies.[28] The only difference is the substitution of the fluorine atom against a third methyl group. Interestingly, all oxygen atoms of the carbonyl groups within one molecule point in the same direction with respect to the aromatic ring system. The corresponding $C_{Ar}C_{Ar}N_HC_O$ torsion angles are quite similar (31.36°, 31.46° and 34.56°) breaking slightly the perfect regularity but, nevertheless, remains a pseudo-C_3 symmetry and, additionally, all three HNCO amide torsion angles show similar values around 180°, too.

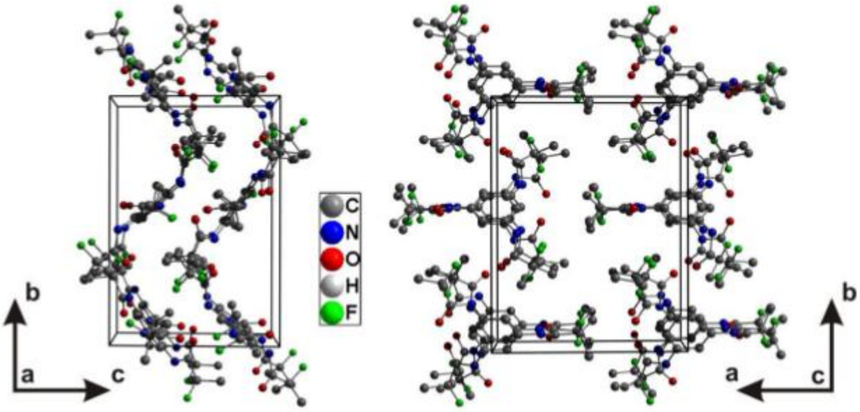

Figure 5. Section of the crystal structure of 1,3,5-tris(2-fluoro-2-methylpropionyl-amino)-benzene. Left: view along the a-axis where the zigzag motif due to the 2_1 screw axis develops along the monoclinic axis perpendicular to the ac-plane; the unit cell contains four molecules arising from two independent molecules in the asymmetric unit. Right: perspective view along the c-axis of a unit cell. All protons were omitted for clarity.

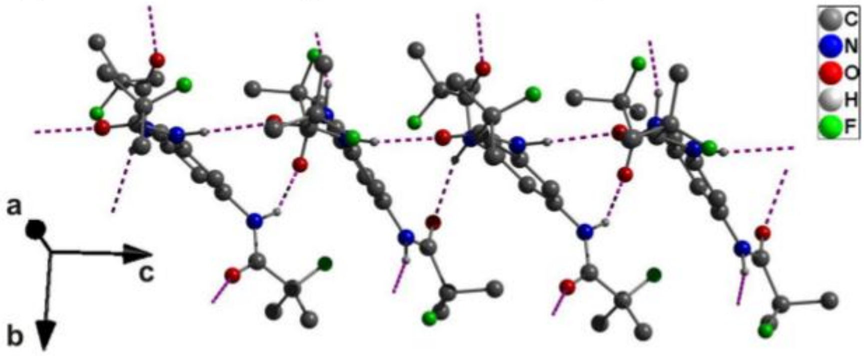

Figure 6. NH---OC hydrogen bond architecture in the crystal structure of compound **1**. Every NH- and CO-group of each molecule is involved in a two-dimensional H-bond pattern along the b- and c-axis of the crystal (dashed pink lines). All protons except the ones connected to the nitrogen atoms were omitted for clarity.

The crystal structure of **1** can be described as a chain-like zigzag motif built by the molecules due to the 2_1 screw axis along the b-axis of the unit cell (see Figure 5, left side). Additionally, the two independent molecules are stacked in a row along the crystals' c-axis (see Figure 5, right side). Here, the distances between the aromatic cores amount to 5.15 Å up to 5.64 Å which is far too long to be identified as π-π-interactions. Moreover, the intermolecular plane angle of the benzene rings accounts for roughly 15.6° which presents a huge discrepancy concerning coplanarity. Both the interaromatic distance as well as the tilt angle between the rings is thereby in good agreement with the results obtained by ^{1}H and ^{13}C solid-state NMR spectroscopy. The driving force of the formation of this structure is an extensive 2D hydrogen bond network between all amide protons and oxygen atoms of neighbored molecules (see Figure 6). These hydrogen bonds, however, are both built along the b-axis with four different NH---O distances between 1.88 Å and 2.19 Å as well as along the crystals' c-axis with 2.09 Å and 2.25 Å. The corresponding NH---O angles show a quite broad distribution with values between 146.2° and 164.2°, respectively. Along the a-axis of the crystal a non-covalent interaction is not observed. Here, only van-der-Waals interactions play the major role with shortest proton-proton distances of roughly 2.20 Å.

In comparison, the compound presented in ref. 28 crystallizes in an orthorhombic non-centrosymmetric structure where the molecules build long columnar strands forming a pseudo-hexagonal rod packing. Due to the pseudo-C_3 symmetry and the 2_1 screw axis the molecules within one column are arranged in helices with a twist of 60°. The structure is thereby characterized by an extensive NH---O hydrogen bond network within the columns but, however, with a more narrow length distribution between 2.04 and 2.14 Å. Additionally, in wide contrast to compound **1** presented here, sandwich-like π-π contacts between the aromatic rings picture the second structure directing interaction where the distances between two benzene rings amount to roughly 3.4 Å which in this case is in good agreement to typical distances in π-stacked discotic liquid crystals.[55] Moreover, the rod-like arrangement leads to macrodipoles[56-59] along the columns which are cancelled by an antiferroelectric arrangement of the strands, facilitating a fast growth along the column axis.

Verification of the structure model by DQ solid state NMR: The structure model obtained from the combination of 1D solid-state NMR experiments and PXRD data was probed using quantitative symmetry-based DQ dipolar recoupling experiments. Hereby the $^{19}F^{19}F$ homonuclear dipolar interaction was selectively recoupled by applying a $SR14_4^5$ sequence leading to an excitation of $^{19}F^{19}F$ double quantum coherences. Since the dipolar interaction constant depends inversely on the third power of the internuclear distance, the recoupling efficiency encodes the structural environment of each spin. The experimental $^{19}F^{19}F$ DQ build-up curves are depicted in Figure 7a.

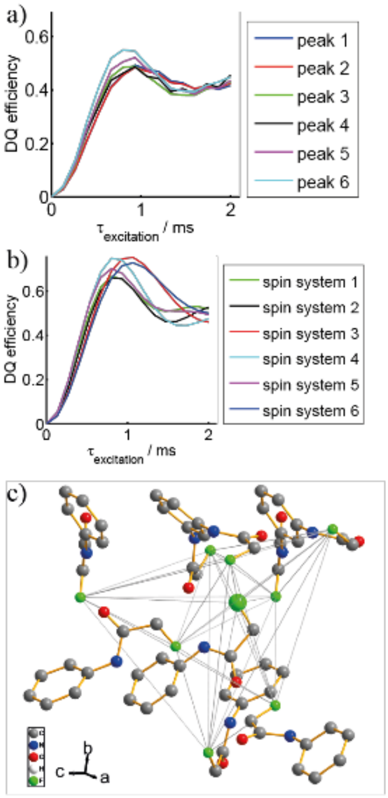

Figure 7. a) Experimental $^{19}F^{19}F$ DQ build-up curves using the $SR14_4^5$ sequence with a symmetric protocol (see Figure 1b for assignment of the peaks). b) Simulations for a nine spin systems. The number of the spin systems are correlated to the number of the observed ^{19}F spins in the asymmetric unit (compare Figure 4). c) Spin system No. 2 with grey lines indicating the ^{19}F-^{19}F couplings. The observed ^{19}F atom is emphasized through a big symbol, and nine ^{19}F were taken into account forming a sphere of 7 Å around the central atom. All hydrogen atoms, CH_3 groups and side chains without participating ^{19}F atoms are omitted for clarity.

For all curves the first maximum and minimum is visible. For signal 1and 2 (see Figure 1b) the maximum is reached around $\tau_{excitation}$ = 1 ms, for all remaining signals around $\tau_{excitation}$ = 0.8 ms. The maximum DQ efficiency is 0.5 % for all signals except signal 6, which shows a maximum slightly higher around 0.58 %. The reason for this might be the small impurity arising from the second polymorph which cannot be perfectly separated by a deconvolution.

For the simulations we used spin systems containing nine spins in order to avoid finite-size effects on the one hand and vast simulation times on the other hand. The spin systems were extracted from the Rietveld-refined structure by taking overall nine spins in a sphere around the observed atoms. Figure 7c exemplarily depicts spin system No. 2, where only the aromatic cores and the side chains carrying fluorine contained in the spin system are shown. All simulations are displayed in Figure 7b.

In accordance with the measurement, spin system No. 3 and No. 6 reach their maximum around $\tau_{excitation}$ = 1 ms, whereas for the remaining curves the maximum is located at around $\tau_{excitation}$ = 0.8 ms. This behaviour can be explained by structural features: four of the six ^{19}F atoms of the asymmetric unit have a distance of 3.9 Å or 4.1 Å to the next fluorine atom, corresponding to couplings constants of d_{Dip} = -1750 Hz and d_{Dip} = -1537 Hz. The two remaining spins have a much higher distance of 4.8 Å and 5.1 Å leading to much weaker couplings of d_{Dip} = -980 Hz and d_{Dip} = -510 Hz. This means a slower DQ build-up and hence the maximum is shifted to longer excitation times. Therefore, we can already reduce the number of possible assignments of simulation and experiment and split both simulation and experimental curves in two groups according to the position of the maxima. In contrast to the experiment, all curves reach DQ efficiencies between 0.6 - 0.75 %. This difference may be explained with remaining proton coupling during double quantum excitation and reconversion shortening the double quantum relaxation time in the experiment and flattens the curves after normalization.

For an assignment within each group, we compared the position of the maxima and the first rise of the curves. These parts contain the sum of all couplings and hence the structural environment, but are less influenced by relaxation due to short excitation times. We compensated the proton influence by multiplying each simulated curve with a constant scaling factor of 0.75 which was found by optimising it for all curves simultaneously (Figure 6). For signal 1 and 2 the curves show a good agreement up to $\tau_{excitation}$ = 0.5 ms (Figure 6a and b), but the maximum DQ efficiency of the measurements are in both cases lower than for the simulated curves. This behaviour may be explained by the weaker coupling so that the dampening influence of the protons greater affects the experimental curves. For the remaining spins the curves agree very well up to $\tau_{excitation}$ = 1.2 ms and show only higher deviations in the last part, but the principal behaviour remain the same. This good agreement proves the correctness of the structure model obtained from the PXRD structure solution and connects directly the signals of the 1D ^{19}F spectrum to a single spin within the asymmetric unit.

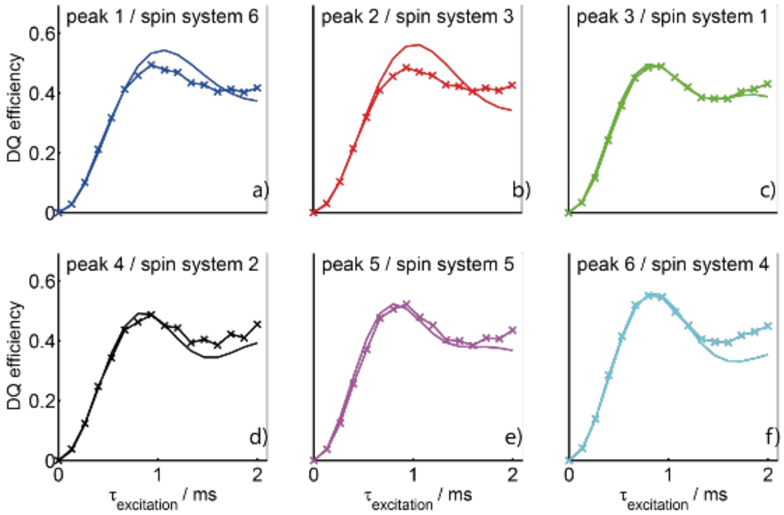

Figure 8. Experimental (line with markers) and simulated (lines) $^{19}F^{19}F$ build-up curves. The assignment of simulation and experiment was chosen by comparing the position of the maxima and the first rise of the buildup curves (see Figure 7a and b). The simulations were fit to the experimental curves by applying a constant scaling factor of 0.75.

Conclusion

We report the structure of 1,3,5-tris(2-fluoro-2-methylpropionylamino)benzene, a member of the new family of fluorinated BTAs. We used a concerted approach of ab initio real space powder x-ray diffraction methods, multinuclear solid-state NMR spectroscopy and computer simulations. Combining 1D NMR experiments, symmetry and extinction conditions, all possible space groups except $P2_1$ were excluded and the Rietveld refinement within this space group led to a wRp value of 5.3 %. The derived structure model was proved using DQ solid-state NMR experiments and computer simulations. Using the $SR14_4^5$ sequence we were able probing the structural environment of each ^{19}F within the asymmetric unit. This facilitated the assignment of each ^{19}F within the asymmetric unit to the six distinct resonances observed in the high-resolution 1D ^{19}F solid-state NMR experiment.

The structure itself can be described by layers arranged parallel to the bc-plane of the unit cell where the driving force for the formation of the lamella are strong to moderate hydrogen bonds with a NH⋯OC distances of 1.88 Å up to 2.55 Å. Neither π-π contacts nor huge dipole moments are observed and between neighboring layers only van-der-Waals interactions are dominant. The chemically similar 3,5-tris(2,2-dimethylpropionylamino)benzene,[28] however, obeys moderate hydrogen bonds with a much smaller length distribution between 2.04 and 2.14 Å. Together with van-der-Waals interactions and cancellation of antiparallel macroscopic dipoles this leads to a hexagonal rod arrangement with a preferred growth along the rod axis. This illustrates the strong influence of variations in the organic residues of BTAs on their structure based on these weak intermolecular interactions.

Acknowledgements

The authors want to thank the DFG (SFB 840, Project B4) for funding this work and Dr. Wolfgang Milius for the fruitful discussions with respect to crystallographic issues.

References

1 Lehn, J.-M. Angew. Chem. Int. Ed. Engl. **1990**, 29, 1304.

2 Lightfoot, M. P.; Mair, F. S.; Pritchard, R. G.; Warren, J. E. Chem. Commun. **1999**, 1945.

3 Brunsveld, L.; Schenning, A. P. H. J.; Broeren, M. A. C.; Janssen, H. M.; Vekemans, J. A. J. M.; Meijer, E. W. Chem. Lett. **2000**, 292.

4 Kristiansen, M.; Smith, P.; Chanzy, H.; Baerlocher, C.; Gramlich, V.; McCusker, L.; Weber, T.; Pattison, P.; Blomenhofer, M.; Schmidt, H.-W. Cryst. Growth Des. **2009**, 9, 2556.

5 Kluge, D.; Abraham, F.; Schmidt, S.; Schmidt, H.-W.; Fery, A. Langmuir **2010**, 26, 3020.

6 Wegner, M.; Dudenko, D.; Sebastiani, D.; Palmans, A. R. A.; de Greef, T. F. A.; Graf, R.; Spiess, H. W. Chem. Sci. **2011**, 2, 2040.

7 Kluge, D.; Singer, J. C.; Neubauer, J. W.; Abraham, F.; Schmidt, H.-W.; Fery, A. Small **2012**, 8, 2563.

8 Cantekin, S.; de Greef, T. F. A.; Palmans, A. R. A. Chem. Soc. Rev. **2012**, 41, 6125.

9 Yasuda, Y.; Iishi, E.; Inada, H.; Shirota, Y. Chem. Lett. **1996**, 25, 575.

10 Hanabusa, K.; Koto, C.; Kimura, M.; Shirai, H.; Kakehi, A. Chem. Lett. **1997**, 26, 429.

11 van Gorp, J. J.; Vekemans, J. A. J. M.; Meijer, E. W. J. Am. Chem. Soc. **2002**, 124, 14759.

12 Shi, N.; Dong, H.; Yin, G.; Xu, Z.; Li, S. Adv. Funct. Mater. **2007**, 17, 1837.

13 Bernet, A.; Albuquerque, R. Q.; Behr, M.; Hoffmann, S. T.; Schmidt, H.-W. Soft Matter **2012**, 8, 66.

14 Matsunaga, Y.; Miyajima, N.; Nakayasu, Y.; Sakai, S.; Yonenaga, M. Bull. Chem. Soc. Jpn. **1988**, 61, 207.

15 Besenius, P.; Heynens, J. L. M.; Straathof, R.; Nieuwenhuizen, M. M. L.; Bomans, P. H. H.; Terreno, E.; Aime, S.; Strijkers, G. J.; Nicolay, K.; Meijer, E. W. Contrast Media Mol. Imaging **2012**, 7, 356.

16 Gelinsky, M.; Vogler, R.; Vahrenkamp, H. Inorg. Chem. **2002**, 41, 2560.

17 Mohmeyer, N.; Behrendt, N.; Zhang, X.; Smith, P.; Altstädt, V.; Sessler, G. M.; Schmidt, H.-W. Polymer **2007**, 48, 1612.

18 Hillenbrand, J.; Motz, T.; Sessler, G. M.; Zhang, X.; Behrendt, N.; von Salis-Soglio, C.; Erhard, D. P.; Altstädt, V.; Schmidt, H.-W. J. Phys. D: Appl. Phys. **2009**, 42, 65410.

19 Erhard, D. P.; Lovera, D.; von Salis-Soglio, C.; Giesa, R.; Altstaedt, V.; Schmidt, H.-W. Adv. Polym. Sci. **2010**, 228, 155.

20 Blomenhofer, M.; Ganzleben, S.; Hanft, D.; Schmidt, H.-W.; Kristiansen, M.; Smith, P.; Stoll, K.; Maeder, D.; Hoffmann, K. Macromolecules **2005**, 38, 3688.

21 Kristiansen, P. M.; Gress, A.; Smith, P.; Hanft, D.; Schmidt, H.-W. Polymer **2006**, 47, 249.

22 Abraham, F.; Ganzleben, S.; Hanft, D.; Smith, P.; Schmidt, H.-W. Macromol. Chem. Phys. **2010**, 211, 171.

23 Richter, F.; Schmidt, H.-W. Macromol. Mater. Eng. **2013**, 298, 190.

24 Wang, J.; Dou, Q.; Chen, X.; Li, D. J. Polym. Sci. B Polym. Phys. **2008**, 46, 1067.

25 Nakajima, H.; Takahashi, M.; Kimura, Y. Macromol. Mater. Eng. **2010**, 295, 460.

26 Bai, H.; Zhang, W.; Deng, H.; Zhang, Q.; Fu, Q. Macromolecules **2011**, 44, 1233.

27 Song, P.; Wei, Z.; Liang, J.; Chen, G.; Zhang, W. Polym. Eng. Sci. **2012**, 52, 1058.

28 Schmidt, M.; Wittmann, J. J.; Kress, R.; Schneider, D.; Steuernagel, S.; Schmidt, H.-W.; Senker, J. Cryst. Growth Des. **2012**, 12, 2543.

29 Schmidt, M.; Wittmann, J. J.; Kress, R.; Schmidt, H. W.; Senker, J. Chem. Commun. **2013**, 49, 267.

30 Harris, R. K. Analyst **2006**, 131, 351.

31 Seyfarth, L.; Sehnert, J.; El-Gamel, N.; Milius, W.; Kroke, E.; Breu, J.; Senker, J. J. Mol. Struct. **2008**, 889, 217.

32 Seyfarth, L.; Seyfarth, J.; Lotsch, B. V.; Schnick, W.; Senker, J. Phys. Chem. Chem. Phys. **2010**, 12, 2227.

33 Wirnhier, E.; Döblinger, M.; Gunzelmann, D.; Senker, J.; Lotsch, B. V.; Schnick, W. Chem. Eur. J. **2011**, 17, 3213.

34 Detken, A.; Hardy, E. H.; Ernst, M.; Meier, B. H. Chem. Phys. Lett. **2002**, 356, 298.

35 Bak, M.; Rasmussen, J. T.; Nielsen, N. C. J. Magn. Reson. **2000**, 147, 296.

36 The language of technical computing. MATLAB; Math Works Inc., 24 Prime Park Way, Natick, MA 01760-1500. Copyright 1984 - 2012.

37 Accelrys software inc. MS Modeling v5.0.0.0 Copyright 2009.

38 Deem, M. W.; Newsam, J. M. Nature **1989**, 342, 260.

39 Deem, M. W.; Newsam, J. M. J. Am. Chem. Soc. **1992**, 114, 7189.

40 Dollase, W. A. J. Appl. Cryst. **1986**, 19, 267.

41 Sun, H. J. Phys. Chem. B **1998**, 102, 7338.

42 Finger, L. W.; E., C. D.; P., J. A. J. Appl. Cryst. **1994**, 27, 892.

43 Perdew, J. P.; Wang, Y. Phys. Rev. B **1992**, 45, 13244.

44 Senker, J.; Seyfarth, L.; Voll, J. Solid State Sci. **2004**, 6, 1039.

45 Karau, F. W.; Seyfarth, L.; Oeckler, O.; Senker, J.; Landskron, K.; Schnick, W. Chem. Eur. J. **2007**, 13, 6841.

46 Seyfarth, L.; Senker, J. Phys. Chem. Chem. Phys. **2009**, 11, 3522.

47 Hirsemann, D.; Köster, T. K.-J.; Wack, J.; van Wüllen, L.; Breu, J.; Senker, J. Chem. Mater. **2011**, 23, 3152.

48 Taulelle, F. Solid State Sci. **2004**, 6, 1053.

49 Senker, J.; Sehnert, J.; Correll, S. J. Am. Chem. Soc. **2005**, 127, 337.

50 Sehnert, J.; Senker, J. Chem. Eur. J. **2007**, 13, 6339.

51 Brouwer, D. H.; Kristiansen, P. E.; Fyfe, C. A.; Levitt, M. H. J. Am. Chem. Soc. **2005**, 127, 542.

52 Brouwer, D. H.; Darton, R. J.; Morris, R. E.; Levitt, M. H. J. Am. Chem. Soc. **2005**, 127, 10365.

53 Schmidt, M.; Zehe, C. S.; Siegel, R.; Heigl, J. U.; Steinlein, C.; Schmidt, H.-W.; Senker, J. CrystEngComm **2013**, 15, 8784.

54 Pawley, G. S. J. Appl. Crystallogr. **1981**, 14, 357.

55 Chandrasekhar, S.; Sadashiva, B. K.; Suresh, K. Pramana **1977**, 9, 471.

56 Sakamoto, A.; Ogata, D.; Shikata, T.; Urakawa, O.; Hanabusa, K. Polymer **2006**, 47, 956.

57 Fitié, C. F. C.; Roelofs, W. S. C.; Kemerink, M.; Sijbesma, R. P. J. Am. Chem. Soc. **2010**, 132, 6892.

58 Kulkarni, C.; Reddy, S. K.; George, S. J.; Balasubramanian, S. Chem. Phys. Lett. **2011**, 515, 226.

59 Albuquerque, R. Q.; Timme, A.; Kress, R.; Senker, J.; Schmidt, H.-W. Chem. Eur. J. **2013**, 19, 1647.

6.3.2 Supporting Information

Electronic Supplementary Information

to

Crystal Structure Determination of a Symmetrically Substituted Fluorine Containing BTA Using NMR-crystallographic Strategies†

Christoph Zehe,[a] Marko Schmidt,[a] Renée Siegel,[a] Venita Daebel,[c] Sandra Ganzleben,[b] Hans-Werner Schmidt,[b] and Jürgen Senker*[a]

[a] Inorganic Chemistry III and Bayreuth Center for Colloids and Interfaces
University of Bayreuth, 95447, Bayreuth, Germany
Fax: (+49) 921-55-2788
E-mail: juergen.senker@uni-bayreuth.de

[b] Macromolecular Chemistry I, Bayreuth Institute of Macromolecular Research and Bayreuth Center for Colloids and Interfaces
University of Bayreuth, 95447, Bayreuth, Germany
Fax: (+49) 921-55-3206
E-mail: hans-werner.schmidt@uni-bayreuth.de

[c] Bruker Biospin GmbH
Silberstreifen 4, 76287 Rheinstetten, Germany
E-mail: venita.daebel@bruker-biospin.de

^{19}F^{19}F DQ-SQ correlation experiment

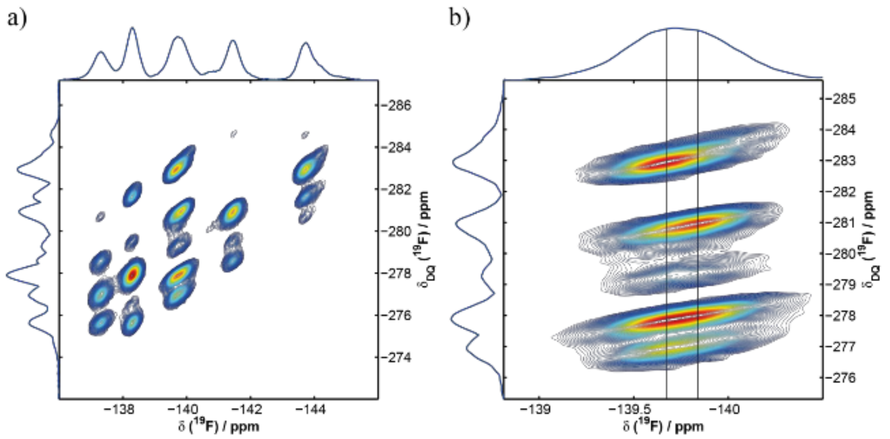

Figure S1. a) ^{19}F^{19}F double-quantum single-quantum correlation spectrum of **1**. b) Close-up, the lines mark the shifts of the two distinct signals.

Input files for Simulations with SIMPSON

Par, pulseq and main section

```
par {
variable         N 14.
variable         n 4.
variable         nu 5.
start_operator   Inz
detect_operator  I1p
spin_rate        60000
gamma_angles     40
crystal_file     zcw232
np               90
sw               spin_rate/$n/2
proton_frequency 600e6
verbose          11110
variable l1      np-1
}

proc pulseq {} {
      global par
      maxdt 1.0

      set rf [expr $par(spin_rate)*$par(N)/$par(n)]
```

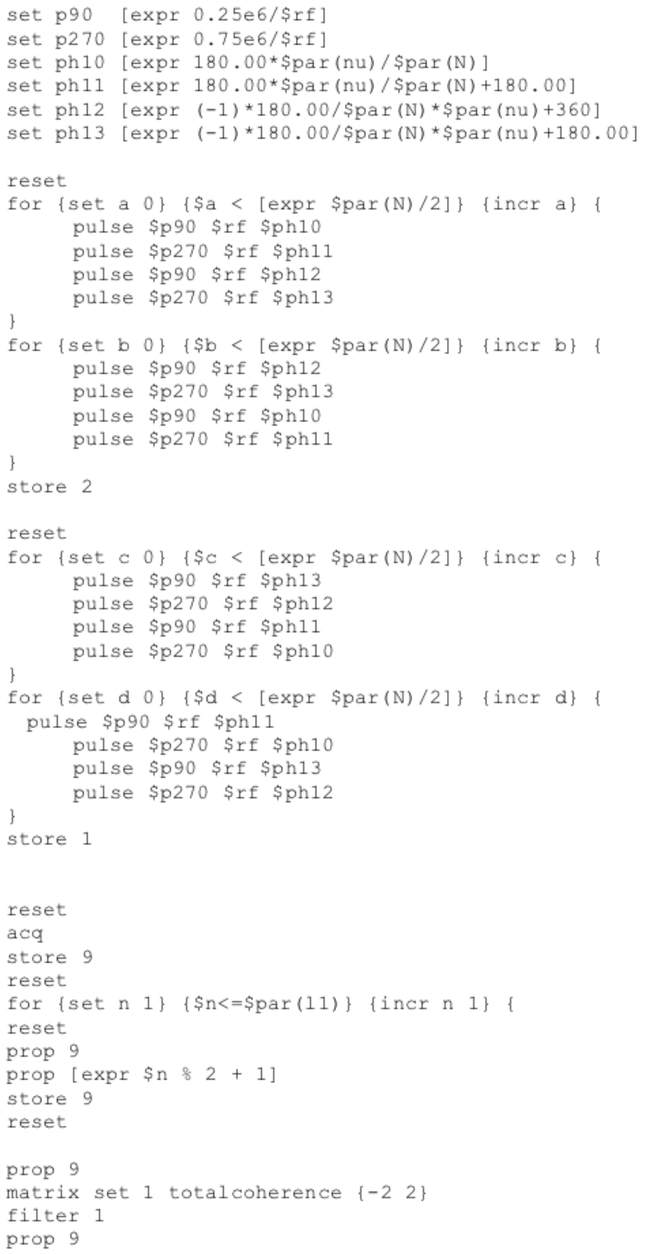

```
set p90  [expr 0.25e6/$rf]
set p270 [expr 0.75e6/$rf]
set ph10 [expr 180.00*$par(nu)/$par(N)]
set ph11 [expr 180.00*$par(nu)/$par(N)+180.00]
set ph12 [expr (-1)*180.00/$par(N)*$par(nu)+360]
set ph13 [expr (-1)*180.00/$par(N)*$par(nu)+180.00]

reset
for {set a 0} {$a < [expr $par(N)/2]} {incr a} {
     pulse $p90 $rf $ph10
     pulse $p270 $rf $ph11
     pulse $p90 $rf $ph12
     pulse $p270 $rf $ph13
}
for {set b 0} {$b < [expr $par(N)/2]} {incr b} {
     pulse $p90 $rf $ph12
     pulse $p270 $rf $ph13
     pulse $p90 $rf $ph10
     pulse $p270 $rf $ph11
}
store 2

reset
for {set c 0} {$c < [expr $par(N)/2]} {incr c} {
     pulse $p90 $rf $ph13
     pulse $p270 $rf $ph12
     pulse $p90 $rf $ph11
     pulse $p270 $rf $ph10
}
for {set d 0} {$d < [expr $par(N)/2]} {incr d} {
  pulse $p90 $rf $ph11
     pulse $p270 $rf $ph10
     pulse $p90 $rf $ph13
     pulse $p270 $rf $ph12
}
store 1


reset
acq
store 9
reset
for {set n 1} {$n<=$par(11)} {incr n 1} {
reset
prop 9
prop [expr $n % 2 + 1]
store 9
reset

prop 9
matrix set 1 totalcoherence {-2 2}
filter 1
prop 9
```

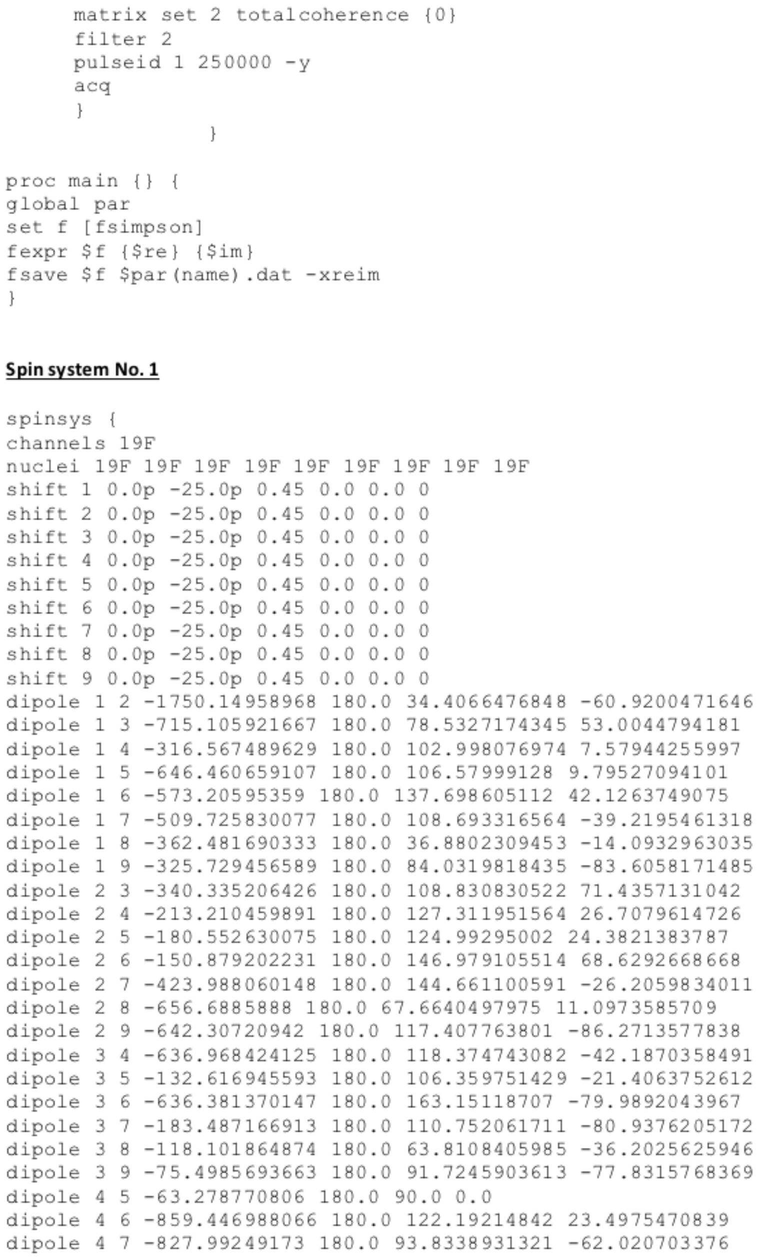

```
      matrix set 2 totalcoherence {0}
      filter 2
      pulseid 1 250000 -y
      acq
      }
                 }

proc main {} {
global par
set f [fsimpson]
fexpr $f {$re} {$im}
fsave $f $par(name).dat -xreim
}
```

Spin system No. 1

```
spinsys {
channels 19F
nuclei 19F 19F 19F 19F 19F 19F 19F 19F 19F
shift 1 0.0p -25.0p 0.45 0.0 0.0 0
shift 2 0.0p -25.0p 0.45 0.0 0.0 0
shift 3 0.0p -25.0p 0.45 0.0 0.0 0
shift 4 0.0p -25.0p 0.45 0.0 0.0 0
shift 5 0.0p -25.0p 0.45 0.0 0.0 0
shift 6 0.0p -25.0p 0.45 0.0 0.0 0
shift 7 0.0p -25.0p 0.45 0.0 0.0 0
shift 8 0.0p -25.0p 0.45 0.0 0.0 0
shift 9 0.0p -25.0p 0.45 0.0 0.0 0
dipole 1 2 -1750.14958968 180.0 34.4066476848 -60.9200471646
dipole 1 3 -715.105921667 180.0 78.5327174345 53.0044794181
dipole 1 4 -316.567489629 180.0 102.998076974 7.57944255997
dipole 1 5 -646.460659107 180.0 106.57999128 9.79527094101
dipole 1 6 -573.20595359 180.0 137.698605112 42.1263749075
dipole 1 7 -509.725830077 180.0 108.693316564 -39.2195461318
dipole 1 8 -362.481690333 180.0 36.8802309453 -14.0932963035
dipole 1 9 -325.729456589 180.0 84.0319818435 -83.6058171485
dipole 2 3 -340.335206426 180.0 108.830830522 71.4357131042
dipole 2 4 -213.210459891 180.0 127.311951564 26.7079614726
dipole 2 5 -180.552630075 180.0 124.99295002 24.3821383787
dipole 2 6 -150.879202231 180.0 146.979105514 68.6292668668
dipole 2 7 -423.988060148 180.0 144.661100591 -26.2059834011
dipole 2 8 -656.6885888 180.0 67.6640497975 11.0973585709
dipole 2 9 -642.30720942 180.0 117.407763801 -86.2713577838
dipole 3 4 -636.968424125 180.0 118.374743082 -42.1870358491
dipole 3 5 -132.616945593 180.0 106.359751429 -21.4063752612
dipole 3 6 -636.381370147 180.0 163.15118707 -79.9892043967
dipole 3 7 -183.487166913 180.0 110.752061711 -80.9376205172
dipole 3 8 -118.101864874 180.0 63.8108405985 -36.2025625946
dipole 3 9 -75.4985693663 180.0 91.7245903613 -77.8315768369
dipole 4 5 -63.278770806 180.0 90.0 0.0
dipole 4 6 -859.446988066 180.0 122.19214842 23.4975470839
dipole 4 7 -827.99249173 180.0 93.8338931321 -62.020703376
```

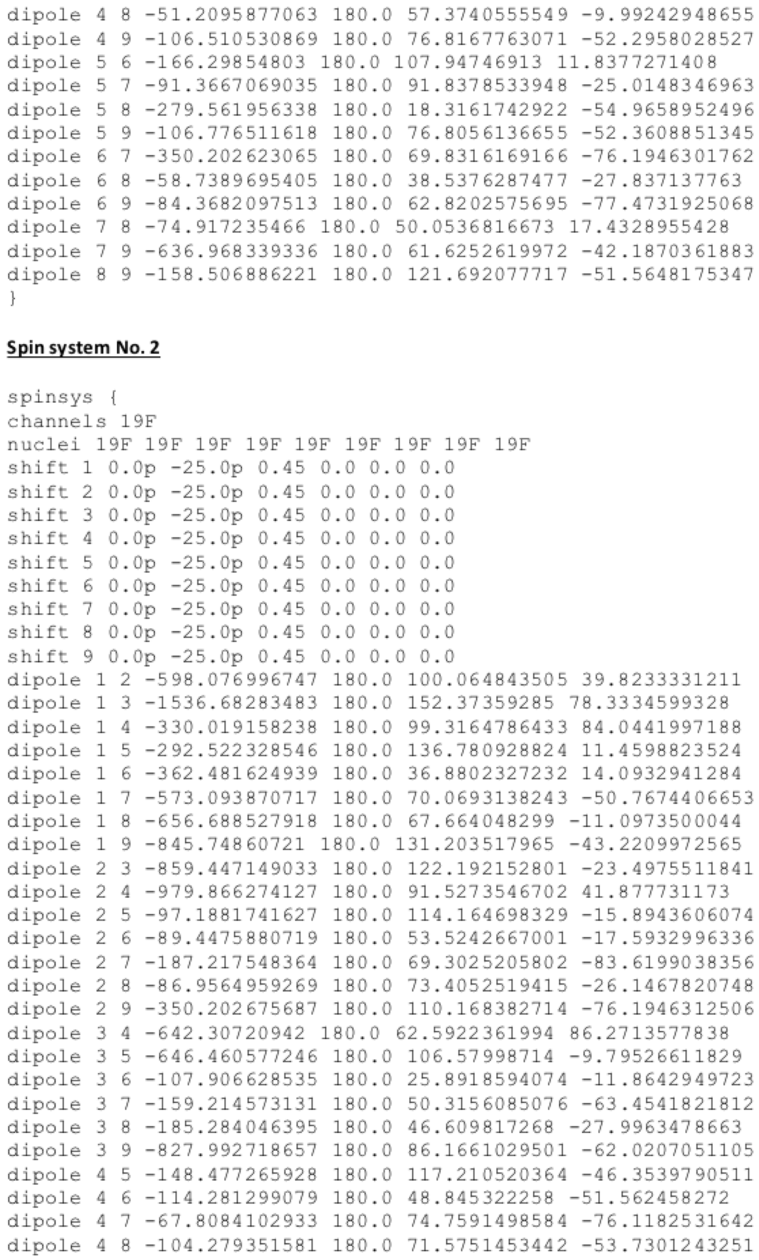

```
dipole 4 8 -51.2095877063 180.0 57.3740555549 -9.99242948655
dipole 4 9 -106.510530869 180.0 76.8167763071 -52.2958028527
dipole 5 6 -166.29854803 180.0 107.94746913 11.8377271408
dipole 5 7 -91.3667069035 180.0 91.8378533948 -25.0148346963
dipole 5 8 -279.561956338 180.0 18.3161742922 -54.9658952496
dipole 5 9 -106.776511618 180.0 76.8056136655 -52.3608851345
dipole 6 7 -350.202623065 180.0 69.8316169166 -76.1946301762
dipole 6 8 -58.7389695405 180.0 38.5376287477 -27.837137763
dipole 6 9 -84.3682097513 180.0 62.8202575695 -77.4731925068
dipole 7 8 -74.917235466 180.0 50.0536816673 17.4328955428
dipole 7 9 -636.968339336 180.0 61.6252619972 -42.1870361883
dipole 8 9 -158.506886221 180.0 121.692077717 -51.5648175347
}
```

Spin system No. 2

```
spinsys {
channels 19F
nuclei 19F 19F 19F 19F 19F 19F 19F 19F 19F
shift 1 0.0p -25.0p 0.45 0.0 0.0 0.0
shift 2 0.0p -25.0p 0.45 0.0 0.0 0.0
shift 3 0.0p -25.0p 0.45 0.0 0.0 0.0
shift 4 0.0p -25.0p 0.45 0.0 0.0 0.0
shift 5 0.0p -25.0p 0.45 0.0 0.0 0.0
shift 6 0.0p -25.0p 0.45 0.0 0.0 0.0
shift 7 0.0p -25.0p 0.45 0.0 0.0 0.0
shift 8 0.0p -25.0p 0.45 0.0 0.0 0.0
shift 9 0.0p -25.0p 0.45 0.0 0.0 0.0
dipole 1 2 -598.076996747 180.0 100.064843505 39.8233331211
dipole 1 3 -1536.68283483 180.0 152.37359285 78.3334599328
dipole 1 4 -330.019158238 180.0 99.3164786433 84.0441997188
dipole 1 5 -292.522328546 180.0 136.780928824 11.4598823524
dipole 1 6 -362.481624939 180.0 36.8802327232 14.0932941284
dipole 1 7 -573.093870717 180.0 70.0693138243 -50.7674406653
dipole 1 8 -656.688527918 180.0 67.664048299 -11.0973500044
dipole 1 9 -845.74860721 180.0 131.203517965 -43.2209972565
dipole 2 3 -859.447149033 180.0 122.192152801 -23.4975511841
dipole 2 4 -979.866274127 180.0 91.5273546702 41.877731173
dipole 2 5 -97.1881741627 180.0 114.164698329 -15.8943606074
dipole 2 6 -89.4475880719 180.0 53.5242667001 -17.5932996336
dipole 2 7 -187.217548364 180.0 69.3025205802 -83.6199038356
dipole 2 8 -86.9564959269 180.0 73.4052519415 -26.1467820748
dipole 2 9 -350.202675687 180.0 110.168382714 -76.1946312506
dipole 3 4 -642.30720942 180.0 62.5922361994 86.2713577838
dipole 3 5 -646.460577246 180.0 106.57998714 -9.79526611829
dipole 3 6 -107.906628535 180.0 25.8918594074 -11.8642949723
dipole 3 7 -159.214573131 180.0 50.3156085076 -63.4541821812
dipole 3 8 -185.284046395 180.0 46.609817268 -27.9963478663
dipole 3 9 -827.992718657 180.0 86.1661029501 -62.0207051105
dipole 4 5 -148.477265928 180.0 117.210520364 -46.3539790511
dipole 4 6 -114.281299079 180.0 48.845322258 -51.562458272
dipole 4 7 -67.8084102933 180.0 74.7591498584 -76.1182531642
dipole 4 8 -104.279351581 180.0 71.5751453442 -53.7301243251
```

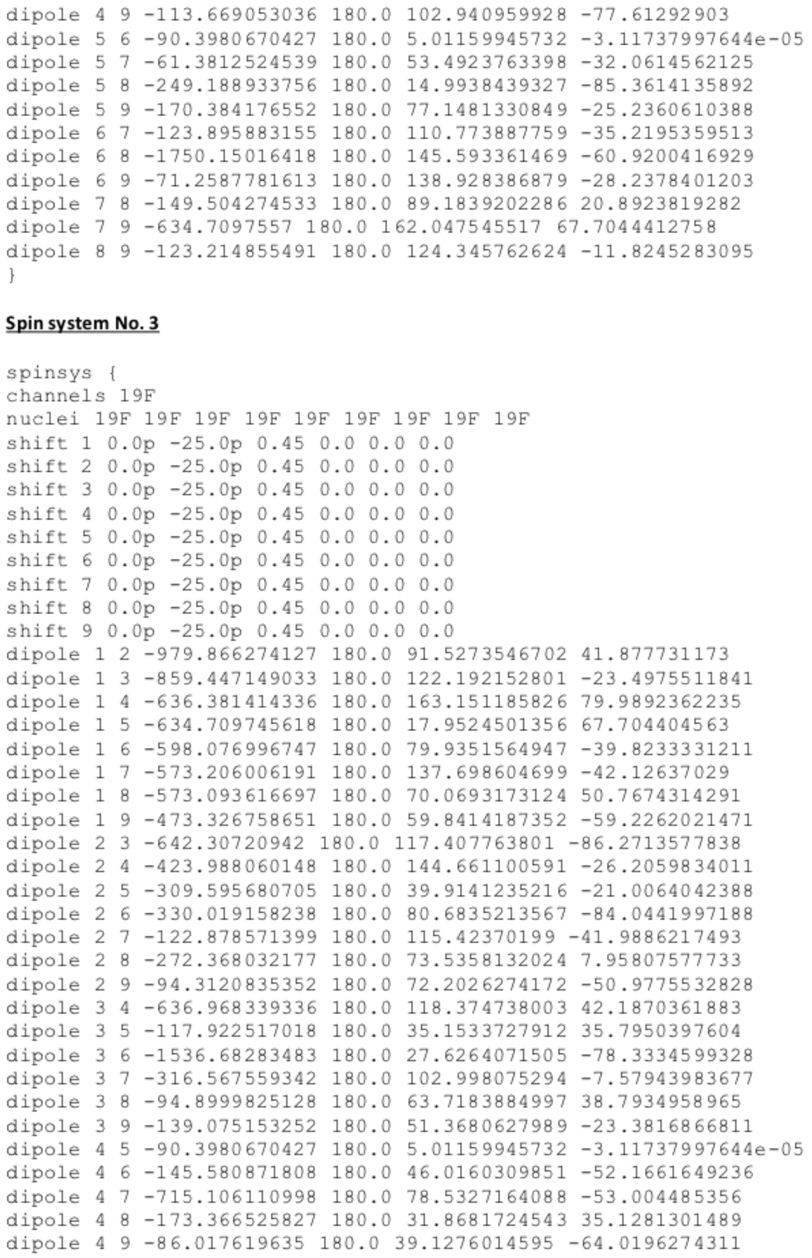

```
dipole 4 9 -113.669053036 180.0 102.940959928 -77.61292903
dipole 5 6 -90.3980670427 180.0 5.01159945732 -3.11737997644e-05
dipole 5 7 -61.3812524539 180.0 53.4923763398 -32.0614562125
dipole 5 8 -249.188933756 180.0 14.9938439327 -85.3614135892
dipole 5 9 -170.384176552 180.0 77.1481330849 -25.2360610388
dipole 6 7 -123.895883155 180.0 110.773887759 -35.2195359513
dipole 6 8 -1750.15016418 180.0 145.593361469 -60.9200416929
dipole 6 9 -71.2587781613 180.0 138.928386879 -28.2378401203
dipole 7 8 -149.504274533 180.0 89.1839202286 20.8923819282
dipole 7 9 -634.7097557 180.0 162.047545517 67.7044412758
dipole 8 9 -123.214855491 180.0 124.345762624 -11.8245283095
}
```

Spin system No. 3

```
spinsys {
channels 19F
nuclei 19F 19F 19F 19F 19F 19F 19F 19F 19F
shift 1 0.0p -25.0p 0.45 0.0 0.0 0.0
shift 2 0.0p -25.0p 0.45 0.0 0.0 0.0
shift 3 0.0p -25.0p 0.45 0.0 0.0 0.0
shift 4 0.0p -25.0p 0.45 0.0 0.0 0.0
shift 5 0.0p -25.0p 0.45 0.0 0.0 0.0
shift 6 0.0p -25.0p 0.45 0.0 0.0 0.0
shift 7 0.0p -25.0p 0.45 0.0 0.0 0.0
shift 8 0.0p -25.0p 0.45 0.0 0.0 0.0
shift 9 0.0p -25.0p 0.45 0.0 0.0 0.0
dipole 1 2 -979.866274127 180.0 91.5273546702 41.877731173
dipole 1 3 -859.447149033 180.0 122.192152801 -23.4975511841
dipole 1 4 -636.381414336 180.0 163.151185826 79.9892362235
dipole 1 5 -634.709745618 180.0 17.9524501356 67.704404563
dipole 1 6 -598.076996747 180.0 79.9351564947 -39.8233331211
dipole 1 7 -573.206006191 180.0 137.698604699 -42.12637029
dipole 1 8 -573.093616697 180.0 70.0693173124 50.7674314291
dipole 1 9 -473.326758651 180.0 59.8414187352 -59.2262021471
dipole 2 3 -642.30720942 180.0 117.407763801 -86.2713577838
dipole 2 4 -423.988060148 180.0 144.661100591 -26.2059834011
dipole 2 5 -309.595680705 180.0 39.9141235216 -21.0064042388
dipole 2 6 -330.019158238 180.0 80.6835213567 -84.0441997188
dipole 2 7 -122.878571399 180.0 115.42370199 -41.9886217493
dipole 2 8 -272.368032177 180.0 73.5358132024 7.95807577733
dipole 2 9 -94.3120835352 180.0 72.2026274172 -50.9775532828
dipole 3 4 -636.968339336 180.0 118.374738003 42.1870361883
dipole 3 5 -117.922517018 180.0 35.1533727912 35.7950397604
dipole 3 6 -1536.68283483 180.0 27.6264071505 -78.3334599328
dipole 3 7 -316.567559342 180.0 102.998075294 -7.57943983677
dipole 3 8 -94.8999825128 180.0 63.7183884997 38.7934958965
dipole 3 9 -139.075153252 180.0 51.3680627989 -23.3816866811
dipole 4 5 -90.3980670427 180.0 5.01159945732 -3.11737997644e-05
dipole 4 6 -145.580871808 180.0 46.0160309851 -52.1661649236
dipole 4 7 -715.106110998 180.0 78.5327164088 -53.004485356
dipole 4 8 -173.366525827 180.0 31.8681724543 35.1281301489
dipole 4 9 -86.017619635 180.0 39.1276014595 -64.0196274311
```

```
dipole 5 6 -188.248518194 180.0 121.033452152 -46.2644017513
dipole 5 7 -90.2117443042 180.0 153.609264938 -62.0291847251
dipole 5 8 -845.74819169 180.0 131.203512727 43.2210035612
dipole 5 9 -340.335342023 180.0 108.830833117 -71.4357152604
dipole 6 7 -153.213519955 180.0 125.974488154 7.78856561245
dipole 6 8 -82.3046549821 180.0 84.9349604508 45.2074863942
dipole 6 9 -272.368062655 180.0 73.5358109696 -7.95807022429
dipole 7 8 -139.26522743 180.0 47.6053671468 85.3735936561
dipole 7 9 -249.188933756 180.0 14.9938439327 -85.3614135892
dipole 8 9 -157.734338895 180.0 82.7283672666 -85.3708660734
}
```

Spin system No. 4

```
spinsys {
channels 19F
nuclei 19F 19F 19F 19F 19F 19F 19F 19F 19F
shift 1 0.0p -25.0p 0.45 0.0 0.0 0.0
shift 2 0.0p -25.0p 0.45 0.0 0.0 0.0
shift 3 0.0p -25.0p 0.45 0.0 0.0 0.0
shift 4 0.0p -25.0p 0.45 0.0 0.0 0.0
shift 5 0.0p -25.0p 0.45 0.0 0.0 0.0
shift 6 0.0p -25.0p 0.45 0.0 0.0 0.0
shift 7 0.0p -25.0p 0.45 0.0 0.0 0.0
shift 8 0.0p -25.0p 0.45 0.0 0.0 0.0
shift 9 0.0p -25.0p 0.45 0.0 0.0 0.0
dipole 1 2 -325.729456589 180.0 95.9680181565 83.6058171485
dipole 1 3 -1536.68283483 180.0 27.6264071505 -78.3334599328
dipole 1 4 -859.447149033 180.0 57.8078471991 23.4975511841
dipole 1 5 -642.30720942 180.0 62.5922361994 86.2713577838
dipole 1 6 -636.968339336 180.0 118.374738003 42.1870361883
dipole 1 7 -316.567559342 180.0 102.998075294 -7.57943983677
dipole 1 8 -646.460577246 180.0 106.57998714 -9.79526611829
dipole 1 9 -827.992718657 180.0 86.1661029501 -62.0207051105
dipole 2 3 -116.187217045 180.0 63.3600268844 -87.5054741556
dipole 2 4 -234.305472778 180.0 63.984702877 -47.9018131252
dipole 2 5 -1750.14958968 180.0 34.4066476848 -60.9200471646
dipole 2 6 -509.725830077 180.0 108.693316564 -39.2195461318
dipole 2 7 -85.2269056022 180.0 94.5156111566 -45.8392037085
dipole 2 8 -150.12464154 180.0 95.4560939951 -60.1842879338
dipole 2 9 -65.9790409074 180.0 84.8458744739 -74.4804651882
dipole 3 4 -598.076996747 180.0 100.064843505 39.8233331211
dipole 3 5 -330.019158238 180.0 99.3164786433 84.0441997188
dipole 3 6 -145.580871808 180.0 133.983969015 52.1661649236
dipole 3 7 -153.213519955 180.0 125.974488154 7.78856561245
dipole 3 8 -292.522328546 180.0 136.780928824 11.4598823524
dipole 3 9 -845.74860721 180.0 131.203517965 -43.2209972565
dipole 4 5 -979.866274127 180.0 91.5273546702 41.877731173
dipole 4 6 -636.381414336 180.0 163.151185826 79.9892362235
dipole 4 7 -573.206006191 180.0 137.698604699 -42.12637029
dipole 4 8 -97.1881741627 180.0 114.164698329 -15.8943606074
dipole 4 9 -350.202675687 180.0 110.168382714 -76.1946312506
dipole 5 6 -423.988060148 180.0 144.661100591 -26.2059834011
```

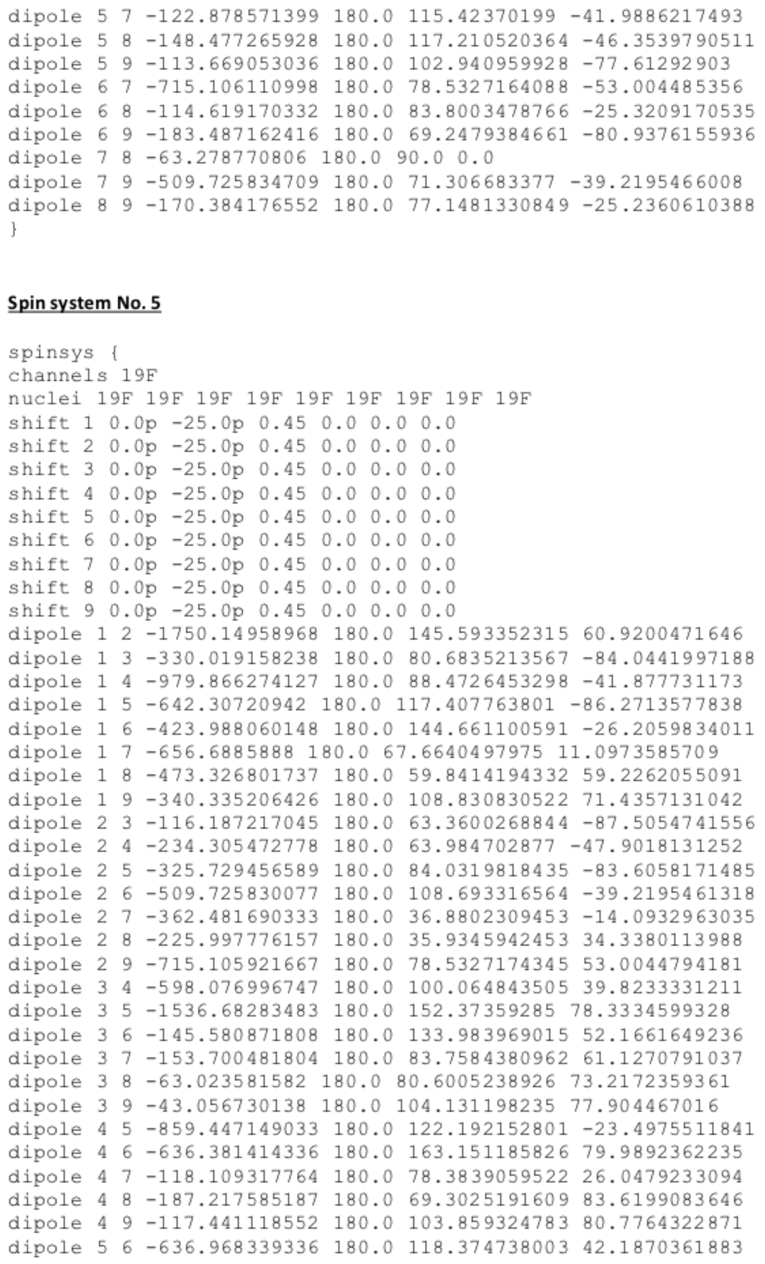

```
dipole 5 7 -122.878571399 180.0 115.42370199 -41.9886217493
dipole 5 8 -148.477265928 180.0 117.210520364 -46.3539790511
dipole 5 9 -113.669053036 180.0 102.940959928 -77.61292903
dipole 6 7 -715.106110998 180.0 78.5327164088 -53.004485356
dipole 6 8 -114.619170332 180.0 83.8003478766 -25.3209170535
dipole 6 9 -183.487162416 180.0 69.2479384661 -80.9376155936
dipole 7 8 -63.278770806 180.0 90.0 0.0
dipole 7 9 -509.725834709 180.0 71.306683377 -39.219546008
dipole 8 9 -170.384176552 180.0 77.1481330849 -25.2360610388
}
```

Spin system No. 5

```
spinsys {
channels 19F
nuclei 19F 19F 19F 19F 19F 19F 19F 19F 19F
shift 1 0.0p -25.0p 0.45 0.0 0.0 0.0
shift 2 0.0p -25.0p 0.45 0.0 0.0 0.0
shift 3 0.0p -25.0p 0.45 0.0 0.0 0.0
shift 4 0.0p -25.0p 0.45 0.0 0.0 0.0
shift 5 0.0p -25.0p 0.45 0.0 0.0 0.0
shift 6 0.0p -25.0p 0.45 0.0 0.0 0.0
shift 7 0.0p -25.0p 0.45 0.0 0.0 0.0
shift 8 0.0p -25.0p 0.45 0.0 0.0 0.0
shift 9 0.0p -25.0p 0.45 0.0 0.0 0.0
dipole 1 2 -1750.14958968 180.0 145.593352315 60.9200471646
dipole 1 3 -330.019158238 180.0 80.6835213567 -84.0441997188
dipole 1 4 -979.866274127 180.0 88.4726453298 -41.877731173
dipole 1 5 -642.30720942 180.0 117.407763801 -86.2713577838
dipole 1 6 -423.988060148 180.0 144.661100591 -26.2059834011
dipole 1 7 -656.6885888 180.0 67.6640497975 11.0973585709
dipole 1 8 -473.326801737 180.0 59.8414194332 59.2262055091
dipole 1 9 -340.335206426 180.0 108.830830522 71.4357131042
dipole 2 3 -116.187217045 180.0 63.3600268844 -87.5054741556
dipole 2 4 -234.305472778 180.0 63.984702877 -47.9018131252
dipole 2 5 -325.729456589 180.0 84.0319818435 -83.6058171485
dipole 2 6 -509.725830077 180.0 108.693316564 -39.2195461318
dipole 2 7 -362.481690333 180.0 36.8802309453 -14.0932963035
dipole 2 8 -225.997776157 180.0 35.9345942453 34.3380113988
dipole 2 9 -715.105921667 180.0 78.5327174345 53.0044794181
dipole 3 4 -598.076996747 180.0 100.064843505 39.8233331211
dipole 3 5 -1536.68283483 180.0 152.37359285 78.3334599328
dipole 3 6 -145.580871808 180.0 133.983969015 52.1661649236
dipole 3 7 -153.700481804 180.0 83.7584380962 61.1270791037
dipole 3 8 -63.023581582 180.0 80.6005238926 73.2172359361
dipole 3 9 -43.056730138 180.0 104.131198235 77.904467016
dipole 4 5 -859.447149033 180.0 122.192152801 -23.4975511841
dipole 4 6 -636.381414336 180.0 163.151185826 79.9892362235
dipole 4 7 -118.109317764 180.0 78.3839059522 26.0479233094
dipole 4 8 -187.217585187 180.0 69.3025191609 83.6199083646
dipole 4 9 -117.441118552 180.0 103.859324783 80.7764322871
dipole 5 6 -636.968339336 180.0 118.374738003 42.1870361883
```

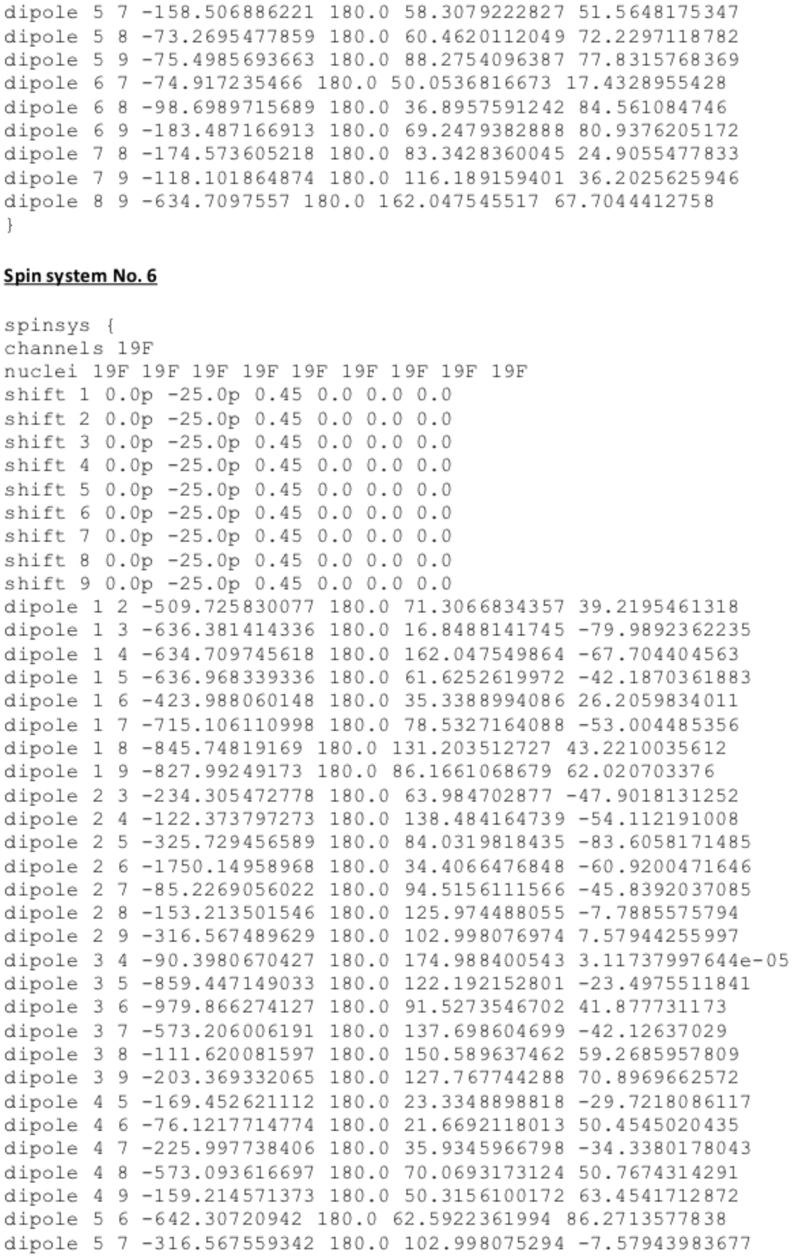

```
dipole 5 7 -158.506886221 180.0 58.3079222827 51.5648175347
dipole 5 8 -73.2695477859 180.0 60.4620112049 72.2297118782
dipole 5 9 -75.4985693663 180.0 88.2754096387 77.8315768369
dipole 6 7 -74.917235466 180.0 50.0536816673 17.4328955428
dipole 6 8 -98.6989715689 180.0 36.8957591242 84.561084746
dipole 6 9 -183.487166913 180.0 69.2479382888 80.9376205172
dipole 7 8 -174.573605218 180.0 83.3428360045 24.9055477833
dipole 7 9 -118.101864874 180.0 116.189159401 36.2025625946
dipole 8 9 -634.7097557 180.0 162.047545517 67.7044412758
}
```

Spin system No. 6

```
spinsys {
channels 19F
nuclei 19F 19F 19F 19F 19F 19F 19F 19F 19F
shift 1 0.0p -25.0p 0.45 0.0 0.0 0.0
shift 2 0.0p -25.0p 0.45 0.0 0.0 0.0
shift 3 0.0p -25.0p 0.45 0.0 0.0 0.0
shift 4 0.0p -25.0p 0.45 0.0 0.0 0.0
shift 5 0.0p -25.0p 0.45 0.0 0.0 0.0
shift 6 0.0p -25.0p 0.45 0.0 0.0 0.0
shift 7 0.0p -25.0p 0.45 0.0 0.0 0.0
shift 8 0.0p -25.0p 0.45 0.0 0.0 0.0
shift 9 0.0p -25.0p 0.45 0.0 0.0 0.0
dipole 1 2 -509.725830077 180.0 71.3066834357 39.2195461318
dipole 1 3 -636.381414336 180.0 16.8488141745 -79.9892362235
dipole 1 4 -634.709745618 180.0 162.047549864 -67.704404563
dipole 1 5 -636.968339336 180.0 61.6252619972 -42.1870361883
dipole 1 6 -423.988060148 180.0 35.3388994086 26.2059834011
dipole 1 7 -715.106110998 180.0 78.5327164088 -53.004485356
dipole 1 8 -845.74819169 180.0 131.203512727 43.2210035612
dipole 1 9 -827.99249173 180.0 86.1661068679 62.020703376
dipole 2 3 -234.305472778 180.0 63.984702877 -47.9018131252
dipole 2 4 -122.373797273 180.0 138.484164739 -54.112191008
dipole 2 5 -325.729456589 180.0 84.0319818435 -83.6058171485
dipole 2 6 -1750.14958968 180.0 34.4066476848 -60.9200471646
dipole 2 7 -85.2269056022 180.0 94.5156111566 -45.8392037085
dipole 2 8 -153.213501546 180.0 125.974488055 -7.7885575794
dipole 2 9 -316.567489629 180.0 102.998076974 7.57944255997
dipole 3 4 -90.3980670427 180.0 174.988400543 3.11737997644e-05
dipole 3 5 -859.447149033 180.0 122.192152801 -23.4975511841
dipole 3 6 -979.866274127 180.0 91.5273546702 41.877731173
dipole 3 7 -573.206006191 180.0 137.698604699 -42.12637029
dipole 3 8 -111.620081597 180.0 150.589637462 59.2685957809
dipole 3 9 -203.369332065 180.0 127.767744288 70.8969662572
dipole 4 5 -169.452621112 180.0 23.3348898818 -29.7218086117
dipole 4 6 -76.1217714774 180.0 21.6692118013 50.4545020435
dipole 4 7 -225.997738406 180.0 35.9345966798 -34.3380178043
dipole 4 8 -573.093616697 180.0 70.0693173124 50.7674314291
dipole 4 9 -159.214571373 180.0 50.3156100172 63.4541712872
dipole 5 6 -642.30720942 180.0 62.5922361994 86.2713577838
dipole 5 7 -316.567559342 180.0 102.998075294 -7.57943983677
```

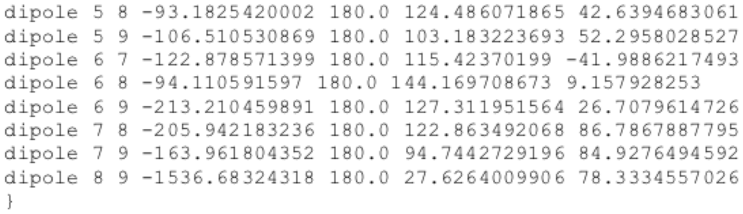

```
dipole 5 8 -93.1825420002 180.0 124.486071865 42.6394683061
dipole 5 9 -106.510530869 180.0 103.183223693 52.2958028527
dipole 6 7 -122.878571399 180.0 115.42370199 -41.9886217493
dipole 6 8 -94.110591597 180.0 144.169708673 9.157928253
dipole 6 9 -213.210459891 180.0 127.311951564 26.7079614726
dipole 7 8 -205.942183236 180.0 122.863492068 86.7867887795
dipole 7 9 -163.961804352 180.0 94.7442729196 84.9276494592
dipole 8 9 -1536.68324318 180.0 27.6264009906 78.3334557026
}
```

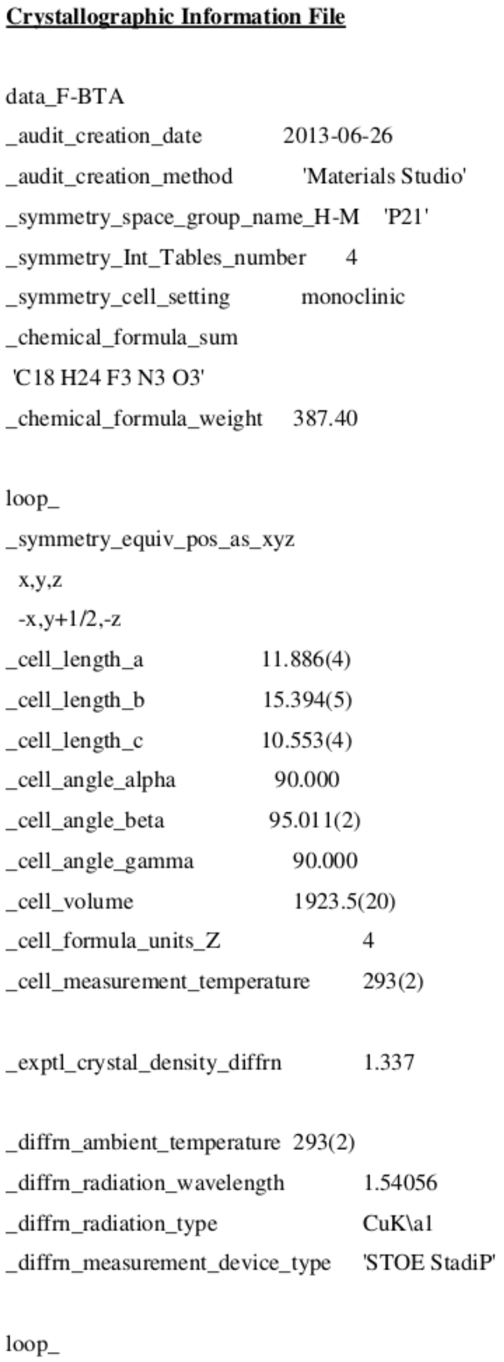

Crystallographic Information File

```
data_F-BTA
_audit_creation_date              2013-06-26
_audit_creation_method            'Materials Studio'
_symmetry_space_group_name_H-M    'P21'
_symmetry_Int_Tables_number       4
_symmetry_cell_setting            monoclinic
_chemical_formula_sum
 'C18 H24 F3 N3 O3'
_chemical_formula_weight    387.40

loop_
_symmetry_equiv_pos_as_xyz
  x,y,z
  -x,y+1/2,-z
_cell_length_a                 11.886(4)
_cell_length_b                 15.394(5)
_cell_length_c                 10.553(4)
_cell_angle_alpha                90.000
_cell_angle_beta               95.011(2)
_cell_angle_gamma                  90.000
_cell_volume                       1923.5(20)
_cell_formula_units_Z                      4
_cell_measurement_temperature          293(2)

_exptl_crystal_density_diffrn          1.337

_diffrn_ambient_temperature  293(2)
_diffrn_radiation_wavelength           1.54056
_diffrn_radiation_type                 CuK\a1
_diffrn_measurement_device_type        'STOE StadiP'

loop_
```

```
_atom_site_label
_atom_site_type_symbol
_atom_site_fract_x
_atom_site_fract_y
_atom_site_fract_z
_atom_site_U_iso_or_equiv
_atom_site_adp_type
_atom_site_occupancy
C1   C  -0.13007(46)   0.06208(51)   0.22853(74)   0.0843(1)  Uiso  1.00
C2   C  -0.06896(46)   0.12312(50)   0.16745(73)   0.0843(1)  Uiso  1.00
C3   C   0.04772(46)   0.12323(51)   0.17581(77)   0.0843(1)  Uiso  1.00
C4   C   0.10345(46)   0.05928(52)   0.24938(79)   0.0843(1)  Uiso  1.00
C5   C   0.04604(46)  -0.00313(50)   0.31322(75)   0.0843(1)  Uiso  1.00
C6   C  -0.07083(46)  -0.00043(50)   0.30085(73)   0.0843(1)  Uiso  1.00
C7  C   0.19861(60)  -0.06251(51)   0.46456(67)   0.0843(1)  Uiso  1.00
C8  C   0.24382(45)  -0.15314(51)   0.51663(59)   0.0843(1)  Uiso  1.00
C9  C   0.20993(61)   0.18372(52)   0.07173(67)   0.0843(1)  Uiso  1.00
C10   C   0.24762(50)   0.27180(53)   0.01166(59)   0.0843(1)  Uiso  1.00
C11   C  -0.31918(48)   0.05680(70)   0.30754(81)   0.0843(1)  Uiso  1.00
C12   C  -0.44606(47)   0.06433(59)   0.25220(97)   0.0843(1)  Uiso  1.00
C13   C   0.37069(73)   0.28872(99)   0.05954(175)  0.0843(1)  Uiso  1.00
C14   C   0.23340(152) -0.15604(75)   0.65997(64)   0.0843(1)  Uiso  1.00
C15   C  -0.51307(83)   0.11206(160)  0.34744(122)  0.0843(1)  Uiso  1.00
C16   C   0.23416(191)  0.26313(90)  -0.13299(58)   0.0843(1)  Uiso  1.00
C17   C  -0.49426(84)  -0.02663(58)   0.22615(271)  0.0843(1)  Uiso  1.00
C18   C   0.36659(55)  -0.16200(80)   0.48613(160)  0.0843(1)  Uiso  1.00
C19   C  -0.11101(44)   0.06272(12)  -0.26030(72)   0.0843(1)  Uiso  1.00
C20   C  -0.05100(44)   0.01552(1)   -0.16506(69)   0.0843(1)  Uiso  1.00
C21   C   0.06595(44)   0.01399(12)  -0.15180(70)   0.0843(1)  Uiso  1.00
C22   C   0.12306(44)   0.06243(13)  -0.23608(70)   0.0843(1)  Uiso  1.00
C23   C   0.06703(44)   0.11080(3)   -0.33224(69)   0.0843(1)  Uiso  1.00
C24   C  -0.04984(44)   0.10946(10)  -0.34308(71)   0.0843(1)  Uiso  1.00
C25   C   0.11847(61)   0.24550(12)  -0.43752(62)   0.0843(1)  Uiso  1.00
C26   C   0.20809(54)   0.28280(7)   -0.52448(56)   0.0843(1)  Uiso  1.00
```

C27	C	0.11665(65)	-0.12138(21)	-0.03682(71)	0.0843(1)	Uiso	1.00
C28	C	0.20920(57)	-0.15896(39)	0.06475(76)	0.0843(1)	Uiso	1.00
C29	C	-0.30400(46)	0.05885(66)	-0.18565(86)	0.0843(1)	Uiso	1.00
C30	C	-0.43053(44)	0.05371(50)	-0.24482(97)	0.0843(1)	Uiso	1.00
C31	C	0.15420(66)	-0.23130(82)	0.13690(133)	0.0843(1)	Uiso	1.00
C32	C	0.31214(86)	0.31304(118)	-0.44051(61)	0.0843(1)	Uiso	1.00
C33	C	-0.47791(96)	0.14527(50)	-0.26797(340)	0.0843(1)	Uiso	1.00
C34	C	0.30825(94)	-0.19284(100)	-0.00487(98)	0.0843(1)	Uiso	1.00
C35	C	-0.49978(69)	0.00443(191)	-0.15309(147)	0.0843(1)	Uiso	1.00
C36	C	0.15285(70)	0.35855(79)	-0.59962(148)	0.0843(1)	Uiso	1.00
H1	H	0.39894(74)	0.34952(99)	0.01817(179)	0.0843(1)	Uiso	1.00
H2	H	0.42658(64)	0.23652(116)	0.03154(302)	0.0843(1)	Uiso	1.00
H3	H	0.38074(189)	0.29468(141)	0.16371(174)	0.0843(1)	Uiso	1.00
H4	H	0.14493(183)	-0.14884(110)	0.68103(140)	0.0843(1)	Uiso	1.00
H5	H	0.28341(223)	-0.10457(73)	0.71018(87)	0.0843(1)	Uiso	1.00
H6	H	0.26457(151)	-0.21902(76)	0.69765(67)	0.0843(1)	Uiso	1.00
H7	H	-0.48066(134)	0.17792(164)	0.36659(245)	0.0843(1)	Uiso	1.00
H8	H	-0.51232(76)	0.07688(258)	0.43813(105)	0.0843(1)	Uiso	1.00
H9	H	-0.60165(81)	0.11732(166)	0.30811(132)	0.0843(1)	Uiso	1.00
H10	H	0.06681(74)	-0.12873(55)	0.37551(137)	0.0843(1)	Uiso	1.00
H11	H	-0.11491(46)	0.17295(50)	0.11002(73)	0.0843(1)	Uiso	1.00
H12	H	0.19594(46)	0.05804(54)	0.25725(86)	0.0843(1)	Uiso	1.00
H13	H	-0.11795(46)	-0.04955(51)	0.34927(75)	0.0843(1)	Uiso	1.00
H14	H	0.06188(57)	0.24417(64)	0.09740(163)	0.0843(1)	Uiso	1.00
H15	H	-0.28173(46)	0.07685(96)	0.12450(91)	0.0843(1)	Uiso	1.00
H16	H	0.28835(284)	0.21160(82)	-0.16620(144)	0.0843(1)	Uiso	1.00
H17	H	0.25816(187)	0.32477(96)	-0.17585(72)	0.0843(1)	Uiso	1.00
H18	H	0.14611(234)	0.24868(140)	-0.16702(129)	0.0843(1)	Uiso	1.00
H19	H	-0.58239(85)	-0.02067(65)	0.18575(277)	0.0843(1)	Uiso	1.00
H20	H	-0.49364(98)	-0.06511(117)	0.31391(357)	0.0843(1)	Uiso	1.00
H21	H	-0.44663(123)	-0.06209(115)	0.15814(338)	0.0843(1)	Uiso	1.00
H22	H	0.42019(58)	-0.11071(86)	0.53162(246)	0.0843(1)	Uiso	1.00
H23	H	0.37338(137)	-0.15938(111)	0.38304(178)	0.0843(1)	Uiso	1.00
H24	H	0.39993(59)	-0.22475(82)	0.52182(161)	0.0843(1)	Uiso	1.00

H25	H	0.21633(61)	-0.25772(93)	0.21018(142)	0.0843(1)	Uiso	1.00
H26	H	0.12453(127)	-0.28529(64)	0.07473(193)	0.0843(1)	Uiso	1.00
H27	H	0.08192(47)	-0.20661(143)	0.18422(137)	0.0843(1)	Uiso	1.00
H28	H	0.35276(67)	0.25897(177)	-0.38633(124)	0.0843(1)	Uiso	1.00
H29	H	0.29062(163)	0.36348(148)	-0.37317(99)	0.0843(1)	Uiso	1.00
H30	H	0.37354(84)	0.34106(117)	-0.50118(68)	0.0843(1)	Uiso	1.00
H31	H	-0.42952(131)	0.18196(138)	-0.33410(442)	0.0843(1)	Uiso	1.00
H32	H	-0.47778(122)	0.18227(142)	-0.17890(453)	0.0843(1)	Uiso	1.00
H33	H	-0.56583(94)	0.14013(59)	-0.30955(340)	0.0843(1)	Uiso	1.00
H34	H	0.18349(76)	0.12436(11)	-0.46441(113)	0.0843(1)	Uiso	1.00
H35	H	-0.09704(44)	-0.02276(2)	-0.09888(69)	0.0843(1)	Uiso	1.00
H36	H	0.21558(44)	0.06224(24)	-0.22659(75)	0.0843(1)	Uiso	1.00
H37	H	-0.09527(44)	0.14656(19)	-0.42016(74)	0.0843(1)	Uiso	1.00
H38	H	0.18390(81)	-0.00093(37)	0.00154(106)	0.0843(1)	Uiso	1.00
H39	H	-0.26167(44)	0.06187(77)	-0.36903(82)	0.0843(1)	Uiso	1.00
H40	H	0.28189(159)	-0.24434(116)	-0.07315(118)	0.0843(1)	Uiso	1.00
H41	H	0.37263(90)	-0.22038(108)	0.06488(116)	0.0843(1)	Uiso	1.00
H42	H	0.34752(82)	-0.14038(146)	-0.05616(124)	0.0843(1)	Uiso	1.00
H43	H	-0.58744(69)	-0.00101(184)	-0.19531(157)	0.0843(1)	Uiso	1.00
H44	H	-0.50135(62)	0.03822(327)	-0.06154(100)	0.0843(1)	Uiso	1.00
H45	H	-0.46667(119)	-0.06141(198)	-0.13509(333)	0.0843(1)	Uiso	1.00
H46	H	0.13015(148)	0.41168(54)	-0.53719(236)	0.0843(1)	Uiso	1.00
H47	H	0.07604(47)	0.33778(162)	-0.65712(157)	0.0843(1)	Uiso	1.00
H48	H	0.21241(67)	0.38458(85)	-0.66412(151)	0.0843(1)	Uiso	1.00
F1	F	0.18243(87)	-0.22170(51)	0.45970(121)	0.0843(1)	Uiso	1.00
F2	F	0.18209(118)	0.34136(56)	0.04572(181)	0.0843(1)	Uiso	1.00
F3	F	-0.45300(52)	0.11109(131)	0.13917(119)	0.0843(1)	Uiso	1.00
F4	F	0.24130(124)	0.22028(33)	-0.60838(127)	0.0843(1)	Uiso	1.00
F5	F	0.24932(97)	-0.09562(58)	0.15126(104)	0.0843(1)	Uiso	1.00
F6	F	-0.43746(53)	0.00899(170)	-0.35954(140)	0.0843(1)	Uiso	1.00
N1	N	0.10136(46)	-0.06880(51)	0.38538(77)	0.0843(1)	Uiso	1.00
N2	N	0.10413(46)	0.18762(53)	0.11307(82)	0.0843(1)	Uiso	1.00
N3	N	-0.24742(46)	0.06402(54)	0.21354(80)	0.0843(1)	Uiso	1.00
N4	N	0.12834(44)	0.15813(5)	-0.41580(69)	0.0843(1)	Uiso	1.00

N5	N	0.12678(45)	-0.03399(23)	-0.05649(74)	0.0843(1)	Uiso	1.00
N6	N	-0.22895(44)	0.06207(25)	-0.27734(80)	0.0843(1)	Uiso	1.00
O1	O	0.24386(117)	0.00605(53)	0.49454(134)	0.0843(1)	Uiso	1.00
O2	O	0.26685(102)	0.11815(62)	0.07586(163)	0.0843(1)	Uiso	1.00
O3	O	-0.28826(53)	0.04484(134)	0.41889(75)	0.0843(1)	Uiso	1.00
O4	O	0.05132(112)	0.29108(25)	-0.38825(114)	0.0843(1)	Uiso	1.00
O5	O	0.04790(122)	-0.16664(24)	-0.09750(106)	0.0843(1)	Uiso	1.00
O6	O	-0.27695(53)	0.06268(139)	-0.07211(86)	0.0843(1)	Uiso	1.00

6.4 Strukturaufklärung von 2D supramolekularen organischen Verbindungen

Marko Schmidt,[a] Christoph S. Zehe,[a] Renée Siegel,[a] Johannes U. Heigl,[b] Christoph Steinlein,[b] Hans-Werner Schmidt[b] and Jürgen Senker*[a]

NMR-Crystallographic Study of Two-Dimensionally Self-Assembled Cyclohexane-Based Low-Molecular-Mass Organic Compounds

Erschienen in: *Cryst. Eng. Comm.* 2013, **15**, 8784. Reproduced by permission of The Royal Society of Chemistry.

[a] Lehrstuhl für Anorganische Chemie III, Universität Bayreuth, 95447 Bayreuth, Deutschland

[b] Lehrstuhl für Makromolekulare Chemie I, Universität Bayreuth, 95447 Bayreuth, Deutschland

* juergen.senker@uni-bayreuth.de

Darstellung des Eigenanteils:

Diese Publikation wurde von Prof. Dr. *Jürgen Senker* und mir konzipiert, ich löste die drei Kristallstrukturen aus Pulverdaten und war teilhabend an der Vorcharakterisierung der Materialien. Die drei Verbindungen wurden von *Johannes U. Heigl* hergestellt. Für die Durchführung der REM-Experimente waren *Christoph Steinlein* und *Johannes U. Heigl* verantwortlich. Die FK-NMR-Experimente sowie Simulationen wurden von *Christoph S. Zehe* unter Beratung von Dr. *Renée Siegel* durchgeführt. Verfasst wurde die Publikation von Prof. Dr. *Jürgen Senker*, Prof. Dr. *Hans-Werner Schmidt*, *Christoph S. Zehe* und mir. Mein Eigenanteil beläuft sich auf ca. 65 %.

6.4.1 NMR-Crystallographic Study of Two-Dimensionally Self-Assembled Cyclohexane-Based Low-Molecular-Mass Organic Compounds

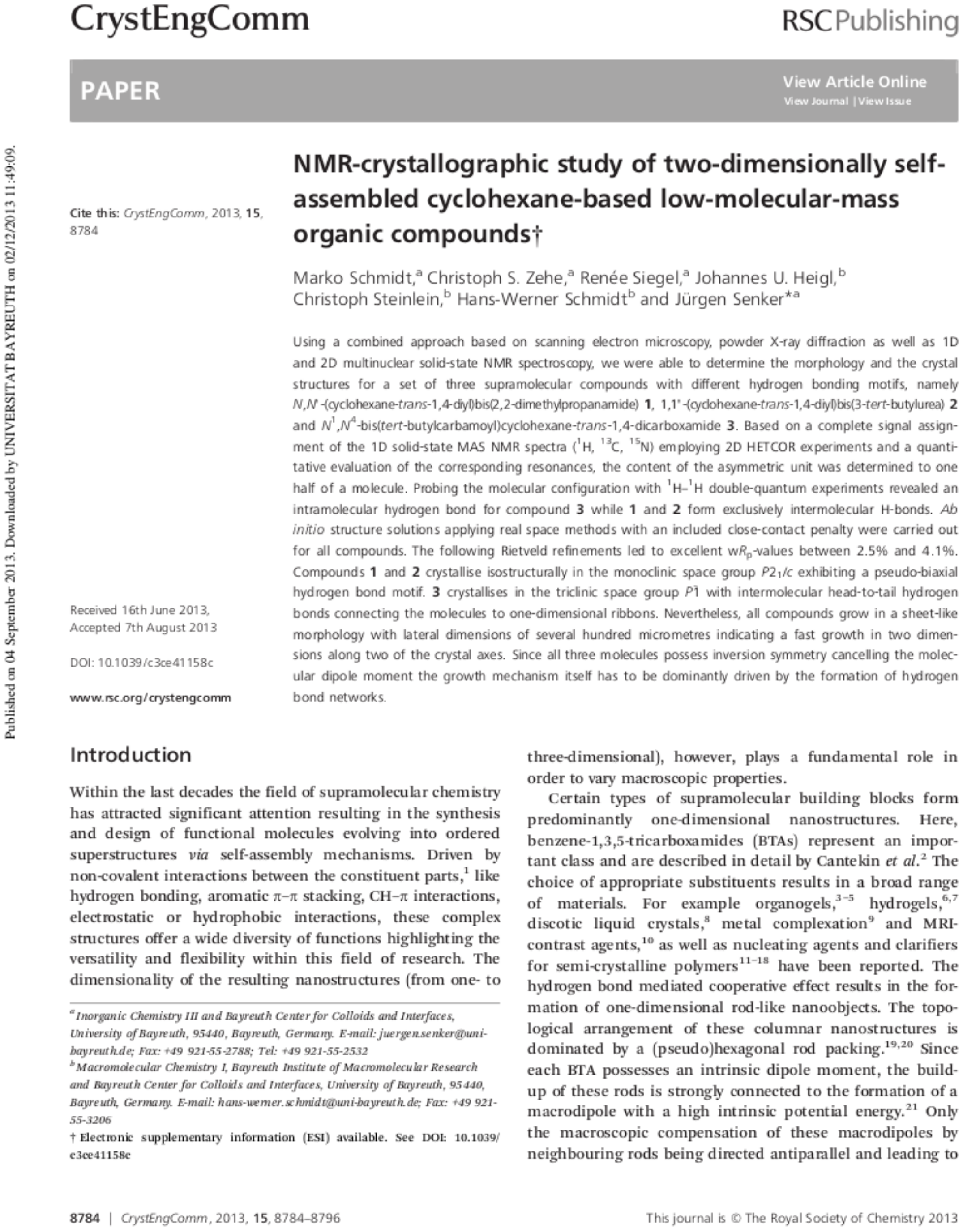

CrystEngComm

RSCPublishing

PAPER

View Article Online
View Journal | View Issue

Cite this: *CrystEngComm*, 2013, **15**, 8784

NMR-crystallographic study of two-dimensionally self-assembled cyclohexane-based low-molecular-mass organic compounds†

Marko Schmidt,[a] Christoph S. Zehe,[a] Renée Siegel,[a] Johannes U. Heigl,[b] Christoph Steinlein,[b] Hans-Werner Schmidt[b] and Jürgen Senker*[a]

Using a combined approach based on scanning electron microscopy, powder X-ray diffraction as well as 1D and 2D multinuclear solid-state NMR spectroscopy, we were able to determine the morphology and the crystal structures for a set of three supramolecular compounds with different hydrogen bonding motifs, namely *N*,*N*'-(cyclohexane-*trans*-1,4-diyl)bis(2,2-dimethylpropanamide) **1**, 1,1'-(cyclohexane-*trans*-1,4-diyl)bis(3-*tert*-butylurea) **2** and N^1,N^4-bis(*tert*-butylcarbamoyl)cyclohexane-*trans*-1,4-dicarboxamide **3**. Based on a complete signal assignment of the 1D solid-state MAS NMR spectra (^{1}H, ^{13}C, ^{15}N) employing 2D HETCOR experiments and a quantitative evaluation of the corresponding resonances, the content of the asymmetric unit was determined to one half of a molecule. Probing the molecular configuration with ^{1}H–^{1}H double-quantum experiments revealed an intramolecular hydrogen bond for compound **3** while **1** and **2** form exclusively intermolecular H-bonds. *Ab initio* structure solutions applying real space methods with an included close-contact penalty were carried out for all compounds. The following Rietveld refinements led to excellent wR_p-values between 2.5% and 4.1%. Compounds **1** and **2** crystallise isostructurally in the monoclinic space group $P2_1/c$ exhibiting a pseudo-biaxial hydrogen bond motif. **3** crystallises in the triclinic space group $P\bar{1}$ with intermolecular head-to-tail hydrogen bonds connecting the molecules to one-dimensional ribbons. Nevertheless, all compounds grow in a sheet-like morphology with lateral dimensions of several hundred micrometres indicating a fast growth in two dimensions along two of the crystal axes. Since all three molecules possess inversion symmetry cancelling the molecular dipole moment the growth mechanism itself has to be dominantly driven by the formation of hydrogen bond networks.

Received 16th June 2013,
Accepted 7th August 2013

DOI: 10.1039/c3ce41158c

www.rsc.org/crystengcomm

Introduction

Within the last decades the field of supramolecular chemistry has attracted significant attention resulting in the synthesis and design of functional molecules evolving into ordered superstructures *via* self-assembly mechanisms. Driven by non-covalent interactions between the constituent parts,[1] like hydrogen bonding, aromatic π–π stacking, CH–π interactions, electrostatic or hydrophobic interactions, these complex structures offer a wide diversity of functions highlighting the versatility and flexibility within this field of research. The dimensionality of the resulting nanostructures (from one- to three-dimensional), however, plays a fundamental role in order to vary macroscopic properties.

Certain types of supramolecular building blocks form predominantly one-dimensional nanostructures. Here, benzene-1,3,5-tricarboxamides (BTAs) represent an important class and are described in detail by Cantekin *et al.*[2] The choice of appropriate substituents results in a broad range of materials. For example organogels,[3–5] hydrogels,[6,7] discotic liquid crystals,[8] metal complexation[9] and MRI-contrast agents,[10] as well as nucleating agents and clarifiers for semi-crystalline polymers[11–18] have been reported. The hydrogen bond mediated cooperative effect results in the formation of one-dimensional rod-like nanoobjects. The topological arrangement of these columnar nanostructures is dominated by a (pseudo)hexagonal rod packing.[19,20] Since each BTA possesses an intrinsic dipole moment, the build-up of these rods is strongly connected to the formation of a macrodipole with a high intrinsic potential energy.[21] Only the macroscopic compensation of these macrodipoles by neighbouring rods being directed antiparallel and leading to

---

[a] *Inorganic Chemistry III and Bayreuth Center for Colloids and Interfaces, University of Bayreuth, 95440, Bayreuth, Germany. E-mail: juergen.senker@uni-bayreuth.de; Fax: +49 921-55-2788; Tel: +49 921-55-2532*

[b] *Macromolecular Chemistry I, Bayreuth Institute of Macromolecular Research and Bayreuth Center for Colloids and Interfaces, University of Bayreuth, 95440, Bayreuth, Germany. E-mail: hans-werner.schmidt@uni-bayreuth.de; Fax: +49 921-55-3206*

† Electronic supplementary information (ESI) available. See DOI: 10.1039/c3ce41158c

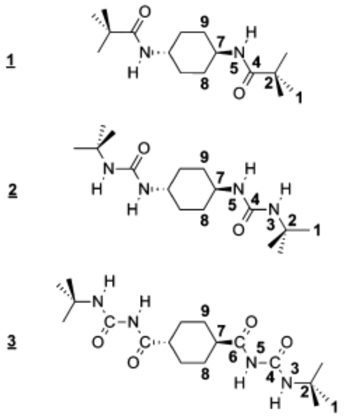

Scheme 1 Chemical structures of *N*,*N*′-(cyclohexane-*trans*-1,4-diyl)bis(2,2-dimethylpropanamide) **1**, 1,1′-(cyclohexane-*trans*-1,4-diyl)bis(3-*tert*-butylurea) **2** and N^1,N^4-bis(*tert*-butylcarbamoyl)cyclohexane-*trans*-1,4-dicarboxamide **3** with labelling of the atoms for the NMR signal assignment.

an antiferroelectric arrangement allows for a fast one-dimensional growth.

Recently, two-dimensional nanostructures with a high aspect ratio have gained increasing interest[22] with lateral dimensions ranging from a few hundred nanometres up to the micron scale. Well known inorganic examples are layered silicates[23] and graphene with exceptional properties.[24–29] Lately, a new pathway to two-dimensional nanoobjects has emerged based on supramolecular self-assembly of low-molecular-mass organic molecules (LMOs).[22] Among others, Zentel and co-workers reported a couple of bis-acylurea compounds possessing a C_5 or C_6 alkyl spacer with different functional end groups.[30,31] An in-depth understanding of the formation of these nanosheets is still challenging. It is quite evident that hydrogen bonding is important. However, the role of dipole moments or even macrodipoles as a driving force for the two-dimensional growth is still an open question.

In order to derive a deeper understanding of the structure–property relations of two-dimensional nanosheets, we selected three compounds with different hydrogen bond motifs. The materials (Scheme 1) are based on symmetric substituted *trans*-(1,4)-cyclohexane derivatives with increasing number of donor (NH) and acceptor groups (CO), namely amide **1**, urea **2** and acylurea **3** moieties. We focus on the *ab initio* structure solutions as well as the hydrogen bond networks of these three LMOs. Since the lack of suitable single crystals prevents using single crystal X-ray diffraction experiments, we employ NMR-crystallographic strategies to derive both detailed local and topological features of these compounds. To complement powder diffraction data with solid-state NMR experiments and computational modeling at various steps of the structure elucidation[32–35] has proven to be an efficient way to validate or disprove structure models.

Experimental section

Materials and instruments

All solvents were purified and dried prior to use according to standard procedures. The starting materials were purchased from ABCR, Acros, Aldrich, and TCI Europe and used as received. Elementary analysis (C, H, N) were carried out using a Vario elementar EL III instrument. Mass spectra were recorded at RT on a FINNIGAN MAT 112S instrument (70 eV) with electronic impact ionisation and direct probe inlet. SEM was performed on a Zeiss 1530 FESEM (3 kV) with a preceding platinum sputtering using a Cressington Sputter Coater 208HR.

Syntheses of 1–3

The general reaction schemes are depicted in Scheme S1 within the ESI.†

N,*N*′-(Cyclohexane-*trans*-1,4-diyl)bis(2,2-dimethylpropanamide) 1

Compound **1** was synthesised by dropping pivalic acid chloride (7.3 g, 61 mmol) to a mixture of *trans*-1,4-diaminocyclohexane (3 g, 26 mmol), pyridine (10 mL), LiCl (0.05 g) and *N*-methyl-2-pyrrolidone (NMP, 180 mL) at 0 °C under nitrogen atmosphere. The reaction mixture was heated to 80 °C and stirred overnight. The mixture was precipitated in cold water and the white solid was filtered off, dried under vacuum for 2 h (70 °C, 100 mbar) and re-crystallised from methanol. Yield: 4.5 g (16 mmol, 61.5%, based on *trans*-1,4-diaminocyclohexane). Anal. calculated for **1**: C, 68.04; H, 10.71; N, 9.92. Found: C, 67.34; H, 12.23; N, 9.80%. MS (70 eV), *m*/*z* (%): 282 (M^+, 3.3); 197 (10.4); 181 (74.5); 127 (5.7); 102 (100); 85 (9.4); 80 (6.6); 57 (3.8).

1,1′-(Cyclohexane-*trans*-1,4-diyl)bis(3-*tert*-butylurea) 2

Compound **2** was synthesised by dropping *tert*-butyl isocyanate (dissolved in 400 mL THF at room temperature, 5 g, 101 mmol) to a solution of *trans*-1,4-diaminocyclohexane in THF (10 g, 44 mmol) at 0 °C under argon atmosphere. The mixture was stirred overnight at 80 °C, filtered off, dried under vacuum and re-crystallised from methanol. Yield: 12 g (38 mmol, 87.3%, based on *trans*-1,4-diaminocyclohexane). Anal. calculated for **2**: C, 61.5; H, 10.32; N, 17.93. Found: C, 61.17; H, 11.10; N, 17.78%. MS (70 eV), *m*/*z* (%): 312 (M^+, 9.4); 212 (29.2); 197 (18.8); 139 (7.5); 113 (13.2); 96 (18.8); 68 (9.4); 58 (100); 41 (11.3).

N^1,N^4-Bis(*tert*-butylcarbamoyl)cyclohexane-*trans*-1,4-dicarboxamide 3

Compound **3** was synthesised by dropping a mixture of cyclohexane-*trans*-1,4-dicarbonyl dichloride (3.14 g, 15 mmol) and 3.65 mL pyridine to a solution of 1-*tert*-butyl urea (3.49 g, 30 mmol) in THF at 0 °C under argon atmosphere. The reaction mixture was stirred overnight at 70 °C, filtered off, dried under vacuum for 2 h at 70 °C and re-crystallised from DMF. Yield: 2.2 g (6 mmol, 40%, based on cyclohexane-*trans*-1,4-dicarbonyl dichloride). Anal. calculated for **3**: C, 58.64; H, 8.75; N, 15.21. Found: C, 58.42; H, 8.81; N, 15.16%. MS (70 eV), *m*/*z* (%): 353 (M^+, 91.5); 313 (4.7); 280 (33.9); 254 (15.1); 240 (7.5); 197 (6.6); 169 (14.1); 126 (29.2); 109 (3.7); 81 (17.9); 59 (100).

Ab initio structure determination with powder X-ray diffraction

PXRD measurements for compounds **1–3** were carried out in Debye–Scherrer geometry on a STOE StadiP diffractometer, which was equipped with Cu Kα_1 radiation (λ = 1.5406 Å) and a curved germanium monochromator (oriented according to the 111 plane). The samples were filled in capillary tubes with a diameter of 0.5 mm and measured in the 2Θ range of 3–50° with a step size of 0.015°. The powder diffractograms were fully handled using the module REFLEX PLUS from the commercial program package Accelrys MS Modeling (version 5.0).[36] After indexing, Pawley refinement and space group assignment, the structure solution step was performed by means of real-space methods using the parallel tempering algorithm. For every structure solution, the molecule was first geometry optimised using DFT methods (see section Computational methods). As starting models for compounds **1–3** only half a molecule was set into the asymmetric unit as one motion group. Besides the possible rotational and translational degrees of freedom, all sustainable torsion angles in each molecule fragment were set free during the structure solution. Additionally, a preferred orientation model (March–Dollase) was applied during the solution with focus on the shape of the crystallites (R_0) as well as the orientation of the normal of the crystal faces (a^*, b^*, c^*).[37]

For the Rietveld refinement, at first four cycles including a relaxation of atomic parameters, a global isotropic temperature factor and a preferred orientation correction according to the Rietveld–Toraya equation[38,39] were carried out. By taking into account energy considerations using the COMPASS force field,[40] the molecular structure was maintained without limiting rotational and translational degrees of freedom. The resulting number of refined structural parameters (see Table 1) is hence not strictly representative due to the application of the energy constraint during the refinement. This force field assisted refinement is based on a combined figure of merit (R_{comb}) with

$$R_{\text{comb}} = (1{-}w_{\text{comb}})wR_{\text{P}} + w_{\text{comb}}R_{\text{Energy}} \tag{1}$$

where w_{comb} represents the energy weighting factor that was set to 0.5. The energetic contribution, R_{Energy}, to the combined figure of merit is defined as follows:

$$R_{\text{Energy}} = \tanh\left(0.1\frac{E-E_{\text{min}}}{E_{\text{tol}}}\right) \tag{2}$$

where E represents the total energy, E_{min} the energy in the global minimum and E_{tol} the energy window above E_{min} in which possible structure solutions are tolerated. Here, the default value of 40 kcal mol^{-1} was used prohibiting the breaking of covalent bonds during the refinement and thus reducing the independent number of refined structural parameters markedly.

Table 1 Relevant crystallographic data for **1–3** from PRXD

	1	**2**	**3**
Formula	$C_{16}H_{30}N_2O_2$	$C_{16}H_{32}N_4O_2$	$C_{18}H_{32}N_4O_4$
M/g mol^{-1}	282.42	312.45	368.47
Crystal system	Monoclinic	Monoclinic	Triclinic
Space group	$P2_1/c$	$P2_1/c$	$P\bar{1}$
a/Å	14.183(3)	15.435(7)	6.092(3)
b/Å	6.159(1)	6.762(3)	7.325(4)
c/Å	9.889(2)	8.883(4)	12.473(6)
α/°	90	90	73.828(3)
β/°	98.383(1)	96.343(2)	83.507(3)
γ/°	90	90	87.597(2)
V/Å^3	854.6(8)	921.4(12)	531.1(8)
Z'/Z	0.5/2	0.5/2	0.5/1
ρ/g cm^{-3}	1.097(1)	1.125(2)	1.151(2)
T/K	293	293	293
U	0.20(1)	0.14(1)	0.23(1)
V	−0.021(3)	0.005(3)	−0.012(4)
W	0.0029(2)	0.0013(2)	0.0025(2)
NA	0.42(2)	0.79(4)	0.76(3)
NB	0.001(1)	0.002(2)	0.00(2)
Zero-point shift	−0.031(1)	0.009(1)	−0.021(1)
R_0[a]	0.223	0.654	0.868
a^*	0.9877(2)	−0.9885(3)	−0.109(5)
b^*	0.137(1)	0.147(2)	−0.087(9)
c^*	0.074(1)	0.030(2)	−0.990(1)
No. ref. struct. par.[b]	81	87	93
R_{p}	0.0272	0.0217	0.0157
wR_{p}	0.0411	0.0301	0.0254

[a] Preferred orientation coefficient of the sample according to the March–Dollase function representing a dimensionless value reflecting the shape of the crystallites; $R_0 < 1$ for platelets, $R_0 > 1$ for needles. [b] The number of refined structural parameters includes one isotropic temperature factor and three translational elements of each atom within the asymmetric unit. Since a COMPASS force field with an energy constraint was applied, the refinement of the atomic positions is not handled independently.

Afterwards, besides the adjustment of the lattice parameters, the pseudo-Voigt peak profile including FWHM with its profile parameters NA and NB were optimized. The pseudo-Voigt peak shape function as a linear combination of a Gaussian (G) and a Lorentzian (L) includes a Θ-dependent mixing parameter η whose Θ-dependence is thus given by

$$\eta(\Theta) = (NA + NB)2\Theta \tag{3}$$

where NA and NB are adjustable parameters. Besides, the zero-point shift, sample off-centering, asymmetry correction (Finger–Cox–Jephcoat)[41] and the experimental background using 20 orthogonal polynomials were refined. For both refinement steps, 15 evaluations per cycle per degree of freedom were performed. Relevant crystallographic data are summarized in Table 1. Atomic parameters, the temperature factor and the occupancy of **1–3** are included in the CIF files which are provided in the ESI.†

Solid-state NMR spectroscopy

^{1}H and ^{13}C chemical shifts are referenced to TMS ($\delta_{\text{ref}}((^1H_3C)_4Si)$ = 0 ppm, $\delta_{\text{ref}}((H_3{}^{13}C)_4Si)$ = 0 ppm), ^{15}N chemical shifts are reported with respect to nitromethane (δ_{ref}(H_3C–$^{15}NO_2$) = 0 ppm). The spin rate for all MAS experiments was set to 10 000 ± 1 Hz. The 1D ^{1}H-DUMBO and 2D ^{1}H–^{1}H double-quantum-single-quantum (DQ-SQ) correlation experiments were performed on a Bruker Avance III spectrometer at a proton resonance frequency of 400 MHz with a 3.2 mm triple resonance probe. The CP and the HETCOR experiments on ^{13}C and ^{15}N were performed on a Bruker Avance II spectrometer with a proton frequency of 300 MHz using a 4 mm triple resonance probe. For the latter experiments proton broadband decoupling was realised with a SPINAL64 sequence during acquisition. The nutation frequency and pulse length were set to 72 kHz and 5.6 µs (^{15}N)/6.8 µs (^{13}C), respectively.

For the ^{1}H-DUMBO experiments the DUMBO pulse length and the nutation frequency were adjusted to 30.50 µs and 89.3 kHz, respectively. The total window length between the DUMBO pulses during acquisition was set to 5.6 µs with a dead time delay of 1.2 µs before acquiring a point. A CRAMPS scaling factor of $\lambda_{scaling} = 0.5$ was determined on glycine, where all isotropic chemical shifts are well known.[42] Subsequently, the shifts of all ^{1}H DUMBO spectra were corrected accordingly.

In the case of the ^{1}H–^{1}H DQ-SQ correlation experiments, double quantum excitation and reconversion was achieved through the $R20_2^9$ sequence[43] and high resolution in both dimensions through a DUMBO sequence.[44] For the R-elements, 90–270° composite pulses were used with 80 µs excitation/reconversion time (corresponding to 8 R-elements each) and 100 kHz of nutation frequency. The desired coherences were selected through an eight-fold phase cycling. For DUMBO in the indirect dimension the window length was set to 4.6 µs with an increment of three DUMBO cycles, whereas all remaining parameters for DUMBO in both dimensions were the same as in the one-dimensional DUMBO experiments. For both the indirect and direct dimension a scaling factor of $\lambda_{scaling} = 0.5$ was determined as described above.

The 1D CP spectra of ^{13}C and ^{15}N were recorded using a ramp on the proton channel and a contact time of 5 ms with nutation frequencies of 35/45 kHz for ^{15}N/^{13}C. For the ^{1}H–^{15}N/^{13}C HETCOR experiments a DUMBO sequence was applied in the indirect dimension with a pulse length of 28.8 µs, a nutation frequency of 91 kHz, a delay of 2 µs and four/three DUMBO cycles as increment. Magnetization transfer was achieved using the PRESTO-II sequence.[45] It ensures that spin diffusion between the protons during the contact time is suppressed in contrast to conventional magnetisation transfer by CP. For all compounds, the transfer time for PRESTO was set to 178 µs according to 16 R-elements before and after the 90° pulse probing only the closest ^{1}H–^{13}C and ^{1}H–^{15}N distances. Thus, correlation signals only correspond to covalently bonded nuclei. The nutation frequency for ^{1}H and ^{15}N/^{13}C during PRESTO was set to 90 kHz and 39/70 kHz, while the FID was recorded after a spin echo for refocusing the chemical shift interaction. The refocusing period was chosen to one/two rotor periods for ^{15}N/^{13}C, respectively. An eight-fold phase cycling allowed the selection of the desired coherences.

Computational methods

Before the *ab initio* structure solutions of compounds **1–3**, all molecules were geometry optimised by DFT methods using the module DMol3 from the program package Accelrys MS Modeling (version 5.0).[36] Here, the double zeta plus polarisation basis set with the GGA functional PW91 was applied.[46] The self-consistent field (SCF) energy convergence was set to 1.0–6 eV per atom.

Results and discussion

Morphology

Morphological analyses using scanning electron microscopy (SEM) reveal a two-dimensional growth of compounds **1**, **2** and **3**. Large platelets possessing a high aspect ratio were obtained from hot isotropic solutions of butan-2-one with concentrations between 50 and 500 ppm depending on their solubility. Bisamide **1** shows platelets with well-defined edges and a widely homogenous surface (Fig. 1a) whereas bisurea **2** exhibits partly fringed edges but also a homogenous surface (Fig. 1b). At a first glance the bisacylurea **3** shows sharp edges and a homogenous surface as well. However, when magnifying the edge of the platelet, it becomes clear that one platelet consists of several thin sheets (Fig. 1c). In contrast, no fine structure can be determined by using SEM in case of **1** and **2**.

Structural information obtained from solid-state NMR spectroscopy

Compounds **1–3** form only microcrystalline powders preventing structure analysis by single crystal X-ray diffraction. Since this circumstance is not specific for our samples but a common case for organic substances, the development of alternative structure elucidation methods for powder samples is necessary. *Ab initio* structure solutions employing solely PXRD data are often hampered by a severe loss of information. Symmetry equivalent reflexes always coincide and higher order reflexes overlap heavily, reducing the number of independent intensity information.[47] While topological information might still be obtained with reasonable accuracy, local structural details are strongly affected.[34,47] In this context, solid-state NMR spectroscopy provides complementary data and thus evolved into an important element of NMR crystallographic strategies. Meanwhile, solid-state NMR is able to participate in nearly all steps of the structure solution process starting from space group selection, over model building up to the final Rietveld refinement.[19,47–50] Symmetry information including the content of the asymmetric unit might be obtained by deriving Wyckoff spectra[48,51] from high-resolution experiments and by determining rotational symmetry elements[47,52,53] based on orientation correlations of CSA tensors of neighbouring nuclei. Analysing hetero- and homonuclear connectivities, distances, distance sums and even torsion angles measured by 1D and 2D dipolar recoupling experiments support the construction of structure models.[19,20,32–34,49,50] The expressiveness of such measurements is significantly increased by

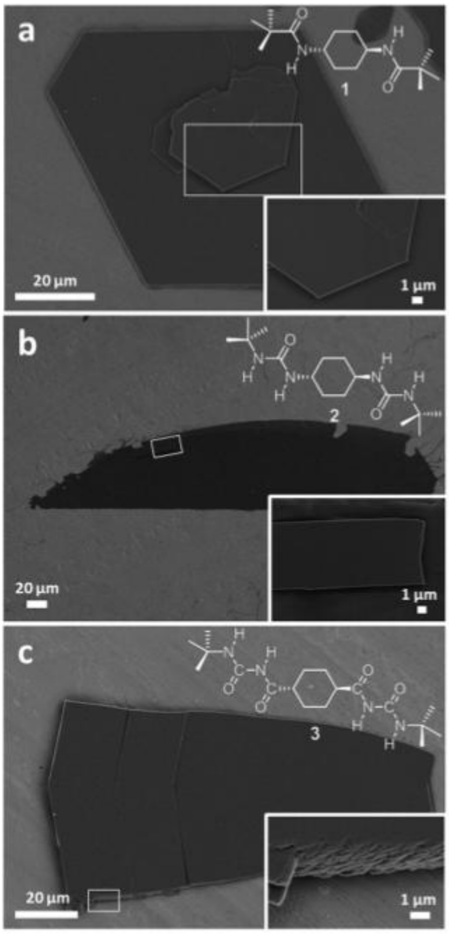

Fig. 1 SEM images of two-dimensional structures of (a) bisamide **1** (500 ppm), (b) bisurea **2** (200 ppm) and (c) bisacylurea **3** (50 ppm) formed in butan-2-one. The regions where the magnified images (insets) have been collected are marked using white boxes.

combination with quantum chemical calculations.[54,55] For instance, hydrogen bond scenarios can be probed by combining *ab initio* chemical shift calculations and high-resolution NMR measurements.[34,54,56] Even the substructure of light atoms like hydrogen has successfully been determined.[32,50] Since most of these methods require high resolution spectra, hetero- and homonuclear decoupling of strongly coupled spin systems like protons is necessary. Moreover, for a correct interpretation of these spectra, a complete assignment of all signals is essential, which can be obtained through 2D heteronuclear correlation experiments.

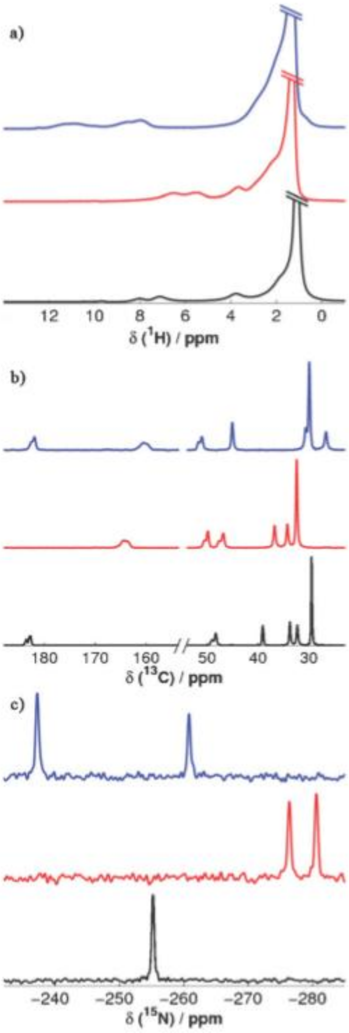

Fig. 2 1D MAS spectra at ν_{MAS} = 10 kHz for compounds **1** (black), **2** (red) and **3** (blue): (a) ^{1}H-DUMBO (B_0 = 9.4 T); the strong signal of the methyl groups is truncated to highlight the weaker resonances, in particular the NH signals; (b) ^{13}C CP-MAS (B_0 = 7.04 T); (c) ^{15}N CP-MAS (B_0 = 7.04 T). For the CRAMPS experiments the chemical shifts are corrected according to glycine ($\lambda_{scaling}$ = 0.5).

Following this strategy, information about hydrogen bond patterns, configurations and symmetries of the crystal structures of compounds **1–3** are deduced. In particular, we support the *ab initio* structure solutions by PXRD through solid-state NMR experiments on the three NMR-active nuclei

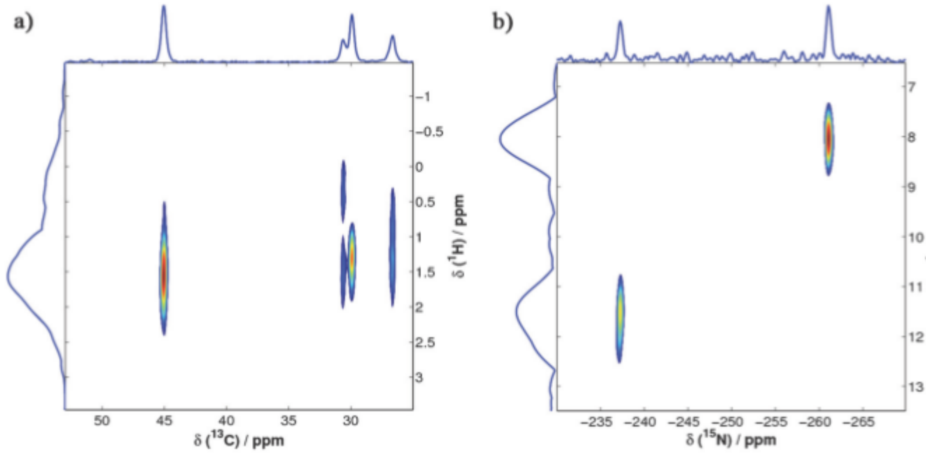

Fig. 3 (a) ^{1}H–^{13}C-HETCOR and (b) ^{1}H–^{15}N-HETCOR spectrum of compound **3**, at B_0 = 7.04 T and ν_{MAS} = 10 kHz. The ^{1}H chemical shifts in the f1 domains are corrected according to glycine ($\lambda_{scaling}$ = 0.5). The transfer time was set to 178 μs visualising only directly bonded protons.

^{1}H, ^{13}C and ^{15}N. First, a complete assignment of 1D high-resolution spectra of ^{1}H, ^{13}C, ^{15}N experiments through 2D ^{1}H–^{13}C and ^{1}H–^{15}N HETCOR spectra is conducted. Fig. 2 depicts high-resolution 1D spectra of ^{1}H, ^{13}C and ^{15}N for all three compounds. The assignment will be done exemplarily for compound 3, since the procedure for the remaining samples is almost identical. The 2D ^{1}H–^{13}C-HETCOR and ^{1}H–^{15}N-HETCOR experiments for that purpose are pictured in Fig. 3a and 3b.

The ^{1}H-DUMBO spectrum of 3 shows a sharp, intense peak at δ = 1.3 ppm (Fig. 2a). This signal couples in the ^{1}H–^{13}C-HETCOR to a carbon signal at δ = 29.9 ppm (Fig. 3a). Both the ^{13}C and ^{1}H shifts are indicative for CH_3 groups. Moreover, the sharpness and high intensity of both peaks are characteristic for CH_3 for the following reasons: first, the well-known rotation of the groups around the C–CH_3 bond truncates dipolar coupling to other spins, which raises the transversal relaxation time and thus reduces the width of the peaks for both spins. Second, the high abundance of CH_3 protons increases their signals in DUMBO as well as in ^{13}C CP. The carbon signals at δ = 30.6 ppm and – remarkably shielded – at δ = 26.6 ppm correspond to the two different sets of CH_2 groups within the cyclohexane ring, one carbon signal with couplings to the resolved proton shifts at δ = 0.4 and 1.6 ppm, the other one with two overlapping proton signals at *ca.* δ = 0.8 and 1.3 ppm. The CH unit of the ring is assigned to the more deshielded peak at δ = 1.6 ppm for ^{1}H, coupling to the carbon signal at δ = 45.0 ppm, since both carbon and proton shifts are typical for CH groups. The remaining signals in the ^{13}C CP (Fig. 2b, δ = 51.2 ppm, 155.3 ppm and 177.2 ppm) do not give rise to cross correlation peaks in the ^{1}H–^{13}C-HETCOR and are thus not covalently bonded to protons. The peak at δ = 51.2 ppm in the ^{13}C CP spectrum is unequivocally assigned to the quaternary carbon atom of the *tert*-butyl group while the two remaining signals at δ = 155.3 ppm and 177.2 ppm belong to the C═O groups. A comparison of their line shapes observed at different magnetic fields of 7.1 T and 9.4 T, respectively, reveals an inverse dependence of the splitting on the field strength. This line shape is, therefore, caused by second order quadrupolar interaction between the neighbouring ^{14}N nucleus and the ^{13}C spins.[57] This was also reproduced by simulations of 1D spectra for a ^{13}C–^{14}N spin pair with the program WSOLIDS1 (see Fig. S2b in the ESI†).[20,58]

To assign the remaining peaks in the ^{1}H-DUMBO at δ = 8.0 ppm, 8.6 ppm and 11.2 ppm, ^{1}H–^{15}N HETCOR experiments were performed (Fig. 3b). The ^{15}N CP spectrum of 3 (Fig. 2c) reveals two different peaks at δ = −237.2 ppm and −261.0 ppm. Here, the ^{15}N site at δ = −261.0 ppm shows correlations with a single proton signal at δ = 8.4 ppm. Since already the carbon atoms directly bound to a nitrogen atom were influenced through second order quadrupolar interaction, a single-pulse experiment under MAS at a higher magnetic field strength and a line shape simulation using WSOLIDS1 were conducted (Fig. S1and Table S1 in the ESI†).[58] It becomes clear that the two peaks at δ = 8.0 and 8.6 ppm correspond to a single proton with an isotropic shift of δ = 8.4 ppm. This effect is well-known for NH groups.[57] The remaining ^{15}N signal at δ = −237.2 ppm shows only one correlation in the ^{1}H–^{15}N HETCOR to the proton signal at δ = 11.2 ppm and thus corresponds to the second NH group.

In order to assign the two carbonyl and the two NH signals to the corresponding chemical units, the experimental resonances were compared to chemical shifts in solution-state NMR, being calculated based on an increment system according to ref. 58 (see Table S2 in the ESI†).[59] Here, the carbon groups C_4 and C_6 of the acylurea group which are

Table 2 Chemical shifts in ppm for all ^{1}H, ^{13}C and ^{15}N of compounds **1–3** (for labelling see Scheme 1). The asterisks indicate average shifts for cases where the corresponding signals show a splitting due to second order quadrupolar interaction with ^{14}N. All spectra used for assignment of **1** and **2** are contained in the ESI† (Fig. S3 and S4)

Atom	1	2	3	Unit
C_1	29.5	32.4	29.9	CH_3
C_2	39.0	50.0*	51.2*	C_q
C_4	178.2*	159.2*	155.3*	C=O
C_6	—	—	177.2*	C=O
C_7	48.7*	47.2*	45.0	CH
C_8	32.3	34.2	26.6	CH_2
C_9	33.7	36.7	30.6	CH_2
N_3	—	−280.6	−261.0	NH
N_5	−255.2	−276.4	−237.2	NH
H_1	1.1	1.3	1.3	CH_3
H_3	—	6.0*	8.4*	NH
H_5	7.4*	6.1*	11.2	NH
H_7	3.5	3.3	1.6	CH
H_8	1.4	0.5/1.0	0.8/1.3	CH_2
H_9	1.0	1.0/1.5	0.4/1.6	CH_2

connected to the *tert*-butyl unit and the cyclohexane ring, respectively, show a shift of δ = 155.7 ppm and δ = 179.4 ppm, which is close to the observed shifts of δ = 155.3 ppm and 177.2 ppm in the solids. In the case of ^{15}N, for the two nitrogen atoms N_3 and N_5 shifts of δ = −277.2 ppm and −246.0 ppm are predicted, whereas the observed shifts are δ = −261.0 ppm and −237.2 ppm. Considering that the solid-state shifts of ^{15}N in NH groups are usually influenced more strongly by *e.g.* hydrogen bonds than in the case of ^{13}C, the predicted values show a sufficient agreement with the observed ones.

Thus, all signals in the 1D ^{1}H, ^{13}C and ^{15}N spectra have unequivocally been assigned to the molecular units of compound 3. This procedure was also applied to compounds 1 and 2. The corresponding values for the chemical shifts are summarized in Table 2.

The 1D CP spectra of ^{15}N show only one NH peak for compound 1 and two peaks for 2 and 3. The molecular structures, however, exhibit two nitrogen atoms in the case of 1 and four in the case of 2 and 3. The same comparison applies for the 1D CP spectra of ^{13}C and the ^{1}H-DUMBO, where the structures always show twice the number of groups than the number of observed resonances. Thus, the asymmetric unit contains just half a molecule and, therefore, both molecular and space group symmetry include a two-fold axis or an inversion centre. The number of possible space groups for structure solutions is thus reduced which will be discussed at a later point.

In order to gain information about spatial proximities of NH protons and thus also possible hydrogen bond patterns of the molecules, we used ^{1}H–^{1}H DQ-SQ correlation experiments. The NH regions of these spectra are exemplarily depicted in Fig. 4 for compound 2 and 3 (for compound 1 see Fig. S5 in the ESI†).

For compound 2, both peaks around δ = 5.4 ppm and 6.4 ppm correspond to two overlapping NH signals of the urea unit with isotropic shifts of δ = 6.0 ppm and 6.1 ppm (extracted from ^{1}H–^{15}N HETCOR, see Fig. S4 in the ESI†), both split by the neighbouring ^{14}N (see Table 2). Besides correlations of the NH protons to the aliphatic region (see Fig. S6 in the ESI†), correlations of the NH signals among themselves between δ = 10.8 ppm and 12.8 ppm in the double-quantum dimension are observed. Since the line shapes are affected by the ^{14}N nuclei, we cannot distinguish between cross correlations and autocorrelations. However, both cases indicate spatial proximity of NH protons to other

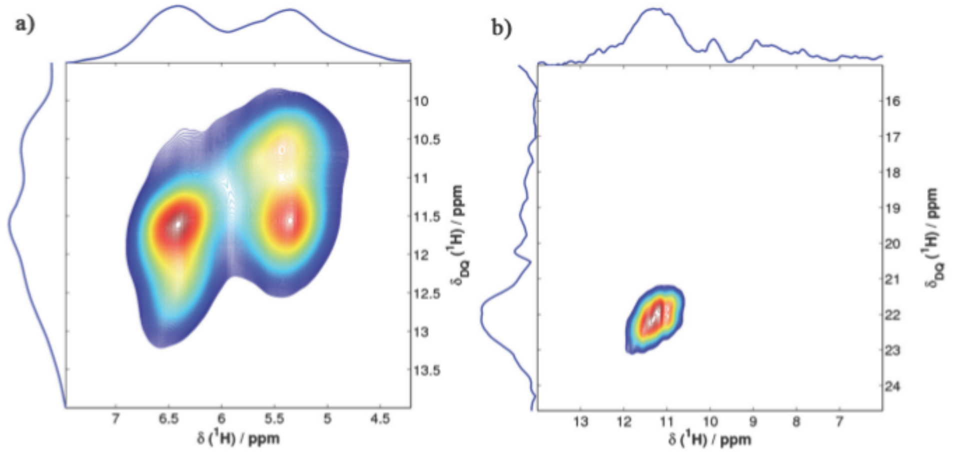

Fig. 4 ^{1}H–^{1}H DQ-SQ correlation spectra of (a) compound **2** and (b) compound **3** at B_0 = 9.4 T and ν_{MAS} = 10 kHz. The excitation and reconversion time was set to 80 μs in both cases for which only the shortest distance correlations are observed. Both chemical shifts of f1 and f2 are corrected according to glycine ($\lambda_{scaling}$ = 0.5). Here, the region around the NH protons is shown (the whole spectra are depicted in Fig. S6 and S7 in the ESI†).

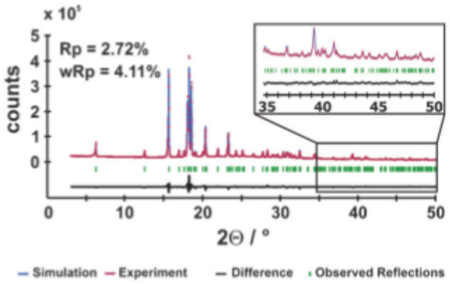

Fig. 5 Rietveld profile plot of the powder X-ray diffraction pattern of **1** for the solution in space group $P2_1/c$ collected at room temperature in the 2θ range 3–50°. The section of the 2θ range of 35–50° shows that even at high 2θ values the simulation fits excellently to the experimental powder pattern.

NH protons. Since the NH units in urea groups usually favour a *trans–trans* configuration each with the connected carbonyl group (*e.g.* as depicted in Scheme 1 for compound 2) due to energetic reasons, typical H–H distances for this configuration score around 2 Å.[60] Strong DQ coherences as detected in Fig. 4a for 2 are thus characteristic for such short distance.

In contrast, for compound 3 only one weak autocorrelation signal is observed for the NH proton H_5 (δ(SQ/DQ) = 11.4 ppm/22.8 ppm). First, this clearly indicates a spatial proximity between H_5 protons of the inner NH groups. This is only possible when neighbouring molecules are arranged in a hydrogen bond pattern. Second, for the NH signal of proton H_3 at δ = 8.4 ppm no self-correlation signal is observed (δ(DQ, theo) = 16.8 ppm) and thus the intermolecular distances of H_3 protons have to be much longer compared to the ones of H_5. Additionally, no correlation between H_3 and H_5 was detected either (δ(DQ,theo) = 19.9 ppm). This implies a long intermolecular distance between those NH protons of the same acylurea unit ($d > 2$ Å) and thus allows determining the molecular configuration. In compound 3 just an additional C═O group is inserted compared to 2 (acylurea compared to urea unit). For an all-*trans* configuration of the acylurea group again a distance around 2 Å between H_3 and H_5 and, therefore, an intense DQ correlation signal similar to Fig. 4a is expected. However, a *trans–cis–trans* configuration leads to a distance of more than 3.5 Å rendering the H_3–H_5 DQ correlation unobservable under the chosen experimental conditions. The resulting spatial proximity between the oxygen atom of the inner C═O group and the NH proton H_3 favours the formation of an intramolecular hydrogen bond which might stabilise this configuration. The encapsulation of H_3 in this intramolecular hydrogen bond might also explain the absence of any autocorrelation signal. These results indicate a pair-like arrangement of the molecules within the crystal structure.

Structural information obtained by powder X-ray diffraction

The crystal structures for **1–3** were all obtained by *ab initio* structure solutions based on powder X-ray diffraction applying real-space methods using the combination of a close-contact penalty and wR_p, respectively, as cost functions. All molecules were DFT geometry optimised before performing the structure solutions revealing in all cases a chair conformation of the cyclohexane ring as well as C_i symmetry which is energetically favoured over the also previously discussed C_2 symmetry. The inversion centre is thereby positioned in the centre of gravity of the cyclohexane ring. In accordance to the ^{1}H–^{1}H DQ-SQ experiments the *trans–cis–trans* configuration of the acylurea unit in compound 3 revealed the lowest energy during DFT optimisation.

$C_{16}H_{30}N_2O_2$ 1 and $C_{16}H_{32}N_4O_2$ 2. The indexing of the powder patterns lead unequivocally to a monoclinic metric in both cases and could subsequently be refined in $P2$ using the Pawley algorithm. Assuming that all non-hydrogen atoms within these compounds possess a volume of roughly 18 Å^3, the molecular volumes can be estimated to 360 Å^3 and 396 Å^3, respectively. This size restriction just allows for two molecules within the unit cell at maximum. The reflection conditions do not provide reasonable results for any of the five *C*-centred space groups but, nevertheless, all remaining 8 primitive ones might be possible. However, based on the symmetry considerations obtained by 1D ^{15}N and ^{13}C solid-state NMR (compare Fig. 3b and 3c) whereupon only half a molecule is located in the asymmetric unit, all possible space groups with the multiplicity of 2 on general positions ($P2$, $P2_1$, Pm and Pc) – then leading to only one molecule in the unit cell – could be excluded. Therefore, only four space groups ($P2/m$, $P2_1/m$, $P2/c$ and $P2_1/c$) remained and, taking into account the reflection conditions, $P2_1/c$ fitted the experimental powder pattern best.

The structure solutions with subsequent Rietveld refinement reveal that **1** and **2** are isostructural and crystallise in the monoclinic space group $P2_1/c$ (for crystallographic information: see Table 1 in the experimental details section). Representative for both compounds, the Rietveld profile plot for **1** is depicted in Fig. 5 (the Rietveld profile plot for **2** is visualised in Fig. S8 in the ESI†). The *a*-axis of **2** is roughly 1.2 Å longer than for **1** while the *c*-axis is shortened by *ca.* 1 Å. The monoclinic angle is slightly reduced by 2° resulting in an increased cell volume of about 65 Å^3 which perfectly agrees with the volume requirement of two additional NH groups.

Fig. 6 shows the molecular crystal structure as well as extended packing plots of *N,N′*-(cyclohexane-*trans*-1,4-diyl)bis(2,2-dimethylpropanamide) **1**. Here, the cyclohexane ring exists in the low-energy chair conformation while the (1,4)-amide linkage exhibits *trans*-configuration on the tertiary carbon atom in the ring as synthesised. The internal $H_4N_4C_4O_4$ torsion angle within the molecule picturing the amide bond is 179.5° which is close to 180° as expected for an amide function (see Fig. 6a) leading to almost coplanarity caused by the inversion symmetry of the molecule itself.

The bisamide compound is characterised by an extended 2D hydrogen bond network. Due to the internal C_i symmetry, only one NH···O length of 2.11 Å is observed. The corresponding N···O distance amounts to 3.1 Å while the NH···O angle of almost 167° is only slightly below the ideal value of 180° demonstrating medium-strong hydrogen bonds. The *trans*-configuration

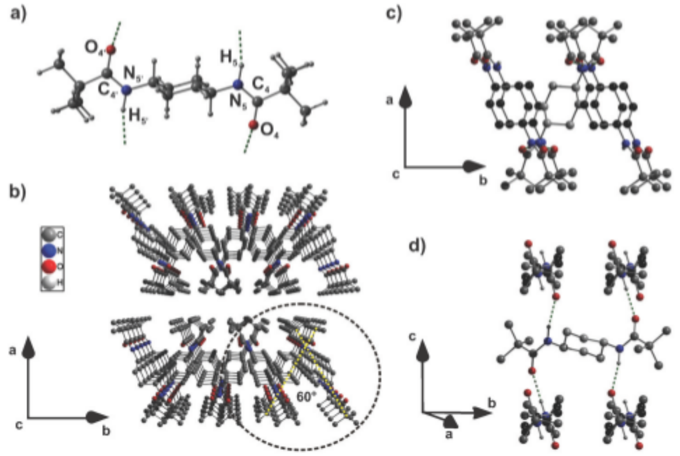

Fig. 6 Molecular structure and extended crystal packing plots of compound **1** with hydrogen bonds highlighted in green dashed lines. (a) Molecular structure of **1** represented with all four hydrogen bond interactions with labelling of the amide function as performed in Scheme 1. (b) Section of the crystal structure viewing along the *c*-axis. The dashed yellow lines represent the opening angle of the molecules main axes projected into the *ab*-plane of the crystal. (c) Cutout of the structure presented in panel b (black dashed circle) showing that one molecule (grey cyclohexane carbon atoms) is enclosed by four molecules (black cyclohexane carbon atoms), two below and two above. This cutout is rotated by 5° along the *b*-axis. (d) Packing plot showing that every molecule builds hydrogen bonds to four neighbouring molecules in one direction. This packing plot is obtained by −90° rotation along the *a*-axis followed by a −35° rotation along the *b*-axis as presented in panel c. All hydrogen atoms except the nitrogen-bonded ones have been omitted in (b)–(d) for clarity.

of the amide functions hence guarantees the formation of two H-bond strands in one direction which is schematically depicted in Fig. 6a.

The propagating direction of the H-bond strands is thereby aligned parallel to the *c*-axis of the crystal leading to a fast growth along this crystal axis. A closer look on the packing motif reveals two additional important features. First, both molecules within the unit cell are twisted towards each other. When assuming a straight line along the main axis of each molecule propagating through the quaternary carbon atoms of the *t*-butyl group followed by a projection into the *ab*-plane of the crystal, an opening angle of 60° is obtained (see Fig. 6b, yellow dashed lines). Second, each amide function within one molecule (NH/CO as donor/acceptor) is connected to one independent counterpart within another molecule. So, every molecule is attached to four neighbouring molecules (see Fig. 6c and 6d) where one donor group interacts with one acceptor group (and *vice versa*). Due to the twist of the molecules, however, a second 'indirect' propagation direction along the *b*-axis that also possesses the tendency of growing fast is observed. Since along the crystals' *a*-axis only van der Waals interactions seem to play the major role – the shortest proton–proton distance being obtained along this crystal axis amounts to 2.44 Å – the corresponding rate of growth is much smaller compared to the growth along the *b*- and *c*-axis, respectively.

Analogous results are obtained for the bisurea compound **2** with an identical molecular geometry as observed for **1** (see Fig. 7a). Nevertheless, the urea group is not perfectly planar with corresponding torsion angles ($H_3N_3C_4O_4$ and $H_5N_5C_4O_4$) of almost 167°. So, the oxygen atom of the carbonyl group is shifted slightly out of the planar $H_3N_3C_4N_5H_5$-plane in order to form a hydrogen bond network properly. Since one urea group possesses two NH-donor groups, two different H-bond lengths might be observed. Nevertheless, the two bonds are almost equal with bond lengths of 2.19 Å and 2.23 Å, which is consistent with the results extracted from the ^{1}H and ^{15}N chemical shifts (compare Fig. 2a and 2b), while the corresponding N···O distances result in 3.13 Å and 3.17 Å. All these distances are slightly longer than found for the bisamide **1**. This tendency is also true for the related NH···O angles which are 154.2° and 153.5°. Therefore, the hydrogen bonds for the bisurea are supposed to be weaker than the ones obtained for the bisamide. However, the H-bond pattern obtained for **2** is more complex than for **1** due to the additional NH group. Compared to **1**, the urea group undertakes the same role as the amide function. Therefore, one acceptor carbonyl group is connected to two NH-donor groups and *vice versa* so that one molecule is H-bond connected to four neighbouring molecules, too (see Fig. 7c and 7d).

This is, for example, in contrast to other bisurea compounds where each molecule is hydrogen-bonded to only two other molecules placed below and above it to self-assemble into 1D fibrillar aggregates.[60,61] Nevertheless, the nature of the urea group itself enables the molecules to form again two H-bond strands as already observed for compound **1**. The propagation direction can also be described as parallel to the *c*-axis of the crystal, so a comparable fast growth in this direction is obtained. Moreover, since also an opening angle

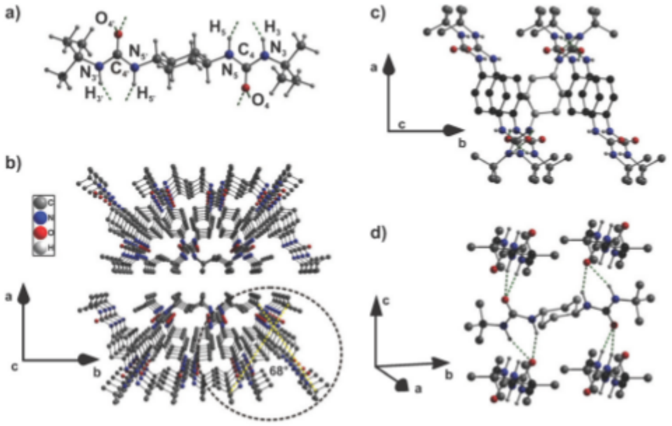

Fig. 7 Molecular structure and extended crystal packing plots of compound **2** with hydrogen bonds highlighted in green dashed lines. (a) Molecular structure of **2** represented with all eight hydrogen bond interactions with labelling of the amide function as performed in Scheme 1. (b) Section of the crystal structure viewing along the *c*-axis. The dashed yellow lines represent the opening angle of the molecules main axes projected into the *ab*-plane of the crystal. (c) Cutout of the structure presented in panel b (black dashed circle) showing that one molecule (grey cyclohexane carbon atoms) is enclosed by four molecules (black cyclohexane carbon atoms), two below and two above. This cutout is rotated by 5° along the *b*-axis. (d) Packing plot showing that every molecule builds hydrogen bonds to four neighbouring molecules in one direction. This packing plot is obtained by −90° rotation along the *a*-axis followed by a −25° rotation along the *b*-axis as presented in panel c. All hydrogen atoms except the nitrogen-bonded ones have been omitted in (b)–(d) for clarity.

between the two twisted molecules within the unit cell of 68° is observed (see Fig. 7b, yellow dashed lines), a second fast growth direction along the *b*-axis is ensured. The discrepancy of 8° is based on the increased length of the bisurea molecule with its accompanying H-bond capabilities that need a broadening of this angle to achieve a sufficient donor–acceptor interaction. Due to the van der Waals forces as the dominating interaction along the crystals' *a*-axis – as already observed for **1** – a fast growth in this direction is inhibited. Here, the shortest intermolecular proton–proton distance with 2.46 Å is thereby identical as obtained for the bisamide.

$C_{18}H_{32}N_4O_4$ 3. The indexing of the powder pattern of compound **3** revealed a triclinic metric that was successfully refined in *P*1 using the Pawley algorithm. Based on the symmetry information obtained by the 1D ^{15}N and ^{13}C spectra (Fig. 2b and 2c), respectively, where the content of the asymmetric unit was limited to half a molecule, $P\bar{1}$ was considered to be the correct space group. Therefore, **3** crystallises in $P\bar{1}$ with crystallographic data summarised in Table 1. The Rietveld profile plot is depicted in Fig. S9 in the ESI.†

The unit cell consists of one C_i-symmetric molecule based on only half a crystallographic independent molecule in the asymmetric unit. The molecule itself possesses similar structural behaviour as already obtained for compounds **1** and **2** (chair conformation of the cyclohexane ring, see Fig. 8a). The acylurea unit itself is perfectly planar with amide torsion angles of 178.8° ($H_3N_3C_4O_4$ and $H_5N_5C_6O_6$, both *trans*-configured) and 0.8° ($H_5N_5C_4O_4$, *cis*-configured) respectively, leading to a perfect coplanarity (see Fig. 8a). Furthermore, the directly bonded non-urea carboxylic group is twisted towards the cyclohexane ring with a torsion angle ($H_7C_7C_6O_6$) of almost 133°. This alignment far beyond the ideal 180° might explain the significant shielding of the CH_2 group with a chemical shift of δ = 26.6 ppm obtained in the ^{13}C CP spectrum (see Fig. 2b) and, moreover, can guarantee the formation of an H-bond network which will be discussed later. As already confirmed by ^{1}H–^{1}H DQ-SQ solid-state NMR (see Fig. 4, right side) and strongly supported by the DFT geometry optimisation, the acylurea unit possesses a *trans–cis–trans* configuration (Fig. 8a). Here, an intrinsic (1,6)-hydrogen bond with a length of 1.96 Å forming a stable six-membered ring is built. The corresponding N···O distance as well as the NH···O angle are 2.69 Å and 126°.

In 2007, Davis *et al.* reported the structure of a similar bisacylurea compound obtained by single crystal X-ray diffraction where an aliphatic pentyl group was chosen as a linker between the acylurea groups (BUC5BU).[31] Here, the molecule possesses an intrinsic C_2 symmetry with the same configuration of the acylurea group as observed for our molecule. The two-fold axis thereby propagates directly through the middle carbon atom of the C_5 linking unit.

Beyond that, the *cis* HNCO units forming the intramolecular hydrogen bond point in the same direction as in contrast to the C_i symmetric compound **3** (see Fig. 8b). However, the intramolecular H-bond distance of 2.09 Å and the corresponding N···O distance of 2.74 Å is longer than observed for the cyclohexane derivative while, surprisingly, the NH···O angle (128.6°) is larger. When comparing the planarity, it becomes obvious that the acylurea group of the BUC5BU compound is slightly out of plane with torsion angles of 169.9° ($H_5N_5C_6O_6$, *trans*),

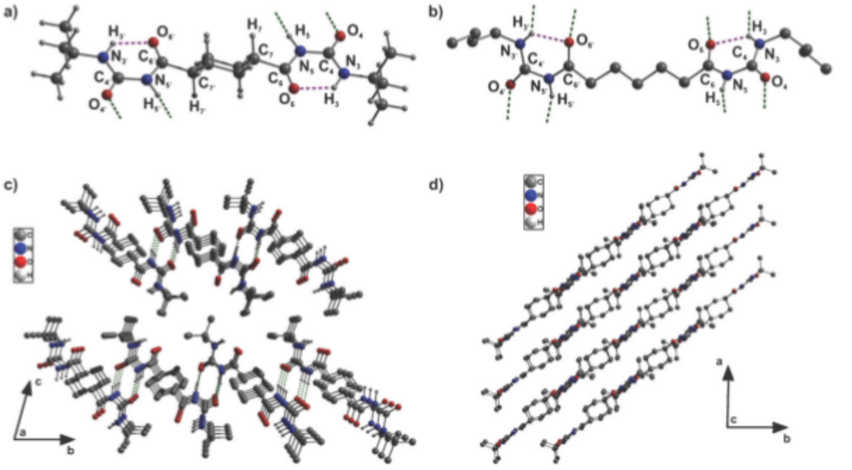

Fig. 8 Molecular structures of compound **3** (a) and BUC5BU[31] (b) represented with intra- and intermolecular hydrogen bonds (dashed pink and green lines, respectively) with labelling of the acylurea units as performed in Scheme 1. (c) Section of the crystal structure of **3** viewed along the *a*-axis. The dashed green lines represent the intermolecular hydrogen bonds to two neighbouring molecules parallel to the crystals' *c*-axis. (d) Section of the crystal structure of **3** viewed along the *c*-axis. This packing plot is obtained by 100° rotation along the *a*-axis, followed by a small rotation (−10°) along the *b*-axis. All hydrogen atoms except the nitrogen-bonded ones have been omitted in (c) and (d) for clarity.

3.9° ($H_5N_5C_4O_4$, *cis*) and 180° ($H_3N_3C_4O_4$, *trans*), respectively, analogous to the angles obtained for **3**. But, moreover, the acylurea moieties of the molecule do show a non-coplanarity with a mutual interplanar angle of 43.3°.

The crystal structure of **3** is schematically pictured in Fig. 8c and 8d. According to the H-bond pattern, it is worth mentioning that only the *cis*-configured amide functions participate in two intermolecular hydrogen bonds each forming in principle one intermolecular six-membered ring (similar to the one already observed in case of the intramolecular H-bond). Interestingly, the corresponding counterpart within a neighbouring molecule also belongs to the *cis*-configured amide function (see Scheme 2a). The number of neighbouring molecules for each molecule therefore is two, which is in contrast to the ones obtained for the compounds **1** and **2**. This alignment in pairs could already be validated by ^{1}H–^{1}H DQ-SQ solid-state NMR experiments (see Fig. 4). While no cross correlation signal between the two different NH-protons (H_3 and H_5) was observed since the proton–proton distance of ~3.6 Å is too long, an auto correlation signal for the NH-protons H_5 was found ($d(H_5–H_5$ = 2.5 Å). In case of the BUC5BU compound from ref. 31, however, a similar ^{1}H–^{1}H DQ-SQ spectrum as obtained for compound **2** could be expected (compare Fig. 4a), since an intermolecular H_3–H_5 distance of ~3 Å might still be detectable within the applied excitation time.

However, an extensive 2D hydrogen bond pattern – as observed for **1** and **2** – is impossible to realise due to this intermolecular *cis*-arrangement of the amide functions (compare Scheme 2a). Nevertheless, the obtained H-bond of 1.75 Å is very short with an N···O distance of 2.75 Å and, therefore, has to be categorised as strong which is in very good agreement with the chemical shift of roughly δ = 11.4 ppm for this NH-proton obtained in the 1D ^{1}H solid-state NMR spectrum (see Table 2). This fact is, furthermore, corroborated by the NH···O angle of 174° which is very close to the ideal 180°. The direction of the intermolecular hydrogen bonds is therefore parallel to the *c*-axis of the crystal. Since only three molecules are involved in this pattern, the self-assembly can – per definition – only be described as classical monoaxial. Though, the self-assembly direction is established by stepwise adding of new molecules along the crystals' *b*-axis *via* hydrogen bonds and, therefore, the fast growth is also observed along this axis. Nevertheless, since the molecules themselves are twisted by almost 45° compared to both the H-bond direction (*c*-axis) as well as the growth direction (*b*-axis), a two-dimensional morphology as observed in SEM can still be obtained (see Fig. 8d).

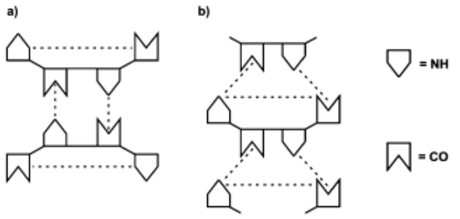

Scheme 2 Donor–acceptor interactions observed for (a) compound **3** forming one intra- and two intermolecular hydrogen bonds per half molecule and (b) BUC5BU forming one intra- and four intermolecular hydrogen bonds per half molecule. The black dashed lines represent the hydrogen bonds between the NH- and CO-groups.

In comparison, the BUC5BU structure presented in ref. 31 shows a different hydrogen bond pattern. It is evident that the *cis*-configured amide function ($O_4C_4N_5H_5$) builds intermolecular hydrogen bonds, but they are not connected to other *cis*-configured amide functions but rather with the appropriate donor/acceptor counterpart that also forms the intramolecular H-bond (see Scheme 2b). So, in principle every molecule is involved in four six-membered rings, two intramolecular and four intermolecular ones. Here, the correspondent hydrogen bond lengths result in 2.11 Å and 2.16 Å, respectively, while the N···O distances of 2.88 Å and 2.99 Å are much longer than observed for the cyclohexane derivative 3. Interestingly, the particular NH···O angles are 135° and 159°, respectively, suggesting that the intermolecular H-bonds for our bisacylurea compound are much stronger than observed for BUC5BU. Nevertheless, the compound investigated by Davis *et al.* possesses a classic biaxial hydrogen bond system where each BUC5BU molecule is hydrogen-bonded to four adjacent molecules as already described for **1** and **2**. This, however, might be caused due to the intrinsic molecular C_2 symmetry while a centrosymmetric molecular symmetry (compound **3**) leads only to a classical monoaxial hydrogen bond system.

Conclusion

In summary, three cyclohexane-based compounds with different hydrogen bond motifs were characterised by scanning electron microscopy, solid-state NMR, PXRD and computational methods based on DFT. SEM measurements revealed sheet-like morphologies for all three compounds with lateral dimensions of several hundred micrometres with substantial aspect ratios. The crystal structures of those compounds were elucidated by means of NMR-crystallographic strategies. Based on an unequivocal signal assignment of the 1D spectra by performing ^1H–^{13}C- and ^1H–^{15}N HETCOR experiments also considering the $^1H/^{14}N$- and $^{13}C/^{14}N$ second-order quadrupolar interaction we were able to restrict the space group symmetry and to determine the content of the asymmetric unit. The evaluation of ^1H–^1H DQ-SQ spectra revealed spatial proton–proton connectivities of the NH groups for all compounds. Additionally for compound **3**, they allowed probing both the molecular configuration such as the existence of the intramolecular hydrogen bond and the local environment like the H-bond pattern leading to a pair-like molecular arrangement. This information was crucial to make the *ab initio* structure solutions by real-space methods more efficient and remove ambiguities.

Compounds **1** and **2** crystallise in $P2_1/c$ and their crystal structures exhibit an interesting "pseudo-biaxial" hydrogen bond system where each molecule is directly connected to four neighbouring molecules *via* moderate H-bonds. Caused by the crossed alignment of the molecules within the unit cell (see Fig. 6d and 7d), the H-bond mediated strands are growing fast in two directions even though both H-bond strands are parallel, while the growth in the third dimension is retarded resulting in two-dimensional nanosheets. Although such a structural motif was also observed for one similar benzene-based compound[62] no connection to a fast two-dimensional growth was made. This arrangement is an alternative to the classical variant where the hydrogen bond strands are crossed instead of the molecules. In compound **3** (crystallising in $P\bar{1}$), on the other hand, each molecule forms H-bonds to two adjacent molecules, leading to a one-dimensional ribbon-like structure per definition. It is remarkable that this compound still shows a sheet-like morphology. This might be caused by the special arrangement of the molecules in the packing with respect to the crystal axes.

An important aspect with respect to the growth process of the sheets deals with the role of dipole moments for the growth mechanism. For the growth of one-dimensional rod like nanostructures – *e.g.* cyclohexane- or benzenetrisamides – it is known that dipole forces play an important role.[21] Here, every molecule possesses an intrinsic dipole moment. Within one rod, this dipole moment strongly increases and so-called macrodipoles are generated. In order to obtain an antiferroelectric crystal being energetically favoured, all macrodipoles must be compensated by an antiparallel arrangement of themselves.[63] The net dipole moment of zero is thereby achieved during the crystallisation process. This argument is also valid for the BUC5BU compound investigated in ref. 31. Even if a two-dimensional self-assembly is achieved, the intrinsic C_2 symmetry of the molecules implies an intrinsic dipole moment, too, which is only compensated due to the space group symmetry during crystallisation as well. In contrast, for the two-dimensional sheet like nanostructures presented here, dipole forces or even macrodipoles do not play a major role. The dipole moment is already cancelled in each molecule due to the inversion symmetry of the molecules themselves. So, the fast growth of the nanostructures in two directions (**1** and **2**) (or one direction for compound **3**, respectively) giving two-dimensional nanosheets is, therefore, mainly induced by the hydrogen bond mediated donor–acceptor interactions between the appropriate molecular counterparts.

Acknowledgements

The authors want to thank the DFG (SFB 840, Project B4) for funding this work, Anna-Maria Dietel for performing the elementary analysis and Dr. Wolfgang Milius for the adjuvant discussions with respect to crystallographic issues.

References

1 J.-M. Lehn, *Angew. Chem., Int. Ed. Engl.*, 1990, **29**, 1304.
2 S. Cantekin, T. F. A. de Greef and A. R. A. Palmans, *Chem. Soc. Rev.*, 2012, **41**, 6125.
3 Y. Yasuda, E. Iishi, H. Inada and Y. Shirota, *Chem. Lett.*, 1996, 575.
4 K. Hanabusa, C. Koto, M. Kimura, H. Shirai and A. Kakehi, *Chem. Lett.*, 1997, 429.
5 J. J. van Gorp, J. A. J. M. Vekemans and E. W. Meijer, *J. Am. Chem. Soc.*, 2002, **124**, 14759.

6 N. Shi, H. Dong, G. Yin, Z. Xu and S. Li, *Adv. Funct. Mater.*, 2007, **17**, 1837.

7 A. Bernet, R. Q. Albuquerque, M. Behr, S. T. Hoffmann and H.-W. Schmidt, *Soft Matter*, 2012, **8**, 66.

8 Y. Matsunaga, N. Miyajima, Y. Nakayasu, S. Sakai and M. Yonenaga, *Bull. Chem. Soc. Jpn.*, 1988, **61**, 207.

9 M. Gelinsky, R. Vogler and H. Vahrenkamp, *Inorg. Chem.*, 2002, **41**, 2560.

10 P. Besenius, J. L. M. Heynens, R. Straathof, M. M. L. Nieuwenhuizen, P. H. H. Bomans, E. Terreno, S. Aime, G. J. Strijkers, K. Nicolay and E. W. Meijer, *Contrast Media Mol. Imaging*, 2012, **7**, 356.

11 M. Blomenhofer, S. Ganzleben, D. Hanft, H.-W. Schmidt, M. Kristiansen, P. Smith, K. Stoll, D. Maeder and K. Hoffmann, *Macromolecules*, 2005, **38**, 3688.

12 P. M. Kristiansen, A. Gress, P. Smith, D. Hanft and H.-W. Schmidt, *Polymer*, 2006, **47**, 249.

13 F. Abraham, S. Ganzleben, D. Hanft, P. Smith and H.-W. Schmidt, *Macromol. Chem. Phys.*, 2010, **211**, 171.

14 J. Wang, Q. Dou, X. Chen and D. Li, *J. Polym. Sci., Part B: Polym. Phys.*, 2008, **46**, 1067.

15 F. Richter and H.-W. Schmidt, *Macromol. Mater. Eng.*, 2013, **298**, 190.

16 H. Nakajima, M. Takahashi and Y. Kimura, *Macromol. Mater. Eng.*, 2010, **295**, 460.

17 H. Bai, W. Zhang, H. Deng, Q. Zhang and Q. Fu, *Macromolecules*, 2011, **44**, 1233.

18 P. Song, Z. Wei, J. Liang, G. Chen and W. Zhang, *Polym. Eng. Sci.*, 2012, **52**, 1058.

19 M. Schmidt, J. J. Wittmann, R. Kress, D. Schneider, S. Steuernagel, H.-W. Schmidt and J. Senker, *Cryst. Growth Des.*, 2012, **12**, 2543.

20 M. Schmidt, J. J. Wittmann, R. Kress, H. W. Schmidt and J. Senker, *Chem. Commun.*, 2013, **49**, 267.

21 R. Q. Albuquerque, A. Timme, R. Kress, J. Senker and H.-W. Schmidt, *Chem.–Eur. J.*, 2013, **19**, 1647.

22 T. Govindaraju and M. B. Avinash, *Nanoscale*, 2012, **4**, 6102.

23 M. Stöter, D. A. Kunz, M. Schmidt, D. Hirsemann, H. Kalo, B. Putz, J. Senker and J. Breu, *Langmuir*, 2013, **29**, 1280.

24 M. B. Avinash, K. S. Subrahmanyam, Y. Sundarayya and T. Govindaraju, *Nanoscale*, 2010, **2**, 1762.

25 K. S. Novoselov, D. Jiang, F. Schedin, T. J. Booth, V. V. Khotkevich, S. V. Morozov and A. K. Geim, *Proc. Natl. Acad. Sci. U. S. A.*, 2005, **102**, 10451.

26 J. C. Meyer, A. K. Geim, M. I. Katsnelson, K. S. Novoselov, T. J. Booth and S. Roth, *Nature*, 2007, **446**, 60.

27 A. K. Geim and K. S. Novoselov, *Nat. Mater.*, 2007, **6**, 183.

28 C. N. R. Rao, A. K. Sood, K. S. Subrahmanyam and A. Govindaraj, *Angew. Chem., Int. Ed.*, 2009, **48**, 7752.

29 K. S. Subrahmanyam, P. Kumar, U. Maitra, A. Govindaraj, K. P. S. S. Hembram, U. V. Waghmare and C. N. R. Rao, *Proc. Natl. Acad. Sci. U. S. A.*, 2011, **108**, 2674.

30 J.-U. Kim, R. Davis and R. Zentel, *J. Colloid Interface Sci.*, 2011, **359**, 428.

31 R. Davis, R. Berger and R. Zentel, *Adv. Mater.*, 2007, **19**, 3878.

32 L. Seyfarth, J. Seyfarth, B. V. Lotsch, W. Schnick and J. Senker, *Phys. Chem. Chem. Phys.*, 2010, **12**, 2227.

33 E. Wirnhier, M. Döblinger, D. Gunzelmann, J. Senker, B. V. Lotsch and W. Schnick, *Chem.–Eur. J.*, 2011, **17**, 3213.

34 L. Seyfarth, J. Sehnert, N. El-Gamel, W. Milius, E. Kroke, J. Breu and J. Senker, *J. Mol. Struct.*, 2008, **889**, 217.

35 R. K. Harris, *Analyst*, 2006, **131**, 351.

36 Accelrys software inc. *MS Modeling v5.0.0.0* Copyright 2009.

37 W. A. Dollase, *J. Appl. Crystallogr.*, 1986, **19**, 267.

38 H. M. Rietveld, *J. Appl. Crystallogr.*, 1969, **2**, 65.

39 H. Toraya and F. Marumo, *Mineral. J.*, 1981, **10**, 211.

40 H. Sun, *J. Phys. Chem. B*, 1998, **102**, 7338.

41 L. W. Finger, D. E. Cox and A. P. Jephcoat, *J. Appl. Crystallogr.*, 1994, **27**, 892.

42 E. Salager, R. S. Stein, S. Steuernagel, A. Lesage, B. Elena and L. Emsley, *Chem. Phys. Lett.*, 2009, **469**, 336.

43 M. H. Levitt, *Encycl. Nucl. Magn. Reson.*, 2002, **9**, 165.

44 D. Sakellariou, A. Lesage, P. Hodgkinson and L. Emsley, *Chem. Phys. Lett.*, 2000, **319**, 253.

45 X. Zhao, W. Hoffbauer, J. S. auf der Günne and M. H. Levitt, *Solid State Nucl. Magn. Reson.*, 2004, **26**, 57.

46 J. P. Perdew and Y. Wang, *Phys. Rev. B: Condens. Matter Mater. Phys.*, 1992, **45**, 13244.

47 J. Senker, L. Seyfarth and J. Voll, *Solid State Sci.*, 2004, **6**, 1039.

48 F. W. Karau, L. Seyfarth, O. Oeckler, J. Senker, K. Landskron and W. Schnick, *Chem.–Eur. J.*, 2007, **13**, 6841.

49 D. Hirsemann, T. K.-J. Köster, J. Wack, L. van Wüllen, J. Breu and J. Senker, *Chem. Mater.*, 2011, **23**, 3152.

50 L. Seyfarth and J. Senker, *Phys. Chem. Chem. Phys.*, 2009, **11**, 3522.

51 F. Taulelle, *Solid State Sci.*, 2004, **6**, 1053.

52 J. Senker, J. Sehnert and S. Correll, *J. Am. Chem. Soc.*, 2005, **127**, 337.

53 J. Sehnert and J. Senker, *Chem.–Eur. J.*, 2007, **13**, 6339.

54 J. Sehnert, K. Bärwinkel and J. Senker, *J. Mol. Struct. (THEOCHEM)*, 2007, **824**, 58.

55 J. Sehnert, K. Baerwinkel and J. Senker, *J. Phys. Chem. B*, 2007, **111**, 10671.

56 J. Schmidt, A. Hoffmann, H. W. Spiess and D. Sebastiani, *J. Phys. Chem. B*, 2006, **110**, 23204.

57 R. Harris and A. Olivieri, *Prog. Nucl. Magn. Reson. Spectrosc.*, 1992, **24**, 435.

58 K. Eichele, *WSolids1, version 1.20.17*, Universität Tübingen, 2012.

59 Predicted NMR data calculated using Advanced Chemistry Development, Inc. (ACD/Labs) *Software V12.5* (© 1994–2013 ACD/Labs).

60 J. H. van Esch, F. Schoonbeek, M. de Loos, H. Kooijman, A. L. Spek, R. M. Kellogg and B. L. Feringa, *Chem.–Eur. J.*, 1999, **5**, 937.

61 M. de Loos, J. van Esch, R. M. Kellogg and B. L. Feringa, *Angew. Chem., Int. Ed.*, 2001, **40**, 613.

62 H.-Z. Guo, G.-D. Yin, N.-F. She and A.-X. Wu, *Acta Cryst.*, 2005, **E61**, 04062.

63 J. Senker and J. Lüdecke, *Z. Naturforsch., B: J. Chem. Sci.*, 2001, **56b**, 1089.

6.4.2 Supporting Information

Electronic Supplementary Information

to

NMR-Crystallographic Study of Two-Dimensionally Self-Assembled Cyclohexane-Based Low-Molecular-Mass Organic Compounds†

Marko Schmidt,[a] Christoph S. Zehe,[a] Renée Siegel,[a] Johannes U. Heigl,[b]
Christoph Steinlein,[b] Hans-Werner Schmidt[b] and Jürgen Senker*[a]

[a] Inorganic Chemistry III and Bayreuth Center for Colloids and Interfaces, University of Bayreuth, Universitätsstr. 30, 95447 Bayreuth, Germany.

Tel: +49(0)921552532; E-mail: juergen.senker@uni-bayreuth.de

[b] Macromolecular Chemistry I, Bayreuth Institute of Macromolecular Research and Bayreuth Center for Colloids and Interfaces, University of Bayreuth, Universitätsstr. 30, 95447 Bayreuth, Germany.

Tel: +49(0)921553200; E-mail: hans-werner.schmidt@uni-bayreuth.de

Synthesis of compounds 1 - 3

The principal reaction schemes of the classical addition and elimination reactions is visualised in Scheme S1. The full conversion of the educts as well as the purity of the products was confirmed by means of elementary analysis (CHN), mass spectrometry and powder X-ray diffraction. The CHN analysis revealed a good agreement between calculated and experimental values (compare experimental section in the main article).

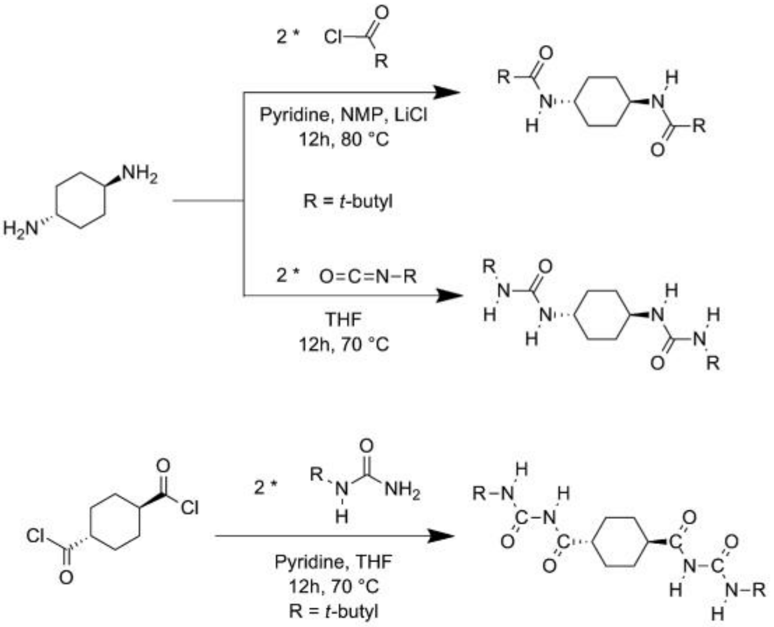

Scheme S1 Schematic representation of the synthetic routes to obtain **1** and **2** (based on *trans*-1,4-diaminocyclohexane) and **3** (based on cyclohexane-*trans*-1,4-dicarbonyl dichloride).

Explanation of the ^{14}N - effect

A comparison of ^{13}C CP measurements on 300 MHz and 400 MHz spectrometers is depicted in Figure S1a. Here, for each compound the spectrum measured at higher field shows a decrease of the splitting. This is in accordance with the trend of the second-order quadrupolar interaction which depends inversely on the field strength. For ^{1}H, the influence of ^{14}N can be visualised in the same way by comparing one-pulse proton spectra measured at different magnetic fields. Exemplarily, this is pointed out for compound **1** in Figure S1b. Here, the blue line represents a ^{1}H one-pulse experiment at a proton frequency of 400 MHz with ν_{rot} = 22.5 kHz (bottom), while the backline corresponds to a measurement at a 300 MHz device with ν_{rot} = 32.5 kHz (top). The former shows only one signal without additional splitting perfectly matching with the molecular structure obtained for **1**. The latter one, on the other hand, possesses a shoulder which can easily be misinterpreted as a second signal but is based on the ^{14}N interaction. Complementary results are obtained for **2** and **3** (not shown here).

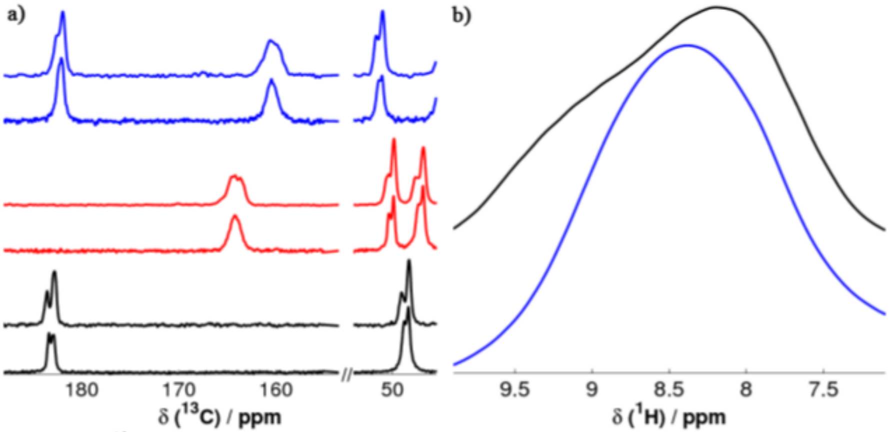

Fig. S1 (a) ^{13}C CP spectra of the three compounds (black = **1**, red = **2**, blue = **3**), where for each compound the lower spectrum corresponds to proton frequency of 400 MHz and the upper spectrum to 300 MHz; all spectra are recorded at a spinning rate of 10 kHz; (b) ^{1}H one-pulse spectra of compound **3** measured at a proton frequency of 400 MHz and a rotation frequency of 22.5 kHz (blue line, bottom) and 300 MHz at a rotation frequency of 32.5 kHz (black line, top).

To strengthen this argument, simulations of both ^{13}C CP and ^{1}H DUMBO spectra (both measured at B_0 = 7.04 T) including a ^{14}N effect were performed using the freeware program WSOLIDS1.[1] The simulations were done exemplarily for C_6 and H_3 (compare Table 2 in the main article) within the acylurea unit of compound **3** since the resonances of these nuclei are sustainably influenced by the neighboured ^{14}N nucleus. For getting reasonable starting values for ^{13}C, a comparable OC-NH system was taken from literature.[2] Here the quadrupolar coupling constant (C_Q = -3.2 MHz), the asymmetry parameter (η = 0.22), the azimuth angle of the internuclear ^{13}C-^{14}N vector in the principal axis system of the electric field gradient (EFG) tensor (α = 43°) as well as the polar angle of the internuclear ^{13}C-^{14}N vector in the principal axis system of the EFG tensor (β = 90°) were extracted. The isotropic chemical shift was set to δ = 177.15 ppm while the direct dipolar coupling constant ($d_{^{13}\text{C-}^{14}\text{N}}$ = 840 Hz) was calculated according to the crystal structure obtained by PXRD. For the indirect scalar dipolar coupling between ^{13}C and ^{14}N ("*J*-coupling") 7 Hz was adjusted. A similar procedure was performed for the ^{1}H spectrum. Due to the same orientations of the EFG tensors of both ^{14}N nuclei the values for C_Q and η are equal. The isotropic chemical shift was set to δ = 8.29 ppm while the direct dipolar coupling constant ($d_{^{1}\text{H-}^{14}\text{N}}$ = 8250 Hz) was calculated according to the crystal structure. For the indirect scalar dipolar coupling between ^{1}H and ^{14}N 65 Hz was chosen which was recalculated from $^{1}J(^{1}\text{H},^{15}\text{N})$-couplings of comparable compounds from literature.[3] For both simulations, the values of the direct as well as scalar dipolar coupling constant were not varied while all other values were refined during the simulation. Both the simulated and experimental spectra are depicted in Figure S2. For a more detailed description of the theoretical background the reader is referred to ref. 2.

Table S1 Summary of the parameters used for the simulations of the ^{1}H and ^{13}C spectrum, respectively.

	^{1}H (H_3)	**^{13}C (C_6)**
δ_{CS} / ppm	**8.29**	**177.15**
$d_{\text{X-}^{14}\text{N}}$ / Hz	**8250**	**840**
$J_{\text{X-}^{14}\text{N}}$ / Hz	**65**	**7**
C_Q / MHz	**-3.1**	**-3.1**
η	**0.42**	**0.4**
α / °	**5**	**44**
β / °	**85**	**85**

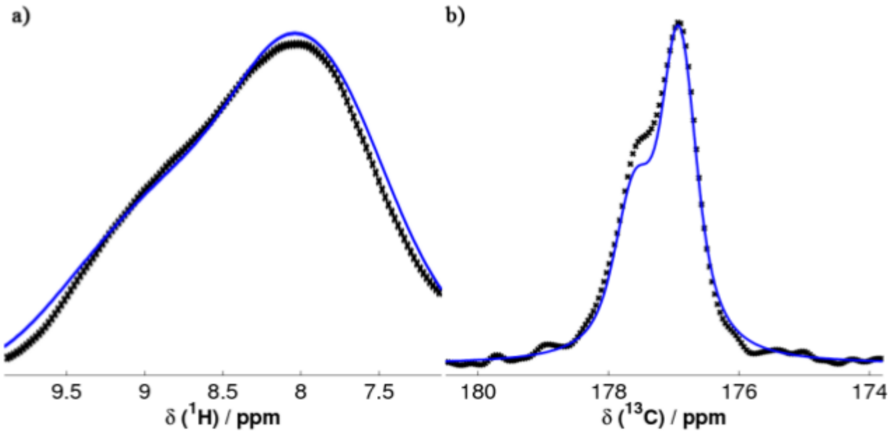

Fig S2 Experimental spectra from Figure S1 (black crosses) and simulated spectra of H_3 (a) and C_6 (b) (blue lines, compare Table S1) of the acylurea unit of compound **3**.

Prediction of ^{13}C and ^{15}N chemical shifts

Table S2 Predicted solution-state NMR chemical shifts[4] for the carbon atoms of the carbonyl groups as well as the nitrogen atoms of compounds **1** - **3**. Since the ^{15}N calculations are performed without proton decoupling only a mean value is shown, without taking into account any $^{1}J(^{1}H,^{15}N)$-couplings. All values are based on single molecule calculations without considering any inter- or intramolecular interaction, e.g. hydrogen bonding.

	1	**2**	**3**	Unit
C_4	178.5	158.1	155.7	C=O
C_6	-	-	179.4	C=O
N_3	-	-278.2	-277.2	NH
N_5	-250.9	-274.8	-246.0	NH

HETCOR spectra of compound 1 and 2

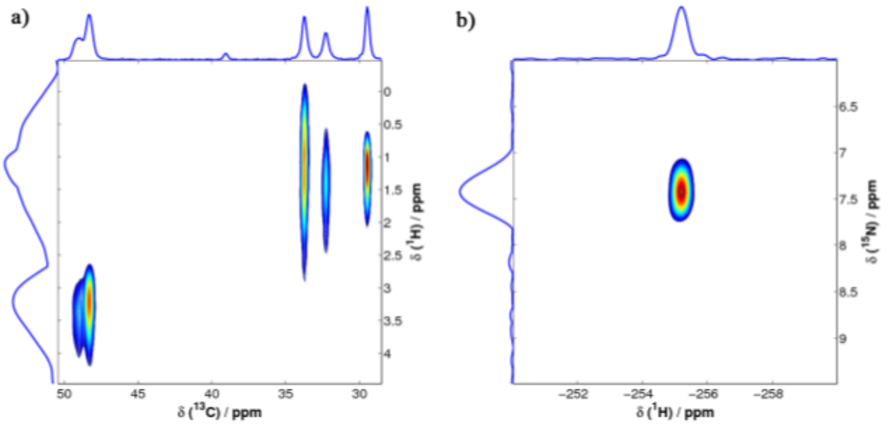

Fig S3 ^{1}H-^{13}C-HETCOR on a 300 MHz spectrometer (left) and ^{1}H-^{15}N-HETCOR on a 400 MHz spectrometer (right) of compound **1** at a spinning speed of 10 kHz each. The contact time was set to 178 µs.

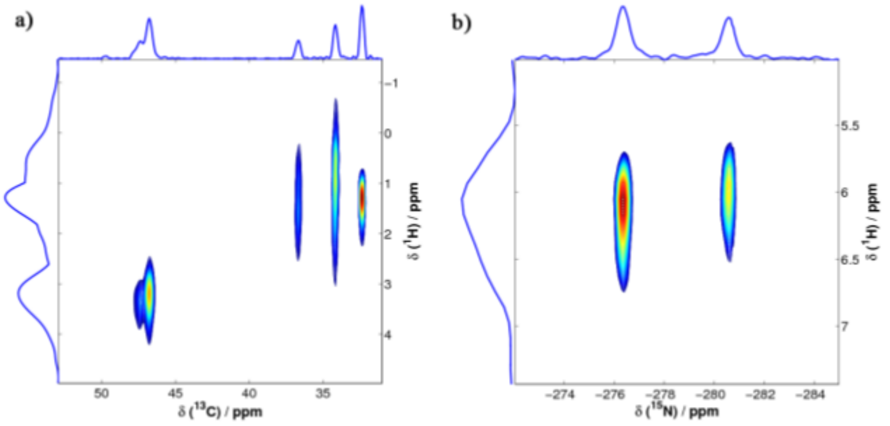

Fig S4 ^{1}H-^{13}C-HETCOR (left) and ^{1}H-^{15}N-HETCOR (right) spectrum of compound **2** at a spinning speed of 10 kHz on a 300 MHz spectrometer. The contact time was set to 178 µs.

^{1}H-^{1}H double-quantum-single-quantum spectra of 1 – 3

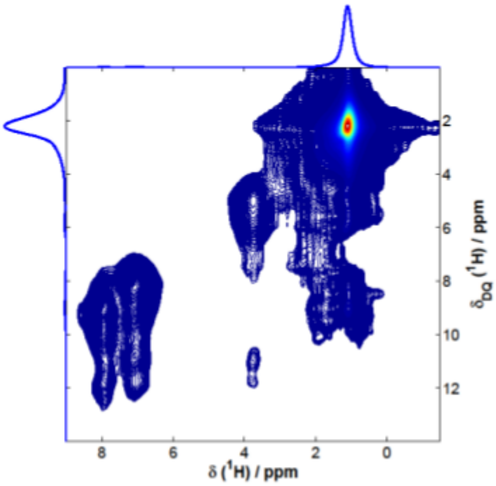

Fig. S5 ^{1}H-^{1}H DQ-SQ correlation spectra of compound **1**. The excitation and reconversion time was set to 80 µs so that only shortest distance correlations are visible. The protons of the CH_3-groups are truncated due to the long relaxation times leading to a streak along both the SQ- as well as the DQ-axis in the spectrum.

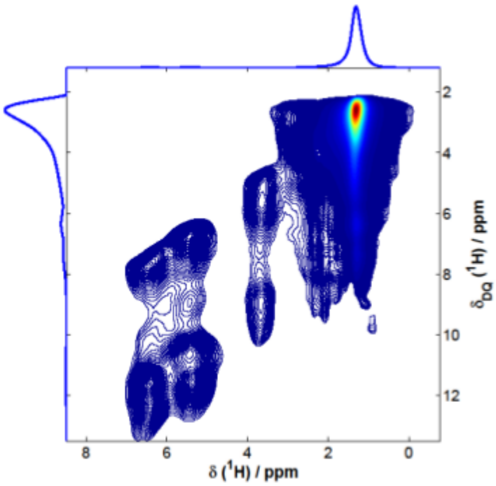

Fig. S6 ^{1}H-^{1}H DQ-SQ correlation spectrum of compound **2**. The excitation and reconversion time was set to 80 µs so that only shortest distance correlations are visible. The protons of the CH_3-groups are truncated due to the long relaxation times leading to a streak along both the SQ- as well as the DQ-axis in the spectrum.

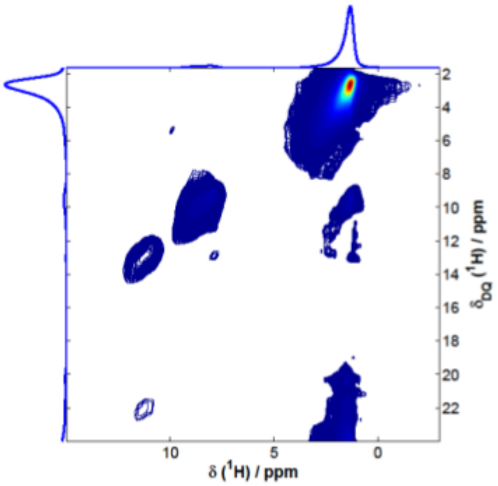

Fig. S7 ^{1}H-^{1}H DQ-SQ correlation spectrum of compound **3**. The excitation and reconversion time was set to 80 µs so that only shortest distance correlations are visible. The protons of the CH_3-groups are truncated due to the long relaxation times leading to a streak along both the SQ- as well as the DQ-axis in the spectrum.

Rietveld profile plots of 2 and 3

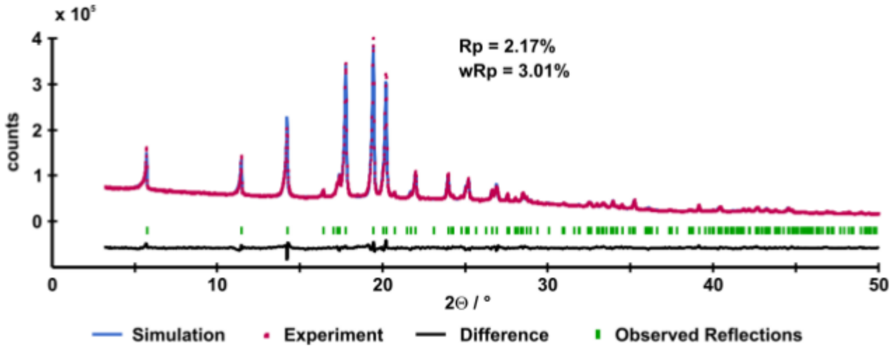

Fig. S8 Rietveld profile plot of compound **2** measured at room temperature in the 2Θ range of 3° - 50° using CuKα_1 radiation (λ = 1.5406 Å).

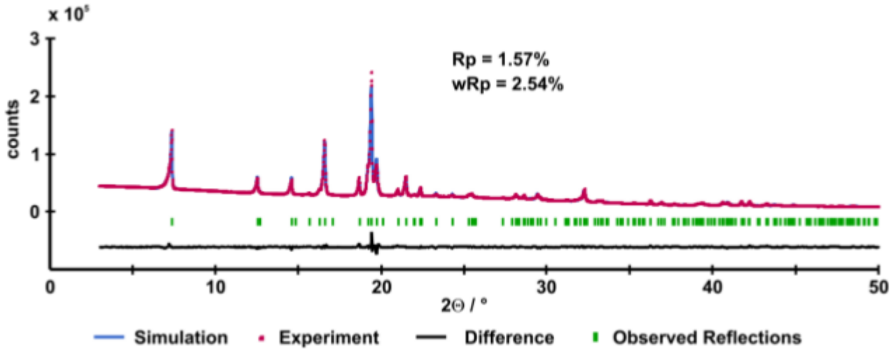

Fig. S9 Rietveld profile plot of compound **3** measured at room temperature in the 2Θ range of 3° - 50° using CuKα_1 radiation (λ = 1.5406 Å).

References

1 K. Eichele, *WSolids1 version 1.20.17, Universität Tübingen*, 2012.

2 K. Eichele, M. D. Lumsden and R. E. Wasylishen, *J. Phys. Chem.*, 1993, **97**, 8909.

3 M. Hesse, H. Meier and B. Zeeh, *Spektroskopische Methoden in der organischen Chemie*, 5th edn., 1995.

4 *Predicted NMR data calculated using Advanced Chemistry Development, Inc. (ACD/Labs) Software V12.5 (© 1994-2013 ACD/Labs).*

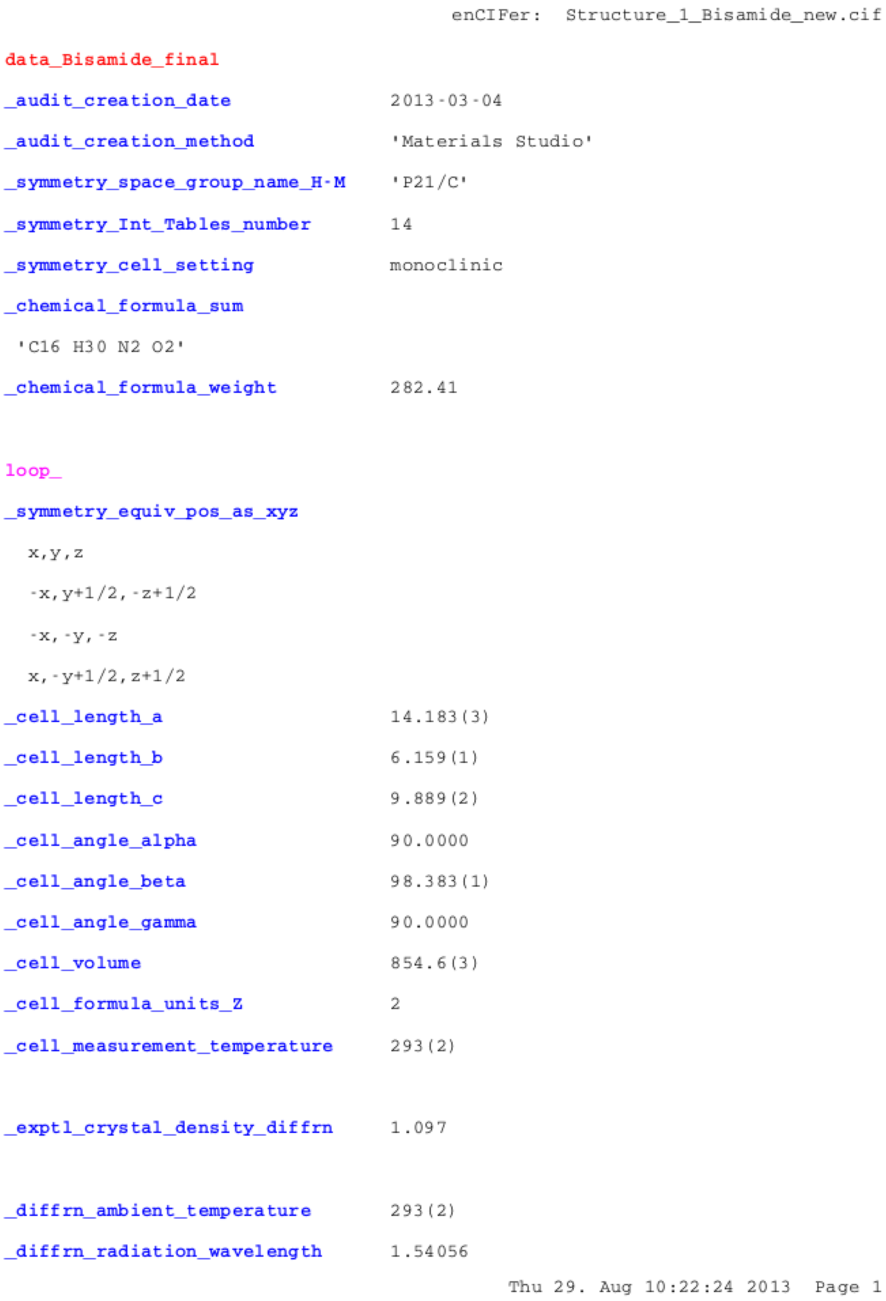

```
                                          enCIFer:  Structure_1_Bisamide_new.cif
data_Bisamide_final
_audit_creation_date                  2013-03-04
_audit_creation_method                'Materials Studio'
_symmetry_space_group_name_H-M        'P21/C'
_symmetry_Int_Tables_number           14
_symmetry_cell_setting                monoclinic
_chemical_formula_sum
 'C16 H30 N2 O2'
_chemical_formula_weight              282.41

loop_
_symmetry_equiv_pos_as_xyz
  x,y,z
  -x,y+1/2,-z+1/2
  -x,-y,-z
  x,-y+1/2,z+1/2
_cell_length_a                        14.183(3)
_cell_length_b                        6.159(1)
_cell_length_c                        9.889(2)
_cell_angle_alpha                     90.0000
_cell_angle_beta                      98.383(1)
_cell_angle_gamma                     90.0000
_cell_volume                          854.6(3)
_cell_formula_units_Z                 2
_cell_measurement_temperature         293(2)

_exptl_crystal_density_diffrn         1.097

_diffrn_ambient_temperature           293(2)
_diffrn_radiation_wavelength          1.54056
                                               Thu 29. Aug 10:22:24 2013   Page 1
```

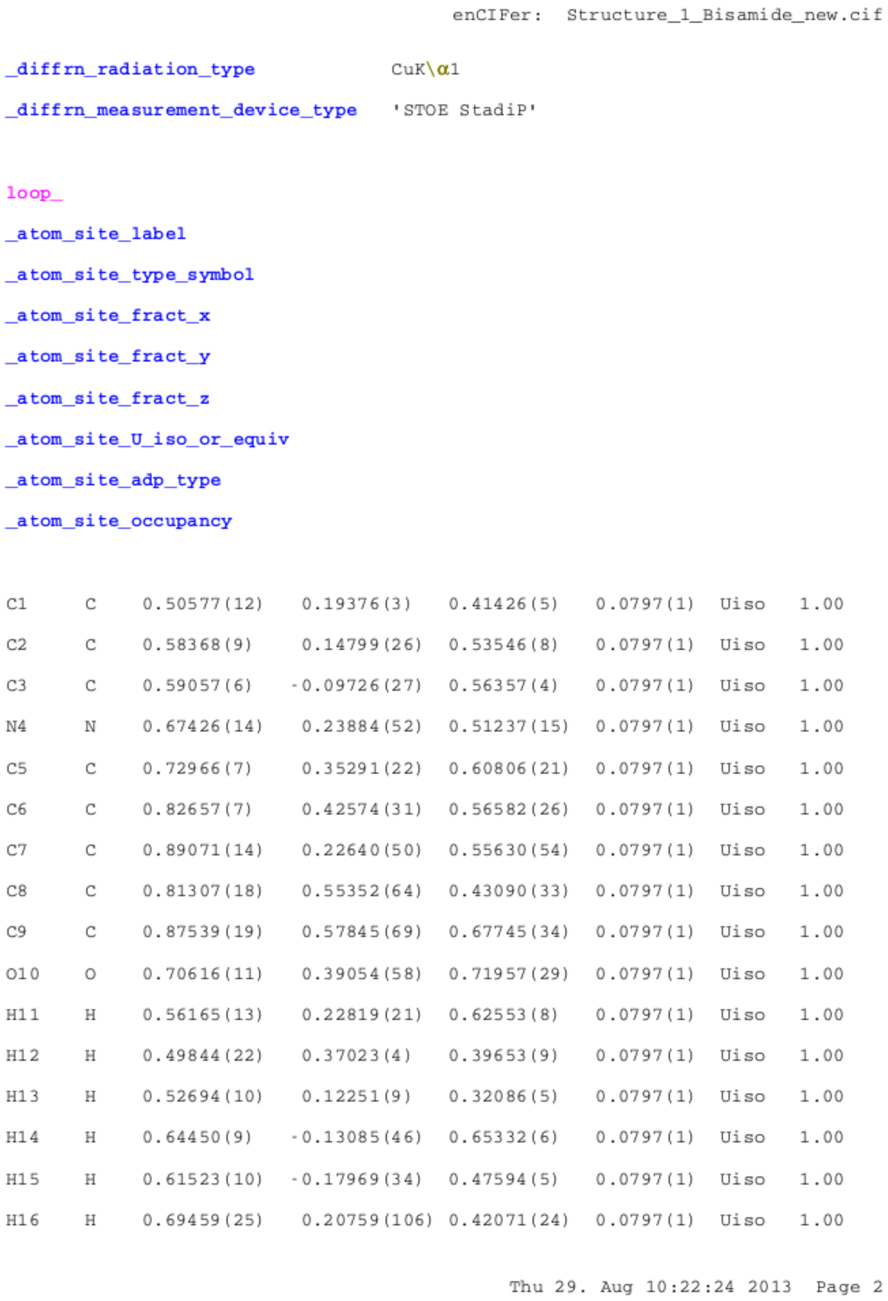

```
                                    enCIFer:  Structure_1_Bisamide_new.cif

_diffrn_radiation_type              CuK\α1
_diffrn_measurement_device_type     'STOE StadiP'

loop_
_atom_site_label
_atom_site_type_symbol
_atom_site_fract_x
_atom_site_fract_y
_atom_site_fract_z
_atom_site_U_iso_or_equiv
_atom_site_adp_type
_atom_site_occupancy

C1     C     0.50577(12)    0.19376(3)     0.41426(5)    0.0797(1)  Uiso   1.00
C2     C     0.58368(9)     0.14799(26)    0.53546(8)    0.0797(1)  Uiso   1.00
C3     C     0.59057(6)    -0.09726(27)    0.56357(4)    0.0797(1)  Uiso   1.00
N4     N     0.67426(14)    0.23884(52)    0.51237(15)   0.0797(1)  Uiso   1.00
C5     C     0.72966(7)     0.35291(22)    0.60806(21)   0.0797(1)  Uiso   1.00
C6     C     0.82657(7)     0.42574(31)    0.56582(26)   0.0797(1)  Uiso   1.00
C7     C     0.89071(14)    0.22640(50)    0.55630(54)   0.0797(1)  Uiso   1.00
C8     C     0.81307(18)    0.55352(64)    0.43090(33)   0.0797(1)  Uiso   1.00
C9     C     0.87539(19)    0.57845(69)    0.67745(34)   0.0797(1)  Uiso   1.00
O10    O     0.70616(11)    0.39054(58)    0.71957(29)   0.0797(1)  Uiso   1.00
H11    H     0.56165(13)    0.22819(21)    0.62553(8)    0.0797(1)  Uiso   1.00
H12    H     0.49844(22)    0.37023(4)     0.39653(9)    0.0797(1)  Uiso   1.00
H13    H     0.52694(10)    0.12251(9)     0.32086(5)    0.0797(1)  Uiso   1.00
H14    H     0.64450(9)    -0.13085(46)    0.65332(6)    0.0797(1)  Uiso   1.00
H15    H     0.61523(10)   -0.17969(34)    0.47594(5)    0.0797(1)  Uiso   1.00
H16    H     0.69459(25)    0.20759(106)   0.42071(24)   0.0797(1)  Uiso   1.00

                                         Thu 29. Aug 10:22:24 2013   Page 2
```

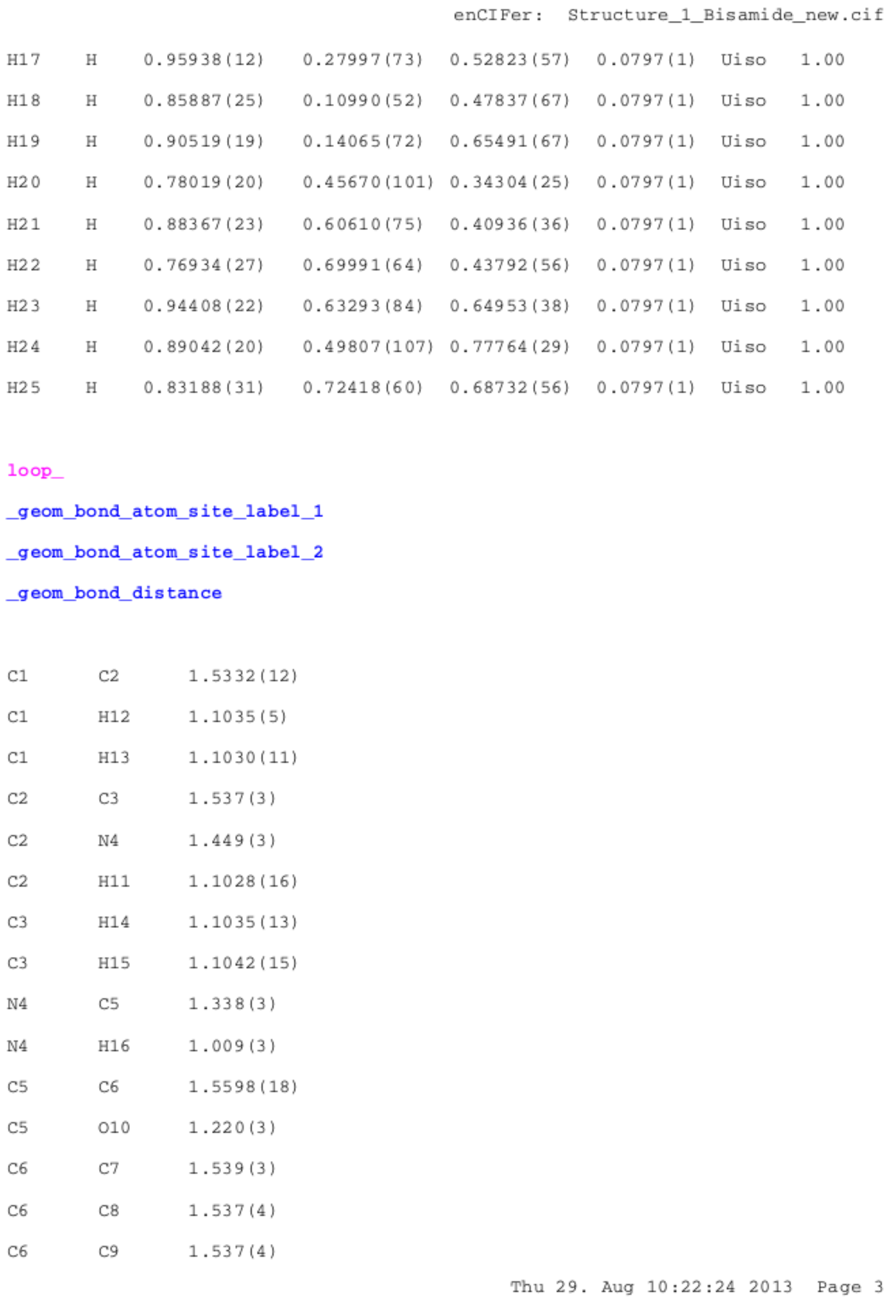

```
                                        enCIFer:  Structure_1_Bisamide_new.cif

H17    H    0.95938(12)   0.27997(73)  0.52823(57)  0.0797(1)   Uiso   1.00
H18    H    0.85887(25)   0.10990(52)  0.47837(67)  0.0797(1)   Uiso   1.00
H19    H    0.90519(19)   0.14065(72)  0.65491(67)  0.0797(1)   Uiso   1.00
H20    H    0.78019(20)   0.45670(101) 0.34304(25)  0.0797(1)   Uiso   1.00
H21    H    0.88367(23)   0.60610(75)  0.40936(36)  0.0797(1)   Uiso   1.00
H22    H    0.76934(27)   0.69991(64)  0.43792(56)  0.0797(1)   Uiso   1.00
H23    H    0.94408(22)   0.63293(84)  0.64953(38)  0.0797(1)   Uiso   1.00
H24    H    0.89042(20)   0.49807(107) 0.77764(29)  0.0797(1)   Uiso   1.00
H25    H    0.83188(31)   0.72418(60)  0.68732(56)  0.0797(1)   Uiso   1.00

loop_
_geom_bond_atom_site_label_1
_geom_bond_atom_site_label_2
_geom_bond_distance

C1      C2      1.5332(12)
C1      H12     1.1035(5)
C1      H13     1.1030(11)
C2      C3      1.537(3)
C2      N4      1.449(3)
C2      H11     1.1028(16)
C3      H14     1.1035(13)
C3      H15     1.1042(15)
N4      C5      1.338(3)
N4      H16     1.009(3)
C5      C6      1.5598(18)
C5      O10     1.220(3)
C6      C7      1.539(3)
C6      C8      1.537(4)
C6      C9      1.537(4)
                                             Thu 29. Aug 10:22:24 2013   Page 3
```

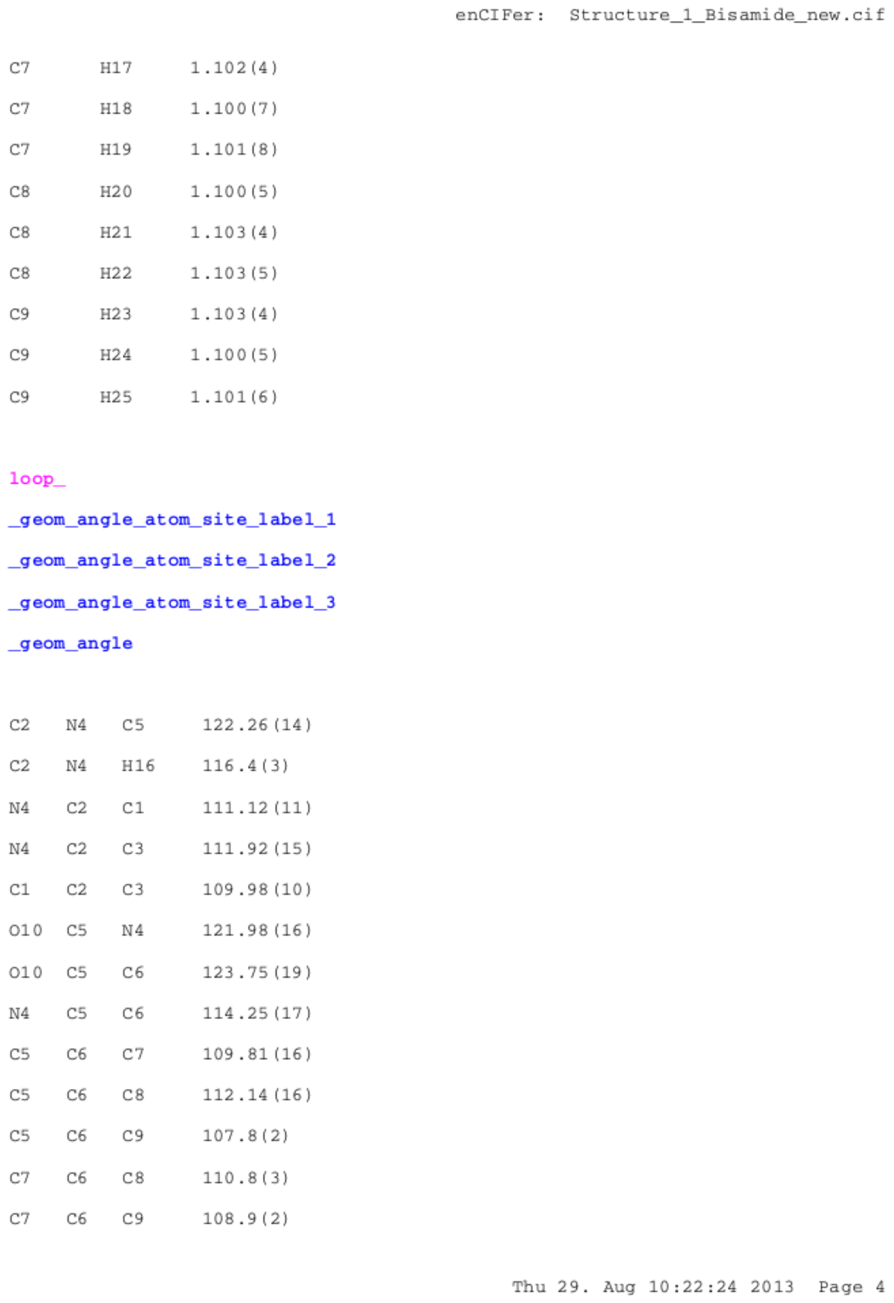

```
                                        enCIFer:  Structure_1_Bisamide_new.cif

C7      H17     1.102(4)

C7      H18     1.100(7)

C7      H19     1.101(8)

C8      H20     1.100(5)

C8      H21     1.103(4)

C8      H22     1.103(5)

C9      H23     1.103(4)

C9      H24     1.100(5)

C9      H25     1.101(6)


loop_

_geom_angle_atom_site_label_1

_geom_angle_atom_site_label_2

_geom_angle_atom_site_label_3

_geom_angle


C2   N4   C5     122.26(14)

C2   N4   H16    116.4(3)

N4   C2   C1     111.12(11)

N4   C2   C3     111.92(15)

C1   C2   C3     109.98(10)

O10  C5   N4     121.98(16)

O10  C5   C6     123.75(19)

N4   C5   C6     114.25(17)

C5   C6   C7     109.81(16)

C5   C6   C8     112.14(16)

C5   C6   C9     107.8(2)

C7   C6   C8     110.8(3)

C7   C6   C9     108.9(2)

                                             Thu 29. Aug 10:22:24 2013   Page 4
```

enCIFer: Structure_1_Bisamide_new.cif

C8	C6	C9	107.2(2)
C2	N4	H16	116.4(3)
C5	N4	H16	121.4(3)
C2	C1	H12	110.25(14)
C2	C1	H13	109.17(13)
H12	C1	H13	106.85(9)
N4	C2	H11	108.45(17)
C1	C2	H11	106.99(14)
C3	C2	H11	108.20(11)
C2	C3	H14	110.4(2)
C2	C3	H15	109.21(12)
H14	C3	H15	106.46(15)
C6	C7	H17	109.2(3)
C6	C7	H18	112.2(3)
C6	C7	H19	111.3(4)
H17	C7	H18	107.8(5)
H17	C7	H19	108.0(4)
H18	C7	H19	108.2(5)
C6	C8	H20	113.2(4)
C6	C8	H21	108.4(3)
C6	C8	H22	111.4(4)
H20	C8	H21	107.4(4)
H20	C8	H22	108.4(4)
H21	C8	H22	107.9(4)
C6	C9	H23	109.1(3)
C6	C9	H24	112.3(5)
C6	C9	H25	111.3(3)
H23	C9	H24	107.5(4)
H23	C9	H25	107.5(5)
H24	C9	H25	109.0(5)

Thu 29. Aug 10:22:24 2013 Page 5

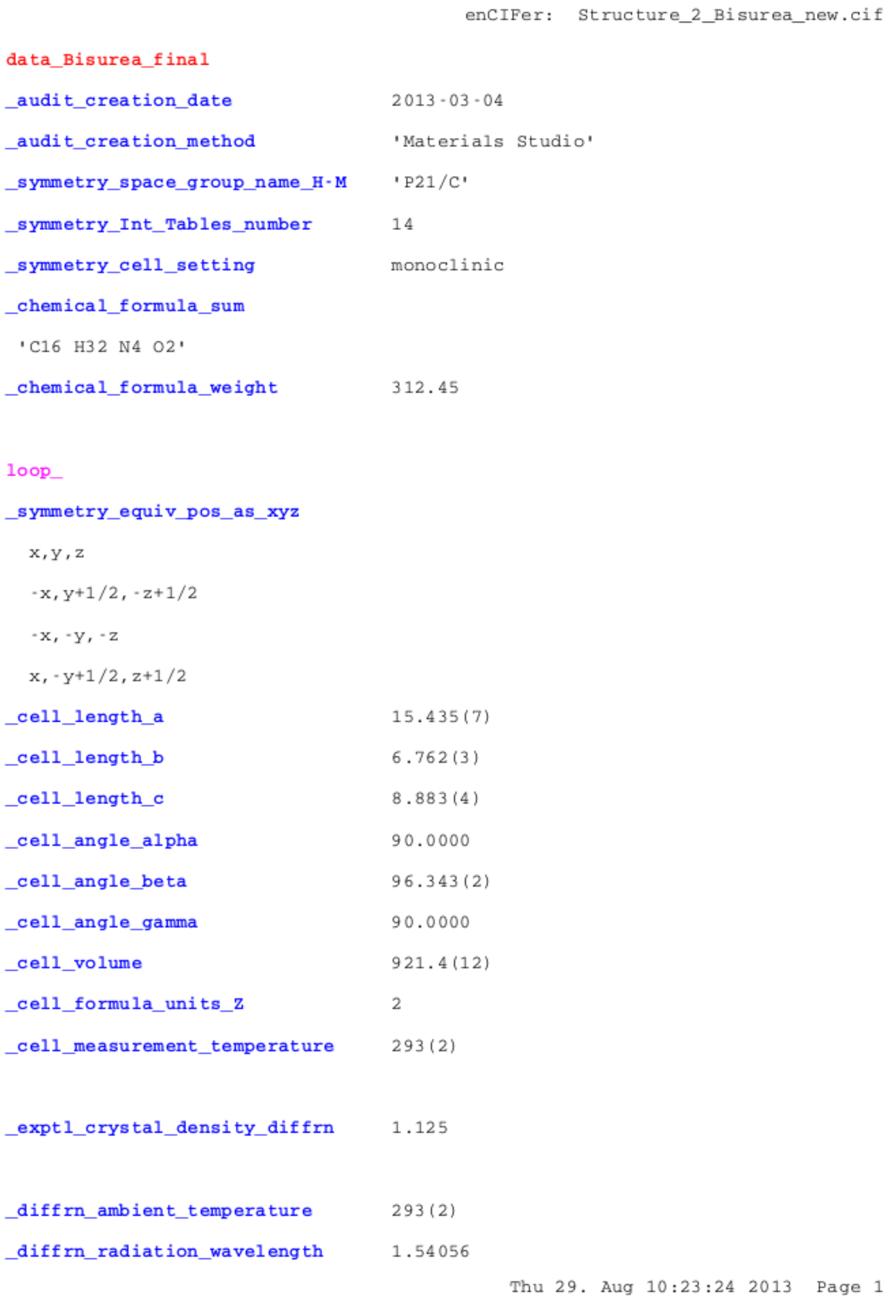

```
                                      enCIFer:  Structure_2_Bisurea_new.cif
data_Bisurea_final
_audit_creation_date                 2013-03-04
_audit_creation_method               'Materials Studio'
_symmetry_space_group_name_H-M       'P21/C'
_symmetry_Int_Tables_number          14
_symmetry_cell_setting               monoclinic
_chemical_formula_sum
 'C16 H32 N4 O2'
_chemical_formula_weight             312.45

loop_
_symmetry_equiv_pos_as_xyz
  x,y,z
  -x,y+1/2,-z+1/2
  -x,-y,-z
  x,-y+1/2,z+1/2
_cell_length_a                       15.435(7)
_cell_length_b                       6.762(3)
_cell_length_c                       8.883(4)
_cell_angle_alpha                    90.0000
_cell_angle_beta                     96.343(2)
_cell_angle_gamma                    90.0000
_cell_volume                         921.4(12)
_cell_formula_units_Z                2
_cell_measurement_temperature        293(2)

_exptl_crystal_density_diffrn        1.125

_diffrn_ambient_temperature          293(2)
_diffrn_radiation_wavelength         1.54056
                                          Thu 29. Aug 10:23:24 2013   Page 1
```

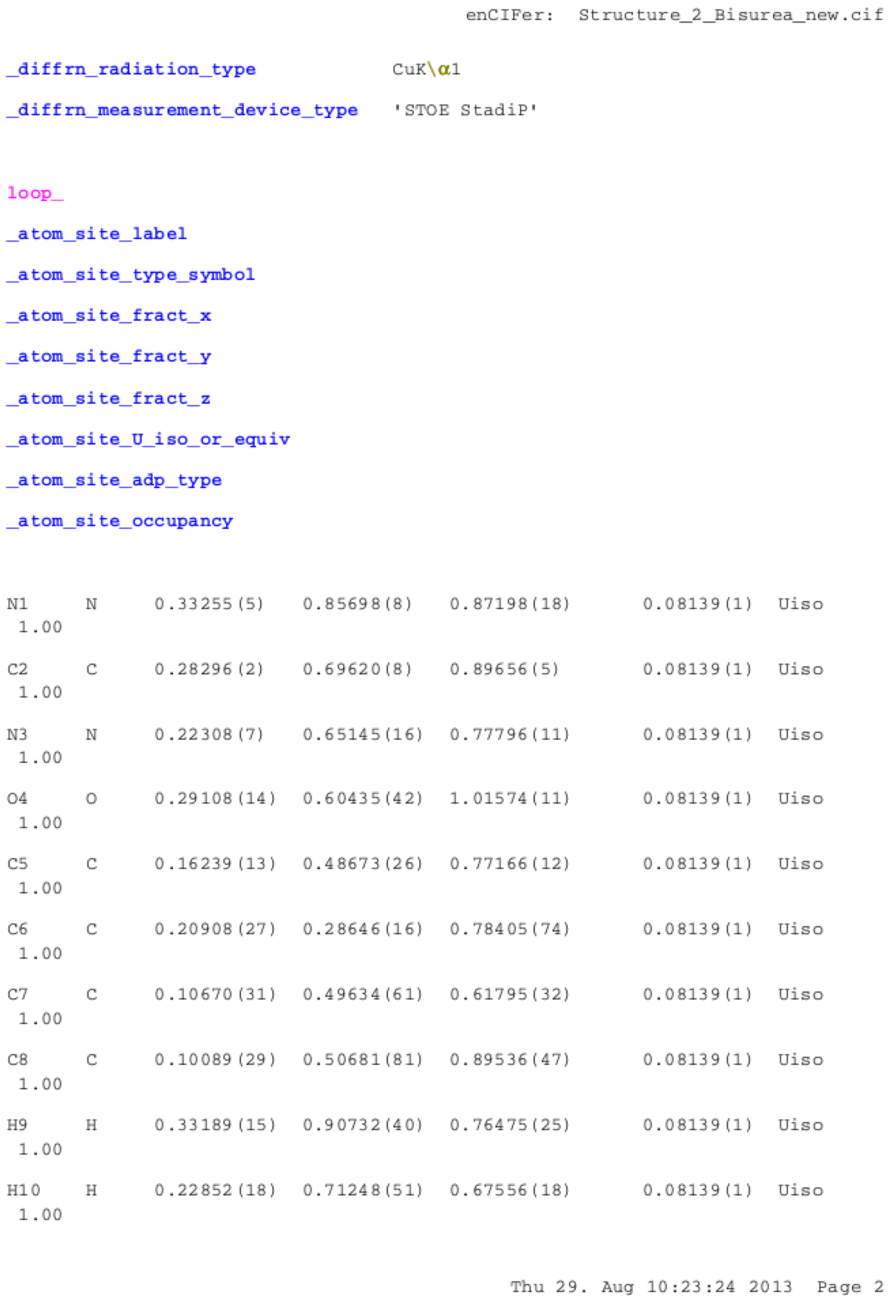

```
                                   enCIFer:  Structure_2_Bisurea_new.cif

_diffrn_radiation_type              CuK\α1
_diffrn_measurement_device_type     'STOE StadiP'

loop_
_atom_site_label
_atom_site_type_symbol
_atom_site_fract_x
_atom_site_fract_y
_atom_site_fract_z
_atom_site_U_iso_or_equiv
_atom_site_adp_type
_atom_site_occupancy

N1     N     0.33255(5)    0.85698(8)    0.87198(18)      0.08139(1)   Uiso
 1.00
C2     C     0.28296(2)    0.69620(8)    0.89656(5)       0.08139(1)   Uiso
 1.00
N3     N     0.22308(7)    0.65145(16)   0.77796(11)      0.08139(1)   Uiso
 1.00
O4     O     0.29108(14)   0.60435(42)   1.01574(11)      0.08139(1)   Uiso
 1.00
C5     C     0.16239(13)   0.48673(26)   0.77166(12)      0.08139(1)   Uiso
 1.00
C6     C     0.20908(27)   0.28646(16)   0.78405(74)      0.08139(1)   Uiso
 1.00
C7     C     0.10670(31)   0.49634(61)   0.61795(32)      0.08139(1)   Uiso
 1.00
C8     C     0.10089(29)   0.50681(81)   0.89536(47)      0.08139(1)   Uiso
 1.00
H9     H     0.33189(15)   0.90732(40)   0.76475(25)      0.08139(1)   Uiso
 1.00
H10    H     0.22852(18)   0.71248(51)   0.67556(18)      0.08139(1)   Uiso
 1.00

                                        Thu 29. Aug 10:23:24 2013   Page 2
```

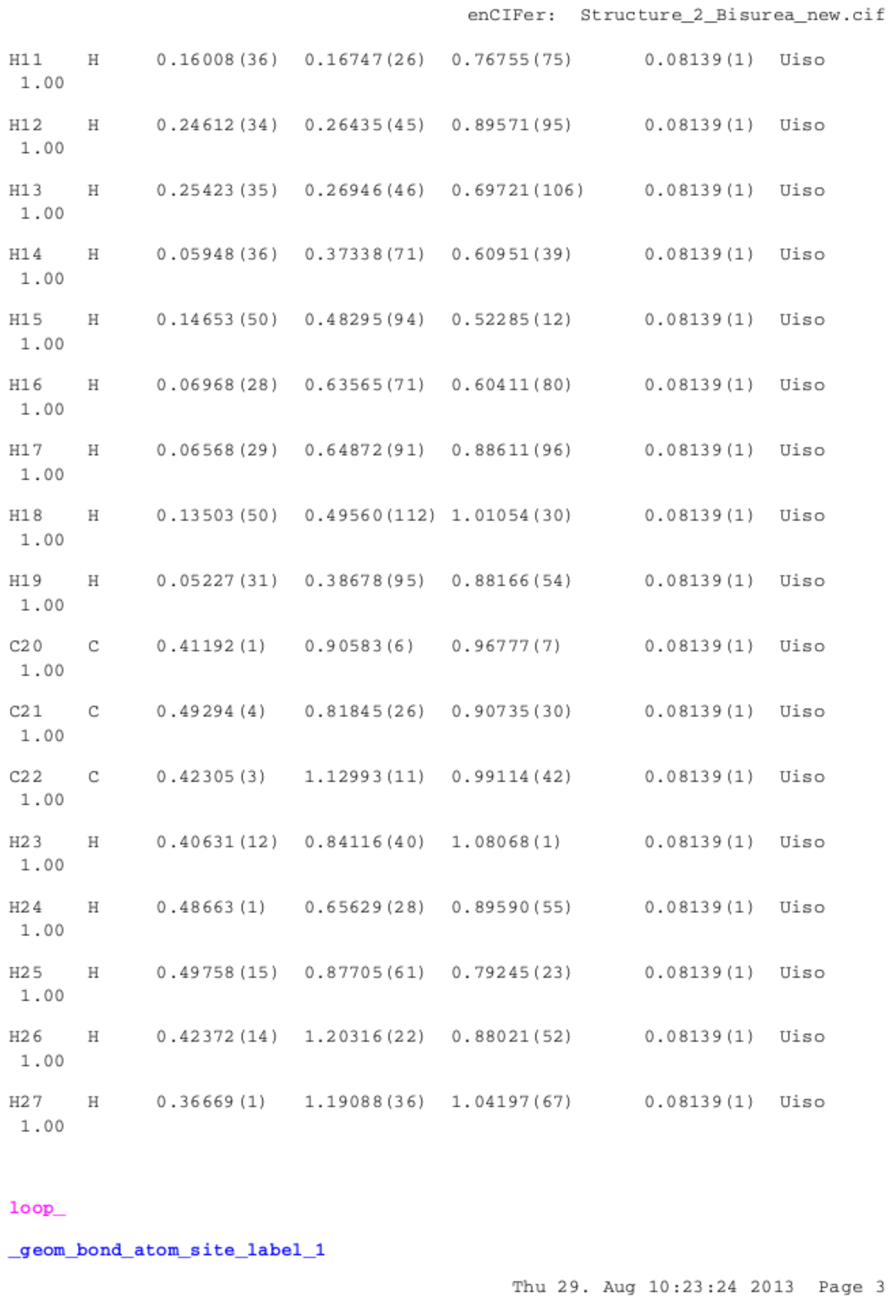

```
                                      enCIFer:  Structure_2_Bisurea_new.cif
H11    H     0.16008(36)  0.16747(26)  0.76755(75)      0.08139(1)   Uiso
 1.00

H12    H     0.24612(34)  0.26435(45)  0.89571(95)      0.08139(1)   Uiso
 1.00

H13    H     0.25423(35)  0.26946(46)  0.69721(106)     0.08139(1)   Uiso
 1.00

H14    H     0.05948(36)  0.37338(71)  0.60951(39)      0.08139(1)   Uiso
 1.00

H15    H     0.14653(50)  0.48295(94)  0.52285(12)      0.08139(1)   Uiso
 1.00

H16    H     0.06968(28)  0.63565(71)  0.60411(80)      0.08139(1)   Uiso
 1.00

H17    H     0.06568(29)  0.64872(91)  0.88611(96)      0.08139(1)   Uiso
 1.00

H18    H     0.13503(50)  0.49560(112) 1.01054(30)      0.08139(1)   Uiso
 1.00

H19    H     0.05227(31)  0.38678(95)  0.88166(54)      0.08139(1)   Uiso
 1.00

C20    C     0.41192(1)   0.90583(6)   0.96777(7)       0.08139(1)   Uiso
 1.00

C21    C     0.49294(4)   0.81845(26)  0.90735(30)      0.08139(1)   Uiso
 1.00

C22    C     0.42305(3)   1.12993(11)  0.99114(42)      0.08139(1)   Uiso
 1.00

H23    H     0.40631(12)  0.84116(40)  1.08068(1)       0.08139(1)   Uiso
 1.00

H24    H     0.48663(1)   0.65629(28)  0.89590(55)      0.08139(1)   Uiso
 1.00

H25    H     0.49758(15)  0.87705(61)  0.79245(23)      0.08139(1)   Uiso
 1.00

H26    H     0.42372(14)  1.20316(22)  0.88021(52)      0.08139(1)   Uiso
 1.00

H27    H     0.36669(1)   1.19088(36)  1.04197(67)      0.08139(1)   Uiso
 1.00


loop_

_geom_bond_atom_site_label_1
                                          Thu 29. Aug 10:23:24 2013   Page 3
```

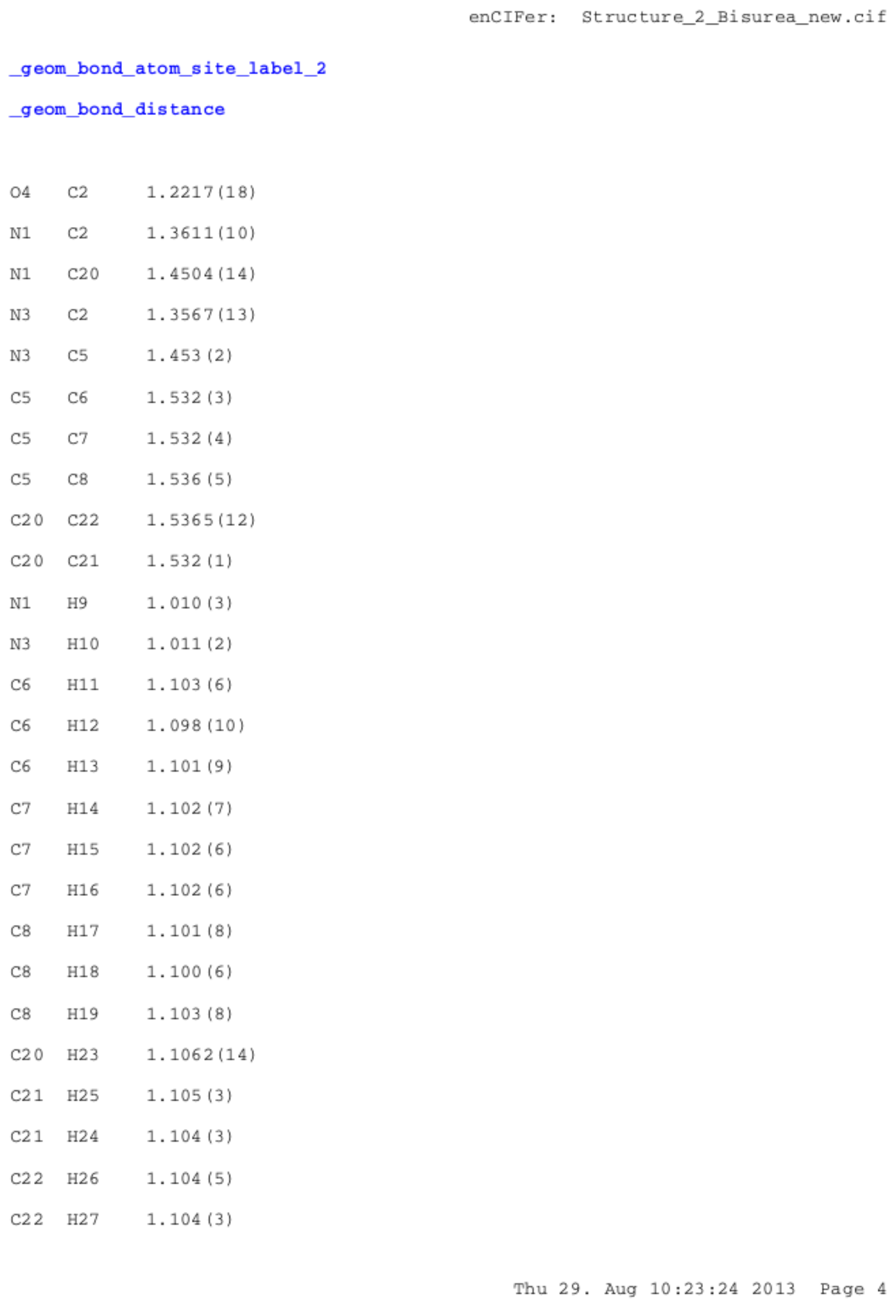

```
                                   enCIFer:  Structure_2_Bisurea_new.cif

_geom_bond_atom_site_label_2

_geom_bond_distance


O4    C2      1.2217(18)

N1    C2      1.3611(10)

N1    C20     1.4504(14)

N3    C2      1.3567(13)

N3    C5      1.453(2)

C5    C6      1.532(3)

C5    C7      1.532(4)

C5    C8      1.536(5)

C20   C22     1.5365(12)

C20   C21     1.532(1)

N1    H9      1.010(3)

N3    H10     1.011(2)

C6    H11     1.103(6)

C6    H12     1.098(10)

C6    H13     1.101(9)

C7    H14     1.102(7)

C7    H15     1.102(6)

C7    H16     1.102(6)

C8    H17     1.101(8)

C8    H18     1.100(6)

C8    H19     1.103(8)

C20   H23     1.1062(14)

C21   H25     1.105(3)

C21   H24     1.104(3)

C22   H26     1.104(5)

C22   H27     1.104(3)

                                       Thu 29. Aug 10:23:24 2013   Page 4
```

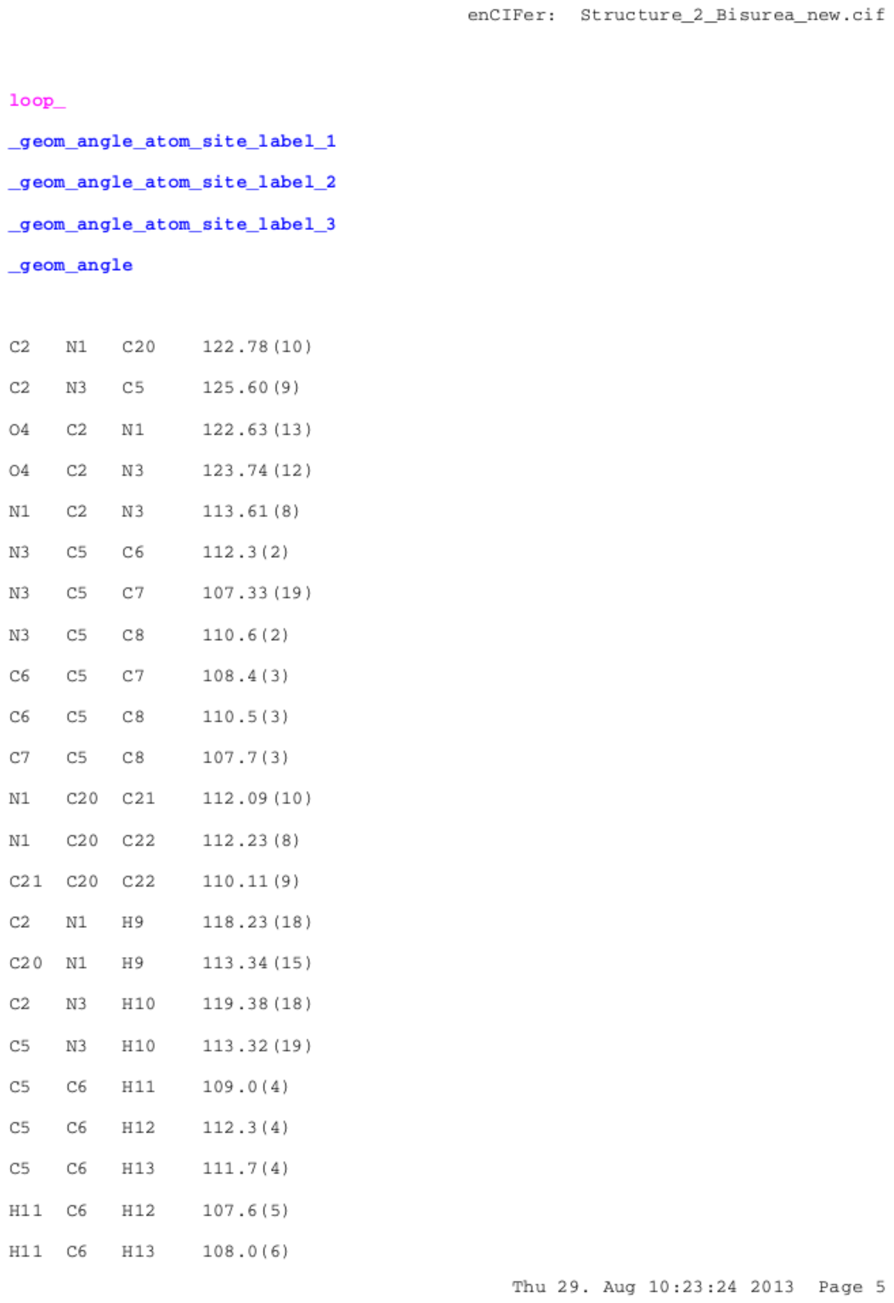

```
                                    enCIFer:  Structure_2_Bisurea_new.cif

loop_
_geom_angle_atom_site_label_1
_geom_angle_atom_site_label_2
_geom_angle_atom_site_label_3
_geom_angle

C2    N1    C20     122.78(10)
C2    N3    C5      125.60(9)
O4    C2    N1      122.63(13)
O4    C2    N3      123.74(12)
N1    C2    N3      113.61(8)
N3    C5    C6      112.3(2)
N3    C5    C7      107.33(19)
N3    C5    C8      110.6(2)
C6    C5    C7      108.4(3)
C6    C5    C8      110.5(3)
C7    C5    C8      107.7(3)
N1    C20   C21     112.09(10)
N1    C20   C22     112.23(8)
C21   C20   C22     110.11(9)
C2    N1    H9      118.23(18)
C20   N1    H9      113.34(15)
C2    N3    H10     119.38(18)
C5    N3    H10     113.32(19)
C5    C6    H11     109.0(4)
C5    C6    H12     112.3(4)
C5    C6    H13     111.7(4)
H11   C6    H12     107.6(5)
H11   C6    H13     108.0(6)
                                        Thu 29. Aug 10:23:24 2013   Page 5
```

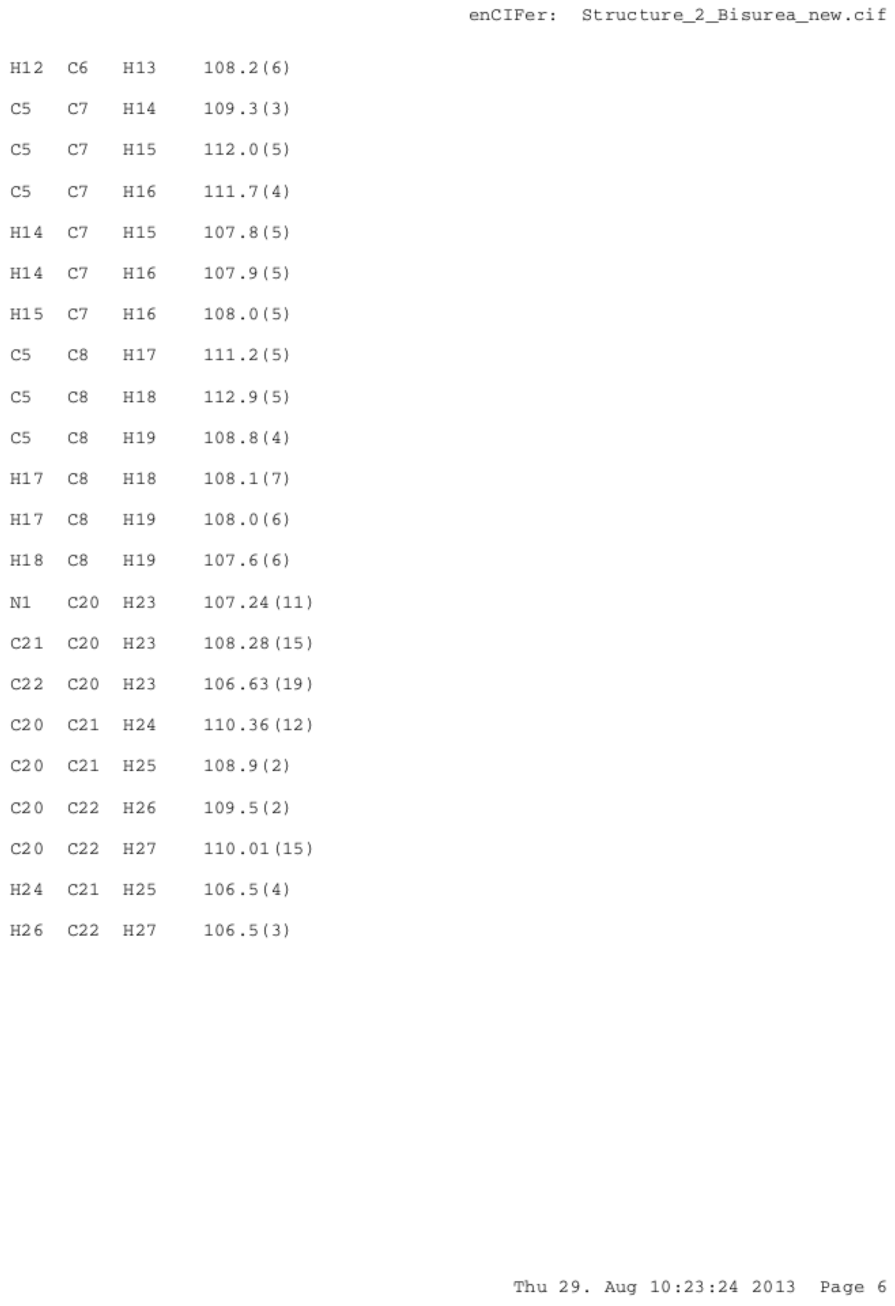

enCIFer: Structure_2_Bisurea_new.cif

H12	C6	H13	108.2(6)
C5	C7	H14	109.3(3)
C5	C7	H15	112.0(5)
C5	C7	H16	111.7(4)
H14	C7	H15	107.8(5)
H14	C7	H16	107.9(5)
H15	C7	H16	108.0(5)
C5	C8	H17	111.2(5)
C5	C8	H18	112.9(5)
C5	C8	H19	108.8(4)
H17	C8	H18	108.1(7)
H17	C8	H19	108.0(6)
H18	C8	H19	107.6(6)
N1	C20	H23	107.24(11)
C21	C20	H23	108.28(15)
C22	C20	H23	106.63(19)
C20	C21	H24	110.36(12)
C20	C21	H25	108.9(2)
C20	C22	H26	109.5(2)
C20	C22	H27	110.01(15)
H24	C21	H25	106.5(4)
H26	C22	H27	106.5(3)

Thu 29. Aug 10:23:24 2013 Page 6

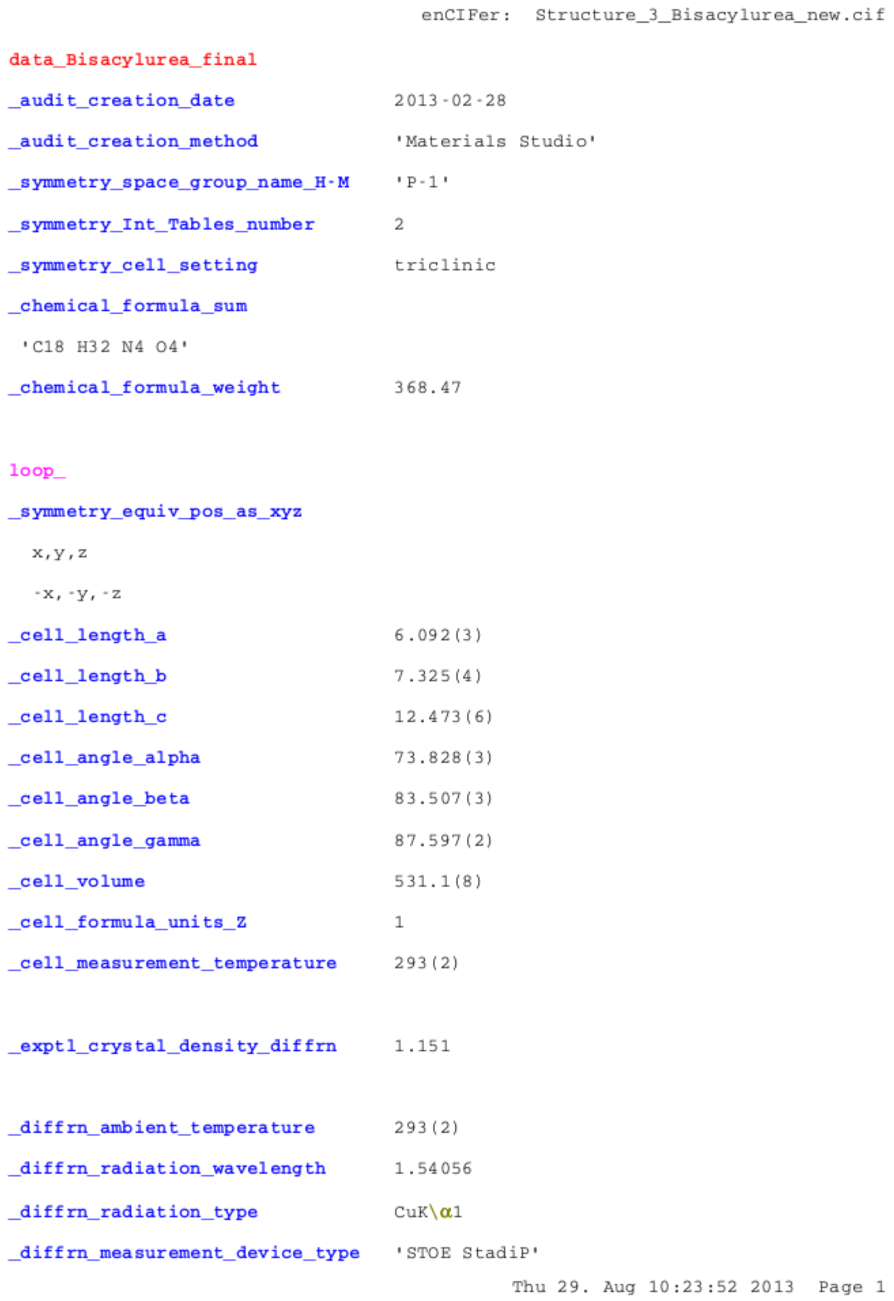

```
                                    enCIFer:  Structure_3_Bisacylurea_new.cif
data_Bisacylurea_final
_audit_creation_date                2013-02-28
_audit_creation_method              'Materials Studio'
_symmetry_space_group_name_H-M      'P-1'
_symmetry_Int_Tables_number         2
_symmetry_cell_setting              triclinic
_chemical_formula_sum
 'C18 H32 N4 O4'
_chemical_formula_weight            368.47

loop_
_symmetry_equiv_pos_as_xyz
  x,y,z
  -x,-y,-z
_cell_length_a                      6.092(3)
_cell_length_b                      7.325(4)
_cell_length_c                      12.473(6)
_cell_angle_alpha                   73.828(3)
_cell_angle_beta                    83.507(3)
_cell_angle_gamma                   87.597(2)
_cell_volume                        531.1(8)
_cell_formula_units_Z               1
_cell_measurement_temperature       293(2)

_exptl_crystal_density_diffrn       1.151

_diffrn_ambient_temperature         293(2)
_diffrn_radiation_wavelength        1.54056
_diffrn_radiation_type              CuK\α1
_diffrn_measurement_device_type     'STOE StadiP'
                                              Thu 29. Aug 10:23:52 2013   Page 1
```

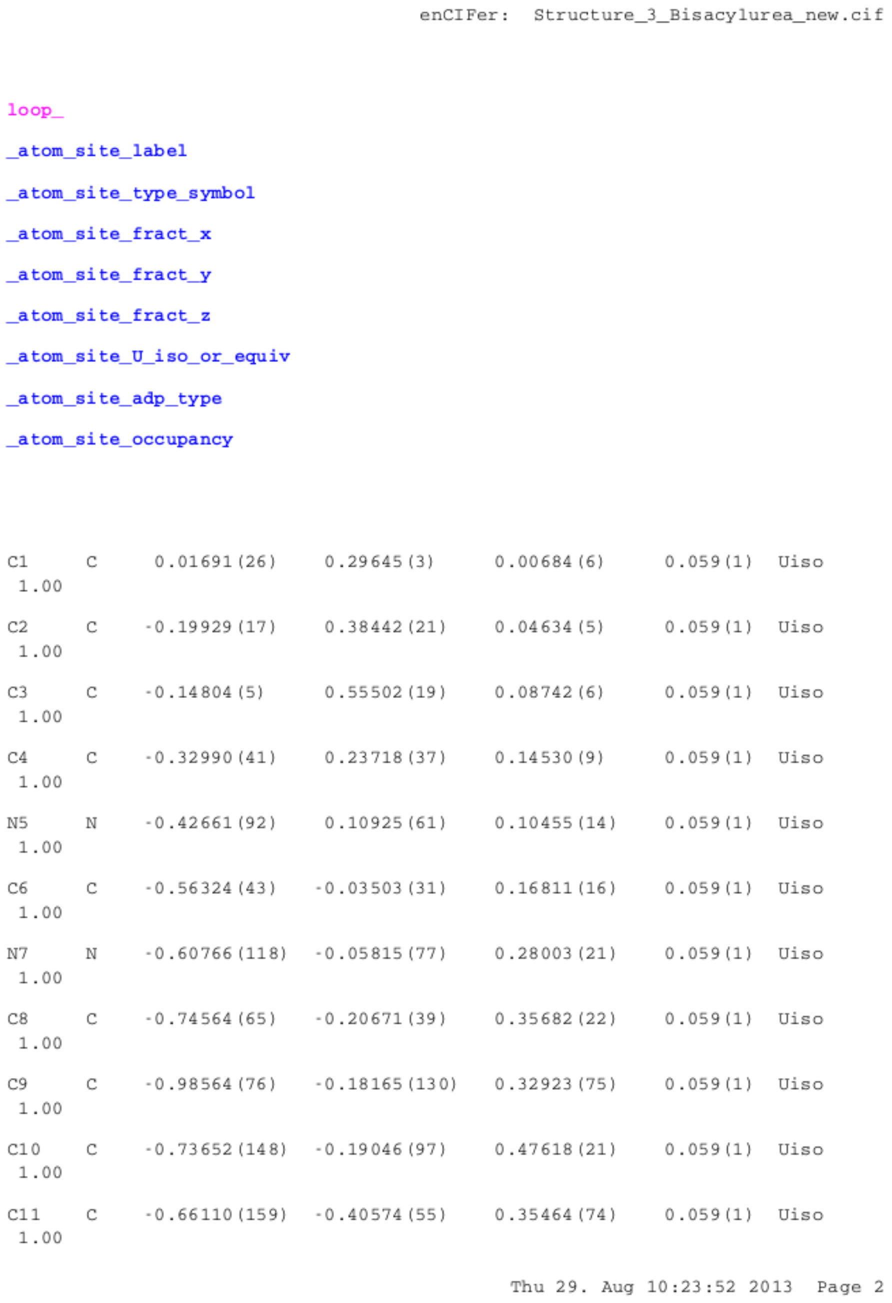

```
                                        enCIFer:  Structure_3_Bisacylurea_new.cif

loop_
_atom_site_label
_atom_site_type_symbol
_atom_site_fract_x
_atom_site_fract_y
_atom_site_fract_z
_atom_site_U_iso_or_equiv
_atom_site_adp_type
_atom_site_occupancy


C1     C      0.01691(26)    0.29645(3)     0.00684(6)     0.059(1)  Uiso
 1.00
C2     C     -0.19929(17)    0.38442(21)    0.04634(5)     0.059(1)  Uiso
 1.00
C3     C     -0.14804(5)     0.55502(19)    0.08742(6)     0.059(1)  Uiso
 1.00
C4     C     -0.32990(41)    0.23718(37)    0.14530(9)     0.059(1)  Uiso
 1.00
N5     N     -0.42661(92)    0.10925(61)    0.10455(14)    0.059(1)  Uiso
 1.00
C6     C     -0.56324(43)   -0.03503(31)    0.16811(16)    0.059(1)  Uiso
 1.00
N7     N     -0.60766(118)  -0.05815(77)    0.28003(21)    0.059(1)  Uiso
 1.00
C8     C     -0.74564(65)   -0.20671(39)    0.35682(22)    0.059(1)  Uiso
 1.00
C9     C     -0.98564(76)   -0.18165(130)   0.32923(75)    0.059(1)  Uiso
 1.00
C10    C     -0.73652(148)  -0.19046(97)    0.47618(21)    0.059(1)  Uiso
 1.00
C11    C     -0.66110(159)  -0.40574(55)    0.35464(74)    0.059(1)  Uiso
 1.00
                                        Thu 29. Aug 10:23:52 2013   Page 2
```

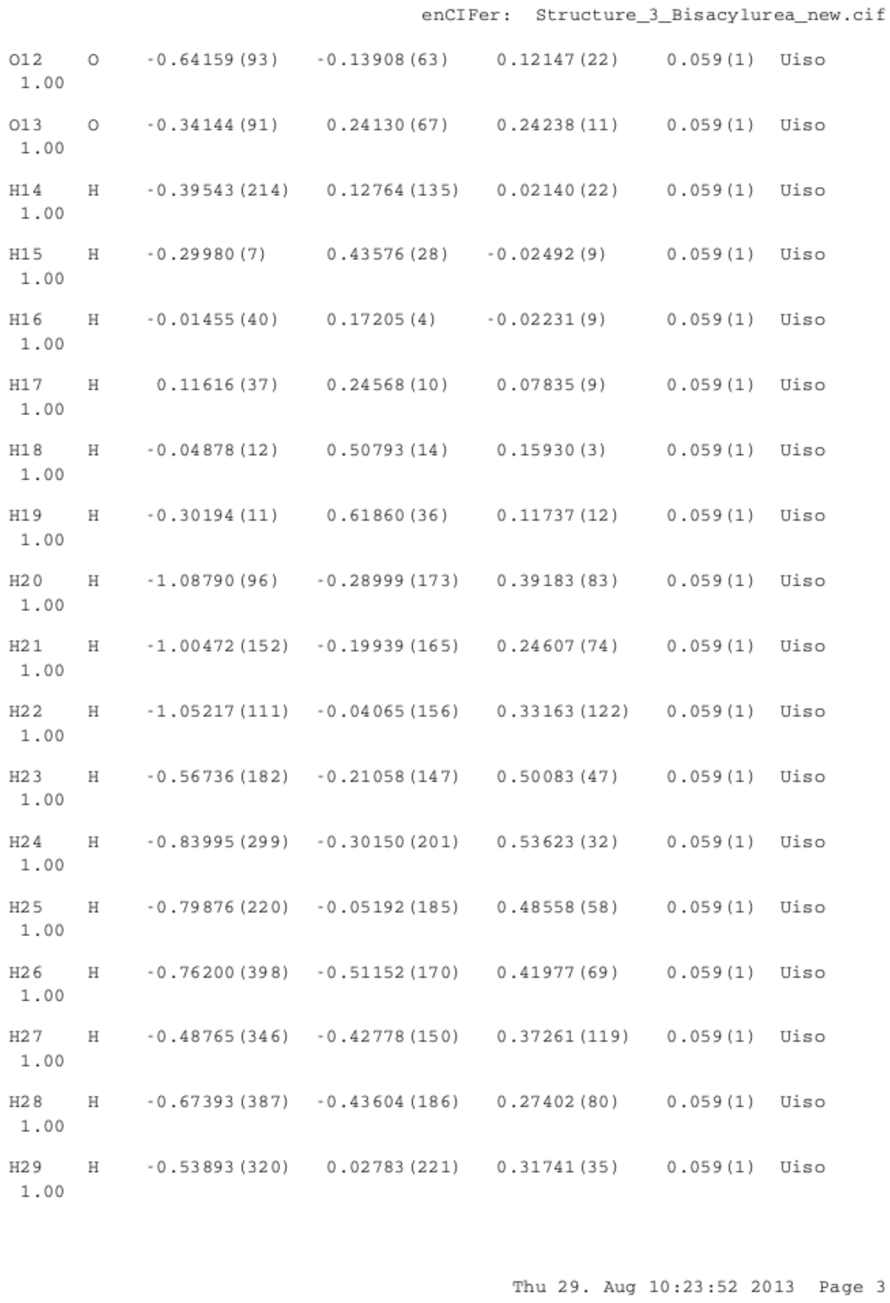

```
                                  enCIFer:  Structure_3_Bisacylurea_new.cif

O12    O    -0.64159(93)   -0.13908(63)    0.12147(22)     0.059(1)  Uiso
 1.00

O13    O    -0.34144(91)    0.24130(67)    0.24238(11)     0.059(1)  Uiso
 1.00

H14    H    -0.39543(214)   0.12764(135)   0.02140(22)     0.059(1)  Uiso
 1.00

H15    H    -0.29980(7)     0.43576(28)   -0.02492(9)      0.059(1)  Uiso
 1.00

H16    H    -0.01455(40)    0.17205(4)    -0.02231(9)      0.059(1)  Uiso
 1.00

H17    H     0.11616(37)    0.24568(10)    0.07835(9)      0.059(1)  Uiso
 1.00

H18    H    -0.04878(12)    0.50793(14)    0.15930(3)      0.059(1)  Uiso
 1.00

H19    H    -0.30194(11)    0.61860(36)    0.11737(12)     0.059(1)  Uiso
 1.00

H20    H    -1.08790(96)   -0.28999(173)   0.39183(83)     0.059(1)  Uiso
 1.00

H21    H    -1.00472(152)  -0.19939(165)   0.24607(74)     0.059(1)  Uiso
 1.00

H22    H    -1.05217(111)  -0.04065(156)   0.33163(122)    0.059(1)  Uiso
 1.00

H23    H    -0.56736(182)  -0.21058(147)   0.50083(47)     0.059(1)  Uiso
 1.00

H24    H    -0.83995(299)  -0.30150(201)   0.53623(32)     0.059(1)  Uiso
 1.00

H25    H    -0.79876(220)  -0.05192(185)   0.48558(58)     0.059(1)  Uiso
 1.00

H26    H    -0.76200(398)  -0.51152(170)   0.41977(69)     0.059(1)  Uiso
 1.00

H27    H    -0.48765(346)  -0.42778(150)   0.37261(119)    0.059(1)  Uiso
 1.00

H28    H    -0.67393(387)  -0.43604(186)   0.27402(80)     0.059(1)  Uiso
 1.00

H29    H    -0.53893(320)   0.02783(221)   0.31741(35)     0.059(1)  Uiso
 1.00


                                          Thu 29. Aug 10:23:52 2013  Page 3
```

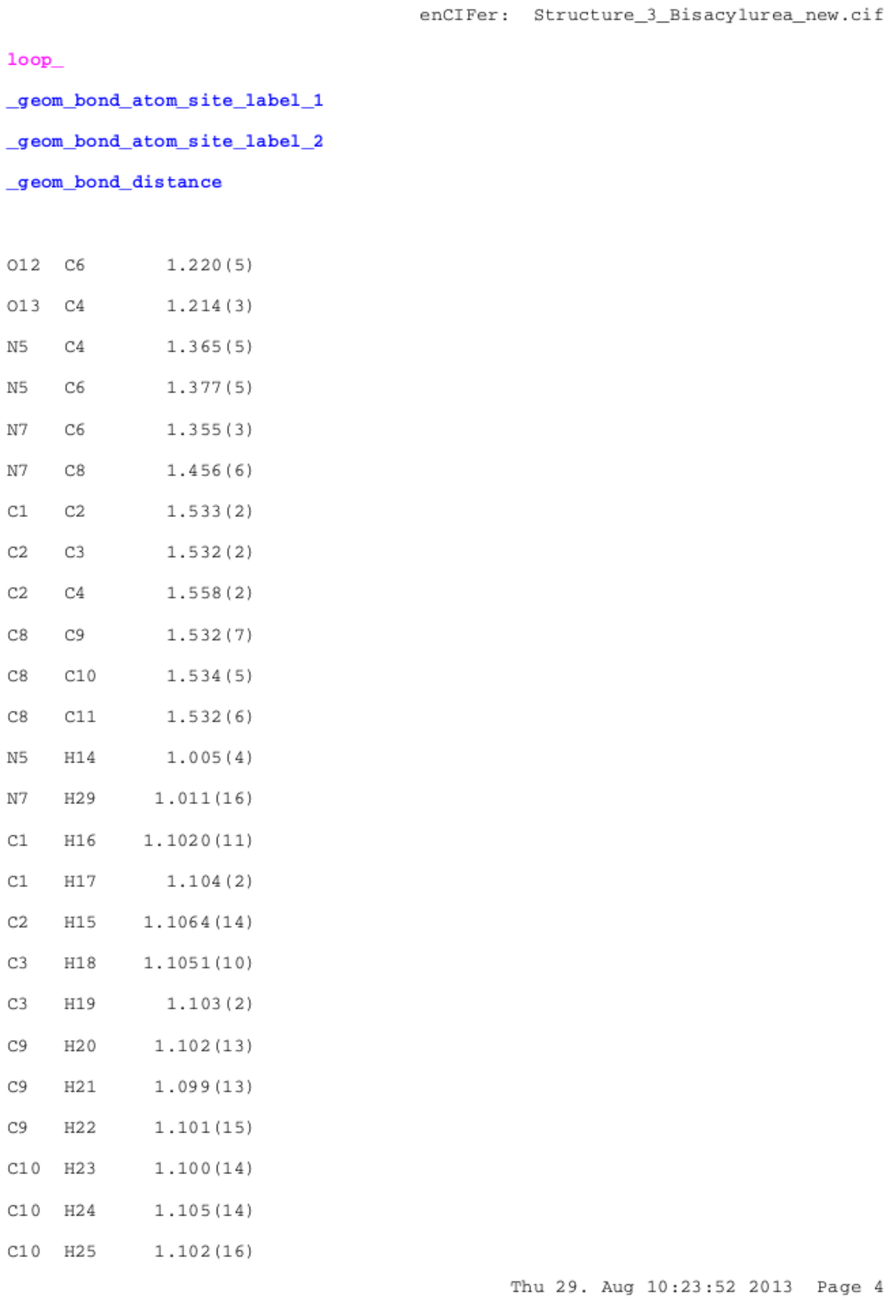

```
                                    enCIFer:  Structure_3_Bisacylurea_new.cif
loop_
_geom_bond_atom_site_label_1
_geom_bond_atom_site_label_2
_geom_bond_distance

O12  C6       1.220(5)
O13  C4       1.214(3)
N5   C4       1.365(5)
N5   C6       1.377(5)
N7   C6       1.355(3)
N7   C8       1.456(6)
C1   C2       1.533(2)
C2   C3       1.532(2)
C2   C4       1.558(2)
C8   C9       1.532(7)
C8   C10      1.534(5)
C8   C11      1.532(6)
N5   H14      1.005(4)
N7   H29     1.011(16)
C1   H16    1.1020(11)
C1   H17      1.104(2)
C2   H15    1.1064(14)
C3   H18    1.1051(10)
C3   H19      1.103(2)
C9   H20     1.102(13)
C9   H21     1.099(13)
C9   H22     1.101(15)
C10  H23     1.100(14)
C10  H24     1.105(14)
C10  H25     1.102(16)
                                        Thu 29. Aug 10:23:52 2013   Page 4
```

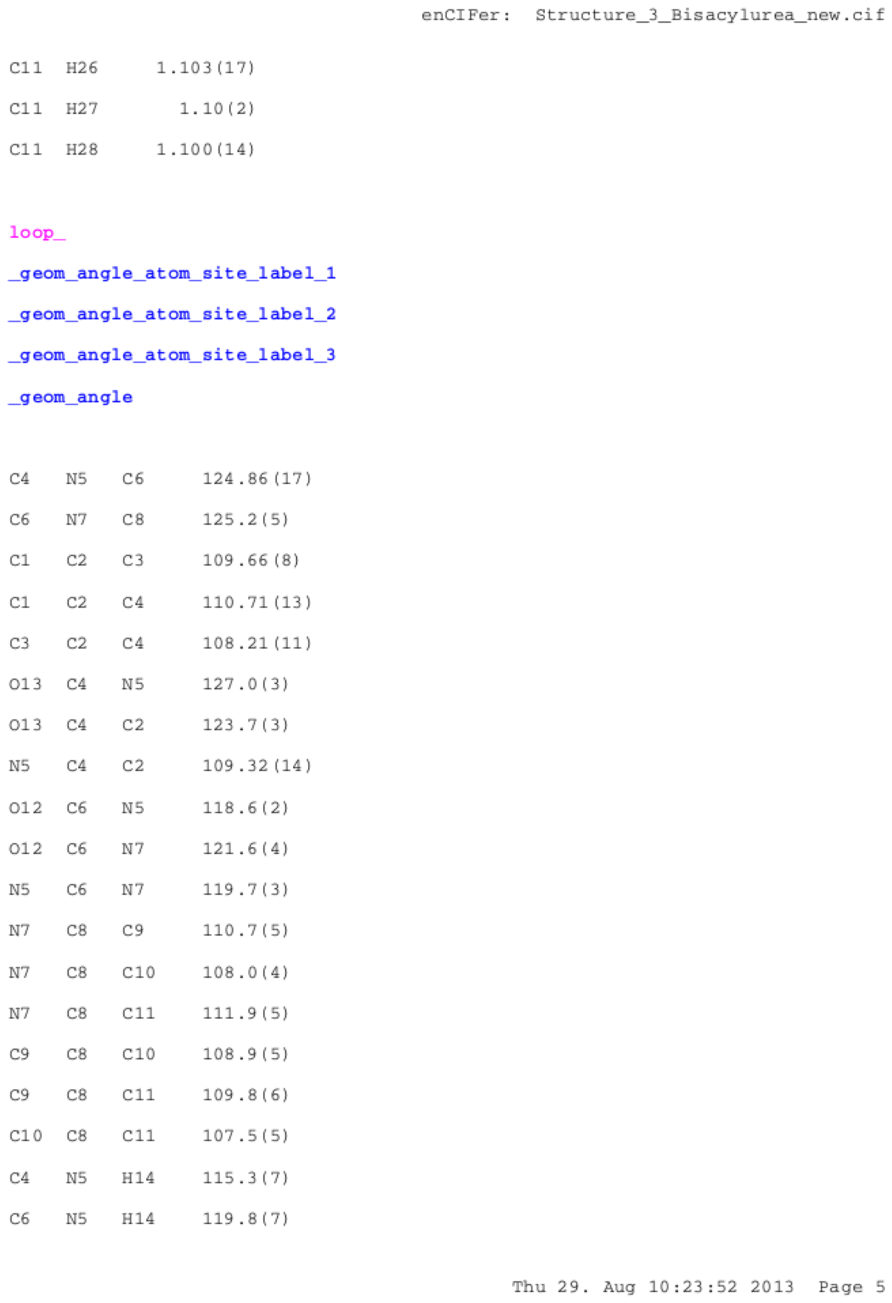

```
                                    enCIFer:  Structure_3_Bisacylurea_new.cif

C11  H26      1.103(17)

C11  H27        1.10(2)

C11  H28      1.100(14)


loop_

_geom_angle_atom_site_label_1

_geom_angle_atom_site_label_2

_geom_angle_atom_site_label_3

_geom_angle


C4   N5   C6      124.86(17)

C6   N7   C8      125.2(5)

C1   C2   C3      109.66(8)

C1   C2   C4      110.71(13)

C3   C2   C4      108.21(11)

O13  C4   N5      127.0(3)

O13  C4   C2      123.7(3)

N5   C4   C2      109.32(14)

O12  C6   N5      118.6(2)

O12  C6   N7      121.6(4)

N5   C6   N7      119.7(3)

N7   C8   C9      110.7(5)

N7   C8   C10     108.0(4)

N7   C8   C11     111.9(5)

C9   C8   C10     108.9(5)

C9   C8   C11     109.8(6)

C10  C8   C11     107.5(5)

C4   N5   H14     115.3(7)

C6   N5   H14     119.8(7)

                                        Thu 29. Aug 10:23:52 2013   Page 5
```

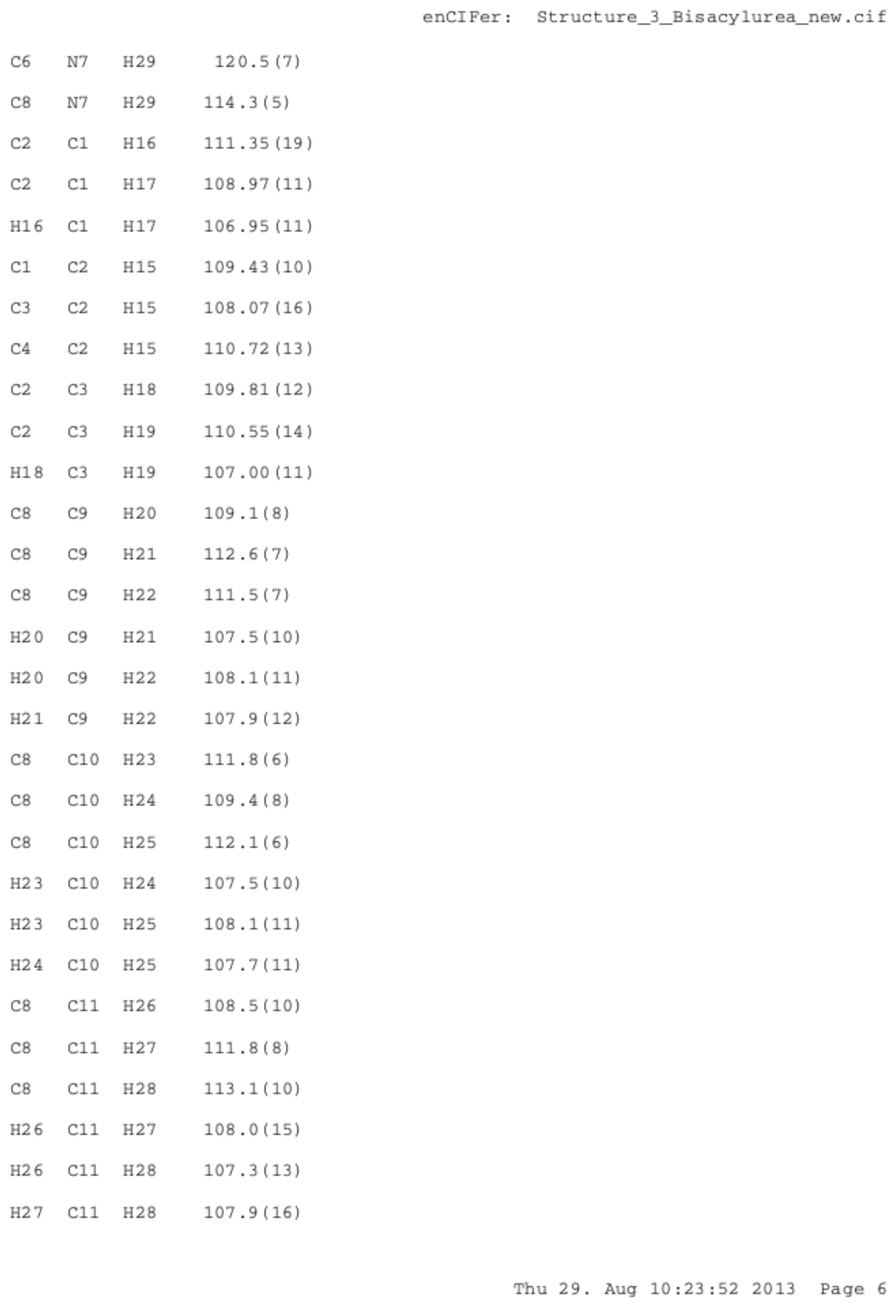

enCIFer: Structure_3_Bisacylurea_new.cif

C6	N7	H29	120.5(7)
C8	N7	H29	114.3(5)
C2	C1	H16	111.35(19)
C2	C1	H17	108.97(11)
H16	C1	H17	106.95(11)
C1	C2	H15	109.43(10)
C3	C2	H15	108.07(16)
C4	C2	H15	110.72(13)
C2	C3	H18	109.81(12)
C2	C3	H19	110.55(14)
H18	C3	H19	107.00(11)
C8	C9	H20	109.1(8)
C8	C9	H21	112.6(7)
C8	C9	H22	111.5(7)
H20	C9	H21	107.5(10)
H20	C9	H22	108.1(11)
H21	C9	H22	107.9(12)
C8	C10	H23	111.8(6)
C8	C10	H24	109.4(8)
C8	C10	H25	112.1(6)
H23	C10	H24	107.5(10)
H23	C10	H25	108.1(11)
H24	C10	H25	107.7(11)
C8	C11	H26	108.5(10)
C8	C11	H27	111.8(8)
C8	C11	H28	113.1(10)
H26	C11	H27	108.0(15)
H26	C11	H28	107.3(13)
H27	C11	H28	107.9(16)

Thu 29. Aug 10:23:52 2013 Page 6

7 Publikationsliste

Marko Schmidt, Johannes J. Wittmann, Roman Kress, Denis Schneider, Stefan Steuernagel, Hans-Werner Schmidt, Jürgen Senker: Crystal Structure of a Highly Efficient Clarifying Agent for Isotactic Polypropylene, *Cryst. Growth & Des.* 2012, **12**(**5**), 2543.

Marko Schmidt, Johannes J. Wittmann, Roman Kress, Hans-Werner Schmidt, Jürgen Senker: Probing self-assembled 1,3,5-benzenetrisamides in isotactic polypropylene by ^{13}C DQ solid-state NMR spectroscopy, *Chem. Commun.* 2013, **49**, 267.

Christoph S. Zehe, **Marko Schmidt**, Renée Siegel, Sandra Ganzleben, Hans-Werner Schmidt, Jürgen Senker: Crystal Structure Determination of a Symmetrically Substituted Fluorine Containing BTA with NMR-crystallographic Strategies, *to be submitted*.

Marko Schmidt, Christoph S. Zehe, Renée Siegel, Johannes U. Heigl, Christoph Steinlein, Hans-Werner Schmidt and Jürgen Senker: NMR-Crystallographic Study of Two-Dimensionally Self-Assembled Cyclohexane-Based Low-Molecular-Mass Organic Compounds, *Cryst. Eng. Comm.* 2013*,* **15**, 8784.

Matthias Stöter, Daniel A. Kunz, **Marko Schmidt**, Dunja Hirsemann, Hussein Kalo, Bernd Putz, Jürgen Senker, Josef Breu: Nanoplatelets of Sodium Hectorite Showing Aspect Ratios of ≈20000 and Superior Purity**,** *Langmuir* 2013, **29**(**4**), 1280.

8 Danksagung

Mein Dank gilt an erster Stelle meinem Doktorvater Prof. Dr. Jürgen Senker, der mir auch nach den ersten 18 Monaten Promotion, in denen nicht wirklich etwas zu Stande kam, weiterhin Vertrauen in mich setzte, mir ein komplett neues Thema übertrug und mich in diesem mit allen Freiheiten ausstattete. Ich danke für die hervorragenden Arbeitsbedingungen sowie die immer und immer wiederkehrenden lehr- aber auch hilfreichen Gespräche und Diskussionen, die gelegentlich durchsetzt waren mit dezent sarkastischen und schwarz-humorigen Untertönen, was mir dann den Tag doch leicht versüßte.

Des Weiteren danke ich Prof. Dr. Hans-Werner Schmidt (Lehrstuhl für Makromolekulare Chemie 1) als universitätsinterner Kooperationspartner für die produktive Zusammenarbeit als auch seine hilfreichen Kommentare und Ratschläge hinsichtlich des Erstellens der gemeinsamen Publikationen. Prof. Dr. Ernst Rößler (Lehrstuhl für Experimentalphysik 2) genießt meinen Dank für seine bereitgestellte Erfahrung, seine pragmatische Objektivität sowie seine unmenschliche stoische Ruhe.

Ein besonderer Dank gilt Dr. Wolfgang Milius für seinen Rat und seine Hilfe bezüglich kristallographischer Fragen sowie den Technikern Bernd und Beate für ihre unermüdliche und vielseitige Unterstützung während meiner gesamten Promotion, besonders für das Aufspannen der gefühlt Tausend Kapillaren.

Außerdem bedanke ich mich bei allen Kollegen und Freunden von früher und heute - nicht nur innerhalb der Lehrstühle AC 1 und AC 3 - sondern auch übergreifend an anderen Fakultäten. Es sind so unzählige Menschen, dass es praktisch unmöglich ist, sie alle namentlich zu erwähnen. Deshalb versuche ich erst gar nicht. Damit sich im Nachhinein keiner beschweren kann, belasse ich es bei dieser doch recht allgemeinen Formulierung. Es war eine sehr schöne und angenehme Zeit, nicht nur fachlich, sondern auch auf sozialer Ebene. Die gemeinsamen kulturellen Erlebnisse im zwischenmenschlichen Bereich inner- und außerhalb der Universität haben viel zu meinem Erfolg beigetragen.

Das werde ich nie vergessen; es war mir eine Ehre, mit diesen Leuten gedient zu haben!

Zum Schluss möchte ich noch meiner Familie danken. Durch ihre immerwährende Unterstützung und vor allem ihre absolute Rücksichtnahme auf mein individuelles Gelingen bei diesem Großprojekt hat mir extrem geholfen, den gewünschten Erfolg zu erzielen. Daher sei diese Arbeit auch meiner Familie gewidmet. Rock’nRoll...

9 (Eidesstattliche) Versicherungen und Erklärungen

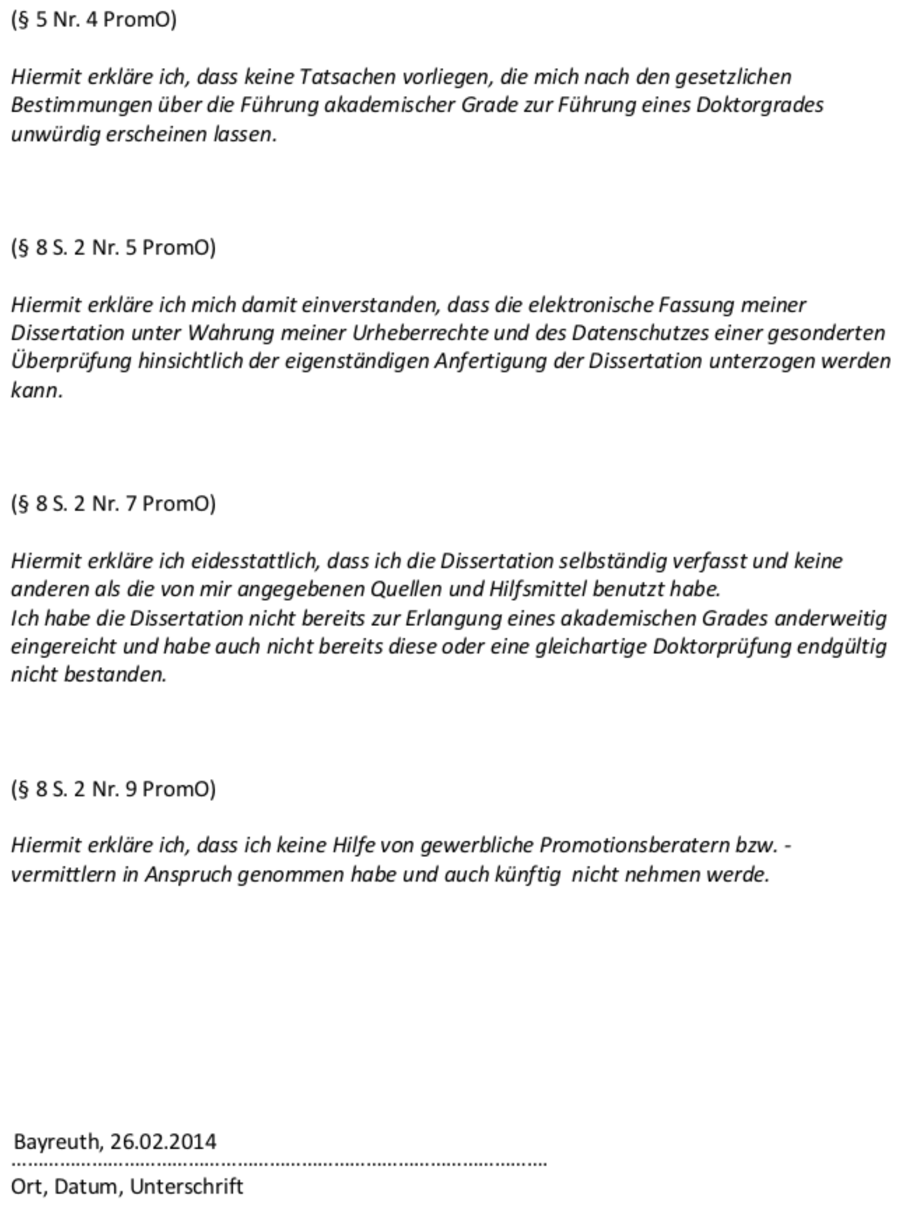

(§ 5 Nr. 4 PromO)

Hiermit erkläre ich, dass keine Tatsachen vorliegen, die mich nach den gesetzlichen Bestimmungen über die Führung akademischer Grade zur Führung eines Doktorgrades unwürdig erscheinen lassen.

(§ 8 S. 2 Nr. 5 PromO)

Hiermit erkläre ich mich damit einverstanden, dass die elektronische Fassung meiner Dissertation unter Wahrung meiner Urheberrechte und des Datenschutzes einer gesonderten Überprüfung hinsichtlich der eigenständigen Anfertigung der Dissertation unterzogen werden kann.

(§ 8 S. 2 Nr. 7 PromO)

Hiermit erkläre ich eidesstattlich, dass ich die Dissertation selbständig verfasst und keine anderen als die von mir angegebenen Quellen und Hilfsmittel benutzt habe.
Ich habe die Dissertation nicht bereits zur Erlangung eines akademischen Grades anderweitig eingereicht und habe auch nicht bereits diese oder eine gleichartige Doktorprüfung endgültig nicht bestanden.

(§ 8 S. 2 Nr. 9 PromO)

Hiermit erkläre ich, dass ich keine Hilfe von gewerbliche Promotionsberatern bzw. -vermittlern in Anspruch genommen habe und auch künftig nicht nehmen werde.

Bayreuth, 26.02.2014
……………………………………………………………………………
Ort, Datum, Unterschrift